THE UNIVERSITY OF CHICAGO

HUNTING FOR NEW PHYSICS IN THE HIGGS AND NEUTRINO SECTORS

A DISSERTATION SUBMITTED TO
THE FACULTY OF THE DIVISION OF THE PHYSICAL SCIENCES
IN CANDIDACY FOR THE DEGREE OF
DOCTOR OF PHILOSOPHY

DEPARTMENT OF PHYSICS

BY
NINA MIREILLE COYLE

CHICAGO, ILLINOIS
JUNE 2023

TABLE OF CONTENTS

LIST OF FIGURES

LIST OF TABLES

ACKNOWLEDGMENTS

Although a thesis has only one author, a PhD is the product of the efforts and support of a whole group of people. First and foremost, I'd like to thank my advisor, Carlos, who has provided guidance, advice, exciting ideas, and quite a few laughs along the way. We began working together when I was still an undergrad, and our work together has been a major part of the last 8 years of my life. I'd also like to thank the other mentor figures I've been lucky enough to pick up along the way. Marcela Carena, who has been so supportive of me not only as a researcher but also as a person, which I appreciate more than I can express. Pedro Machado and Shirley Li, who have been incredibly supportive along my path to neutrino physics and who have acted as mentors far beyond what I could have asked of them as collaborators.

I also have a number of friends and family to thank. First, the Lace group, who have been in contact almost daily in one form or another ever since we met in intro physics as undergraduates. Next, Claire Baum and Emily Smith, who acted as my crisis support crew more often than they probably intended to sign up for, and without whom the last 6 years would have been a lot more painful and a whole lot less fun. And finally, thank you to my family, for always believing that this moment would eventually arrive, probably more than I did.

ABSTRACT

While the Standard Model (SM) of particle physics presents a complete and well-tested theory, there remain important pieces missing from our understanding of high energy physics. Two of the most promising sectors in which to search for beyond the SM (BSM) physics are the Higgs and neutrino sectors, which are the two least well-understood of the Standard Model. In this work, we examine these two sectors and their interplay with BSM models through the lens of experimental evidence. We begin with an examination of the Large Hadron Collider (LHC) Higgs, which appears so far to be SM-like, in a number of contexts. We first examine the indirect constraints one may impose on light Higgs Yukawa couplings given existing rate measurements from the ATLAS and CMS experiments. We then move to an examination of low energy minimal supersymmetric models, focusing on an inversion of the bottom Yukawa and its phenomenological consequences. Finally, we analyze a high-energy theory in which one may dynamically obtain alignment of the physical and SM-like Higgs states. The results of these studies illustrate that there are a number of ways in which new physics may still manifest in the Higgs sector. We then move to an examination of new physics searches in the neutrino sector, focusing on the impact of neutrino-nucleus cross section modeling on new physics signals in neutrino accelerator experiments. While neutrino experiments provide a rich environment to study BSM physics, we find that cross section uncertainties limit our sensitivity to new physics. Finally, we end with an analysis of theoretical bounds on two Higgs doublet models (2HDM), with an application of these bounds on the phenomenology of general 2HDMs.

CHAPTER 1

INTRODUCTION

Over the past century, the field of particle physics has undergone a series of major shifts and differing eras: the development of quantum field theory (QFT) in the 1920's and 30's, the subsequent skepticism and discarding of the QFT formalism, the resuscitation of QFT through the renormalization group in the 50's, the discovery of the top quark in the 90's, and the completion of the Standard Model (SM) of particle physics in 2012 with the discovery of the Higgs boson. At present, the field at first glance appears to be a solved problem: we have a self-consistent, complete theory that does an excellent job at explaining almost all experimental results of the past century.

One might therefore ask why physicists are working so hard to find something that is *inconsistent* with the Standard Model. Why are we so intent on breaking our hard-earned, well-functioning theory? As always in physics, the answer lies in the hope of finding something new. While the SM successfully models everything that it *attempts* to explain, there are observed phenomena for which the SM simply does not have any explanation. In addition, there are lingering theoretical concerns that, while not directly linked to any specific experimental result, indicate to physicists that there must be something further going on. Two particular sectors of the SM stand out as promising places in which new physics might be hiding: the Higgs and neutrino sectors, which are the two least well-understood sectors of the SM. Our level of precision in the Higgs sector is still on the order of a few to ten percent, leaving room for the observed Higgs to either be SM-like or depart from our SM expectations. The consequences of these results on possible new physics models would be significant in either case. The neutrino sector, meanwhile, is still incomplete based on experimental measurements: we do not know their mass ordering, nor do we understand how they gain their masses in the first place or why they are so much less massive than everything else in the SM. The richness of these sectors lies in both identifying what these sectors truly look like and understanding *why* they look the way they do.

This thesis explores the current landscape of searches for new physics in these two sectors, with an emphasis on the theoretical models that attempt to explain these outstanding questions and the effects of their confrontation with experimental results. We analyze the impacts of current experimental results on the allowed parameter spaces of these models, and examine new ways in which we can search for these models using results from our flagship particle physics experiments. The aim of this work is to maximize our understanding of potential new physics given the current reach of our experiments, and work towards charting a course for future searches. Without understanding what we know and can extract now, we will not know where to look next and what might still be hiding just beyond reach.

In the following chapters, we discuss these issues in detail. In Chapter 2, we introduce the Standard Model in its current form, with a particular emphasis on the Higgs and neutrino sectors, and discuss the open questions which the SM is unable to answer. We then move to models of beyond the Standard Model (BSM) physics in Chapter 3, introducing each model that will be examined in detail in later chapters. We identify the open questions which each model aims to address and introduce the basic framework of each BSM model. In Chapter 4 we begin a more detailed phenomenological examination of the LHC Higgs, with an emphasis on understanding the limits we can place on Higgs parameters that are not yet directly observable. We then move to an analysis of minimal supersymmetric models in the context of the LHC results in Chapter 5, examining two potential realizations of supersymmetry and identifying the ways in which they may be consistent with the LHC observations. In Chapter 6 we pivot to an examination of new physics searches in neutrino experiments, while in Chapter 7 we derive theoretical bounds on extended Higgs sectors. Finally, we conclude in Chapter 8.

CHAPTER 2

THE STANDARD MODEL: WHERE ARE WE NOW?

This thesis focuses on analyses of experimental observations within the context of new physics models beyond the Standard Model. In order to understand why we undertake these analyses, we first need to understand the state of the Standard Model in its current form; this will provide context for these searches and motivate the reasons behind searching for new physics. In this chapter, we discuss the gauge structure upon which the SM is built, the particle content of the SM, the SM Higgs mechanism, and the neutrino sector. We then introduce the outstanding puzzles in particle physics which motivate us to search for physics beyond the Standard Model.

2.1 Gauge structure of the SM

Let us start with an explicit example of the simplest case of gauge invariance: a $U(1)$ symmetry. Consider a fermion ψ that transforms under this $U(1)$ symmetry under the fundamental representation:

$$\psi(x) \to e^{i\alpha(x)}\psi(x). \tag{2.1}$$

Because the symmetry is a gauge symmetry, depending on x, the derivative term in the Lagrangian will have a nontrivial transformation:

$$\begin{aligned} \bar{\psi} i \not{\partial} \psi &\to \bar{\psi} e^{-i\alpha(x)} i e^{i\alpha(x)} \not{\partial} \psi + \bar{\psi} e^{-i\alpha(x)} i \gamma \psi \partial_\mu e^{i\alpha(x)} && (2.2) \\ &= \bar{\psi} i \not{\partial} \psi - \bar{\psi} i \gamma^\mu \psi \partial_\mu \alpha && (2.3) \end{aligned}$$

Our goal is to write a covariant derivative $D_\mu \psi$ such that the fermion kinetic term $\bar{\psi} i \not{D} \psi$ is invariant under the $U(1)$ gauge transformation. To obtain this behavior, we need $D_\mu \psi \to$

$e^{i\alpha(x)}D_\mu\psi$, meaning we must cancel this extra term coming from the derivative of $\alpha(x)$. One introduces a gauge field A_μ with the following transformation:

$$A_\mu(x) \to A_\mu(x) - \frac{1}{g}\partial_\mu\alpha(x) \tag{2.4}$$

which we include in the definition of the covariant derivative in the following way:

$$D_\mu\psi = (\partial_\mu + igA_\mu)\psi. \tag{2.5}$$

With this additional field included in the covariant derivative, the derivative term $\partial_\mu\alpha(x)$ coming from the transformation of $\partial_\mu\psi$ is canceled by the transformation of A_μ.

The gauge field also has a kinetic term in the Lagrangian, constructed from the field strength tensor:

$$\mathcal{L}_{\text{gauge,kin}} = -\frac{1}{4}F^{\mu\nu}F_{\mu\nu} \tag{2.6}$$

where

$$F_{\mu\nu} = \partial_\mu A_\nu - \partial_\nu A_\mu. \tag{2.7}$$

For non-abelian gauge groups, the above formalism is modified slightly. The single variable α is replaced by $t^a\theta^a(x)$, where t^a are the generators of the n-dimensional representation of the gauge group. These generators satisfy the Lie algebra of the group:

$$[t^a, t^b] = if^{abc}t^c \tag{2.8}$$

The gauge fields are introduced into the covariant derivative as

$$D_\mu = \partial_\mu + igt^a A^a_\mu. \tag{2.9}$$

In this case, the field strength tensor is given by

$$F^a_{\mu\nu} = \partial_\mu A^a_\nu - \partial_\nu A^a_\mu - gf^{abc}A^b_\mu a^c_\nu. \tag{2.10}$$

The interaction of the fermionic and scalar particles under a particular gauge group is defined by the representation under which each particle transforms. In the Standard Model, all particles transform under either the fundamental or trivial representations of the SM gauge groups. If a particle transforms under the trivial representation, it does not interact through the related force.

The Standard Model is built on the gauge symmetries $SU(3)_C \times SU(2)_L \times U(1)_Y$: the $SU(3)$ “color" associated with quantum chromodynamics (QCD) and the strong interaction, the $SU(2)_L$ associated with weak isospin, and $U(1)_Y$ the weak hypercharge. The latter two groups will be broken under electroweak symmetry breaking down to $U(1)_{EM}$, giving rise to our more familiar weak and electromagnetic interactions. We will see this mechanism in detail in Section 2.3.

Before electroweak symmetry breaking, the Lagrangian obeys this full $SU(3)_C \times SU(2)_L \times U(1)_Y$ gauge group; thus, to retain gauge invariance in the kinetic terms for the fermionic content, one requires gauge bosons, identified as:

1. eight G^a_μ associated with $SU(3)_C$;
2. three W^a_μ associated with $SU(2)_L$;
3. one B_μ associated with $U(1)_Y$.

Let us identify the $SU(3)_C$ generators as T^a_C, and the $SU(2)_L$ generators as T^a_L. The covariant derivative for the SM is then written as

$$D_\mu \psi = (\partial_\mu + i g_s T^a_c G^a_\mu + i g T^a_L W^a_\mu + i g' Y B_\mu)\psi \tag{2.11}$$

where Y is the hypercharge of the particle ψ, defining how it transforms under $U(1)_Y$. In the fundamental representation of $SU(2)_L$, the generators are $T^a_L = \frac{1}{2}\tau^a$, where τ^a are the Pauli matrices.

2.2 Particle content of the SM

The full set of the SM fermionic content and each particle's representation under the SM gauge groups is shown in Table 2.1. Note that **3** indicates the fundamental 3-dimensional representation under $SU(3)_C$, and similarly for **2** and $SU(2)_L$. A **1** for either of these indicates the trivial (1-dimensional) representation.

Field	$SU(3)_C$	$SU(2)_L$	$U(1)_Y$
L	**1**	**2**	-1/2
l_R	**1**	**1**	-1
Q	**3**	**2**	1/6
u_R	**3**	**1**	2/3
d_R	**3**	**1**	-1/3

Table 2.1: The fermionic content of the Standard Model

We can write the $SU(2)_L$ doublets L and Q more clearly, including all three generations, as:

$$L_1 = \begin{pmatrix} \nu_e \\ e_L \end{pmatrix}, \quad L_2 = \begin{pmatrix} \nu_\mu \\ \mu_L \end{pmatrix}, \quad L_3 = \begin{pmatrix} \nu_\tau \\ \tau_L \end{pmatrix}, \tag{2.12}$$

while the left-handed quark doublets are

$$Q_1 = \begin{pmatrix} u_L \\ d_L \end{pmatrix}, \quad Q_2 = \begin{pmatrix} c_L \\ s_L \end{pmatrix}, \quad Q_3 = \begin{pmatrix} t_L \\ b_L \end{pmatrix}. \tag{2.13}$$

As we will see in the next section, the EM charge is given in terms of the $SU(2)_L$ and $U(1)_Y$ quantum numbers as[1] $Q = T^3 + Y$. As such, we identify the hypercharge of each particle in terms of its EM charge and it transformation under $SU(2)_L$. As an illustration, consider the right- and left-handed up quarks: u_R transforms trivially under $SU(2)_L$, meaning that $Y = Q = 2/3$. The left-handed up quark, meanwhile, has $T^3 = 1/2$, and therefore $Y = 2/3 - 1/2 = 1/6$. On the other hand, d_L has $T^3 = -1/2$ and $Q = -1/3$, leading to $Y = 1/6$.

Putting everything together, the full SM Lagrangian before electroweak symmetry breaking is

$$\mathcal{L}_{SM} = -\frac{1}{4}G^a_{\mu\nu}G^{a\mu\nu} - \frac{1}{4}W^a_{\mu\nu}W^{a\mu\nu} - \frac{1}{4}B_{\mu\nu}B^{a\mu\nu} \tag{2.14}$$

$$+ \bar{L}_i i\not{D} L_i + \bar{l}_{Ri} i\not{D} l_{Ri} + \bar{Q}_i i\not{D} Q_i + \bar{u}_{Ri} i\not{D} u_{Ri} + \bar{d}_{Ri} i\not{D} d_{Ri} \tag{2.15}$$

where i are generation indices for the fermions.

2.3 The Higgs Mechanism

We now turn to the Higgs mechanism and the generation of fermion and weak gauge boson masses. A nice overview of this topic may be found in e.g. Ref. [1].

For fermions in the SM, mass terms have the form

$$m_e \bar{e} e = m_e(\bar{e}_L e_R + \bar{e}_R e_L) \tag{2.16}$$

---

[1] There is an alternative convention in which $Q = T^3 + \frac{1}{2}Y$. In this case one would find values for Y that are twice what we identify here.

where e is a four-component spinor and $e_{L,R}$ are two-component spinors. From this expression, it is clear that the $SU(2)_L$ symmetry of the Standard Model prohibits one from simply writing down a mass term, since e_L will transform non-trivially under $SU(2)_L$ while e_R will transform trivially. Meanwhile, masses for the weak gauge bosons of the form $\frac{1}{2}M^2 W_\mu W^\mu$ will break the $SU(2)_L \times U(1)_Y$ gauge symmetry. To illustrate this, we can take for example the photon, which is massless due to the unbroken $U(1)_{QED}$ symmetry:

$$\frac{1}{2}M^2 A_\mu A^\mu \to \frac{1}{2}M^2 (A_\mu - \frac{1}{e}\partial_\mu \alpha)(A^\mu - \frac{1}{e}\partial^\mu \alpha) \neq \frac{1}{2}M^2 A_\mu A^\mu \tag{2.17}$$

The gauge structure of the SM therefore prohibits us from simply writing down mass terms for the massive gauge bosons and fermions. This presents an issue for the SM theory, as we have experimentally observed that the weak gauge bosons and the fermions are massive. However, if the underlying theory obeys the full SM gauge group, and it is the particular choice of vacuum that breaks this symmetry, one can obtain mass terms. This mechanism is generally known as spontaneous symmetry breaking, and in the particular case of the generation of SM masses it is known as the Higgs mechanism.

In addition to the rest of the SM particle content, one introduces a complex $SU(2)_L$ doublet Φ:

$$\Phi = \begin{pmatrix} \phi^+ \\ \phi^0 \end{pmatrix} \tag{2.18}$$

with hypercharge $Y_\Phi = +1/2$, such that one may write down $U(1)_Y$-invariant couplings of Φ with, for example, $\bar{d}_L d_R$, which has $Y = -1/2$.

This doublet interacts with the fermions of the SM through Yukawa couplings:

$$\mathcal{L}_Y = y_u \bar{Q}\tilde{\Phi} u_R + y_d \bar{Q}\Phi d_R + y_e \bar{L}\Phi e_R + h.c. \tag{2.19}$$

where we have defined $\tilde{\Phi} = i\tau_2\Phi^*$, which has hypercharge $Y_\Phi = -1/2$. The Higgs kinetic and potential terms of the Lagrangian are given by

$$\mathcal{L}_H = (D^\mu\Phi)^\dagger(D_\mu\Phi) - \mu^2\Phi^\dagger\Phi - \lambda(\Phi^\dagger\Phi)^2 \tag{2.20}$$

In the case where $\mu^2 < 0$, the Higgs potential gains a minimum away from the origin, located at the vacuum expectation value (vev) $v = \sqrt{-\mu^2/\lambda}$. To preserve QED charge conservation, the vev must be in the neutral component of the Higgs doublet, i.e.

$$\langle 0|\Phi|0\rangle = \begin{pmatrix} 0 \\ \frac{v}{\sqrt{2}} \end{pmatrix} \tag{2.21}$$

Now one expands about the vacuum, defining the SM Higgs field H as fluctuations about the vacuum,

$$\Phi = \begin{pmatrix} \theta_2 + i\theta_1 \\ \frac{v+H}{\sqrt{2}} - i\theta_3 \end{pmatrix} \tag{2.22}$$

where $\theta_{1,2,3}$ are real fields, with the notation chosen such that it is easier to see that

$$\Phi = e^{i\tau^a\theta_a} \begin{pmatrix} 0 \\ \frac{v+H}{\sqrt{2}} \end{pmatrix} \tag{2.23}$$

where $a = 1, 2, 3$. We may absorb this exponential piece through a transformation to the so-called unitary gauge, $\Phi \to e^{-i\tau^a\theta_a}\Phi$, in which

$$\Phi = \begin{pmatrix} 0 \\ \frac{v+H}{\sqrt{2}} \end{pmatrix}. \tag{2.24}$$

With this expansion, the kinetic term becomes

$$
\begin{aligned}
(D^\mu\Phi)^\dagger D_\mu\Phi &= \left|\left(\partial_\mu + \frac{i}{2}g\tau^a W_\mu^a + \frac{i}{2}g' B_\mu\right)\Phi\right|^2 \qquad (2.25)\\
&= \frac{1}{2}\partial^\mu H \partial_\mu H + \frac{1}{8}\left(g^2(v+H)^2|W_\mu^1 + iW_\mu^2|^2 + (v+H)^2|gW_\mu^3 - g'B_\mu|^2\right).
\end{aligned}
$$

We define the gauge bosons $W^\pm$, Z, and A by

$$W_\mu^\pm = W_\mu^1 \mp iW_\mu^2 \qquad (2.26)$$

$$Z_\mu = \frac{1}{\sqrt{g^2+(g')^2}}\left(gW_\mu^3 - g'B_\mu\right) \qquad (2.27)$$

$$A_\mu = \frac{1}{\sqrt{g^2+(g')^2}}\left(g'W_\mu^3 + gB_\mu\right). \qquad (2.28)$$

With this identification, the $U(1)_{QED}$ photon remains massless, while the weak gauge bosons $W^\pm$ and Z gain masses

$$M_W = \frac{vg}{2} \qquad (2.29)$$

$$M_Z = \frac{v\sqrt{g^2+(g')^2}}{2}. \qquad (2.30)$$

As we see in the definition of A and Z, this mechanism induces mixing between the $SU(2)_L$ gauge boson W^3 and the $U(1)_Y$ gauge boson B. The related mixing angle is known as the Weinberg angle, θ_W, defined by:

$$\begin{pmatrix} Z \\ A \end{pmatrix} = \begin{pmatrix} \cos\theta_W & -\sin\theta_W \\ \sin\theta_W & \cos\theta_W \end{pmatrix}\begin{pmatrix} W^3 \\ B \end{pmatrix}. \qquad (2.31)$$

The angle θ_W may be written in terms of g and g' as

$$\cos\theta_W = \frac{g}{\sqrt{g^2 + (g')^2}}. \tag{2.32}$$

The weak gauge boson masses have been measured experimentally as [2]

$$M_W = 80.377 \pm 0.012 \text{ GeV} \qquad M_Z = 91.1876 \pm 0.0021 \text{ GeV}. \tag{2.33}$$

The Higgs vev v has been measured to be $v \simeq 246$ GeV.

Let's examine the couplings of these newly-defined bosons to matter. To do so, we define $T^{\pm} = T^1 \pm iT^2$ and rewrite the covariant derivative in terms of $W^{\pm}_{\mu}$, Z_{μ}, and A_{μ}:

$$\begin{aligned}
D_\mu = \partial_\mu + i\frac{g}{\sqrt{2}}(T^+ W^+_\mu + T^- W^-_\mu) \qquad (2.34)\\
+ igT_3(\sin\theta_W A_\mu + \cos\theta_W Z_\mu) + ig'Y(\cos\theta_W A_\mu - \sin\theta_W Z_\mu)\\
= \partial_\mu + i\frac{g}{\sqrt{2}}(T^+ W^+_\mu + T^- W^-_\mu) \qquad (2.35)\\
+ \frac{ig}{\cos\theta_W} Z_\mu(\cos^2\theta_W\, T^3 - \sin^2\theta_W\, Y) + ig\sin\theta_W A_\mu(T^3 + Y)
\end{aligned}$$

Given the above expressions, we identify the $U(1)$ EM charge as $Q = T^3 + Y$.

Meanwhile, the Yukawa sector of the SM becomes

$$\begin{aligned}
\mathcal{L} \supset \frac{y_u}{\sqrt{2}}\bar{u}_L(v+H)u_R + \frac{y_d}{\sqrt{2}}\bar{d}_L(v+H)d_R + \frac{y_e}{\sqrt{2}}\bar{e}_L(v+H)e_R + h.c. \qquad (2.36)\\
\supset \frac{y_u v}{\sqrt{2}}\bar{u}_L u_R + \frac{y_u}{\sqrt{2}}\bar{u}_L H u_R + ... \qquad (2.37)
\end{aligned}$$

We have now obtained mass terms for the SM fermions, with the identification that

$$m_f = \frac{y_f v}{\sqrt{2}} \tag{2.38}$$

In other words, the Yukawa couplings must be directly proportional to the fermion masses:

$$y_f = \frac{\sqrt{2}m_f}{v} \tag{2.39}$$

In this manner, the SM Higgs couplings to fermions are predicted to have specific values. Deviations from these predicted couplings would indicate non-Standard physics, and it is therefore of great interest to measure the observed LHC Higgs couplings to high precision.

An observant reader might have noticed that while we have written down Yukawa terms for both the up- and down-type quarks, in the lepton sector we have a term only for the electron, muon, and tau; the neutrinos are missing. Since the SM does not include right-handed neutrinos, the Higgs mechanism cannot provide a mass term for the neutrinos. We will discuss this issue in the later sections.

2.4 The neutrino sector

Within the Standard Model, neutrinos are unique in a few aspects. Firstly, they are the only fermion for which we have not yet observed a right-handed particle. As a consequence of this fact, neutrinos do not currently obtain a mass through the Higgs mechanism, which as we saw in the previous section requires both a left- and right-handed component. While not an issue on its own—in the SM, neutrinos can be massless—this becomes an interesting puzzle because of the second manner in which neutrinos are unique: neutrino oscillations. Neutrino oscillations indicate that neutrinos must be massive, and new physics is therefore required to introduce mass terms for the neutrinos. The final manner in which neutrinos are unique is their small mass scale: cosmology and terrestrial experiments bound the neutrino mass scale to be on the order of 1 eV or less. The tiny scale of the neutrino masses introduces a further new physics puzzle: how might the neutrino mass mechanism explain the hierarchy between the neutrino masses and the rest of the fermions? All of these considerations together make the neutrino sector an extremely promising sector in which to search for new physics. In this section, we present the basics of neutrino oscillations and long-baseline oscillation experiments; we reserve a discussion of solutions to the above puzzles for the next chapter.

To describe neutrino oscillations, we can turn to basic quantum mechanics. We will examine the propogation of a neutrino flavor eigenstate through vacuum, in which case the mass eigenstates will be the propogating eigenstates. Suppose there is mixing between the interaction eigenstates and the mass eigenstates, and consider a two-flavor scenario:

$$|\nu_\alpha\rangle = \cos\theta\,|\nu_1\rangle + \sin\theta\,|\nu_2\rangle \tag{2.40}$$

$$|\nu_\beta\rangle = -\sin\theta\,|\nu_1\rangle + \cos\theta\,|\nu_2\rangle \tag{2.41}$$

where $|\nu_{\alpha,\beta}\rangle$ are the interaction eigenstates and $|\nu_{1,2}\rangle$ are the mass eigenstates.

Suppose we create flavor eigenstate ν_α in an interaction, and want to examine the state after propagating a time t. The time evolution is simply given by

$$|\nu_\alpha(t)\rangle = \cos\theta e^{-iE_1t}\,|\nu_1\rangle + \sin\theta e^{-iE_2t}\,|\nu_2\rangle \tag{2.42}$$

Now consider the probability of measuring $|\nu_\beta\rangle$ after time t:

$$\begin{aligned} P(\nu_\alpha \to \nu_\beta) &= |\,\langle\nu_\beta|\nu_\alpha(t)\rangle\,|^2 &(2.43)\\ &= \left|-\sin\theta\cos\theta e^{-iE_1t} + \sin\theta\cos\theta e^{-iE_2t}\right|^2 &(2.44)\end{aligned}$$

Note that the difference in energy arises from the mass difference. By approximating small mass relative to p, with $p \approx E$, and taking $L = ct$, one can obtain

$$P(\nu_\alpha \to \nu_\beta) = \sin^2(2\theta)\sin^2\left(\frac{\Delta m^2_{21}L}{4E}\right) \tag{2.45}$$

where $\Delta m_{21}^2 = m_2^2 - m_1^2$.

In the Standard Model, there are (at least) three flavors of neutrinos. In this case, the above oscillation expression is generalized to

$$P(\nu_\alpha \to \nu_\beta) = \delta_{\alpha\beta} - 4 \sum_{i<j}^{1 \ldots n} \mathrm{Re}(U_{\alpha i}^* U_{\beta i} U_{\alpha j} U_{\beta j}^*) \sin^2\left(\frac{\Delta m_{ij}^2 L}{4E}\right) \tag{2.46}$$

$$+ 2 \sum_{i<j}^{1 \ldots n} \mathrm{Im}(U_{\alpha i}^* U_{\beta i} U_{\alpha j} U_{\beta j}^*) \sin^2\left(\frac{\Delta m_{ij}^2 L}{2E}\right) \tag{2.47}$$

where U is the mixing matrix that relates the flavor and mass eigenstates; in particular,

$$|\nu_\alpha\rangle = \sum_{i=1}^{3} U_{\alpha i}^* \, |\nu_i\rangle \tag{2.48}$$

Assuming only three flavors of neutrinos, U is a unitary 3x3 matrix known as the Pontecorvo-Maki-Nakagawa-Sakata (PMNS) matrix [3, 4]. In general such matrices have 9 degrees of freedom; however, for Dirac neutrinos 5 of those parameters can be absorbed into lepton phases, leaving 4 remaining degrees of freedom. This can be parametrized in a number of ways, but the most common is in terms of three mixing angles and one CP-violating phase.

In particular,

$$\begin{aligned} U_{PMNS} &= \begin{pmatrix} U_{e1} & U_{e2} & U_{e3} \\ U_{\mu 1} & U_{\mu 2} & U_{\mu 3} \\ U_{\tau 1} & U_{\tau 2} & U_{\tau 3} \end{pmatrix} && (2.49) \\ &= \begin{pmatrix} 1 & 0 & 0 \\ 0 & c_{23} & s_{23} \\ 0 & -s_{23} & c_{23} \end{pmatrix} \begin{pmatrix} c_{13} & 0 & s_{13}e^{-i\delta_{CP}} \\ 0 & 1 & 0 \\ -s_{13}e^{i\delta_{CP}} & 0 & c_{13} \end{pmatrix} \begin{pmatrix} c_{12} & s_{12} & 0 \\ -s_{12} & c_{12} & 0 \\ 0 & 0 & 1 \end{pmatrix} && (2.50) \\ &= \begin{pmatrix} c_{12}c_{13} & s_{12}c_{13} & s_{13}e^{-\delta} \\ -s_{12}c_{23} - c_{12}s_{13}s_{23}e^{i\delta} & c_{12}c_{23} - s_{12}s_{13}s_{23}e^{i\delta} & c_{13}s_{23} \\ s_{12}s_{23} - c_{12}s_{13}c_{23}e^{i\delta} & -c_{12}s_{23} - s_{12}s_{13}c_{23}e^{i\delta} & c_{13}c_{23} \end{pmatrix} && (2.51) \end{aligned}$$

For Majorana neutrinos, one would introduce two further complex phases, as the Majorana condition fixes two phases, leading to the following parametrization:

$$U_{PMNS} = \begin{pmatrix} c_{12}c_{13} & s_{12}c_{13} & s_{13}e^{-\delta} \\ -s_{12}c_{23} - c_{12}s_{13}s_{23}e^{i\delta} & c_{12}c_{23} - s_{12}s_{13}s_{23}e^{i\delta} & c_{13}s_{23} \\ s_{12}s_{23} - c_{12}s_{13}c_{23}e^{i\delta} & -c_{12}s_{23} - s_{12}s_{13}c_{23}e^{i\delta} & c_{13}c_{23} \end{pmatrix} \begin{pmatrix} e^{i\eta_1} & 0 & 0 \\ 0 & e^{i\eta_2} & 0 \\ 0 & 0 & 1 \end{pmatrix} \tag{2.52}$$

The two mass splittings in the SM have been measured to be [5]

$$\Delta m^2_{21} = 7.39^{+0.21}_{-0.20} \times 10^{-5}\ \mathrm{eV}^2 \tag{2.53}$$

$$|\Delta m^2_{32}| = 2.449^{+0.032}_{-0.030}\ \times 10^{-3}\mathrm{eV}^2 \tag{2.54}$$

The best-fit value of Δm^2_{32} depends slightly on the choice of ordering for the neutrino masses; here we present the best-fit value for normal ordering, which we will define shortly. Due to the neutrino sources from which these mass splittings were originally measured, the splitting

Δm^2_{12} is often called the "solar" mass splitting, while Δm^2_{32} is referred to as the "atmospheric" mass splitting. You may notice that while we have written an absolute value of Δm^2_{32}, we have specified the sign of Δm^2_{21}. Although vacuum oscillations are insensitive to the sign of the mass splittings, matter effects are impacted by the sign [6]; the sign of Δm^2_{21} has been identified through the impact of matter effects within the sun, known as the MSW effect.

Meanwhile, the mixing angles have been measured as [5]

$$\sin^2\theta_{12} = 0.310^{+0.013}_{-0.012} \tag{2.55}$$

$$\sin^2\theta_{23} = 0.558^{+0.020}_{-0.033} \tag{2.56}$$

$$\sin^2\theta_{13} = \left(2.241^{+0.066}_{-0.065}\right) \times 10^{-2} \tag{2.57}$$

2.5 What's missing?

With the introduction of the Higgs mechanism and the discovery of the Higgs boson in 2012, the Standard Model as described above is a complete theory. However, while the SM is internally complete and self-consistent, a number of experimental observations as well as theoretical considerations indicate that there must be new physics beyond the SM. In this section, we review the observed phenomena and theoretical concerns which motivate searches for new physics.

A very notable gap in the SM, perhaps the most notable, has been left out of this chapter: the description of gravity. To many theorists, the unification of QFT and gravity is the ultimate goal, and has inspired a great deal of research efforts. While this question can be linked to the motivation for supersymmetry—string theory, one potential unified theory, requires supersymmetry—the work of this thesis is not directly motivated by a search for a unified theory. We therefore do not dive into a detailed discussion of this topic.

2.5.1 Dark matter

Dark matter (DM) presents one of the most concrete indications of new physics observed to date. Astrophysical observations of galaxy rotation curves have identified that the rotation speed of the galaxies corresponds to a gravitational force greater than that generated by the visible matter [7–10]. Additionally, the cosmological evolution of the universe indicates that there must be an additional matter density, contributing to the formation of large structures at late times.

A dark matter candidate must satisfy a few important conditions. Firstly, it must be stable relative to cosmological timescales in order to contribute the required matter density [11]. Secondly, it must be neutral or very weakly charged under the electromagnetic and strong interactions. Finally, it must be massive such that it contributes to the matter density of the universe, rather than radiation density.

The SM does not contain a viable dark matter candidate within its particle content. Neutrinos have some of the relevant properties, but their small mass means that they behave as radiation until very late time and do not contribute as matter density in the formation of large structures. Black holes have been proposed as an alternative non-BSM source of the required DM matter density, but these have run into a number of experimental constraints.

Due to these considerations, it is widely accepted that new physics is required to model dark matter. In the next chapter, we will introduce a few models which provide a dark matter candidate and discuss the details of the particular DM candidates for each model.

2.5.2 Neutrino masses

In examining the formulae for neutrino oscillations, one may notice that the oscillations vanish for massless neutrinos, where $\Delta m_{ij}^2 = 0$. Because we have observed neutrino oscillations in a wide range of experiments, we know that at least two flavors of neutrinos must have non-zero mass. As noted in the discussion of the Higgs mechanism, the SM in its current formulation does not include a mass mechanism for neutrinos, and the observation of neutrino oscillations therefore provides clear, concrete evidence that there is new physics beyond the SM.

Within the question of neutrino masses lurks another theoretical concern. Tritium β-decay experiment KATRIN place an upper bound on the neutrino mass scale of approximately 1 eV [12]; as such, the neutrinos are orders of magnitude less massive than the other fermions in the SM. Models of neutrino masses typically aim to both introduce a mass mechanism and explain why the neutrino masses are so small relative to the scale of the other fermion masses.

Broadly speaking, there are two possible types of neutrino mass terms, related to the nature of the neutrino and its antiparticle. In the first case, the neutrino is a Dirac fermion, and can gain its mass through the Higgs mechanism with the simple addition of right-handed neutrinos. In the second case, the neutrino is a Majorana fermion, meaning that the neutrino is its own antiparticle. Although there is a wide range of specific possibilities, we discuss here two possible mechanisms as an illustration: a straightforward Dirac neutrino realization, and a Majorana mass mechanism derived through a seesaw mechanism.

First, we examine the case that the neutrino is a Dirac fermion, similarly to the other fermions in the SM. In this case, there will be an independent right-handed component which we denote as ν_R. Then we can write a neutrino mass term similarly to the up-type quark mass terms:

$$\mathcal{L}_{mass,\nu} = y_\nu \bar{L}\tilde{\Phi}\nu_R + h.c. \tag{2.58}$$

As before, spontaneous symmetry breaking yields mass terms of the form

$$\mathcal{L}_{mass,\nu} = m_\nu(\bar{\nu}_L\nu_R + \bar{\nu}_R\nu_L). \tag{2.59}$$

Although this method successfully introduces neutrino masses to the SM Lagrangian, the Yukawa couplings alone (along with the fixed scale v) are responsible for defining the mass scale of the neutrinos. In this case, the neutrino Yukawa couplings must be on the order of $\mathcal{O}(10^{-12})$ to reproduce neutrino masses of $\mathcal{O}(10^{-1})$ eV. These values of the Yukawa couplings are many orders of magnitude smaller than those of the other fermionic SM particles. Additionally, the most general Lagrangian can contain a Majorana mass term for the right-handed neutrinos, as they transform as singlets under the entire $SU(3)_C \times SU(2)_L \times U(1)_Y$ gauge group. These two considerations help motivate an analysis of the Majorana case.

Thus, we now turn to an examination of the seesaw mechanism that gives rise to Majorana neutrinos. Here we present material contained in Ref [13]. For a particle to be a Majorana fermion, the operator which creates and annihilates the particle must be the same. In this case, the charge-conjugate field $\nu^c(x) = C\bar{\nu}^T(x)$ is equal to the original field $\nu(x)$, and therefore the right-handed component is not an independent component of the field but rather the charge-conjugate of the left-handed component: $\nu_R = \nu_L^c$. Majorana mass terms are therefore given by

$$\mathcal{L}_{mass,\nu} = -\frac{1}{2} m_\nu \left(\bar{\nu}_L^c \nu_L + \bar{\nu}_L \nu_L^c \right) . \tag{2.60}$$

As before, such mass terms explicitly break $SU(2)$ symmetry. One may in fact obtain terms of this form through the Higgs mechanism by including the previous Higgs-neutrino interaction term as well as introducing Majorana mass terms for heavy right-handed neutrinos of the form

$$\mathcal{L}_{H,\text{lept}} \supset -\lambda_\nu^{i\alpha} \bar{L}^i \tilde{\Phi} N^\alpha - \frac{1}{2} M^{\alpha\beta} \bar{N}^\alpha (N^\beta)^c + h.c. \tag{2.61}$$

The generation indices on the left-handed and right-handed neutrinos are differentiated to indicate that the number of right-handed neutrino generations has not been specified, and may not be equal to 3. With these terms, the diagonalization of the resulting mass matrix after EWSB leads to Majorana mass terms for the left-handed neutrino. Explicitly, EWSB yields a Dirac mass matrix $m_D^{i\alpha}$, which combines with the Majorana mass matrix $M^{\alpha\beta}$ to give

$$\mathcal{L}_{H,\mathrm{lept}} \supset -\frac{1}{2} \begin{pmatrix} (\bar{\nu}_L^i)^c & \bar{N}^\alpha \end{pmatrix} \begin{pmatrix} 0^{ij} & (m_D^T)^{i\beta} \\ m_D^{\alpha j} & M^{\alpha\beta} \end{pmatrix} \begin{pmatrix} \nu_L^j \\ (N^\beta)^c \end{pmatrix} \tag{2.62}$$

For $M \gg m_D$, this matrix gives approximate Majorana mass terms for the left-handed neutrinos of the form

$$m^{ij} \approx -(m_D^T)^{i\alpha}(M^{-1})^{\alpha\beta} m_D^{\beta j} \tag{2.63}$$

and the mass matrix becomes approximately block diagonal, with the heavy right-handed neutrinos effectively decoupling from the light left-handed neutrinos.

An advantage of the Majorana case is that the presence of the heavy right-handed Majorana neutrinos introduces a seesaw mechanism, in which the left-handed neutrino masses are suppressed by M^{-1} as seen in Eq. (2.63). As such, the small left-handed neutrino masses may be achieved without very small Yukawa couplings if the right-handed neutrinos are taken to be sufficiently massive.

2.5.3 Matter/antimatter asymmetry

The universe at current times is composed almost entirely of matter, with very little antimatter present with which matter might annihilate. This presents an obvious question: why did the universe end up with so much more matter than antimatter? In particular, this requires that at some point in the evolution of the early universe, the fundamental physics had some preference towards matter rather than antimatter; otherwise, any fleeting asymmetry in the number density of matter relative to antimatter would have been equilibrated.

One may formulate this discussion more precisely using the Sakharov conditions [14]. There are three conditions that must be satisfied for a process to be capable of generating the observed matter/antimatter asymmetry:

1. Baryon number violation
2. C and CP violation
3. interactions out of thermal equilibrium.

It is quite reasonable to ask whether there is a process in the Standard Model that might be able to fulfill these requirements. A potential process which uses SM baryon-violating processes is the mechanism of electroweak baryogenesis (EWBG), which is discussed in detail in [15]. In this model, the asymmetry is generated during the electroweak phase transition, during which there are bubbles of electroweak symmetry-violating regions. Particles within the symmetric-phase plasma will scatter off the bubble wall through a process with CP and C violation, thereby generating an asymmetry in the particle number just outside the bubble wall and satisfying point (2). Electroweak sphaleron processes then translate this asymmetry into a baryon number asymmetry, generating a greater number of baryons than antibaryons (satisfying point (1)); the bubble wall then sweeps up this asymmetry, and because the sphaleron processes are heavily suppressed within the broken-phase region, the asymmetry is preserved (satisfying point (3)).

Hypothetically, all of these ingredients could be contained in the SM; however, the SM as realized in our universe does not fulfill all of the necessary requirements. Firstly, the bubble nucleation upon which EWBG relies requires a first-order phase transition. In the SM, the EW phase transition would be first-order for $m_H \lesssim 70$ GeV; however, the observed Higgs at the LHC has a mass of $m_H \simeq 125$ GeV. Additionally, the CP-violation in the SM, contained in the CKM phase, is too small to generate the required initial asymmetry at the bubble wall. As such, any model of electroweak baryogenesis necessarily requires the introduction of new physics.

A wide range of further mechanisms have also been explored in recent years, including leptogenesis [16], axiogenesis [17], and more. In leptogenesis models, heavy Majorana neutrinos generate a lepton number asymmetry, which is then converted to a baryon number asymmetry through sphaleron processes. In axiogenesis, one introduces an axion, which is related to a new symmetry known as a Peccei-Quinn (PQ) symmetry. An explicit breaking of the PQ symmetry in the early universe induces rotations of the axion, and the asymmetry of the PQ charge is then translated into a baryon number asymmetry.

2.5.4 The hierarchy problem

In the SM, there is in fact more than one so-called “hierarchy problem": this term may be applied to any large discrepancy in scales that has no current explanation in the SM. One sometimes hears the small magnitude of the neutrino masses relative to the other SM fermions as a hierarchy problem. In this thesis, however, we will use the term “hierarchy problem" to refer specifically to the scale of the Higgs mass relative to the Planck scale.

Let us again write down the SM Higgs potential in terms of the field H:

$$V = \mu^2 |H|^2 + \lambda |H|^4 \tag{2.64}$$

Based on results from the ATLAS and CMS experiments at the LHC, we know that $m_H \approx 125$ GeV and thus in the SM, $\lambda = 0.126$ and $\mu^2 = -(93 \text{ GeV})^2$. However, the μ^2 term can receive contributions from any new physics introduced at a scale Λ, and therefore without any sort of cancellation or protection would naturally be pushed up to the scale Λ. The electroweak scale is therefore highly sensitive to new physics.

Another way to think about the hierarchy problem is through the SM as an effective field theory. Suppose the SM is valid as an effective theory up to some scale Λ. Loop diagrams will contribute terms of order Λ^2 to the H mass term, thus pushing this scale up towards the new physics scale Λ.

Due to these concerns, theorists are motivated to introduce new physics which might protect the Higgs mass scale or cancel these loop contributions. This is one primary motivation for supersymmetry, which we will see in the next chapter.

2.5.5 Short baseline anomalies

Over the last two decades, the standard three neutrino paradigm introduced above has been confronted with experimental anomalies that could indicate oscillations due to a mass splitting much larger than the measured solar and atmospheric ones. These anomalies are fourfold: LSND [18], MiniBooNE [19], reactor [20–22], and gallium [23–28] anomalies. The LSND anomaly resides in the $\bar{\nu}_\mu \to \bar{\nu}_e$ appearance channel, with an excess of electron antineutrino appearance events corresponding to an oscillation probability of $P(\bar{\nu}_\mu \to \bar{\mu}_e) \approx 0.26\%$. The MiniBooNE experiment followed up on these results with a similar L/E ratio, but a different baseline and energy, and a different set of systematics. The resulting analyses found an excess of ν_e appearance events in the low-energy bins of 0.2-0.4 GeV for a baseline of approximately 0.5 km, consistent with the LSND results. The reactor anomalies observe a deficit of $\bar{\nu}_e$ neutrinos produced by nuclear reactors; however, questions about the flux predictions have indicated that this anomaly may be driven more by initial flux uncertainties than short-baseline oscillations.

All these anomalies seem consistent with oscillations at a baseline distance much shorter than expected from the SM splittings, pointing to a new mass splitting $\Delta m^2_{41} \sim \mathcal{O}(1 \text{ eV}^2)$. On the other hand, direct [29–31] and indirect [32] measurements of the Z invisible width at LEP would imply that this state does not interact via weak interactions and thus has no standard model gauge quantum number whatsoever. In the next chapter, we will introduce the light sterile neutrino model, which has been proposed as a solution to the short baseline anomalies.

CHAPTER 3

BEYOND THE STANDARD MODEL

In the previous chapter, we discussed the current formulation of the Standard Model and introduced a number of motivations for looking for new physics. In this chapter, we introduce the models of BSM physics that will be examined in detail in the following chapters. We discuss two Higgs doublet models (2HDM), minimal supersymmetric models, and light sterile neutrinos. In each case, we will make note of the outstanding questions that each model aims to address, and note some of the challenges each model faces.

3.1 Two Higgs doublet models

2HDM's extend the SM Higgs sector by adding an additional Higgs doublet, leading to two total Higgs doublets. This introduces a great deal of additional parameters to the Higgs sector, and additionally significantly relaxes the SM restrictions on the Higgs couplings to the rest of the SM particle content. One motivation of 2HDM's is that the Higgs potential has a greater number of parameters and can have a first-order EW phase transition, thus providing the potential to include electroweak baryogensis [33]. Additionally, 2HDM's are necessarily included in models of supersymmetry, which we will introduce in the next section.

The most general scalar potential in the 2HDM is given by

$$\begin{aligned} V = {} & m_{11}^2\Phi_1^\dagger\Phi_1 + m_{22}^2\Phi_2^\dagger\Phi_2 - (m_{12}^2\Phi_1^\dagger\Phi_2 + h.c.) \\ & + \frac{\lambda_1}{2}(\Phi_1^\dagger\Phi_1)^2 + \frac{\lambda_2}{2}(\Phi_2^\dagger\Phi_2)^2 + \lambda_3(\Phi_1^\dagger\Phi_1)(\Phi_2^\dagger\Phi_2) + \lambda_4|\Phi_1^\dagger\Phi_2|^2 \\ & + \left(\frac{\lambda_5}{2}(\Phi_1^\dagger\Phi_2)^2 + \lambda_6(\Phi_1^\dagger\Phi_1)(\Phi_1^\dagger\Phi_2) + \lambda_7(\Phi_2^\dagger\Phi_2)(\Phi_1^\dagger\Phi_2) + h.c.\right) \end{aligned} \tag{3.1}$$

where $\Phi_{1,2}$ are complex $SU(2)$ doublets with hypercharge $Y = +1/2$. Notice that since the potential must be real, the parameters $\lambda_{1,\ldots 4}$ must be real, but $\lambda_5, \lambda_6, \lambda_7$ can be complex.

Since there are now two Higgs doublets, the SM particle content recieves contributions to their masses from both doublets. In the most general formulation, the fermions can have interactions with both Higgs doublets, leading to mass matrices of the form

$$M_{ij} = \frac{1}{\sqrt{2}} \left(y^1_{ij} v_1 + y^2_{ij} v_2 \right) \tag{3.2}$$

where i, j are generation indices, and the y matrices represent the Yukawa matrices for up quarks, down quarks, or leptons.

We define the quantity $\tan\beta = v_2/v_1$, the ratio of the vacuum expecation values of the two doublets. The total vacuum expecation value is $v = \sqrt{v_1^2 + v_2^2} = 246$ GeV. We may write the Higgs doublets in terms of real scalar fields as

$$\Phi_j = \begin{pmatrix} \phi_j^+ \\ (v_j + \phi_j + i\eta_j)/\sqrt{2} \end{pmatrix} \tag{3.3}$$

Let us move to a basis in which only one of the doublets obtains a vev, which we call the Higgs basis. Let H_{SM} be the field associated with the doublet that obtains the full vev, $v = 246$ GeV, and H_{NSM} the field associated with the doublet which does not obtain a vev; the reason for this specific notation will become clear shortly. The initial basis and the Higgs basis are related by β:

$$H_{\text{SM}} = \phi_1 \cos\beta + \phi_2 \sin\beta \tag{3.4}$$

$$H_{\text{NSM}} = -\phi_1 \sin\beta + \phi_2 \cos\beta \tag{3.5}$$

The fermion couplings will be

$$\begin{aligned}\mathcal{L}_{\text{Yuk}} &= \frac{1}{\sqrt{2}}\left(y^1_{ij}\cos\beta + y^2_{ij}\sin\beta\right)H_{\text{SM}}\bar{f}^i_L f^j_R \\ &\quad + \frac{1}{\sqrt{2}}\left(-y^1_{ij}\sin\beta + y^2_{ij}\cos\beta\right)H_{\text{NSM}}\bar{f}^i_L f^j_R + h.c. \qquad (3.6)\\ &\equiv Y^1_{ij}H_{\text{SM}}\bar{f}^i_L f^j_R + Y^2_{ij}H_{\text{NSM}}\bar{f}^i_L f^j_R + h.c. \qquad (3.7)\end{aligned}$$

Since only H_{SM} has a non-zero vev, the fermion mass matrices arise entirely from the Y^1_{ij} Yukawas. Moving to the fermion mass basis, in which this first term is diagonal, one has

$$Y^1_{ij} = \frac{\sqrt{2}m_i}{v}\delta_{ij} \tag{3.8}$$

Thus, the Yukawa couplings of H_{SM} must be Standard Model-like. However, Y^2_{ij} is not necessarily diagonalized along with Y^1_{ij}, and as the physical Higgs states will include some H_{NSM} component, this can lead to tree-level flavor-changing neutral currents (FCNC). Since such interactions have not been observed experimentally, one must introduce some method of suppressing them; the different approaches to restricting Y^2_{ij} to diagonal form differentiate types of 2HDMs. The different types of 2HDMs typically involve up- and down-type fermions coupling to only one of the Higgs doublets; to implement the specific structures, different types of $\mathbb{Z}_2$ symmetries are implemented to allow certain Yukawa terms while forbidding others.

In anticipation of the following discussion, it is worth introducing the mass eigenstate basis. In the 2HDM, one obtains five physical Higgs fields rather than just one: two CP-even fields h and H, one CP-odd field A, and a charged Higgs $H^{\pm}$ with two possible charges.

Define α as the angle of rotation from the ϕ basis to the mass basis for the CP-even fields:

$$h = \phi_1 \sin\alpha - \phi_2 \cos\alpha \tag{3.9}$$

$$H = \phi_2 \cos\alpha + \phi_2 \sin\alpha \tag{3.10}$$

It is often more instructive to write h and H in terms of the Higgs basis fields, which are related as

$$h = H_{\text{SM}} \sin(\beta - \alpha) + H_{\text{NSM}} \cos(\beta - \alpha) \tag{3.11}$$

$$H = H_{\text{SM}} \cos(\beta - \alpha) - H_{\text{NSM}} \sin(\beta - \alpha) \tag{3.12}$$

Thus, the couplings $\mathcal{Y}^{1,2}$ of the physical neutral, CP-even Higgs fields to the fermions are given by

$$\mathcal{Y}^1_{ij} = Y^1_{ij} \sin(\beta - \alpha) + Y^2_{ij} \cos(\beta - \alpha) \tag{3.13}$$

$$\mathcal{Y}^1_{ij} = Y^1_{ij} \cos(\beta - \alpha) - Y^2_{ij} \sin(\beta - \alpha) \tag{3.14}$$

We will derive more explicit expressions for these couplings for each type of 2HDM in the following subsections.

While the fermionic couplings differ amongst the various 2HDM types, the vector gauge boson couplings and are given by

$$g_{hVV} = g^{SM}_{hVV} \sin(\beta - \alpha) \tag{3.15}$$

One can immediately see that such a relation places strong bounds on 2HDMs under the requirement that one obtain an SM-like lighter Higgs eigenstate; this consequence will be seen later in a number of contexts.

3.1.1 Type I 2HDM

In a Type I 2HDM, all fermions couple to only one of the two $\Phi_{1,2}$ doublets; take this doublet to be Φ_2. In this case, y^1_{ij} vanishes the the two Higgs basis matrices are directly proportional:

$$Y^1_{ij} = y^2_{ij} \sin\beta \tag{3.16}$$

$$Y^2_{ij} = y^2_{ij} \cos\beta \tag{3.17}$$

In this case, Y^2_{ij} will be diagonalized simultaneously with Y^1_{ij}, and FCNCs are avoided.

The physical Higgs couplings can be found by writing the $Y^{1,2}_{ij}$ in terms of the fermion masses, using the relations

$$\frac{\sqrt{2}m_i}{v}\delta_{ij} = Y^1_{ij} \tag{3.18}$$

and

$$Y^2_{ij} = Y^1_{ij} \cot\beta \tag{3.19}$$

For the lighter physical state, therefore, one obtains couplings

$$\mathcal{Y}^1_{ij} = \frac{\sqrt{2}m_i}{v}\delta_{ij}\Big(\sin(\beta-\alpha) + \cos(\beta-\alpha)\cot\beta\Big) \tag{3.20}$$

From this expression, we see that h will have approximately SM-like couplings to all fermions for $\sin(\beta-\alpha) \approx 1$ and $\cos(\beta-\alpha)\cot\beta \ll 1$.

3.1.2 Type II 2HDM

In defining the Type I 2HDM, we assumed that all fermions coupled only to the second doublet Φ_2, which resulted in Higgs basis matrices which were directly proportional. The principle behind the Type II 2HDM is quite similar; however, in this model up-type quarks couple only to Φ_2, while down-type fermions (down-type quarks and leptons) couple to Φ_1.

In this case, the up-type quark couplings to the lighter mass eigenstate look exactly the same as in Type I. The down-type fermions, on the other hand, will have couplings of the form

$$\mathcal{Y}^1_{ij} = \frac{\sqrt{2} m_i}{v} \delta_{ij} \Big(\sin(\beta - \alpha) - \cos(\beta - \alpha) \tan\beta \Big) \tag{3.21}$$

Notice that in a Type II model, modifications to the up-type quarks are suppressed by a factor of $\tan\beta$, while modifications to down-type fermions are enhanced by $\tan\beta$; in this case, one may obtain significant modifications to down-type fermion couplings without major deviations of the up-type couplings from SM values. This feature of Type-II 2HDMs will be revisited in later chapters.

3.1.3 Basic phenomenology

Introducing a second doublet to the Higgs sector provides a number of additional degrees of freedom, thereby presenting the opportunity to approach, for instance, the problem of matter/antimatter asymmetry [33]; however, this also gives rise to a number of phenomenological consequences that place bounds on the parameter values the 2HDM can take on. Firstly, the 125 GeV Higgs observed at the LHC thus far appears to be SM-like at the level of about 10% precision [34, 35]. In this case, 2HDM parameters must take on values such that the phenomenology of the lighter CP-even Higgs eigenstate is consistent with the SM predictions at this level of precision. Secondly, the Higgs sector now has a heavier CP-even Higgs, a CP-odd Higgs, and a charged Higgs; all of these can potentially be observed at the LHC, for example through a search for $H, A \to \tau\tau$ processes. The fact that we have not yet observed such processes indicates that either the masses of the new Higgs states are beyond the current reach of the LHC, or that the Yukawas and Higgs potential parameters take on values such that these processes are suppressed or otherwise avoid detection in LHC searches. These types of constraints and phenomenological considerations will be examined in more detail in the following chapters.

3.1.4 Higgs basis conversion

For completeness, we present the relations between the mass terms and the quartic couplings in the weak eigenstate basis and in the Higgs basis. The potential in the Higgs basis reads:

$$\begin{aligned} V = {}& M_{11}^2 H_1^\dagger H_1 + M_{22}^2 H_2^\dagger H_2 - (M_{12}^2 H_1^\dagger H_2 + h.c.) \\ &+ \frac{1}{2} Z_1 (H_1^\dagger H_1)^2 + \frac{1}{2} Z_2 (H_2^\dagger H_2)^2 + Z_3 (H_1^\dagger H_1)(H_2^\dagger H_2) + Z_4 (H_1^\dagger H_2)(H_2^\dagger H_1) \\ &+ \left[\frac{1}{2} Z_5 (H_1^\dagger H_2)^2 + Z_6 (H_1^\dagger H_1)(H_1^\dagger H_2) + Z_7 (H_2^\dagger H_2)(H_1^\dagger H_2) + h.c. \right] . \end{aligned} \tag{3.22}$$

The conversion between the potential parameters in the weak eigenstate basis and those in the Higgs basis have been worked out in [36]. They are obtained by a rotation by an angle β in field space of the original two Higgs doublets. The mass terms in the two bases are related as:

$$m_{11}^2 = M_{11}^2 c_\beta^2 + M_{22}^2 s_\beta^2 + \mathrm{Re}[M_{12}^2 e^{i\eta}] s_{2\beta} \,, \tag{3.23a}$$

$$m_{22}^2 = M_{11}^2 s_\beta^2 + M_{22}^2 c_\beta^2 - \mathrm{Re}[M_{12}^2 e^{i\eta}] s_{2\beta} \,, \tag{3.23b}$$

$$m_{12}^2 e^{i\eta} = \frac{1}{2} (M_{22}^2 - M_{11}^2) s_{2\beta} + \mathrm{Re}[M_{12}^2 e^{i\eta}] c_{2\beta} + i \, \mathrm{Im}[M_{12}^2 e^{i\eta}] \,, \tag{3.23c}$$

where $\tan\beta = v_2/v_1$ with range $0 \le \beta \le \frac{\pi}{2}$, and η is the phase accompanying v_2 in the Φ basis. The relations between the quartic couplings are:

$$\lambda_1 = Z_1 c_\beta^4 + Z_2 s_\beta^4 + \frac{1}{2} Z_{345} s_{2\beta}^2 - 2 s_{2\beta}\left(\mathrm{Re}[Z_6 e^{i\eta}] c_\beta^2 + \mathrm{Re}[Z_7 e^{i\eta}] s_\beta^2\right)\,, \tag{3.24a}$$

$$\lambda_2 = Z_1 s_\beta^4 + Z_2 c_\beta^4 + \frac{1}{2} Z_{345} s_{2\beta}^2 + 2 s_{2\beta}\left(\mathrm{Re}[Z_6 e^{i\eta}] s_\beta^2 + \mathrm{Re}[Z_7 e^{i\eta}] c_\beta^2\right)\,, \tag{3.24b}$$

$$\lambda_3 = \frac{1}{4}\left(Z_1 + Z_2 - 2Z_{345}\right) s_{2\beta}^2 + Z_3 + \mathrm{Re}[(Z_6 - Z_7) e^{i\eta}] s_{2\beta} c_{2\beta}\,, \tag{3.24c}$$

$$\lambda_4 = \frac{1}{4}\left(Z_1 + Z_2 - 2Z_{345}\right) s_{2\beta}^2 + Z_4 + \mathrm{Re}[(Z_6 - Z_7) e^{i\eta}] s_{2\beta} c_{2\beta}\,, \tag{3.24d}$$

$$\begin{aligned}\lambda_5 e^{2i\eta} = {}& \frac{1}{4}(Z_1 + Z_2 - 2Z_{345}) s_{2\beta}^2 + \mathrm{Re}[Z_5 e^{2i\eta}] + i\,\mathrm{Im}[Z_5 e^{2i\eta}] c_{2\beta} \\ & + \mathrm{Re}[(Z_6 - Z_7) e^{i\eta}] s_{2\beta} c_{2\beta} + i\,\mathrm{Im}[(Z_6 - Z_7) e^{i\eta}] s_{2\beta}\,,\end{aligned} \tag{3.24e}$$

$$\begin{aligned}\lambda_6 e^{i\eta} = {}& \frac{1}{2}(Z_1 c_\beta^2 - Z_2 s_\beta^2 - Z_{345} c_{2\beta} - i\,\mathrm{Im}[Z_5 e^{2i\eta}]) s_{2\beta} \\ & + \mathrm{Re}[Z_6 e^{i\eta}] c_\beta c_{3\beta} + i\,\mathrm{Im}[Z_6 e^{i\eta}] c_\beta^2 + \mathrm{Re}[Z_7 e^{i\eta}] s_\beta s_{3\beta} + i\,\mathrm{Im}[Z_7 e^{i\eta}] s_\beta^2\,,\end{aligned} \tag{3.24f}$$

$$\begin{aligned}\lambda_7 e^{i\eta} = {}& \frac{1}{2}(Z_1 s_\beta^2 - Z_2 c_\beta^2 + Z_{345} c_{2\beta} + i\,\mathrm{Im}[Z_5 e^{2i\eta}]) s_{2\beta} \\ & + \mathrm{Re}[Z_6 e^{i\eta}] s_\beta s_{3\beta} + i\,\mathrm{Im}[Z_6 e^{i\eta}] s_\beta^2 + \mathrm{Re}[Z_7 e^{i\eta}] c_\beta c_{3\beta} + i\,\mathrm{Im}[Z_7 e^{i\eta}] c_\beta^2\,,\end{aligned} \tag{3.24g}$$

where we have defined $Z_{345} \equiv (Z_3 + Z_4 + \mathrm{Re}[Z_5 e^{2i\eta}])$. For the reverse conversion from the Higgs basis to the general basis, one can perform the same series of identifications, substituting $\lambda_i \leftrightarrow Z_i$ and $\beta \leftrightarrow -\beta$.

3.1.5 2HDM RGE equations

The RGE equations for couplings in both the SM and the 2HDM can be compactly written as [37]

$$
\begin{aligned}
\frac{d\alpha_3}{dt} &= 7\frac{\alpha_3^2}{4\pi} \\
\frac{d\alpha_2}{dt} &= \beta_2\frac{\alpha_2^2}{4\pi} \\
\frac{d\alpha_1}{dt} &= -\beta_1\frac{\alpha_1^2}{4\pi} \\
\frac{dY_t}{dt} &= Y_t\left(8\tilde{\alpha}_3 + \frac{9}{4}\tilde{\alpha}_2 + \frac{17}{12}\tilde{\alpha}_1 - \frac{9}{2}Y_t - \frac{\alpha_b}{2}Y_b - \alpha_\tau Y_\tau\right) \\
\frac{dY_b}{dt} &= Y_b\left(8\tilde{\alpha}_3 + \frac{9}{4}\tilde{\alpha}_2 + \frac{5}{12}\tilde{\alpha}_1 - \frac{9}{2}Y_b - \frac{\alpha_t}{2}Y_t - Y_\tau\right) \\
\frac{dY_\tau}{dt} &= Y_\tau\left(\frac{9}{4}\tilde{\alpha}_2 + \frac{15}{4}\tilde{\alpha}_1 - \frac{5}{2}Y_\tau - 3Y_b - \alpha_t' Y_t\right)
\end{aligned}
\tag{3.25}
$$

where $\alpha_i = g_i^2/4\pi$, $\tilde{\alpha}_i = \alpha_i/4\pi$, $Y_{t,b} = h_{t,b}^2/16\pi^2$, and $t = \log(M_{GUT}^2/\mu^2)$. The parameters $(\beta_2, \beta_1, \alpha_b, \alpha_t, \alpha_t', \alpha_\tau)$ are equal to $(3, 7, 1, 1, 0, 0)$ for the 2HDM and $(19/6, 41/6, 3, 3, 3, 1)$ for the SM running.

3.2 Supersymmetry

In this section, we introduce the two minimal implementations of a supersymmetric Standard Model: the Minimal Supersymmetric Standard Model (MSSM) and the Next-to-Minimal Supersymmetric Standard Model (NMSSM). Supersymmetry has been a primary target for the LHC over the course of its first two runs and subsequent analysis for a few reasons. Firstly, the particular symmetry from which the name "supersymmetry" arises is the remaining spacetime symmetry that can be added to our current model of physics, and it is therefore quite interesting from a theoretical perspective. In addition, supersymmetry aims to resolve multiple outstanding issues with the Standard Model. The most well-known motivation may be the hierarchy problem, which can be resolved through a cancellation of the loop contributions from the SM particles and their respective superpartners. Additionally, many SUSY models provide a dark matter candidate in the form of the lightest supersymmetric particle (LSP). Furthermore, there is unification of the strong, weak, and electromagnetic gauge couplings at high scales, thus moving towards the possibility of a grand unified theory (GUT) at the so-called GUT scale. Such a unification is motivated by the idea that, at high scales, there is a single unified theory which is broken to the SM gauge group that we observe at lower energies. GUT theories are also motivated by their natural inclusion of right-handed neutrinos, thus approaching a potential solution to neutrino masses. A detailed discussion of unified theories is the realm of a different thesis; here we simply comment on the connection, and focus on the details of minimal supersymmetric standard models.

3.2.1 Minimal Supersymmetric Standard Model

An introduction to supersymmetry and the MSSM can be found in [38, 39]. Because this is the minimal supersymmetric extension of the Standard Model, one simply extends the particle content to include a superfield for each SM particle and a 2HDM in the Higgs sector (as will be discussed shortly). The spin-1 gauge bosons are in vector supermultiplets with their spin-1/2 fermionic counterparts:

- Gluons and gluinos G_a^μ and $\tilde{G}_a$ in a superfield $\hat{G}_a$, with representation (8,1,0)
- W bosons and winos W_a^μ and $\tilde{W}_a$ in superfield $\hat{W}_a$, with representation (1,3,0)
- B boson and bino B_a^μ and $\tilde{B}_a$ in superfield $\hat{B}_a$, with representation (1,1,0)

where we have quoted their representations under the SM gauge group by $(SU(3)_C, SU(2)_L, U(1)_Y)$. The neutral winos, the bino, and neutral Higgsinos mix for form neutral fermionic mass eigenstates called neutralinos, while the charged wino and charged Higgsino mix to form mass eigenstates known as charginos. If R-parity symmetry is imposed, the lightest neutralino will be stable and can be a candidate for dark matter, as it is electrically neutral and interacts only weakly.

Meanwhile, the fermionic content remains constricted to three generations, and no right-handed neutrinos are added to the theory. The quarks, squarks, leptons, and sleptons are placed in chiral superfields,

- (u_L, d_L) and $(\tilde{u}_L, \tilde{d}_L)$ in superfield $\hat{Q}$, representation (3,2,$\frac{1}{3}$)
- $\bar{u}_R$ and $\tilde{u}^*_R$ in $\hat{U}^c$, representation $(\bar{3}, 1, -\frac{4}{3})$
- $\bar{d}_R$ and $\tilde{d}^*_R$ in $\hat{D}^c$, representation $(\bar{3}, 1, \frac{2}{3})$
- (ν_L, e_L) and $(\tilde{\nu}_L, \tilde{e}_L)$ in $\hat{L}$, representation (1,2,-1)
- $\bar{e}_R$ and $\tilde{e}^*_R$ in $\hat{E}^c$, representation (1,1,2)

This is the simplest extension of the SM particle content, with each fermionic particle placed in a superfield with a spin-0 supersymmetric partner. Written as $SU(2)_L$ doublets, the left-handed fields above are

$$\hat{Q} = \begin{pmatrix} \hat{U}_L \\ \hat{D}_L \end{pmatrix}, \quad \hat{L} = \begin{pmatrix} \hat{\nu}_L \\ \hat{E}_L \end{pmatrix} \tag{3.26}$$

In the Higgs sector, one requires two Higgs doublet superfields $\hat{H}_u$ and $\hat{H}_d$ to cancel chiral anomalies. In particular, loops of chiral fermions can lead to a breaking of $U(1)_Y$ symmetry; while these contributions are canceled within each SM fermion family, the addition of a Higgsino from the superfield $\hat{H}_u$ leads to a nonzero contribution that must be canceled by a Higgsino with opposite hypercharge, coming from $\hat{H}_d$. Note that this therefore must be a Type-II 2HDM theory, where there is one Higgs doublet coupling to up-type fermions and another to down-type, so that the two Higgsinos have opposite hypercharge (to see this, compare the required hypercharge for the doublet in each term as shown in the discussion of Eq. 2.19). Thus the Higgs sector is composed of

- H_d and $\tilde{H}_d$ in $\hat{H}_d$, with (1,2,-1)

- H_u and $\tilde{H}_u$ in $\hat{H}_u$, with (1,2,1)

Written as $SU(2)_L$ doublets,

$$\hat{H}_u = \begin{pmatrix} \hat{H}_u^+ \\ \hat{H}_u^0 \end{pmatrix}, \quad \hat{H}_d = \begin{pmatrix} \hat{H}_d^0 \\ \hat{H}_d^- \end{pmatrix} \tag{3.27}$$

The superpotential W of the MSSM is given by

$$W = -Y_{ij}^u \hat{U}_i^c \hat{H}_u \cdot \hat{Q}_j + Y_{ij}^d \hat{D}_i^c \hat{H}_d \cdot \hat{Q}_j + Y_{ij}^l \hat{E}_i^c \hat{H}_d \cdot \hat{L}_j + \mu \hat{H}_u \cdot \hat{H}_d \tag{3.28}$$

where $\hat{H} \cdot \hat{Q} = \epsilon_{ab} \hat{H}^a \hat{Q}^b$, with a, b $SU(2)_L$ indices. Explicitly, for example, $\hat{H}_u \cdot \hat{H}_d = H_u^+ H_d^- - H_u^0 H_d^0$.

In an unbroken supersymmetry, the particles and their SUSY partners have the same mass. Given results from the LHC, where no supersymmetric partners have yet been observed up to about a TeV scale, any supersymmetric theory must have soft SUSY breaking terms; namely, one includes mass terms for the supersymmetric particles. In particular, for an R-parity conserving case the soft SUSY-breaking Lagrangian is given by

$$\begin{aligned} \mathcal{L}_{SU\!\!\!/SY} = {} & \frac{1}{2} M_1 \tilde{B} \tilde{B} + \frac{1}{2} M_2 \tilde{W}^a \tilde{W}_a + \frac{1}{2} M_3 \tilde{G}^a \tilde{G}_a \\ & + m_{H_d}^2 |H_d|^2 + m_{H_u}^2 |H_u|^2 + \mu B (H_d H_u + h.c.) \\ & + \tilde{Q}_i^* (m_{\tilde{Q}}^2)_{ij} \tilde{Q}_j + \tilde{L}_i^* (m_{\tilde{L}}^2)_{ij} \tilde{L}_j + \tilde{u}_{Ri} (m_{\tilde{u}}^2)_{ij} \tilde{u}_{Rj}^* + \tilde{d}_{Ri} (m_{\tilde{d}}^2)_{ij} \tilde{d}_{Rj}^* + \tilde{e}_{Ri} (m_{\tilde{e}}^2)_{ij} \tilde{e}_{Rj}^* \\ & + (A_U)_{ij} \tilde{Q}_i H_u \tilde{u}_{Rj}^* + (A_D)_{ij} \tilde{Q}_i H_d \tilde{d}_{Rj}^* + (A_l)_{ij} \tilde{L}_i H_d \tilde{e}_{Rj}^* \end{aligned} \tag{3.29}$$

This soft supersymmetry breaking introduces an enormous number of additional degrees of freedom: counting them all adds up to 105 new degrees of freedom added on to the 19 SM degrees of freedom. However, applying some constraints inspired by phenomenological considerations can reduce this number significantly. An unconstrained MSSM with soft breaking will introduce significant CP-violating and flavor-changing interactions. Constraints on these processes lead one to impose certain assumptions ("universality") on the soft SUSY-breaking parameters to avoid violating these constraints. This reduces the number of degrees of freedom down to 22.

Let us consider the Higgs part of the Lagrangian more closely, specifically focusing on electroweak symmetry breaking. In the scalar Higgs potential, we have a positive $|\mu|^2$ mass term and a negative soft SUSY breaking μB mass term. To achieve electroweak symmetry breaking with a vev on the order of 10^2 GeV without a fine-tuned cancellation, we expect the soft term and the $|\mu|^2$ term to be on the order of 10^{2-3}. However, these are two very different dimensionful parameters, and there is no apparent reason why their orders of magnitude might be similar. The problem ultimately boils down to explaining why $\mu \simeq M_{SUSY}$, where M_{SUSY} is the soft SUSY breaking scale. This is known as the "μ problem" of the MSSM, and inspires extensions such as the NMSSM, which we will discuss in the next section.

3.2.2 Next-to-Minimal Supersymmetric Standard Model

In the above discussion of the MSSM, we identified a theoretical issue with the model: namely, we encountered the μ problem, which spoils a potentially interesting feature of a supersymmetric Standard Model. The NMSSM is, in part, a model intended to resolve this issue and introduce a model with a single scale M_{SUSY} in the electroweak sector that requires explanation. Reviews of the NMSSM and its phenomenology can be found in [40, 41].

In particular, one introduces a singlet Higgs superfield $\hat{S}$ in addition to the doublets seen in the MSSM. The Higgs part of the superpotential of the NMSSM has the form

$$W_{\text{Higgs}} = (\mu + \lambda \hat{S})\hat{H}_u \cdot \hat{H}_d + \xi_F \hat{S} + \frac{1}{2}\mu' \hat{S}^2 + \frac{\kappa}{3}\hat{S}^3 \tag{3.30}$$

The parameters μ and μ' are supersymmetric mass parameters, while ξ_F has dimension mass^2. The Yukawa couplings, meanwhile, are the same as in the MSSM,

$$W_{\text{Yuk}} = Y^u_{ij}\hat{U}^c_i\hat{Q}_j \cdot \hat{H}_u + Y^d_{ij}\hat{D}^c_i\hat{H}_d \cdot \hat{Q}_j + Y^l_{ij}\hat{E}^c_i\hat{H}_d \cdot \hat{L}_j \tag{3.31}$$

In the scale-invariant NMSSM, the dimensionful parameters μ, μ', ξ_F are set to 0, which gives the following NMSSM Higgs superpotential,

$$W = \lambda\hat{S}\hat{H}_u \cdot \hat{H}_d + \frac{\kappa}{3}\hat{S}^3 + Y^u_{ij}\hat{U}^c_i\hat{Q}_j \cdot \hat{H}_u + Y^d_{ij}\hat{D}^c_i\hat{H}_d \cdot \hat{Q}_j + Y^l_{ij}\hat{E}^c_i\hat{H}_d \cdot \hat{L}_j \tag{3.32}$$

With this superpotential, the μ term is an effective $\mu_{\text{eff}} = \lambda s$ generated when the singlet $\hat{S}$ gains a vev s, which is on the weak or SUSY scale. Through this mechanism, the NMSSM resolves the μ-problem of the MSSM. This scale invariant version of the NMSSM contains an accidental $\mathbb{Z}_3$ symmetry where the chiral superfields are transformed with a phase $e^{2\pi i/3}$; it is therefore often referred to as the "$\mathbb{Z}_3$-invariant NMSSM".

With these assumptions, the Higgs sector of the NMSSM superpotential is specified by the parameters

$$\lambda,\ \kappa,\ m^2_{H_u},\ m^2_{H_d},\ m^2_S,\ A_\lambda,\ A_\kappa \tag{3.33}$$

where m^2_S is appears in the new soft SUSY-breaking term $m^2_S|S^2|$, and A_λ and A_κ appear in the trilinear terms $\lambda A_\lambda H_u \cdot H_d S$ and $\frac{1}{3}\kappa A_\kappa S^3$, respectively.

Note that now there is a neutral singlino, and thus the neutralino sector has mixing amonst five neutral gauginos. This can modify the phenomenology of the lightest supersymmetric particle, thus affecting the dark matter phenomenology of the model. We will see this in a bit more detail in Chapter 5.

NMSSM RGE equations

In later chapters, we will examine the running of couplings in the NMSSM. The 2-loop RGE [40] for the NMSSM parameters are listed below; the running parameter t is defined here as $t = \ln\left(Q^2/M_Z^2\right)$.

$$
\begin{aligned}
16\pi^2\frac{dg_1^2}{dt} &= 11g_1^4 + \frac{g_1^4}{16\pi^2}\left(\frac{199}{9}g_1^2 + 9g_2^2 + \frac{88}{3}g_3^2 - \frac{26}{3}h_t^2 - \frac{14}{3}h_b^2 - 6h_\tau^2 - 2\lambda^2\right)\\
16\pi^2\frac{dg_2^2}{dt} &= g_2^4 + \frac{g_2^4}{16\pi^2}\left(3g_1^2 + 25g_2^2 + 24g_3^2 - 6h_t^2 - 6h_b^2 - 2h_\tau^2 - 2\lambda^2\right)\\
16\pi^2\frac{dg_3^2}{dt} &= -3g_3^4 + \frac{g_3^4}{16\pi^2}\left(\frac{11}{3}g_1^2 + 9g_2^2 + 14g_3^2 - 4h_t^2 - 4h_b^2\right)\\
16\pi^2\frac{dh_t^2}{dt} &= h_t^2\left(6h_t^2 + h_b^2 + \lambda^2 - \frac{13}{9}g_1^2 - 3g_2^2 - \frac{16}{3}g_3^2\right)\\
&+ \frac{h_t^2}{16\pi^2}\Bigg(- 22h_t^4 - 5h_b^4 - 3\lambda^4 - 5h_t^2h_b^2 - 3h_t^2\lambda^2 - h_b^2h_\tau^2 - 4h_b^2\lambda^2\\
&- h_\tau^2\lambda^2 - 2\lambda^2\kappa^2 + 2g_1^2h_t^2 + \frac{2}{3}g_1^2h_b^2 + 6g_2^2h_t^2 + 16g_3^2h_t^2\\
&+ \frac{2743}{162}g_1^4 + \frac{15}{2}g_2^4 - \frac{16}{9}g_3^4 + \frac{5}{3}g_1^2g_2^2 + \frac{136}{27}g_1^2g_3^2 + 8g_2^2g_3^2\Bigg)\\
16\pi^2\frac{dh_b^2}{dt} &= h_b^2\left(6h_b^2 + h_t^2 + h_\tau^2 + \lambda^2 - \frac{7}{9}g_1^2 - 3g_2^2 - \frac{16}{3}g_3^2\right)\\
&+ \frac{h_b^2}{16\pi^2}\Bigg(- 22h_b^4 - 5h_t^4 - 3h_\tau^4 - 3\lambda^4 - 5h_b^2h_t^2 - 3h_b^2h_\tau^2 - 3h_b^2\lambda^2 \qquad (3.34)\\
&- 4h_t^2\lambda^2 - 2\lambda^2\kappa^2 + \frac{2}{3}g_1^2h_b^2 + \frac{4}{3}g_1^2h_t^2 + 2g_1^2h_\tau^2 + 6g_2^2h_b^2 + 16g_3^2h_b^2\\
&+ \frac{1435}{162}g_1^4 + \frac{15}{2}g_2^4 - \frac{16}{9}g_3^4 + \frac{5}{3}g_1^2g_2^2 + \frac{40}{27}g_1^2g_3^2 + 8g_2^2g_3^2\Bigg)
\end{aligned}
$$

(3.35)

$$
\begin{aligned}
16\pi^2 \frac{dh_\tau^2}{dt} &= h_\tau^2 \left(4h_\tau^2 + 3h_b^2 + \lambda^2 - 3g_1^2 - 3g_2^2\right) \\
&+ \frac{h_\tau^2}{16\pi^2}\Bigg(- 10h_\tau^4 - 9h_b^4 - 3\lambda^4 - 9h_\tau^2 h_b^2 - 3h_\tau^2\lambda^2 - 3h_t^2 h_b^2 - 3h_t^2\lambda^2 \\
&- 2\lambda^2\kappa^2 + 2g_1^2 h_\tau^2 - \frac{2}{3}g_1^2 h_b^2 + 6g_2^2 h_\tau^2 + 16g_3^2 h_b^2 + \frac{75}{2}g_1^4 + \frac{15}{2}g_2^4 + 3g_1^2 g_2^2\Bigg) \\
16\pi^2 \frac{d\lambda^2}{dt} &= \lambda^2 \left(3h_t^2 + 3h_b^2 + h_\tau^2 + 4\lambda^2 + 2\kappa^2 - g_1^2 - 3g_2^2\right) \\
&+ \frac{\lambda^2}{16\pi^2}\Bigg(- 10\lambda^4 - 9h_t^4 - 9h_b^4 - 3h_\tau^4 - 8\kappa^4 - 9\lambda^2 h_t^2 - 9\lambda^2 h_b^2 \\
&- 3\lambda^2 h_\tau^2 - 12\lambda^2\kappa^2 - 6h_t^2 h_b^2 + 2g_1^2\lambda^2 + \frac{4}{3}g_1^2 h_t^2 - \frac{2}{3}g_1^2 h_b^2 + 2g_1^2 h_\tau^2 \\
&+ 6g_2^2\lambda^2 + 16g_3^2 h_t^2 + 16g_3^2 h_b^2 + \frac{23}{2}g_1^4 + \frac{15}{2}g_2^4 + 3g_1^2 g_2^2\Bigg) \\
16\pi^2 \frac{d\kappa^2}{dt} &= \kappa^2 \left(6\lambda^2 + 6\kappa^2\right) + \frac{\kappa^2}{16\pi^2}\Big(- 24\kappa^4 - 12\lambda^4 - 24\kappa^2\lambda^2 \\
&- 18h_t^2\lambda^2 - 18h_b^2\lambda^2 - 6h_\tau^2\lambda^2 + 6g_1^2\lambda^2 + 18g_2^2\lambda^2\Big)
\end{aligned}
$$

3.3 Light sterile neutrinos

As discussed in the previous chapter, short-baseline appearance anomalies in terrestrial neutrino experiments hint that some new physics is present in the oscillations of neutrinos over short baselines. One potential way to model these anomalies is to introduce a sterile (right-handed) neutrino on the scale of about 1 eV, which has a small amount of mixing with the active neutrinos. The mass of the sterile neutrino results in a mass splitting with the other three mass eigenstates of about 1 eV^2, leading to oscillations on much shorter baselines than those present in the SM.

In the most minimal model, one introduces a single sterile neutrino ν_s, which is approximately aligned with a new mass eigenstate ν_4 and has some small mixing with the active neutrinos. The mixing matrix U is extended from a 3-flavor mixing matrix to a 4-flavor one, and can be written as

$$U = \begin{pmatrix} U_{e1} & U_{e2} & U_{e3} & U_{e4} \\ U_{\mu 1} & U_{\mu 2} & U_{\mu 3} & U_{\mu 4} \\ U_{\tau 1} & U_{\tau 2} & U_{\tau 3} & U_{\tau 4} \\ U_{s1} & U_{s2} & U_{s3} & U_{s4} \end{pmatrix} \tag{3.36}$$

Consider the channel $\nu_\alpha \to \nu_\beta$ on short baselines, where SM oscillations are expected to be irrelevant. In this case, the expression for the oscillation probability reduces to a single term, arising from the ν_α and ν_β mixing with the ν_4 eigenstate. In particular,

$$P(\nu_\alpha \to \nu_\beta) \approx \delta_{\alpha\beta} - 4\sum_{i=1}^{3} U^*_{\alpha i} U_{\beta i} U_{\alpha 4} U^*_{\beta 4} \sin^2\left(\frac{\Delta m^2_{4i} L}{4E}\right) \tag{3.37}$$

where we have assumed real mixing matrix elements for ease of illustration. Because $\Delta m^2_{21}, \Delta m^2_{32} \ll 1\ \mathrm{eV}^2$, we can approximate all Δm^2_{4i} to be equal; call this splitting Δm^2_{41}. Now we employ the unitarity of U, specifically the condition $\sum_{i=1}^{4} U^*_{\alpha i} U_{\beta i} = \delta_{\alpha\beta}$, to rewrite

$$P(\nu_\alpha \to \nu_\beta) \approx \delta_{\alpha\beta} - 4(\delta_{\alpha\beta} - U^*_{\alpha 4} U_{\beta 4}) U_{\alpha 4} U^*_{\beta 4} \sin^2\left(\frac{\Delta m^2_{4i} L}{4E}\right) \tag{3.38}$$

$$\approx \delta_{\alpha\beta} - 4|U_{\alpha 4}|^2(\delta_{\alpha\beta} - |U_{\beta 4}|^2) \sin^2\left(\frac{\Delta m^2_{41} L}{4E}\right) \tag{3.39}$$

where in going from the first line to the second, we have identified that in the case $\alpha = \beta$, $U_{\alpha 4} U^*_{\beta 4} = |U_{\alpha 4}|^2 = |U_{\beta 4}|^2$.

We are in particular interested in modeling short-baseline appearance oscillations of $\nu_\mu \to \nu_e$, and we thus identify that we require nonzero mixing for both U_{e4} and $U_{\mu 4}$; the most minimal approach assumes $U_{\tau 4} = 0$. The appearance probability is

$$P(\nu_\mu \to \nu_e) = 4|U_{e4}|^2 |U_{\mu 4}|^2 \sin^2 \left(\frac{\Delta m^2_{41} L}{4E} \right) \tag{3.40}$$

Notice that this probability is proportional to small mixings to the fourth power; on the other hand, disappearance channels $\nu_e \to \nu_e$ and $\nu_\mu \to \nu_\mu$ are proportional to small mixings squared:

$$P(\nu_\mu \to \nu_\mu) = 1 - 4|U_{\mu 4}|^2 (1 - |U_{\mu 4}|^2) \sin^2 \left(\frac{\Delta m^2_{41} L}{4E} \right) \tag{3.41}$$

and similarly for the ν_e channel. This means that any modeling of the appearance signal through the introduction of a sterile neutrino will necessarily affect disappearance rates, with the appearance rate suppressed by two factors of the mixings relative to the disappearance rates. The presence of appearance anomalies and lack of disappearance anomalies at short baselines leads to significant tension for the 3+1 light sterile neutrino model [42–44]. This tension is mainly driven by the following experiments: MINOS/MINOS+ [45] and IceCube[46, 47] for ν_μ disappearance; Daya Bay [45], as well as solar [48–50], short baseline [51, 52], and radioactive source experiments [28] for ν_e disappearance; and LSND and MiniBooNE for $\nu_\mu \to \nu_e$ appearance. Consequently, the short baseline anomalies remain an open question, and a great deal of experimental efforts focus on following up on these anomalies and probing the sterile neutrino explanation—the short baseline neutrino program (SBN) at Fermilab, including MicroBooNE, is one such example.

CHAPTER 4

BOUNDING THE CHARM YUKAWA

As discussed in the previous sections, the SM Higgs mechanism predicts very specific values for the couplings of the Higgs to the various SM particles. Deviations from these values would indicate a departure from the SM mechanism, and thus hint towards the presence of new physics in the Higgs sector. The Higgs production at the LHC has been probed in many different channels and the rates are in agreement with the SM predicted ones at a level of a few tens of percent [53–55]. Since in the SM those rates are mostly governed by the coupling of the Higgs to weak gauge bosons and third generation quarks, this suggests that the observed Higgs production rates are governed by SM interactions and that those couplings are within tens of percents of their SM predicted values. Global fits to the Higgs precision measurements confirm this picture, showing no clear evidence of new physics coupled to the Higgs [53],[55].

In spite of these facts, it is still very relevant to continue studying the properties of the Higgs boson in great detail. First of all, there could be deviations from the SM predictions at a level not yet probed by the LHC, which may reveal the presence of new physics at the weak scale. Second, the couplings to the first and second generation of quarks and leptons have not been tested and deviations from their SM predicted values may point towards a more complex mechanism of mass generation than the one present in the SM. Third, there may be decays of the Higgs bosons into exotic particles not yet detected by the LHC. Last but not least, there may be hidden correlations between the Higgs couplings that may lead to rates in agreement with the SM predicted ones, in spite of deviations of the couplings from the SM values. In this work, we shall present examples of such possible correlations.

In this work, we study possible effects of the deviations of the charm-quark Higgs coupling with respect to the SM value in the κ framework [56, 57], in which κ_i characterize the ratio of a given coupling with respect to its SM value. Large deviations of κ_c from one affect the

Higgs width and therefore its decay branching ratios, and therefore the couplings of the Higgs to gauge bosons and third generation fermions must be modified as well in order to preserve the agreement with experimental observations. We study these modifications in detail and discuss their impact on the determination of the charm quark coupling to the Higgs boson. The material in this chapter is based on work with Viska Wei and Carlos Wagner.

It is important to note that the κ framework can not replace a more complete study of the Higgs properties based on higher order operators coming from integrating out the new physics at the TeV scale [58–61]. In particular, important effects related to, for instance, the energy dependence of the form factors associated with these operators, or the correlation of the modification of the Higgs couplings with electroweak precision measurements, are missed in the κ framework. However, this framework is appropriate to obtain an estimate of the possible sensitivity to unknown couplings, like the one of the charm quark to the Higgs, where the current bounds are far from the SM values. Moreover, the κ framework is used by the ATLAS and CMS collaborations and hence allows a direct comparison with the experimental results for values of $\kappa_c \simeq 1$.

4.1 Best-fit values on Higgs rates

The rate of a Higgs production and decay process relative to the Standard Model rate is represented by the signal strength μ_{if}, where

$$\mu_{if} = \frac{\sigma_i \times B_f}{(\sigma_i \times B_f)^{SM}}, \tag{4.1}$$

is the ratio of the product of the Higgs production cross section σ_i in a given i-channel and its decay branching ratio B_f in a given f-channel to their SM predicted values. Within the κ framework, the quantity $\sigma_i \times B_f$ can be obtained by a simple rescaling of each couplings by a corresponding factor κ and it is therefore expressed as

$$\sigma_i \times B_f = \kappa_{r,i}^2 \sigma_i^{SM} \times \frac{\kappa_f^2 \Gamma_f^{SM}}{\Gamma_H} \tag{4.2}$$

where $\kappa_{r,i}$ is associated with the relevant Higgs coupling governing the i production mode, while κ_f is associated with the Higgs coupling governing the decay into particles f, with SM partial width Γ_f^{SM}. The total Higgs width Γ_H is hence calculated as

$$\begin{aligned}\Gamma_H =& \Gamma_H^{SM}\big(\kappa_b^2 B_{bb}^{SM} + \kappa_W^2 B_{WW}^{SM} + \kappa_g^2 B_{gg}^{SM} + \kappa_\tau^2 B_{\tau\tau}^{SM} + \kappa_Z^2 B_{ZZ}^{SM} + \kappa_c^2 B_{cc}^{SM} + \kappa_\gamma^2 B_{\gamma\gamma}^{SM} \\ &+ \kappa_{Z\gamma}^2 B_{Z\gamma}^{SM} + \kappa_s^2 B_{ss}^{SM} + \kappa_\mu^2 B_{\mu\mu}^{SM}\big)/(1 - B_{BSM}) \qquad (4.3) \\ \equiv& \, \Gamma_H^{SM} \kappa_H^2, \qquad (4.4)\end{aligned}$$

where B_f^{SM} is the decay branching ratio in a given f channel within the SM and B_{BSM} is the branching ratio of the Higgs decay into beyond the SM particles. Here and in the following we have treated the loop-induced coupling of the Higgs to gluons and photons as independent quantities, and therefore not restricted to the loop contributions of only SM particles.

The rates relative to the SM ones in this framework are therefore written as

$$\mu_{if} = \frac{\kappa_{r,i}^2 \kappa_f^2}{\kappa_H^2}. \tag{4.5}$$

It is important to remark that, considering the photon and gluon couplings as independent variables, the Higgs production rates in the standard channels (gluon fusion, weak boson fusion and associated production of the Higgs with gauge bosons, top and bottom pairs) are not affected in any relevant way by the charm Yukawa coupling. However, the decay rates are affected in a clear way by a modification of κ_c. Indeed, the value of κ_c influences κ_H^2, therefore decreasing the rates of the observed processes by increasing the total width.

Because we are interested in finding an upper bound on $|\kappa_c|$, we will not include a non-zero B_{BSM} term, which would have the same effect on the rates as increases in $|\kappa_c|$.

In order to obtain bounds on $|\kappa_c|$, we examine how well the measured rates can be fitted for increasing values of the charm Yukawa. The fit includes the most recent 13 TeV results for the observed rates from ATLAS, contained in Refs. [53] and [54], and CMS, contained in Ref. [55]. We fit to a weighted average of the experiments' measurements. The free parameters included in our fit are $\{\kappa_b,\ \kappa_W,\ \kappa_t,\ \kappa_Z,\ \kappa_\tau,\ \kappa_g,\ \kappa_\gamma\}$ with κ_c as an input. We examine three scenarios: one in which the values of κ_W and κ_Z are unconstrained, one based on estimates of the bounds coming from precision electroweak measurements, and the last in which $\kappa_W, \kappa_Z \leq 1$. The latter situation is less general but is well motivated by theory. We take $\kappa_{Z\gamma}$, κ_s, and κ_μ to be equal to 1 since they are not directly involved in the fitted processes and may contribute in a relevant way to the total width only for extreme values of their respective κ values.

While performing a fit to the Higgs couplings based on only the currently measured production rates, we found that no meaningful bound on κ_c could be obtained. The reason for this behavior is the existence of a flat direction in the fit for which all κ's increase along with the increasing κ_c. This fact was already emphasized for instance by the authors of Refs. [62–65], who noticed that no additional, unobserved decays may be constrained by a simple fit to the observed production and decay rates. Although this observation was related to a possible invisible decay width, it can also be applied to the case of unobserved decays into charm quarks, in which case, by a suitable modification of the κ_i, the observed rates can be modeled equally well for any value of κ_c. To see this, we can write down the rate for a given observed process as

$$\mu_{if} = \frac{\kappa^4}{\kappa^2(1 - B_{cc}^{SM}) + \kappa_c^2 B_{cc}^{SM}} \tag{4.6}$$

where since all $\mu_{if} \simeq 1$ we have considered that all non-charm Higgs couplings scale together by a single κ value. If we require the signal strengths μ_{if} to be given by a value μ, Eq. (4.6) provides a quadratic equation on κ^2. The solution to this quadratic equation leads to a correlation between the necessary values of the generic κ and κ_c, namely

$$\kappa^2 = \frac{(1 - B_{cc}^{SM})\mu}{2} + \frac{\sqrt{(1 - B_{cc}^{SM})^2\mu^2 + 4\mu B_{cc}^{SM}\kappa_c^2}}{2}. \tag{4.7}$$

Since, as stressed before, the observed rates are all within tens of percents of the SM values, one should require $\mu \approx 1$ in order to obtain agreement with the precision Higgs measurements. Therefore, given that $B_{cc}^{SM} \simeq 0.03$, an unconstrained fit to all couplings will lead to the following approximate correlation between the Higgs couplings

$$\kappa^2 \approx \frac{0.97}{2} + \frac{\sqrt{(0.97)^2 + 0.12\kappa_c^2}}{2} \tag{4.8}$$

which clearly has a solution for all real κ_c.

4.2 Constraints on κ_c from Higgs precision measurements

The existence of the flat direction described in Eq. (4.8) implies that no contraints on the κ_c values may be obtained by considering only the current Higgs precision measurements. Additional constraints are therefore necessary to put a bound on κ_c. In this section, we shall describe the constraints imposed by the bounds on the total Higgs width, the ones coming from precision electroweak measurements, and finally the ones coming from the theoretical prejudice that, in most extensions of the SM, $\kappa_V \leq 1$.

In all cases we perform a fit to κ_c marginalizing over all the other couplings. The channels included in the fit are shown in Table 4.1. In addition to the individual decay channels listed in the table, we also include the combined results for each given production mode. We combine the ATLAS and CMS results given in [53–55] by a weighted average, weighting by the squared inverse of the respective 1σ uncertainties. The uncertainty in the combined observation is given by

$$\sigma_{if}^{comb.} = \frac{1}{\sqrt{1/(\sigma_{if}^{ATLAS})^2 + 1/(\sigma_{if}^{CMS})^2}} \tag{4.9}$$

where σ_{if} indicates the uncertainty in the corresponding observed value of μ_{if}.

Production mode	Decay mode	Production mode	Decay mode
ggF	$H \to \gamma\gamma$ $H \to ZZ$ $H \to WW$ $H \to \tau\tau$	VH	$H \to \gamma\gamma$ $H \to ZZ$ $H \to bb$
VBF	$H \to \gamma\gamma$ $H \to ZZ$ $H \to WW$ $H \to \tau\tau$	ttH	$H \to \gamma\gamma$ $H \to VV$ $H \to \tau\tau$ $H \to bb$

Table 4.1: The production and decay channels included in the fit over κ's. We also include the combined results for each production mode.

The χ^2 value for a given fit is calculated as

$$\chi^2 = \sum_{if} \frac{(\mu_{if}(\kappa) - \mu_{if}^{obs})^2}{\sigma_{if}^2} \tag{4.10}$$

where $\mu_{if}(\kappa)$ represents the calculated value of μ_{if}, using Eq. (4.5), for the given set of κ's. We find the best fit at each κ_c by minimizing the value of χ^2 for the given κ_c.

In the cases where κ_V is constrained, we obtain a 95% CL bound by placing a limit on $\Delta\chi^2$ relative to the best fit at $\kappa_c = 1$. In order to identify the appropriate $\Delta\chi^2$ cut, we performed a principle component analysis [66, 67] on a centralized data set of $\{\kappa_b, \kappa_W, \kappa_t, \kappa_\tau, \kappa_Z, \kappa_\gamma, \kappa_g\}$ for $\kappa_c \in [1.0, 4.0]$, for $\kappa_V \leq 1$. We converted the 7-dimensional correlated κ data into a

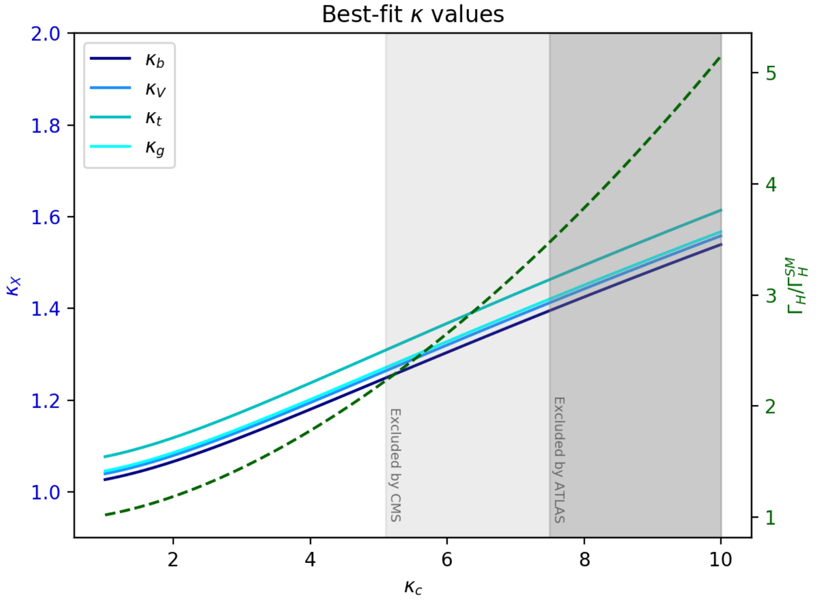

Figure 4.1: Plots of the best-fit values of κ's, represented by solid lines, to the precision rate measurements μ_{if}. The grey regions are excluded by constraints on the total Higgs width, which is normalized to the SM value and represented by a dashed line.

set of uncorrelated principle components, and observed that the 99%-dominant principle component is an approximately equally-weighted linear combination of $\{\kappa_b, \kappa_t, \kappa_\tau, \kappa_\gamma, \kappa_g\}$. κ_W and κ_Z contribute trivially to the principle direction due to the constraint $\kappa_V \leq 1$. Thus we treat $\{\kappa_b, \kappa_W, \kappa_t, \kappa_\tau, \kappa_Z, \kappa_\gamma, \kappa_g\}$ as one fit parameter. Including the fit parameter coming from κ_c, our χ^2 fit is effectively a 2-parameter fit. As a result, we will employ a 95% CL cut corresponding to $\Delta\chi^2 = 5.99$.

4.2.1 Higgs decay width

The increase in all κ's following the flat direction described in Eq. (4.8) leads to an increase in the total width Γ_H, and one may therefore place a bound on $|\kappa_c|$ using bounds on the Higgs width. ATLAS and CMS have performed maximum likelihood fits using on-shell and off-shell $H \to ZZ$ measurements to obtain a bound on the total Higgs width; they find

$$\begin{aligned} \Gamma_H &< 14.4 \text{ MeV} \quad \text{(ATLAS)} \\ \Gamma_H &< 9.16 \text{ MeV} \quad \text{(CMS)} \end{aligned} \tag{4.11}$$

or $\Gamma_H/\Gamma_H^{SM} < 3.5$ and $\Gamma_H/\Gamma_H^{SM} < 2.2$, respectively, at 95% CL [68, 69]. It is necessary to note that these limits are obtained by making certain assumptions, in particular that the κ values do not depend on the momentum transfer of the Higgs production mechanism and that $\kappa_V = \kappa_g$. Because κ_V and κ_g naturally have nearly equal values in the best fits, this second condition is indeed approximately satisfied.

We perform a χ^2 fit to the LHC measurements of all measured signal strengths μ_{if}, Eq. (4.5), for increasing values of κ_c and find that the 95% C.L. limits on the Higgs width lead to a bound of $|\kappa_c| < 7.5$ from ATLAS and $|\kappa_c| < 5.1$ from CMS. Figure 4.1 shows a plot of the best-fit κ's for increasing κ_c, and indicates the regions for which the total Higgs width, represented by the dashed-line, exceeds the current bounds. The spread in values for the various κ's arises from the differences in individual rate measurements.

4.2.2 Precision Electroweak Measurements

It is also worth noting that the necessary increases in all κ values to be consistent with the Higgs production rates result in $\kappa_V > 1$. In particular, for $|\kappa_c| = 7.5$ the least-squares fit gives values of $\kappa_W = 1.42$ and $\kappa_Z = 1.38$, which are consistent with the approximate flat direction values given by Eq. (4.8). These large values for κ_V result in divergences in electroweak precision parameters which are not canceled by the Higgs contribution, as they are in the SM. In this case one would require an extension of the SM which cancels the divergent contributions to the precision measurement variables. One can replace the divergence by a parametric logarithmic dependence on an effective cutoff that characterizes the new physics.

In such a case, for instance, if one assumes a cutoff scale of the order of $\Lambda = 3$ TeV, a fit to the precision electroweak measurements leads to a value of $\kappa_V = 1.08 \pm 0.07$ [70]. Since κ_V is now constrained to values lower than the ones necessary to reach the bounds on the Higgs width, there will be a stronger upper bound on κ_c.

In order to find a bound on κ_c from this limit on κ_V, we include the deviation of κ_V from $\kappa_V = 1.08$ in the calculation of χ^2 and perform a χ^2 fit for increasing κ_c. We examine the $\Delta\chi^2$ relative to the fit at $\kappa_c = 1$. Performing a fit to the Higgs rates using this constraint on κ_V, one obtains $|\kappa_c| < 4.9$. Observe, however, that this bound depends on specific assumptions about the new physics scale.

4.2.3 Constrained κ_V

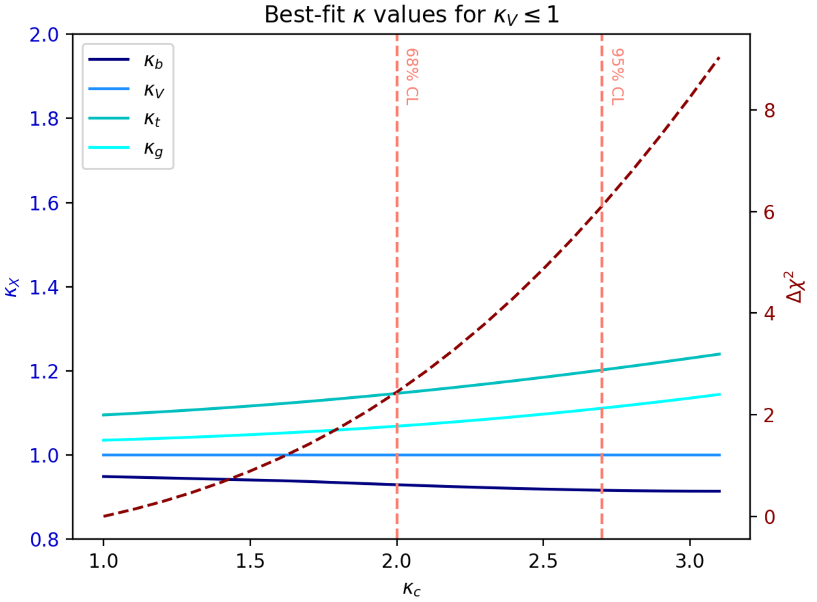

Figure 4.2: Plots of the best-fit values of κ's for $\kappa_V \leq 1$. Although we plot κ_W and κ_Z together as κ_V, the two differ very slightly due to the differences in the W and Z rate measurements. The dashed line represents the $\Delta\chi^2$ of the fit at a given κ_c relative to the χ^2 of the fit at $\kappa_c = 1$.

In this third scenario, the flat direction is removed by constraining $\kappa_W, \kappa_Z \leq 1$. This constraint is well motivated, as models with extended Higgs sectors such as a 2HDM will typically include couplings to the weak gauge bosons lower than the SM values for the individual Higgs particles. Similarly to the previous case, the κ's cannot increase uniformly to maintain the same relative strengths, so we expect that the fit will become less accurate as the total width increases through κ_c. As in the previous section, we obtain a 95% CL bound on κ_c by identifying the value of κ_c for which the least-squares fit has $\Delta\chi^2 = 5.99$ relative to the best fit at $\kappa_c = 1$. We find a bound of $|\kappa_c| < 2.7$ at 95% CL. Figure 4.2 shows a plot of the behavior of the best-fit κ's, represented by solid lines, for increasing κ_c along with the value of $\Delta\chi^2$, represented by a dashed line.

4.2.4 Future prospects for the HL-LHC

We can examine these cases for the HL-LHC, for which the projected uncertainties of the rate measurements have been examined for ATLAS [71] and CMS [72]. We update the 1σ uncertainties used in our χ^2 fit using the combined expected errors quoted in the two studies. In the case of the width constraint, if only the on-shell rate measurements are considered, the bound on $|\kappa_c|$ remains approximately the same, as the κ values along the flat direction are similar regardless of the uncertainties in μ_{if}. However, the width bound is also expected to improve with higher luminosity. According to an ATLAS study of off-shell Higgs to ZZ measurements for the HL-LHC [73], assuming the observed on-shell and off-shell rates are equal to the SM prediction, the expected determination of Γ_H with 3 ab^{-1} is

$$\Gamma_H = 4.2^{+1.5}_{-2.1} \text{ MeV} \tag{4.12}$$

or $\Gamma_H/\Gamma_H^{SM} = 1.0^{+0.4}_{-0.5}$. Requiring that the width remains consistent with this expectation corresponds to a bound of $|\kappa_c| \lesssim 3.0$.

The projected constraints for $\kappa_V \leq 1$ depend somewhat on the values of μ_{if} one uses in the fit. The projection studies use $\mu_{if} = 1$ for all initial and final states to estimate the percent uncertainty on each measurement. An alternative method is to adjust the percent uncertainty to the expected HL-LHC values but use the current measurements; this method is not ideal, as limiting the uncertainties without changing the values of μ_{if} is unlikely to accurately reflect the HL-LHC results. However, the comparison of the bounds on κ_c obtained in the two scenarios provide a good picture of the likely constraints on this quantity. For μ_{if} equal to the current measurements, we find an expected bound of $|\kappa_c| < 2.2$. On the other hand, for $\mu_{if} = 1$, the expected bound is given by $|\kappa_c| < 2.1$. We therefore expect the HL-LHC to provide an indirect limit of $|\kappa_c| \lesssim 2.1$ in the $\kappa_V \leq 1$ case.

4.3 Radiative Higgs Decay to J/ψ

Radiative decays of the Higgs boson into charmonium states are known to provide a sensitive probe of the charm coupling, and have been previously examined in this context in [74–77]. This is due to the fact that the charm-coupling induced rates interfere with those induced by the top and W couplings in a well-defined way. For instance, the width for $H \to J/\psi + \gamma$ is given by [78]

$$\Gamma(H \to J/\psi + \gamma) = |(11.9 \pm 0.2)\kappa_\gamma - (1.04 \pm 0.14)\kappa_c|^2 \times 10^{-10} \text{ GeV} \tag{4.13}$$

where the first term arises from the amplitude which contains no dependence on κ_c and the second from the κ_c-dependent amplitude. Plugging in $\kappa_\gamma, \kappa_c = 1$ and $\Gamma_H^{SM} = 4.195 \times 10^{-3}$ GeV gives the SM value for the branching ratio as

$$BR^{SM}(H \to J/\psi + \gamma) = 2.79 \times 10^{-6}. \tag{4.14}$$

The current bound on this process is

$$\sigma \times BR(H \to J/\psi + \gamma) < 19 \text{ fb}. \tag{4.15}$$

at 95% CL. Assuming the SM production cross section [79], this limit corresponds to

$$BR(H \to J/\psi + \gamma) < 3.5 \times 10^{-4}. \tag{4.16}$$

Since the production cross section depends on the values of $\kappa' s$, which should increase together with $|\kappa_c|$ in order to keep agreement with the Higgs production rates, this bound on the branching ratio is only useful for moderate values of κ_c, for which $\sigma_H \approx \sigma_H^{SM}$. However, the bound on the branching ratio is two orders of magnitude larger than the SM branching ratio, and therefore cannot currently probe moderate values of κ_c. Additionally, the branching ratio displays asymptotic behavior for large κ_c, as there are also κ_c-dependent enhancements of the Higgs total width. For large κ_c, the approximate expression for the branching ratio along the flat direction is given by

$$BR(H \to J/\psi + \gamma) \approx \frac{(5|\kappa_c|^{1/2} - 1.04\kappa_c)^2 \times 10^{-10} \text{ GeV}}{(0.16|\kappa_c| + 0.03\kappa_c^2) \times \Gamma_H^{SM}}. \tag{4.17}$$

Figure 4.3 shows a plot of the behavior of this Higgs radiative decay branching ratio along the flat direction as well as with SM-like values for the other couplings. We stress again that setting the other Higgs couplings to SM values for large $|\kappa_c|$ does not align well with rate measurements from the LHC, and it is therefore more instructive to examine the flat direction for large $|\kappa_c|$. In both cases, the branching ratio peaks at moderate negative values of κ_c, at a maximum value of approximately 4×10^{-6}, two orders of magnitude below the current limit for SM production rates.

Given the non-SM production rate and asymptotic behavior of the branching ratio for

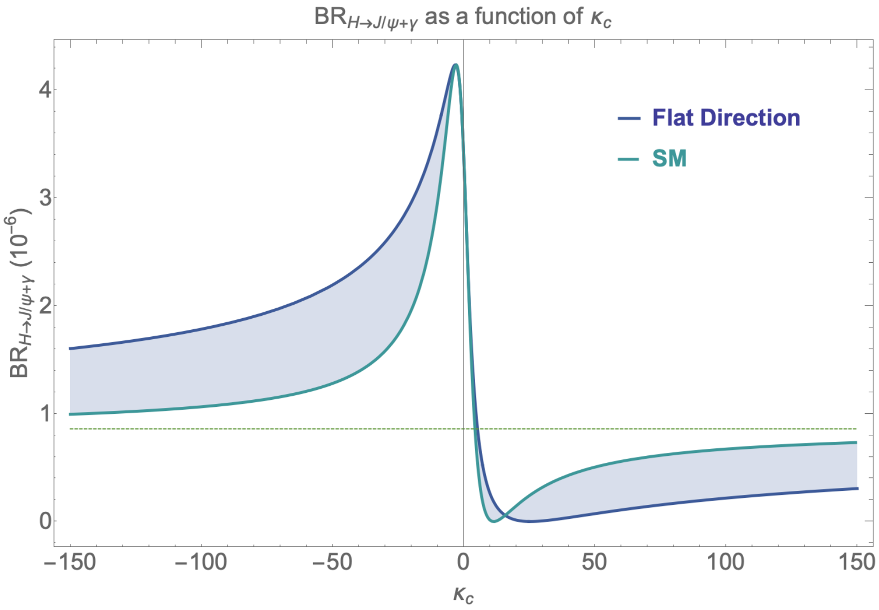

Figure 4.3: Plot of the branching ratio of $H \to J/\psi + \gamma$ varying along the flat direction (dark blue) and with other Higgs couplings fixed to SM values (light blue). The expected asymptote of approximately 8×10^{-7} is indicated by the green dashed line.

large κ_c, we consider the limit on $\sigma \times BR$ rather than only the branching ratio. The production cross section increases due to both κ^2 enhancements given by Eq. (4.8) as well as κ_c-dependent processes such as $c\bar{c}H$ production, which become relevant for very large κ_c. We fit data produced with MadGraph 5 [80] at leading order to obtain an expression for the approximate scaling of $\sigma_{c\bar{c}H}$ for large κ_c at 13 TeV, which is given by

$$\sigma_{c\bar{c}H} \approx \left| 5.24 \times 10^{-2} + 2.76 \times 10^{-2}\kappa_c - 5.45 \times 10^{-6}\kappa_c^2 + 1.30 \times 10^{-6}\kappa_c^3 \right|^2 \text{pb} \qquad (4.18)$$

We also include contributions to VH production from $c + \bar{c}/\bar{s}$ initial states. Figure 4.4 shows a plot of $\sigma \times BR_{J/\psi}$ in fb for the flat direction.

Considering properly the rate, instead of just the radiative decay branching ratio, a limit can now be set for very large values of κ_c. By the end of the HL-LHC, the expected 95% CL upper bound on $\sigma \times BR(H \to J/\psi + \gamma)$ from ATLAS is approximately 3 fb [81]. We therefore expect this process to place a limit of $\kappa_c \in [-180, 330]$ at the HL-LHC for the

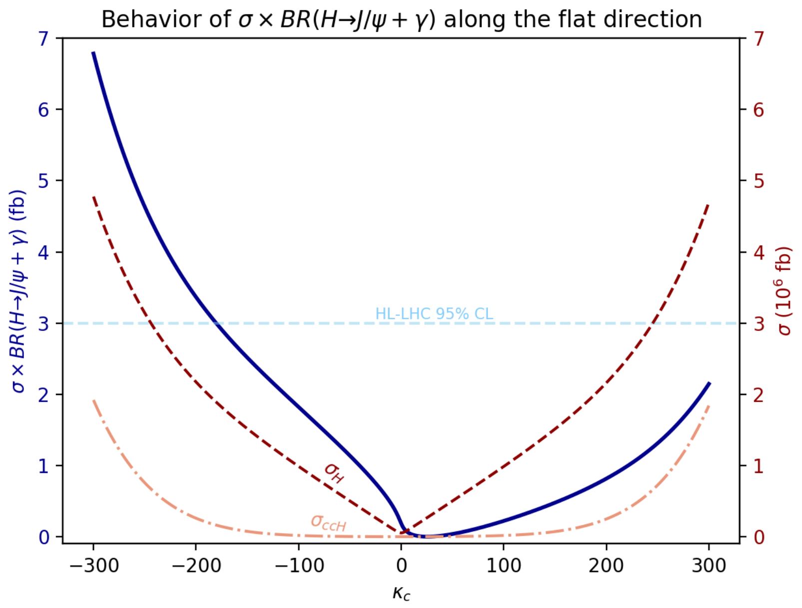

Figure 4.4: Plot of $\sigma \times BR(H \to J/\psi + \gamma)$ for the flat direction. The blue line indicates $\sigma \times BR$ in fb, while the pink dot-dashed (dashed) lines indicate the $c\bar{c}H$ (total) production cross section in fb. The dashed grey line shows the expected HL-LHC 95% CL bounds.

flat direction. This limit is two orders of magnitude larger than those from other HL-LHC prospects discussed previously. A strong improvement, of an order of magnitude of the present expected sensitivity, would be necessary for this channel to provide a competitive bound on κ_c.

The authors of Ref. [78] have updated the partial width expression with a new approach to the resummation of logarithms, and quote a new width of [82]

$$\Gamma(H \to J/\psi + \gamma) = \left|(11.71 \pm 0.16)\kappa_V - ((0.627^{+0.092}_{-0.094}) + i(0.118^{+0.054}_{-0.054}))\kappa_c\right|^2 . \qquad (4.19)$$

This expression has a reduced dependence on κ_c, and therefore gives even weaker bounds on κ_c than those found above.

It is important to note that such large values of κ_c encounter strong experimental and theoretical issues. On the one hand, following the flat direction in order to retain consistency with precision Higgs measurements leads to large values of the top-quark coupling to the Higgs $g_{ht\bar{t}}$. In particular, for values of $\kappa_c \gtrsim 100$ one requires values of $\kappa_t \gtrsim 17$. In this case, the value of $g^2_{ht\bar{t}}$ is greater than 4π, and a perturbative examination of the Higgs sector becomes unreliable. One may attempt to avoid this issue by fixing κ_t to be less than a certain value, in which case the Higgs rates would become inconsistent with those observed at the LHC. We therefore note that such large values of κ_c are problematic for either LHC Higgs rates or perturbativity concerns. Moreover, as stressed in Section 4.2, unless a very particular momentum dependence of the effective couplings is present, large values of $\kappa_c \gg 10$ would lead to a value of the Higgs width that is under strong tension with current LHC measurements.

4.4 Higgs Production Rates induced by the charm Higgs coupling

As stressed before, Higgs production may be induced in proton collisions via its coupling to the charm quark. Moreover, the Higgs boson may decay into charm quarks and may be detected in this decay channel, provided these decays may be disentangled from the ones into bottom quarks.

4.4.1 Higgs associated production with charm quarks

The cH production mode has also been proposed as a search method for κ_c. Because this channel has a lesser dependence on κ_c at very large $|\kappa_c|$ than $c\bar{c}H$, it was not included in the analysis of radiative Higgs decays in Section 4.3. However, the cH channel has a higher production cross section at small or moderate values of $|\kappa_c|$, preferred by the total Higgs width constraints and precision electroweak measurements analyzed in Section 4.2. A previous study of this channel [83] shows that a high luminosity LHC, with 3000 fb^{-1} integrated luminosity at ATLAS and CMS, should be able to probe values of $\kappa_c < 2.5$ at the 95% C.L. This study leaves all other κ's fixed to the SM expectation, varying only κ_c, and therefore we should reanalyze it taking into account the rise of the κ_i along the flat direction.

The cH production process involves three diagrams at leading order: s-channel and t-channel diagrams with a c propagator and a $c\bar{c}H$ vertex, and an s-channel diagram with a gluon propagator and a ggH vertex. Since the diagram with the ggH vertex is dominant for SM values of the Higgs couplings, we expect that following the flat direction would further enhance the cH production beyond the values found in [83]. However, this also further enhances the background processes $pp \to gH$ and $pp \to bH$ in addition to the $pp \to c\bar{c}H$ background.

We use MadGraph at leading order in a specialized model file, which includes an effective ggH vertex, to calculate the production rates. We vary the values of κ_c and increase κ_g and κ_b proportionally according to Eq. (4.8) to obtain the production cross section for each process. Using a charm tagging efficiency of 30%, a $c\bar{c}H$ mistag rate as cH of 5%, and b and g mistag rates of 20% and 1%, respectively [84], we obtain the expected number of events for $\sigma(pp \to XH) \times BR(H \to \gamma\gamma)$ for 3 ab^{-1} integrated luminosity. Although $\sigma(pp \to gH) \gg \sigma(pp \to bH)$, the larger b mistag rate leads to similar background contributions from the two processes. The $c\bar{c}H$ background has a stronger dependence on κ_c and therefore contributes an increasing fraction of the background for larger κ_c. The results are shown in Figure 4.5.

The cH process includes dependence on both the κ_c enhancement and the κ_g enhancement along the flat direction. It therefore increases more quickly with κ_c than the background processes, which each depend on only one of these enhancements; in particular, the dominant backgrounds of $pp \to bH, gH$ depend only on the flat direction enhancements of κ_b, κ_g. We show the number of signal and background events, along with their ratio, for a range of κ_c values in Table 4.2.

Since variations in σ_{cH} depend weakly on κ_c alone along the flat direction, it would be very difficult to identify the precise value of κ_c from a measurement of $N = S + B$. However, we may use these signal and background rates to estimate the sensitivity to κ_c

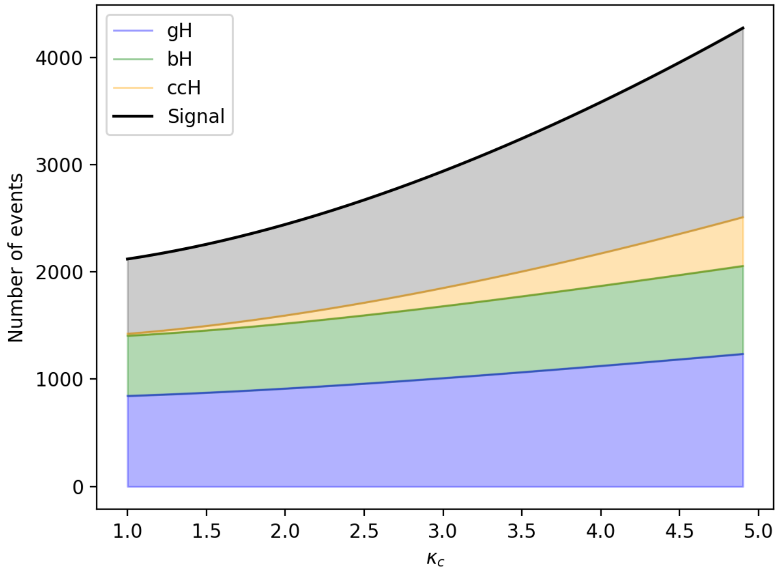

Figure 4.5: The expected number of background and signal events for cH production at the HL-LHC with 3 ab^{-1} integrated luminosity.

κ_c	1.0	1.5	2.0	2.5	3.0	3.5	4.0	4.5	5.0
S	687	758	840	961	1085	1230	1408	1598	1822
B	1425	1498	1595	1714	1852	2005	2174	2356	2551
S/B	0.33	0.34	0.35	0.36	0.37	0.38	0.39	0.40	0.42

Table 4.2: The number of signal events, number of background events, and signal to background ratio for values of κ_c between 1 and 5. Due to the increase in κ_g, κ_b along the flat direction, the background increases in addition to the signal.

following a similar analysis to the one in Ref. [83]. Assuming the true value of κ_c is 1, we find the expected 1σ and 2σ upper bounds on κ_c from this process by identifying the value of κ_c for which $N(\kappa_c) - N(1) = 1\sigma, 2\sigma$. We take the statistical uncertainty to be $\Delta N^{stat}(\kappa_c) = \sqrt{S(\kappa_c) + B(\kappa_c)}$ and the theoretical uncertainty in the signal and background, which we have calculated at LO, to be 20%. Because our background is now also being estimated for varying κ_c using MadGraph5, we examine two cases for the uncertainty in the background. In the first case, we apply no uncertainty to the number of background events. In the second case, we apply a 20% uncertainty to the number of background events $B(\kappa_c)$ in addition to the number of signal events. We find ΔN^{tot} by adding the statistical and theoretical uncertainties in quadrature. Let us stress that this analysis assumes that the dominant uncertainties are the statistical and theoretical ones and ignores the possible impact of systematic and experimental uncertainties. The sensitivity on κ_c depends strongly on these assumptions, and may become weaker after a realistic experimental analysis of this process is performed.

We take $\Delta N^{tot} = \sigma$ to parametrize the number of standard deviations of $N(\kappa_c) - N(1) = n\sigma$ for the two uncertainty cases. The value of n is plotted versus κ_c in Fig. 4.6. We find a 1σ (2σ) deviations for

$$|\kappa_c| < 1.6 \ (2.1) \tag{4.20}$$

in the first case, and

$$|\kappa_c| < 2.5 \ (4.0) \tag{4.21}$$

in the second case. In the first case the increase of the expected sensitivity relative to [83], in which no uncertainty was applied to the background estimates, arises from the enhancement of the background events in addition to the signal events. In the second case, we find approximately the same expected sensitivity as in Ref. [83].

Although the best-fit κ values for low values of κ_c tend to follow the flat direction, we note that taking SM-like values for the other couplings can still retain some level of consistency with LHC results for this range of κ_c; therefore, our results do not invalidate the analysis of Ref. [83] but show the variation of the LHC sensitivity for slightly larger values of κ_g, for which an improvement of the fit to the Higgs precision measurement data is obtained.

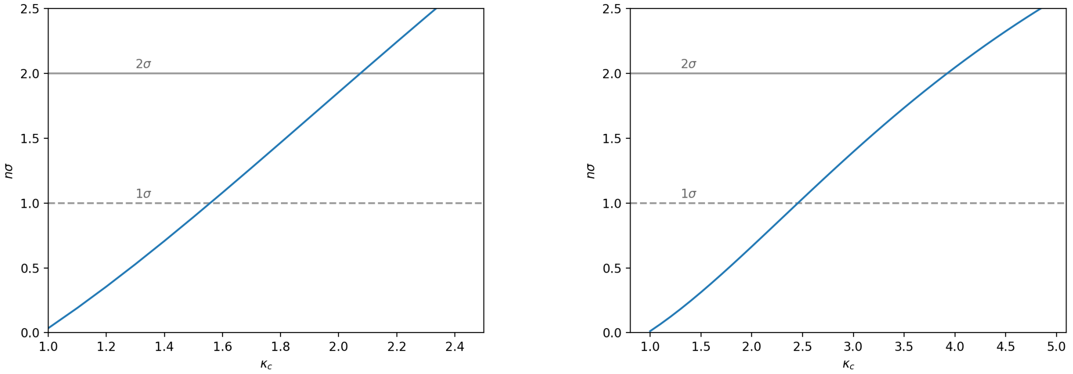

(a) (b)

Figure 4.6: Number of standard deviations of $N(\kappa_c)$ from $N(1)$, as a function of κ_c. The dashed (solid) grey lines indicate the 1σ (2σ) bounds. The two cases represent (left) no uncertainty in background and (right) 20% uncertainty on the number of background events.

4.4.2 Higgs decay into charm-quark pairs

Direct Searches

Searches have been performed for $ZH \to l^+l^-c\bar{c}$ with 36.1 fb^{-1} integrated luminosity, with ATLAS publishing an upper bound of $\sigma(pp \to ZH) \times B(H \to cc) < 2.7$ pb at 95% CL [84]. This corresponds to about 110 times the SM rate. Thus we require that $\kappa_Z^2\kappa_c^2/\kappa_H^2 \lesssim 110$; moving along the flat direction, one reaches this limit at a value of $|\kappa_c| = 20.9$, which is a far weaker bound than the one provided by the total width constraints. However, HL-LHC studies from ATLAS [85] have found an expected upper bound of $\mu_{ZH\to c\bar{c}} < 6.3$ at 95% CL with an integrated luminosity of 3 ab^{-1}. Unconstrained fits of the rate measurements remain within this limit for $|\kappa_c| \lesssim 2.7$; this channel may therefore provide a bound of similar magnitude to those from constrained-fit bounds at the HL-LHC.

The $ZH \to l^+l^-c\bar{c}$ limit obtained in the ATLAS HL-LHC study uses a tighter charm tagging working point than the working point employed in Run 2, thereby reducing the background contribution from processes such as $ZH \to Zb\bar{b}$. In particular, the tagging efficiency for c-jet, and mis-tagging rates for b-jet, and light-flavor jets are 18%, 5%, and 0.5%, respectively, for the HL-LHC study, while these values are 41%, 25%, and 5% for the Run 2 analysis. This stricter working point takes advantage of the higher expected signal yield at the HL-LHC to provide a 7% additional improvement on the limit relative to Run 2. However, charm tagging algorithms are currently being improved, in part through the use of deep neural networks. For example, CMS deep tagging algorithms have achieved a 24% tagging efficiency with 1% b-jet and 0.2% light jet mis-tagging rates [86]. This algorithm therefore has a 6% improvement in efficiency over the HL-LHC study working point along with a factor 5 improvement in the b-jet mis-tag rate. The use of new tagging algorithms could therefore further improve the limit obtained at the HL-LHC.

Indirect Searches

The $H \to c\bar{c}$ decay can also be examined in the context of $H \to b\bar{b}$ decays to place a bound on κ_c using current data [74, 75]. We examine the effect of $c\bar{c}$ mistagging as $b\bar{b}$ on the observed $H \to b\bar{b}$ rates. This results in κ_c being a factor in the numerator of $\mu_{i,b\bar{b}}$, thereby limiting the flat direction described by Eq. (4.8) for large values of κ_c. We include the $c\bar{c}$ contributions to $b\bar{b}$ rates by

$$\mu_{i,b\bar{b}} = \kappa_i^2 \frac{\kappa_b^2 + \kappa_c^2 (BR_{c\bar{c}}\epsilon_c^2/BR_{b\bar{b}}\epsilon_b^2)}{\kappa_H^2} \tag{4.22}$$

where ϵ_c is the mistag rate of c-jets as b-jets and ϵ_b is the tagging efficiency of b-jets and we have defined $\mu_{i,b\bar{b}}$ as the observed rate normalized to the uncontaminated SM rate. Our analysis of this bound differs from that by Perez et. al., Ref. [75], in two primary ways. Firstly, we include this altered expression for $\mu_{i,b\bar{b}}$ in our fit to all of the LHC observed rates listed in Table 4.1, thereby removing the 'flat direction' for $\mu_{i,b\bar{b}}$ along $\kappa_b = \kappa_c$ encountered in [74], which examines only $H \to b\bar{b}$ processes. We therefore do not need to employ multiple tagging points to obtain a bound for κ_c, since for sizable values of κ_c, raising κ_b and κ_c together will spoil the fit to other observables. Consequently, we allow variations in the other κ's, which approximately follow the flat direction described by Eq. (4.8). Because of this, κ_b and κ_c may have greater variations that those found in Refs. [74, 75] while remaining consistent with observed $b\bar{b}$ (and all other) Higgs rates. We therefore expect to find weaker bounds in our analysis of this potential bound.

We employ the ATLAS working point of $\epsilon_b = 0.70$, $\epsilon_c = 0.20$ and the CMS working point of $\epsilon_b = 0.78$, $\epsilon_c = 0.27$. To obtain a bound, we perform a fit to the Higgs rate measurements and place a limit on $\Delta\chi^2$. Following this analysis, the ATLAS and CMS tagging efficiencies provide bounds of $|\kappa_c| \lesssim 23$ and $|\kappa_c| \lesssim 16$, respectively. Using the HL-LHC expected uncertainties [71, 72] along with best-fit rates of $\mu = 1.0$, this approach places bounds of $|\kappa_c| \lesssim 8.7$ and $|\kappa_c| \lesssim 6.5$, respectively.

4.4.3 Asymmetry in W^+H and W^-H production

The measurement of asymmetry in $\sigma(pp \to W^+H)$ and $\sigma(pp \to W^-H)$ production has also been proposed as a channel through which one can place limits on κ_c [87]. The relevant diagrams for this process are shown in Fig. 4.7. The SM asymmetry is driven by the Higgs-Strahlung processes; in the Higgs-Strahlung diagrams, the difference in W^+ and W^- production arises from the asymmetry of $u\bar{d}$ and $\bar{u}d$ in the proton PDF. The charm Yukawa appears in diagrams with $s\bar{c}$ and $\bar{s}c$ initial states, which are symmetric in the proton PDF. Therefore, when the charm Yukawa is increased significantly, the symmetric $s\bar{c}/\bar{s}c$ diagrams reduce the asymmetry with respect to the SM expected value. The $W^{\pm}H$ production asymmetry therefore decreases with large κ_c. One can therefore use the sensitivity of this asymmetry on κ_c to get bounds on the charm coupling [87].

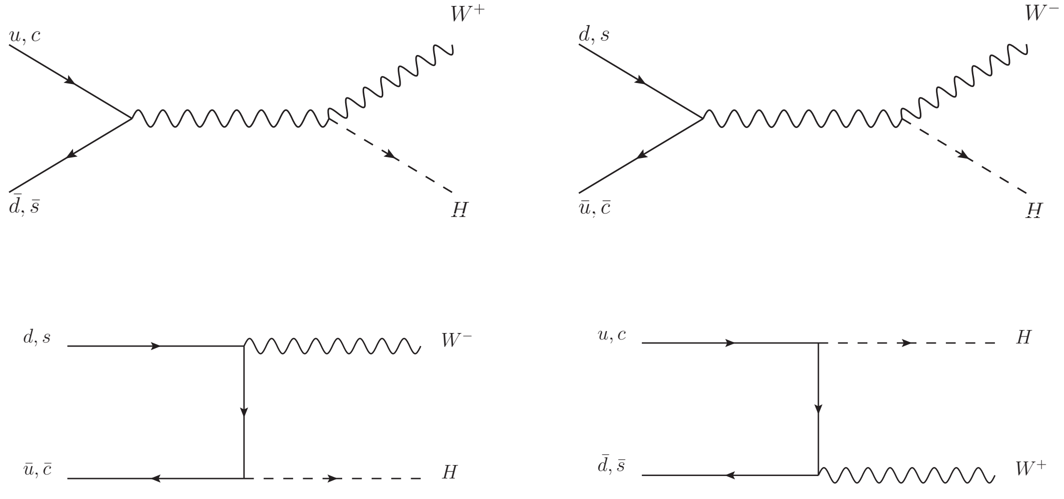

Figure 4.7: Diagrams for the two relevant types of $W^{\pm}H$ production processes at leading order. The top row shows the Higgstrahlung processes, which are dominant in the SM, while the bottom row shows the diagrams proportional to the charm Yukawa.

Given the relative contributions of the two types of diagrams, however, we note that enhancements of κ_W alongside enhancements of κ_c will reduce the symmetrizing effect of increasing κ_c. In order to examine this quantitatively, we use MadGraph5 to calculate the LO cross sections at 14 TeV for W^+H and W^-H production along the flat direction. Figure 4.8 shows the results of this analysis. We plot the percent asymmetry of the production modes, quantified as

$$A_{W^\pm} = \frac{\sigma_{W^+H} - \sigma_{W^-H}}{\sigma_{W^+H} + \sigma_{W^-H}}, \tag{4.23}$$

as a function of κ_c along the flat direction, as well as for $\kappa_X = 1$ with $X \neq c$.

We find that the asymmetry is reduced to less than 0.02 up to $\kappa_c = 100$. Using MadGraph5 and detector simulations, Ref. [87] found that the uncertainty in the asymmetry may be reduced to approximately 0.004 with 3 ab^{-1} integrated luminosity. In this case, the $W^{\pm}$ asymmetry would be able to place a limit of $|\kappa_c| \lesssim 30$ along the flat direction. This still provides a weaker bound than other proposed methods by approximately an order of magnitude, and we therefore conclude that if one requires consistency with LHC precision Higgs measurements, the $W^{\pm}H$ asymmetry does not provide a sensitive probe of κ_c.

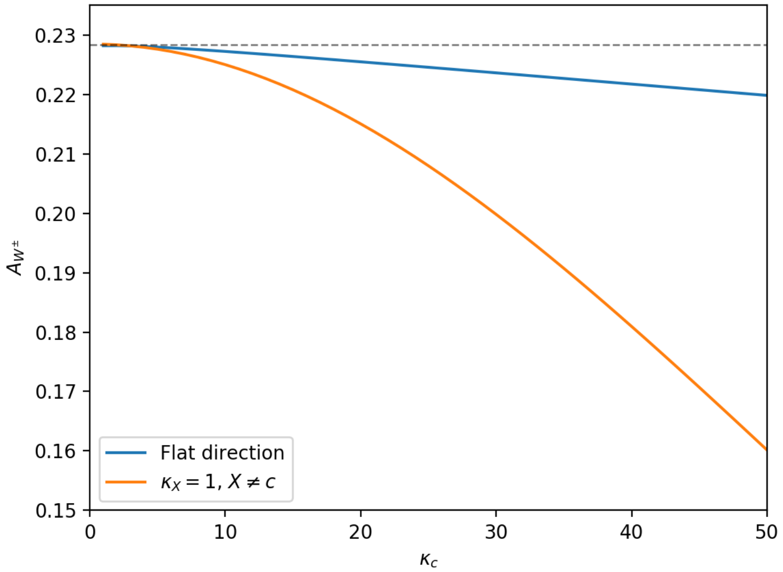

Figure 4.8: Plot of the percent asymmtry in $W^{\pm}H$ production versus κ_c, for the flat direction and for SM-like κ_X, $X \neq c$. While large κ_c significantly reduces the asymmetry in the second case, the enhancement of κ_W alongside κ_c in the flat direction reduces the relative effect of the symmetrizing κ_c-proportional contributions.

4.4.4 Differential cross sections

The distribution of the Higgs production differential cross section as a function of transverse momentum has also been proposed as a probe of κ_c [88–90] and has been examined for 35.9 fb^{-1} of data by CMS [91]. This method of bounding κ_c may provide an interesting complementary bound to those from the fit to precision rate measurements, as the flat direction along which the rates remain constant may not reproduce the expected SM cross section distribution as a function of transverse momentum. The CMS study examines the $H \to \gamma\gamma$ and $H \to ZZ$ decay channels, as well as their combination, and identifies bounds by varying κ_b and κ_c and examining two cases: the first in which the branching fractions are dependent on $\kappa_{b,c}$, and the second in which they are independent. In the dependent case, they quote a bound of $-4.9 < \kappa_c < 4.8$, while in the independent case the bound is $-33 < \kappa_c < 38$. The uncertainties in the cross section distribution, which are on the order of 10-20%, are currently dominated by statistical uncertainty, while the systematic uncertainty is on the order of about 5%. The bounds quoted above would therefore be expected to improve with more data.

However, we again note that varying $\kappa_{b,c}$ to values as large as 5 would significantly affect the other observed channels, and that therefore the flat direction is necessary to ensure consistency with the current Higgs observations. It is likely that varying the other couplings along the flat direction will affect the bound in this case. In particular, the variation of κ_t in addition to κ_b and κ_c should affect the expected distribution and would likely weaken the identified bounds, while the branching fractions would vary less dramatically with increases in $\kappa_{b,c}$. One might expect that along the flat direction the bounds will be similar to the one found in the unconstrained case. A study of this bound with the addition of the flat direction is necessary to provide a bound on κ_c that is consistent with the other LHC measurements.

Ref. [88] has predicted the possible HL-LHC bounds from the differential cross section distributions. Assuming a theory uncertainty of 2.5% and systematic uncertainty of 1.5%, they find a 95% CL bound of $\kappa_c \in [-0.6, 3.0]$. However, we emphasize that these bounds do not take into account the rate measurements and the flat direction, and also assume significant improvements in the theoretical and systematic uncertainties.

CHAPTER 5

SUPERSYMMETRY AND THE LHC HIGGS

In this chapter, we investigate the interplay between minimal supersymmetric models and the measurements of the properties of the observed LHC Higgs. In general, there is no reason why a supersymmetric model might include an SM-like physical Higgs eigenstate; however, the LHC has thus far observed a Higgs which behaves like an SM Higgs at the order of about 10% precision. It is therefore reasonable to ask how these results impact the allowed parameter space of supersymmetric models, how one might look for hints of supersymmetric models that fall within this parameter space, and why a supersymmetric model might be consistent with such observations. We first examine the possibility of inverting the bottom Yukawa in the MSSM and NMSSM, which can be related to enhanced production of heavy Higgses alongside $b\bar{b}$ as well as to potential lepton flavor violating Higgs decays. We then move to a more theoretically-motivated examination of a high-energy theory which may run down to the NMSSM alignment limit at low energies, thus providing a dynamical manner through which a supersymmetric theory may be consistent with the LHC results.

5.1 Inverting the bottom Yukawa

5.1.1 Motivation

In this work, we consider the possibility that not only the magnitude but also the sign of the Higgs coupling to bottom quarks differ from the Standard Model predictions. This is an intriguing possibility that could be realized in the simplest two Higgs doublet extension of the Standard Model [92], as we will see in the next section. Such region of parameters has also been invoked recently in models that lead to large rates of lepton flavor violating decays of the Higgs bosons $h \to \tau\mu$ [93] and on theories of flavor at the weak scale [94]. In this article we study the possible realization of this scenario within the minimal supersymmetric extensions of the SM, namely the MSSM [95–99] and the NMSSM[40]. We also examine the possibility of modeling an enhanced rate of a 400 GeV CP-odd Higgs produced in association with b quarks, of which hints were seen in early Run 2 ATLAS data. The material in this chapter is based on work with Bing Li and Carlos Wagner.

5.1.2 Wrong sign Yukawa in Type II Two Higgs Doublet Models

The tree-level couplings of the lightest Higgs boson to Gauge bosons and fermions in type II 2HDM Higgs are listed as below,

$$g_{hVV} = g_{hVV}^{SM} s_{\beta-\alpha}\,, \tag{5.1}$$

$$g_{ht\bar{t}} = \frac{m_t}{v}\frac{c_\alpha}{s_\beta} \equiv \frac{m_t}{v}\left(s_{\beta-\alpha} + c_{\beta-\alpha} t_\beta^{-1}\right), \tag{5.2}$$

$$g_{hb\bar{b}} = -\frac{m_b}{v}\frac{s_\alpha}{c_\beta} \equiv \frac{m_b}{v}\left(s_{\beta-\alpha} - c_{\beta-\alpha} t_\beta\right), \tag{5.3}$$

where s_α (s_β) $=$ $\sin\alpha$ $(\sin\beta)$, c_α (c_β) $=$ $\cos\alpha$ $(\cos\beta)$, t_β $=$ $\tan\beta$ and $s_{\beta-\alpha}$ $(c_{\beta-\alpha})$ $=$ $\sin(\beta-\alpha)$ $(c_{\beta-\alpha})$. As we can see from Eq. (5.2), for the gauge boson couplings to be SM-like, we need $s_{\beta-\alpha} \approx 1$. In this case, for moderate values of t_β, the Higgs coupling to top-quarks or other up type fermions becomes SM-like due the t_β suppression of the second term on the right hand side of Eq. (5.2). However, for the Higgs to b-quark coupling, Eq. (5.3), a wrong sign could arise without changing the Higgs decay width and branching ratio when $g_{hb\bar{b}}/g_{hb\bar{b}}^{SM} \simeq -1$. This could be achieved with minor changes of the Higgs couplings to top-quarks and weak gauge bosons for sizable values of t_β and [100, 101]

$$t_\beta\, c_{\beta-\alpha} \approx 2. \tag{5.4}$$

This is in contrast with the condition $t_\beta c_{\beta-\alpha} \simeq 0$ that ensures a SM-like coupling of the bottom-quark to the Higgs boson.

Recall from Section 3.1 that the scalar potential of the most general two-Higgs-doublet extension of the SM may be written as:

$$\begin{aligned} V = \quad & m_{11}^2\Phi_1^\dagger\Phi_1 + m_{22}^2\Phi_2^\dagger\Phi_2 - m_{12}^2(\Phi_1^\dagger\Phi_2 + \text{h.c.}) + \tfrac{1}{2}\lambda_1(\Phi_1^\dagger\Phi_1)^2 + \tfrac{1}{2}\lambda_2(\Phi_2^\dagger\Phi_2)^2 \\ & \qquad + \lambda_3(\Phi_1^\dagger\Phi_1)(\Phi_2^\dagger\Phi_2) + \lambda_4(\Phi_1^\dagger\Phi_2)(\Phi_2^\dagger\Phi_1) \\ & \qquad + \left\{\tfrac{1}{2}\lambda_5(\Phi_1^\dagger\Phi_2)^2 + [\lambda_6(\Phi_1^\dagger\Phi_1) + \lambda_7(\Phi_2^\dagger\Phi_2)]\Phi_1^\dagger\Phi_2 + \text{h.c.}\right\} \ , \end{aligned} \tag{5.5}$$

After converting to the Higgs basis [102–107], the Higgs potential above could be rewritten as:

$$\mathcal{V} \supset \ldots + \frac{1}{2}Z_1(H_1^\dagger H_1)^2 + \ldots + \left[Z_5(H_1^\dagger H_2)^2 + Z_6(H_1^\dagger H_1)H_1^\dagger H_2 + \text{h.c.}\right] + \ldots\,, \tag{5.6}$$

where we have only retained those terms relevant for the following discussion and the new couplings $Z_i's$ are associated with previous $\lambda_i's$ by the following relations, as presented in Section 3.1.4 [108–110]

$$Z_1 \equiv \lambda_1 c_\beta^4 + \lambda_2 s_\beta^4 + \frac{1}{2}(\lambda_3+\lambda_4+\lambda_5)s_{2\beta}^2 + 2s_{2\beta}\left[c_\beta^2\lambda_6 + s_\beta^2\lambda_7\right], \tag{5.7}$$

$$Z_5 \equiv \tfrac{1}{4}s_{2\beta}^2\left[\lambda_1+\lambda_2-2(\lambda_3+\lambda_4+\lambda_5)\right] + \lambda_5 - s_{2\beta}c_{2\beta}(\lambda_6-\lambda_7)\,, \tag{5.8}$$

$$Z_6 \equiv -\frac{1}{2}s_{2\beta}\left[\lambda_1 c_\beta^2 - \lambda_2 s_\beta^2 - (\lambda_3+\lambda_4+\lambda_5)c_{2\beta}\right] + c_\beta c_{3\beta}\lambda_6 + s_\beta s_{3\beta}\lambda_7\,, \tag{5.9}$$

The CP-even Higgs mixing angle in this basis is identified with $\beta-\alpha$. Consequently, we have [108, 110–112]

$$c_{\beta-\alpha} = \frac{-Z_6 v^2}{\sqrt{(m_H^2 - m_h^2)(m_H^2 - Z_1 v^2)}}\,. \tag{5.10}$$

As stressed before, since the observed Higgs boson has SM-like properties, which requires $s_{\beta-\alpha} \simeq 1$, in order to fulfill the requirement to obtain a negative sign of the bottom Yukawa coupling, Eq. (5.4), sizable values of t_β are required. For large values of t_β, $s_\beta \simeq 1$, $c_\beta \simeq 1/t_\beta$

and $s_{2\beta} \simeq 2/t_\beta$. Since $Z_1 v^2 \simeq m_h^2$, the denominator becomes approximately $m_H^2 - m_h^2$. From the relation of Z_6 to the quartic couplings λ_i we obtain that, ignoring subdominant terms in $1/t_\beta$, an inversion of the sign of the Yukawa coupling leads to the following condition

$$[(\lambda_3 + \lambda_4 + \lambda_5) - \lambda_2 + \lambda_7 t_\beta] v^2 \simeq 2(m_H^2 - m_h^2). \tag{5.11}$$

or, equivalently,

$$[(\lambda_3 + \lambda_4 + \lambda_5) + \lambda_7 t_\beta] v^2 \simeq 2m_H^2 - m_h^2. \tag{5.12}$$

where we have used the fact that, at large values of t_β, $m_h^2 \simeq \lambda_2 v^2$. Hence, considering perturbative values of the quartic couplings λ_i, it is straightforward to see that, unless $\lambda_7 \simeq \mathcal{O}(1)$, the values of m_H must be of order of a few hundred GeV.

The relation between the charged and neutral Higgs masses is given by

$$m_{H^\pm}^2 = m_A^2 + \frac{v^2}{2}(\lambda_5 - \lambda_4) \tag{5.13}$$

and hence large values of λ_4 and λ_5 may induce a large splitting between the charged and the CP-odd Higgs boson masses.

5.1.3 Wrong sign Yukawa couplings in the MSSM and the NMSSM

MSSM and minimal NMSSM

The tree-level Higgs sector of the MSSM is a type-II 2HDM and consists of two Higgs doublets with quartic couplings which are related to the squares of the weak gauge couplings. Since Supersymmetry imposes concrete values for the quartic couplings λ_i it is interesting to check whether the wrong sign Yukawa coupling could arise in the frame of the MSSM without conflicting with other Higgs phenomenology. For this, one has to take into account the relevant radiative corrections arising from the interaction of the Higgs field with the third generation fermions and their scalar superpartners. In the MSSM, it's usually argued that a SM-like neutral Higgs boson could only be obtained in two distinct scenarios, i.e. the decoupling limit [108, 113] and the alignment limit [108, 109, 113, 114]. The decoupling limit happens when $m_h \ll m_H$, while the alignment limit arises when one of the CP-even Higgs bosons, when expressed as a linear combination of the real parts of the two neutral Higgs fields, lies in the same direction in the two Higgs doublet field space as neutral Higgs vacuum expectation values. This alignment does not in general depend on the masses of the non-standard Higgs bosons. The region of parameters under investigation requires a nonvanishing value of $c_{\beta-\alpha}$ and therefore a departure from the alignment limit. Hence, some departures from the SM behavior of the lightest Higgs are expected.

In the MSSM, it's not difficult to work out an approximate expression for Z_6 at the one-loop level. Taking into account that the most relevant radiative corrections may be absorbed in the definition of the Higgs mass at large values of t_β, one gets

$$\begin{aligned}
\lambda_2 &\simeq \frac{m_h^2}{v^2} \\
\lambda_3 &\simeq \frac{1}{4}\left(g_2^2 - g_1^2\right) \\
\lambda_4 &\simeq -\frac{1}{2}g_2^2 \\
\lambda_7 &\simeq \frac{3h_t^4}{16\pi^2}\frac{\mu}{M_S}\left(\frac{A_t^3}{6M_S^3} - \frac{A_t}{M_S}\right) \\
m_t &\simeq h_t\frac{v}{\sqrt{2}}
\end{aligned} \tag{5.14}$$

where m_t is the top quark mass, M_S is the stop mass scale, A_t is the trilinear stop-Higgs coupling and μ is the Higgsino mass parameter (for a more complete expression, see

Refs. [115], [116], [117]). Taking into account Eq. (5.10), we get the following estimate [110]:

$$t_\beta\, c_{\beta-\alpha} \simeq \frac{1}{m_H^2 - m_h^2}\left[-m_h^2 - m_Z^2 + \frac{3m_t^4}{4\pi^2 v^2}\frac{\mu}{M_S}\left(\frac{A_t^3}{6M_S^3} - \frac{A_t}{M_S}\right)t_\beta\right] \tag{5.15}$$

where the first two terms inside the square bracket comes from $(\lambda_3 + \lambda_4 + \lambda_5 - \lambda_2)v^2$, while the last term comes from the radiatively induced $\lambda_7 v^2 t_\beta$ contribution.

If we want $t_\beta\, c_{\beta-\alpha}$ to be as large as 2, it's clear that we need the third term in the square bracket to be quite large. Unfortunately, this will lead to an unacceptably large value of t_β, which pushes the Yukawa coupling to third generation down-type fermions to large values that are restricted by heavy Higgs searches [118, 119]. In order to see that, let's recall the fact that stability of the Higgs potential demands that $|A_t|$ and $|\mu|$ should both be smaller than 3 M_S [120]. Under this constraint, the maximum of the expression $\frac{\mu}{M_S}\left(\frac{A_t^3}{6M_S^3} - \frac{A_t}{M_S}\right)$ is 4.5, which is achieved for $A_t/M_S = 3$ and $\mu/M_S = 3$. When normalized in terms of the square of the Higgs mass, the coefficient $\frac{3m_t^4}{4\pi^2 v^2}$ is about $m_h^2/16$, which is very small compared to the first two positive terms in the square bracket. Thus, for $t_\beta\, c_{\beta-\alpha}$ to reach the target value 2, t_β needs to be very large. More specifically, for $m_H \approx 250\ GeV$, one requires values of $t_\beta \approx 30$, while for $m_H \approx 500\ GeV$, $t_\beta \approx 120$. These values of m_H and t_β are excluded by heavy Higgs searches at the LHC [118, 119]. One could avoid these constraints for larger values of the heavy Higgs mass, larger than 1 TeV. However, for $m_H \approx 1$ TeV one requires $t_\beta \approx 500$, and it is difficult to keep the perturbative consistency of the theory at such large values of t_β.

In order to address the question of perturbative consistency of the MSSM at large values of t_β, we should stress that in supersymmetric models there are relevant radiatively generated couplings of the H_u Higgs boson to the bottom quarks, which imply a departure from the simple type II 2HDM. These modifications are particularly important for large values of the Higgsino mass parameter μ and lead to a modification of κ_b [121]:

$$\kappa_b = \frac{g_{hbb}}{g_{hbb}^{\rm SM}} = -\frac{s_\alpha}{c_\beta}\left[1 - \frac{\Delta_b}{1+\Delta_b}\left(1 + \frac{1}{t_\alpha t_\beta}\right)\right] \tag{5.16}$$

where Δ_b is given by [122],[123],[124]

$$\Delta_b \simeq \left(\frac{2\alpha_3}{3\pi} M_3 \mu \; I(m_{\tilde{b}_1}, m_{\tilde{b}_2}, M_3) + \frac{h_t^2}{(4\pi)^2} A_t \mu \; I(m_{\tilde{t}_1}, m_{\tilde{t}_2}, \mu)\right) t_\beta \tag{5.17}$$

and the function $I(a, b, c)$ is given by

$$I(a,b,c) = \frac{a^2 b^2 \ln(a^2/b^2) + b^2 c^2 \ln(b^2/c^2) + c^2 a^2 \ln(c^2/a^2)}{(a^2 - c^2)(a^2 - b^2)(b^2 - c^2)} \tag{5.18}$$

and M_3, $m_{\tilde{b}_i}$, $m_{\tilde{t}_i}$ are the gluino, sbottom and stop mass eigenvalues.

There are similar corrections to the tau coupling, but they are governed by weak coupling effects and are therefore less significant. The above corrections imply a difference between κ_b and κ_τ and therefore have relevant phenomenological consequences for sizable values of t_β. In particular, in the region of parameters under investigation, κ_τ tends to differ from κ_b by a few tens of percent.

Moreover, the coupling of the heavy MSSM-like Higgs bosons to bottom quarks becomes

$$g_{Hb\bar{b}} \simeq g_{Ab\bar{b}} \simeq h_b \simeq \frac{m_b t_\beta}{v(1+\Delta_b)}. \tag{5.19}$$

These corrections must be in general considered when studying the production and decay of the heavy CP-even and CP-odd Higgs bosons and lead to some moderate modification of these rates with respect to the ones expected in the type II 2HDM.

At very large values of t_β, the bottom Yukawa coupling h_b and the τ Yukawa coupling $h_\tau \simeq m_\tau t_\beta / v$ become large. For positive values of Δ_b, the increase of the bottom-Yukawa coupling is slower than what is expected using the tree-level relations and hence perturbative consistency can be kept for larger values of t_β. However, for sizable Δ_b, it can be easily shown that the condition to invert the sign of the bottom Yukawa coupling becomes

$$t_\beta c_{\beta-\alpha} = 2(1+\Delta_b). \tag{5.20}$$

Therefore, for very large values of t_β there is a tension between maintaining the perturbative consistency of the theory, which depends on h_b and as shown in Eq. (5.19) is more easily fulfilled for positive Δ_b, and the fulfillment of Eqs. (5.15) and (5.20). Thus we reach the conclusion that within the MSSM the current LHC bounds make it very difficult to invert the sign of the Higgs coupling to bottom quarks while keeping the perturbative consistency of the theory at low energies.

Next let's turn to the Next-to-Minimal supersymmetric extension of the SM (NMSSM) [40], with only an extra singlet superfield added on top of the MSSM. The CP-even singlet will mix with the two neutral CP-even Higgs bosons. We consider first the simpler case when the superpotential is scale invariant and thus the complete Lagrangian would have an accidental $\mathbb{Z}_3$ symmetry. The superpotential is given by

$$W = \lambda \widehat{S}\widehat{H}_u \cdot \widehat{H}_d + \frac{\kappa}{3}\widehat{S}^3 + h_u \widehat{Q} \cdot \widehat{H}_u \, \widehat{U}_R^c + h_d \widehat{H}_d \cdot \widehat{Q}\, \widehat{D}_R^c + h_\ell \widehat{H}_d \cdot \widehat{L}\, \widehat{E}_R^c\,, \tag{5.21}$$

where $\widehat{S}, \widehat{H_u}, \widehat{H_d}$ denote the singlet and doublet Higgs superfields, and $\widehat{Q}, \widehat{D}_R, \widehat{U}_R$ are the quark superfields, while $\widehat{L}, \widehat{E}_R$ are the lepton superfields, h_i are the Yukawa couplings and λ and κ are both dimensionless couplings. Note that in this case, μ is an effective mass parameter generated by the vev of the singlet, $\mu_{\text{eff}} = \lambda s$; we will use μ in the following discussions to refer to μ_{eff}. Observe that the fields H_u and H_d have opposite hypercharge. These fields can be related to the fields Φ_1 and Φ_2 introduced before by the relations

$$H_d^i = \epsilon_{ij}\Phi_1^{j*} \qquad H_u^i = \Phi_2^i \tag{5.22}$$

and therefore

$$H_u H_d = -\Phi_2^\dagger \Phi_1 \tag{5.23}$$

The most significant change in the NMSSM would be that at tree level,

$$\delta\lambda_4 = \lambda^2 \tag{5.24}$$

and therefore there is an extra correction proportional to $\frac{1}{2}\lambda^2 v^2 s_{2\beta}^2$ in the M_{11}^2 term of the Higgs basis. This term is relevant since it can lift up the upper limit of the lightest Higgs mass at tree level [125], thus making it possible to reach 125 GeV without the large quantum corrections needed in the MSSM [115, 126–134]. What's more important in this case is that it can modify the Z_6 term introduced earlier in the MSSM case and release the strong tension between t_β and M_A present in the MSSM to make $c_{\beta-\alpha} t_\beta = 2$ feasible. In the NMSSM, considering heavy singlets, it's straightforward to get the expression for Z_6 at moderate or large values of t_β, including only the stop loop corrections, namely [135]:

$$Z_6 v^2 \approx \frac{1}{t_\beta}\left[m_h^2 + m_Z^2 - \lambda^2 v^2\right] + \frac{3v^2 h_t^4 \mu X_t}{16\pi^2 M_S^2}\left(1 - \frac{X_t^2}{6M_S^2}\right) \tag{5.25}$$

where $X_t = A_t - \mu/t_\beta$, which leads to

$$t_\beta\, c_{\beta-\alpha} \approx \frac{-1}{m_H^2 - m_h^2}\left[\left(m_h^2 + m_Z^2 - \lambda^2 v^2\right) + \frac{3m_t^4 A_t \mu t_\beta}{4\pi^2 v^2 M_S^2}\left(1 - \frac{A_t^2}{6M_S^2}\right)\right] \tag{5.26}$$

Compared with Equation (5.15), we have an extra $-\lambda^2 v^2$ term in the parenthesis, which comes from $\delta\lambda_4$, Eq. (5.24), and tends to push $t_\beta\, c_{\beta-\alpha}$ towards positive values, making it promising to get $t_\beta\, c_{\beta-\alpha} = 2$ with smaller values of t_β. However, for that purpose we need λ to be of order 1. For λ or κ of order 1, one can no longer neglect the chargino, neutralino and Higgs loop contributions when evaluating the Higgs mass and couplings. Although approximate analytical expressions exist in this case, the formulae become complicated and beyond some approximate formulae we will present in the next section, we will mostly base our results in a numerical analysis with full quantum corrections up to two-loop level, which are necessary to select the proper region of parameter space leading to the inversion of the bottom coupling. Moreover, large λ could lead to a Landau pole problem at energies lower than the Grand Unification scale.

Moderate values of t_β

As we discussed before, the MSSM is highly constrained for the large values of t_β necessary to achieve an inversion of the bottom couplings. These constraints tend to translate into the NMSSM since for very large values of t_β the decay of the MSSM-like CP-even and CP-odd Higgs bosons into bottom-quarks and τ-leptons remain relevant. In the NMSSM, however, for sufficiently large values of λ, an inversion of the sign of the SM-like Higgs boson coupling to bottom quarks may be achieved at moderate values of $t_\beta \simeq$ 5–10. For this range of values of t_β the constraints from direct searches for heavy Higgs bosons become weaker, but some of the approximations performed before cease to be valid. In particular, the effects of the mixing between the CP-even Higgs bosons become relevant and cannot be dismissed. Due to these mixing effects, and ignoring the mixing with singlets, we obtain

$$m_h^2 \simeq Z_1 v^2 - \frac{Z_6^2 v^4}{m_H^2} \tag{5.27}$$

or, equivalently

$$m_h^2 \simeq Z_1 v^2 - c_{\beta-\alpha}^2 m_H^2 \simeq \lambda_2 v^2 - \frac{4 m_H^2}{t_\beta^2}. \tag{5.28}$$

For very large values of t_β the last term may be safely ignored. However, for moderate values of t_β this term cannot be ignored and tends to push the mass of the Higgs boson to values that are below the experimentally observed value. Mixing with the singlets only worsen this situation. In order to address this problem, a departure from the simple $\mathbb{Z}_3$ invariant

NMSSM is necessary.

NMSSM with singlet tadpole terms

As discussed above, we are interested in the inversion of the sign of the coupling of the bottom-quark to the Higgs in the simplest NMSSM case, with sizable values of λ and moderate values of t_β. This simple framework tends to lead to problems in the CP-even Higgs sector, since as we discussed in the previous section, the lightest CP-even Higgs boson mass is generically pushed to values below the experimentally observed ones due to large mixing effects. A possible solution to this problem is to include a non-zero singlet tadpole term ξ_S to the potential

$$\Delta V = \ \xi_S \ S + h.c. \tag{5.29}$$

This term, which could be a result of the supersymmetry breaking mechanism at high scales [136–138], serves to break the $\mathbb{Z}_3$ symmetry explicitly and get rid of unwanted domain walls. For values of μ of the order of the weak scale and λ couplings of order one, a sizable value of $|\xi_S|$ leads to large values of the singlet mass. Ignoring other terms that become subdominant for large value of $|\xi_S|$, one obtains

$$\langle S \rangle = \frac{\mu}{\lambda} \simeq -\frac{\xi_S}{m_S^2} \tag{5.30}$$

or, equivalently

$$m_S^2 \simeq -\frac{\lambda \xi_S}{\mu} \tag{5.31}$$

A sizable $|\xi_S|$ could keep the singlet decoupled from the two neutral Higgs bosons, reducing the problem to an approximate 2x2 Higgs mixing one, with low energy quartic couplings that are modified by terms proportional to powers of the couplings λ and κ. For moderate values of ξ_S, the decoupling effects may affect the low energy theory in a relevant way. We shall discuss these effects in more detail below.

An additional consequence of large values of ξ_S is that the singlet mass may become much larger than the mass of the singlino. In this case, the quartic coupling of H_u has sizable corrections produced by λ^4 loop contributions from singlets and singlinos. The correction to λ_2 from these contributions is given by

$$\delta\lambda_2 \simeq \frac{\lambda^4}{16\pi^2} \ln\left(\frac{m_S^2}{\mu^2}\right) \simeq \frac{\lambda^4}{16\pi^2} \ln\left(\left|\frac{\lambda\xi_S}{\mu^3}\right|\right) \tag{5.32}$$

where we have used the expression for m_S^2 given in Eq. (5.31). It is therefore clear that for values of $|\mu|$ of the order of the weak scale, large values of ξ_S result in large positive corrections to λ_2. These corrections can compensate the negative contributions to the Higgs mass induced by mixing effects and constrain the allowable values of ξ_S via the experimental constraints on the lightest CP-even Higgs mass, which will be examined in more specificity in the next section.

A further possible modification to the NMSSM is the inclusion of a similar tadpole term in the superpotential, namely beyond the trilinear terms associated with the Yukawa, λ and κ couplings, one may add a tadpole term of the form [40]

$$\delta W = \xi_F S \tag{5.33}$$

where ξ_F is a dimension 2 parameter. One action of such a term, as we shall discuss, is to modify the spectral relationships between the neutral and charged Higgs bosons. In our initial analysis, we first set $\xi_F = 0$; however, we shall discuss the impact of this term in later examinations of pseudoscalar decays in Section 5.1.6.

The decoupling of the singlet induces corrections to λ_4 and λ_5, and a sizable correction to the quartic coupling λ_7. This can be seen by ignoring subdominant terms and reducing the singlet-dependent terms in the scalar potential to

$$(m_S^2 + \lambda^2 |H_u|^2)|S|^2 + [S(\lambda A_\lambda H_u H_d + \xi_S) + h.c.] + \left|\xi_F + \lambda H_u H_d + \kappa S^2\right|^2 \tag{5.34}$$

where we shall assume that, due to the effect of the tadpole terms, m_S^2 is much larger than $\lambda^2 H_u^2 \simeq \lambda^2 v^2$. From Eq. (5.34), and ignoring small corrections induced by the vacuum expectation values of the singlet and doublet fields, we can see that the masses of the CP-even and CP-odd singlet eigenstates are approximately given by

$$m_{h_S}^2 = m_S^2 + 2\xi_F \kappa, \qquad m_{A_S}^2 = m_S^2 - 2\xi_F \kappa, \tag{5.35}$$

repsectively. Now, one can integrate out the singlets, replacing the singlet fields by their equation of motion. This is roughly

$$\mathrm{Re}(S) \simeq -\frac{\lambda A_\lambda (H_u H_d + h.c.) + \xi_S}{2\ m_{h_S}^2}, \qquad \mathrm{Im}(S) \simeq -i\frac{\lambda A_\lambda (H_u H_d - h.c.)}{2\ m_{A_S}^2}. \tag{5.36}$$

Replacing this expression into the orginal Lagrangian density, Eq. (5.34), one obtains contributions to λ_4, λ_5, and λ_7 given by

$$\begin{aligned}
\delta\lambda_4 &\simeq -\lambda^2\left(\frac{A_\lambda^2}{2m_{h_S}^2} + \frac{A_\lambda^2}{2m_{A_S}^2}\right) + 2\lambda^2\kappa\frac{\xi_S A_\lambda}{m_{h_S}^2}\left(\frac{1}{m_{h_S}^2} - \frac{1}{m_{A_S}^2}\right) \\
&+ \frac{\xi_F A_\lambda^2 \kappa\lambda^2}{2}\left(\frac{1}{m_{h_S}^4} - \frac{1}{m_{A_S}^4}\right) + \frac{\kappa^2\lambda^2 A_\lambda^2 \xi_S^2}{m_{h_S}^4}\left(\frac{3}{m_{h_S}^4} + \frac{1}{m_{A_S}^4}\right) \\
\delta\lambda_5 &\simeq -\lambda^2\left(\frac{A_\lambda^2}{2m_{h_S}^2} - \frac{A_\lambda^2}{2m_{A_S}^2}\right) + 2\lambda^2\kappa\frac{\xi_S A_\lambda}{m_{h_S}^2}\left(\frac{1}{m_{h_S}^2} + \frac{1}{m_{A_S}^2}\right) \\
&+ \frac{\xi_F A_\lambda^2 \kappa\lambda^2}{2}\left(\frac{1}{m_{h_S}^4} + \frac{1}{m_{A_S}^4}\right) + \frac{\kappa^2\lambda^2 A_\lambda^2 \xi_S^2}{m_{h_S}^4}\left(\frac{3}{m_{h_S}^4} - \frac{1}{m_{A_S}^4}\right) \\
\delta\lambda_7 &\simeq -\lambda^3\frac{\xi_S A_\lambda}{m_{h_S}^4}
\end{aligned} \tag{5.37}$$

The value of μA_λ is related to the CP-odd Higgs spectrum by the relation

$$\left[\mu\left(A_\lambda + \frac{\kappa}{\lambda}\mu\right) + \lambda\xi_F\right] t_\beta \simeq M_A^2 \tag{5.38}$$

and therefore for fixed M_A and moderate values of κ, sizable negative values of ξ_F result in large positive values of μA_λ. Hence, for values of μ at the weak scale, the presence of negative ξ_F can lead to sizable values of A_λ and therefore to large corrections to λ_7. Such large corrections may induce a modification of the value of $c_{\beta-\alpha}$, which including only the dominant terms becomes

$$\begin{aligned} t_\beta\, c_{\beta-\alpha} \approx \frac{1}{m_H^2 - m_h^2}\Bigg[\left(\lambda^2\left(1 - \frac{A_\lambda^2}{m_{h_S}^2}\right)v^2 - \lambda_2 v^2 - M_Z^2\right) + \frac{3m_t^4 A_t \mu t_\beta}{4\pi^2 v^2 M_S^2}\left(\frac{A_t^2}{6M_S^2} - 1\right) \\ - \lambda^3 v^2 \frac{\xi_S A_\lambda t_\beta}{m_{h_S}^4}\Bigg]. \end{aligned} \tag{5.39}$$

Hence, the reduction of the λ^2 contribution due to sizable values of A_λ may be compensated by the explicit ξ_S dependence appearing in the last term of Eq. (5.39).

Moreover, including the above corrections to λ_4 and λ_5 modifies the difference between the charged and neutral CP-odd Higgs boson masses, Eq. (5.13),

$$(\lambda_5 - \lambda_4)\frac{v^2}{2} \simeq M_W^2 + \left\{\left(\frac{A_\lambda^2}{m_{A_S}^2} - 1\right) + \kappa\left[\frac{4\xi_S A_\lambda}{m_{A_S}^2 m_{h_S}^2} + \left(\xi_F - \frac{2\kappa\xi_S^2}{m_{h_S}^4}\right)\frac{A_\lambda^2}{m_{A_S}^4}\right]\right\}\frac{\lambda^2 v^2}{2}. \tag{5.40}$$

Hence for sizable A_λ, the splitting between the CP-odd and the charged Higgs mass induced by the large values of λ, Eq. (5.13), may be reduced by the effects associated with the singlet decoupling. These observations will be important in examining the constraints from precision measurements and the decay mode $A_1 \to hZ$.

5.1.4 NMSSM Results: Full Analysis

In this section, we conduct a numerical search for a wrong-sign Yukawa coupling within the NMSSM model using NMSSMTools [139], which includes the most relevant one and two-loop radiative corrections to the Higgs mass matrix elements. In this calculation, we scan over 6 independent parameters: $t_\beta, M_A, \mu, \lambda$, κ, and ξ_S. We fix the gaugino and third generation scalar mass parameters to values that are not constrained by present experimental bounds and that contribute to the obtention of a proper SM-like Higgs mass at sizable values of t_β. This selection is somewhat arbitrary and does not play a relevant role in the Higgs phenomenology at moderate values of t_β. However, as we will discuss below, it has an impact on the analysis of the flavor and Dark Matter constraints. In our analysis we set $A_t = 1700$ GeV, A_τ,A_b = 1500 GeV, and the squark and slepton masses at $M_S = 1$ TeV. The weak gauginos were assumed to be heavy, $M_{1,2} = 1$ TeV, while the gluino mass was fixed at $M_3 = 2$ TeV.

As discussed in the previous section, taking into account the strong constraints on large t_β for the relatively low values of the MSSM-like CP-odd Higgs mass [118, 119] necessary to induce a large correction to the bottom coupling, we concentrate on moderate values of t_β. In particular, values of t_β in the range 6–10 and values of the CP-odd Higgs mass m_A within the interval of 300 GeV to 500 GeV are preferred due to these considerations. While larger values of m_A make it more difficult to obtain a large correction to the bottom coupling, smaller values of m_A lead to tension with the current CP-even and CP-odd neutral Higgs searches and, for $\xi_F = 0$, to low values of the charged Higgs mass, excluded by top-quark decay studies.

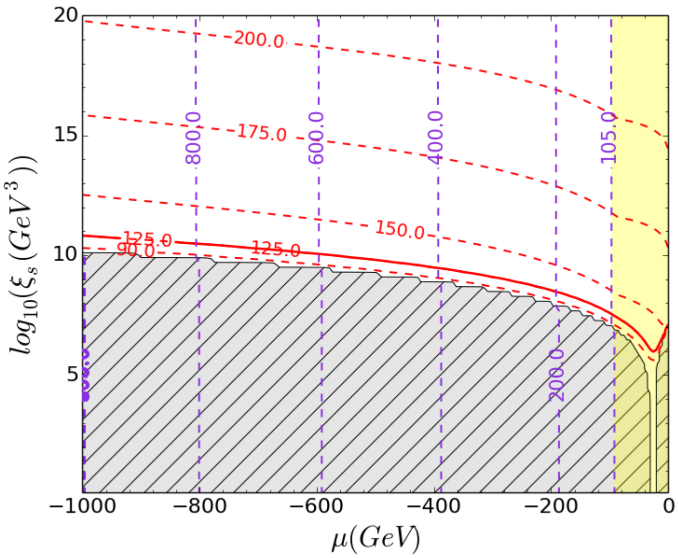

Figure 5.1: In this plot, $\lambda = 1.3$ and $\kappa = 0.1$ are fixed, and μ and ξ_s are varied to examine the allowable values of these parameters. The gray area is excluded for negative Higgs mass. Red contour lines indicate values of the lightest Higgs mass, with 125 GeV represented by the solid contour. The lightest chargino mass contours are displayed in purple.

In order to identify the possible ranges of ξ_S, we first performed a scan over a wide range of values of ξ_S and μ for some characteristic parameters of the theory leading to a variation of the coupling of the Higgs to the bottom-quark. An examination of Eq. (5.39) indicates that to obtain $t_\beta c_{\beta-\alpha} = 2$, one requires negative values of $\mu \times \xi_S$. The values of $|\mu|$ are required to be at the weak scale and lead to allowed values of the chargino and neutralino masses. Taking ξ_S to be positive, we therefore scan a range for μ from -1000 GeV to 0 GeV. All other parameters are fixed at values that favor positive values of $t_\beta c_{\beta-\alpha}$: $\lambda = 1.3$, $\kappa = 0.1$, $M_A = 350$, and $t_\beta = 7$. The result of this scan is shown in Fig. 1. We find that the value of the lightest CP-even Higgs mass m_1 does indeed increase with ξ_S, as expected from Eq. (5.32). The contour with $m_1 = 125$ GeV is indicated by the solid red line; the constraint of $m_1 = 125 \pm 3$ GeV, which takes into account the uncertainty in the determination of the Higgs mass, therefore constrains the value of ξ_S to be on the order of 10^9 to 10^{11} GeV^3 for values of $|\mu|$ at the weak scale.

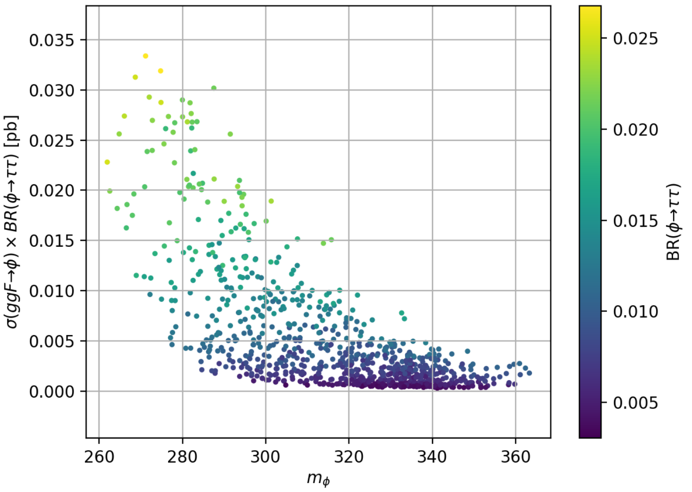

Figure 5.2: Predicted rate of gluon fusion production of a heavy neutral Higgs ϕ decaying into $\tau\tau$, where the values are calculated including H and A_1. The heavily suppressed branching ratio of $\phi \to \tau\tau$ in our models, which is discussed further below, results in a suppressed rate which is within the most recent limits.

In the rest of this section, we examine the results of a scan to search for models which produce a wrong-sign bottom Yukawa coupling. Based on the above analysis, we fix the supersymmetry mass parameters to the values given above and vary the tadpole term ξ_S in the range of 1.25×10^{10} and 1×10^{11} GeV^3 and μ in the range -1300 to -800 GeV. Beyond these ranges, the number of successful points decreases quickly due to experimental limits. For larger ξ_S and $|\mu|$, the charged Higgs mass becomes too low; for lower ξ_S and $|\mu|$, the range of ξ_S and μ which passes experimental constraints and gives the correct SM-like Higgs mass becomes quite narrow, and κ_b can become positive for μ close enough to 0. We therefore do not include these ranges in the main scan. Additionally, the following parameters were varied within the ranges of $t_\beta \in [6, 10]$, $M_A \in [300, 400]$ GeV, $\lambda \in [1.0, 1.8]$, $\kappa \in [0.0, 1.0]$. Parameters are randomly drawn from uniform distributions and we discard all points which give the wrong lightest Higgs mass or fail other collider direct experimental constraints as defined in NMSSMTools version 5.1.2. These constraints include constraints from heavy Higgs searches through $t \to bH^\pm$, $H/A \to \tau\tau$, $H \to AA \to 4l/2l + 2b$, and

$ggF \to H/A \to \gamma\gamma$, as well as lower limits on the masses of squarks, gluino, sfermions, neutralinos, and charginos. More recent ATLAS and CMS constraints from $\phi \to \tau\tau$ [118, 119] are available, where ϕ is an additional neutral Higgs boson, which are not included in version 5.1.2. The rate of these processes at ATLAS and CMS have been checked separately and we find that we are well within the bounds, which are of order of a few tenths of pb at masses of the order of 300 GeV, due to a production cross section for H or A_1 of about 1 pb for both ggF and b-associated production and a branching ratio around 2%. Figure 5.2 shows the predicted rate in our models for ggF production of ϕ and subsequently ϕ decaying into $\tau\tau$. We did not impose any flavor or Dark Matter constraints, but we shall discuss these constraints in separate sections. The results of the numerical scan are shown in Fig. 5.3.

It is clear that the requirement of a wrong-sign bottom Yukawa indeed fixes λ to be of order 1, a reflection of the strong tree-level dependence of the bottom coupling on this parameter. Additionally, larger values of ξ_S allow λ to take on lower values; however, as shown in Fig. 5.1, ξ_S is also restricted from the requirement of obtaining the proper Higgs mass and cannot take arbitrary large values. Therefore, it is difficult to push λ down below order 1 using the tadpole contribution. The constraint on κ is significantly relaxed by the large value of ξ_S, which allows κ to take on values from 0 to 1, with a gentle dependence on λ for given ξ_S. Further parameters and relevant outputs for five sample points which were successful are provided in Table 1. It is clear from Table 1 that in this region of parameters $A_\lambda \ll m_S$ and therefore the effects associated with the singlet decoupling, Eq. (5.37), become small. As we shall see in later sections, this situation will change when we consider values of $\xi_F \neq 0$.

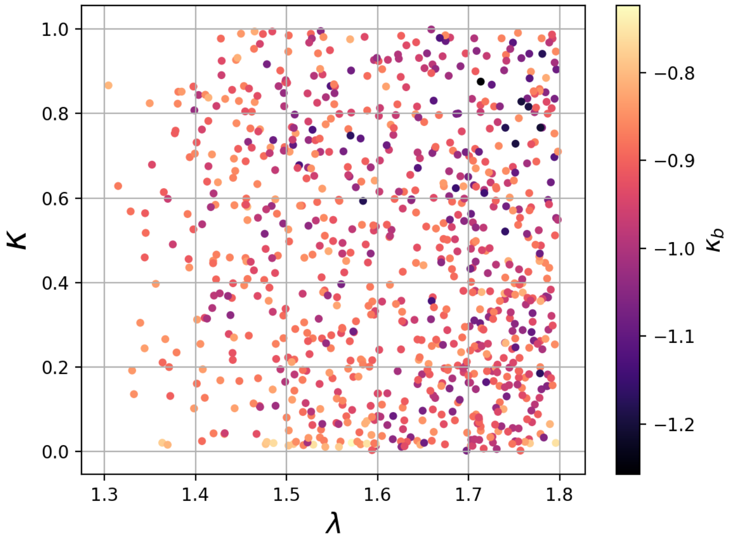

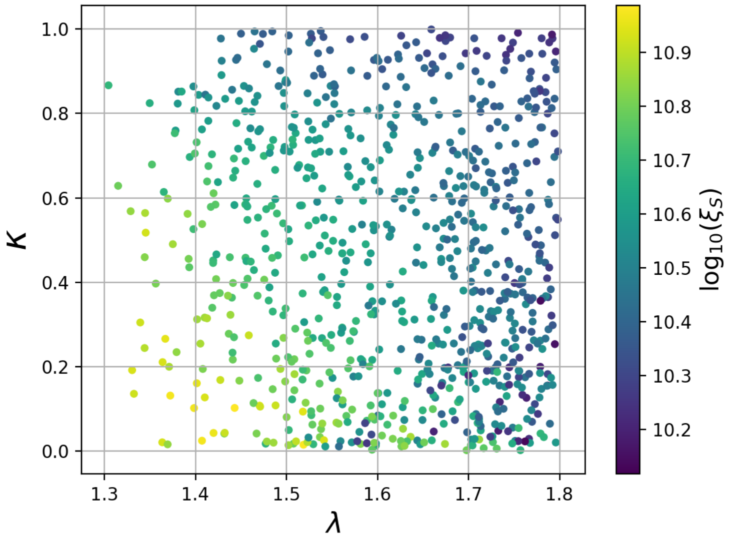

Figure 5.3: Scatter plot of points that survive the 125 GeV mass constraint and predict a wrong-sign bottom Yukawa coupling. The colorbar on the upper plot shows the value of κ_b, which is the ratio between Higgs to $b\bar{b}$ coupling and its SM value, i.e. $g_{hb\bar{b}}^{NMSSM}/g_{hb\bar{b}}^{SM}$. All points have κ_b close to -1 as demanded. The lower plot shows the relationship between the values of λ, κ, and the tadpole contribution.

$No.$	t_β	M_A	μ	λ	κ	A_λ	ξ_S	κ_b	$BR(h \to b\bar{b})$	m_h	m_H	$m_{H^\pm}$	m_S
1	9.7	374	-1283	1.41	0.024	11.0	9.79×10^{10}	-0.98	64.9%	123.1	278	159	10360
2	8.5	398	-1294	1.37	0.131	109.3	9.38×10^{10}	-0.90	63.2%	122.3	271	158	9973
3	7.7	369	-1190	1.62	0.063	31.5	6.27×10^{10}	-0.98	58.6%	127.1	310	158	9242
4	8.5	362	-1119	1.41	0.398	302.3	6.92×10^{10}	-0.97	58.9%	126.5	277	156	9344
5	8.9	331	-1109	1.37	0.200	150.4	7.51×10^{10}	-0.89	56.3%	125.9	273	159	9634

Table 5.1: Typical parameters found by NMSSMTools that gave negative Higgs to $b\bar{b}$ couplings

All points shown above pass the experimental limits included in NMSSMTools v5.1.2. Additionally, an approximately linear, t_β-dependent cut is applied to $m_{H^\pm}$ based on the constraints provided by CMS [140]; a plot of the charged Higgs mass as a function of m_H is shown in Fig. 5.4. These mass ranges allow for enhanced $H \to H^\pm W^\mp$ and $A_1 \to H^\pm W^\mp$ decays, which will be discussed further in Sections 5.1.5 and 5.1.6.

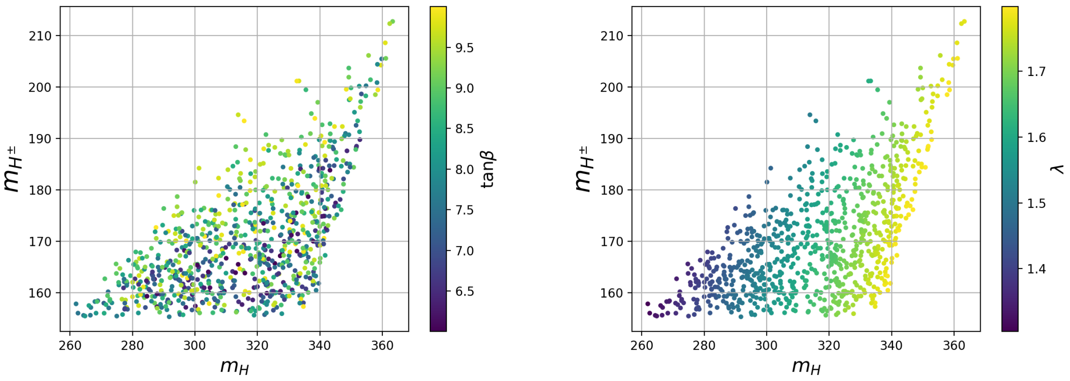

Figure 5.4: Scatter plot of the charged Higgs mass $m_{H^\pm}$ against m_H, with the colorbar showing the value of t_β (left) and λ (right). A t_β-dependent mass cut on $m_{H^\pm}$, with a lowest limit of 155 GeV, has been applied to satisfy experimental constraints.

5.1.5 Implications for LHC Physics

SM-like Higgs boson properties

The change of sign of the bottom coupling has implications for the loop-induced coupling of the SM-like Higgs to gluons and photons and is also correlated with changes to the couplings of non-standard Higgs doublets to third generation quarks.

In Fig. 5.5, we plot the values of κ_g and κ_γ against κ_b, where κ_i is the ratio of the Higgs coupling to the particle i to its value in the SM. The $h \to gg$ and $h \to \gamma\gamma$ amplitudes have contributions from bottom quark loops, and will therefore be modified within our models. Charged Higgs loops also provide a small contribution to $h \to \gamma\gamma$ within our models given the low value of $m_{H^\pm}$. All solutions show values of the couplings that are within 20% of the SM values, which are in agreement with current experimental constraints. These results coincide with those obtained by the authors of Ref. [92]. Interestingly enough, CMS presents a global fit to the couplings of the SM-like Higgs, assuming no new physics in either the decay or in the loop-induced couplings, leading to a marginal preference towards a wrong-sign bottom Yukawa coupling [55]. Although in our model there is a small contribution to the Higgs-photon coming from the charged Higgs, the CMS preference is mostly due to an apparent enhancement of the gluon fusion-induced processes compared to the SM values, that is not present in the ATLAS data [141]. On the other hand, our values for κ_g and κ_γ are within 1 standard deviation of the most recent best-fit values from both experiments. This shows that the LHC experiments have not yet the sensitivity to distinguish between a SM-like Higgs with wrong-sign bottom Yukawa couplings and the SM Higgs.

As can be seen in Fig. 5.5, the values of κ_g for our set of points range between 1.10 and 1.13. Since we have assumed heavy supersymmetric particles, these modifications are governed by just the modifications of the bottom couplings. This is a reasonably large effect, but observing this effect at the LHC is complicated by systematic errors in the primary gg

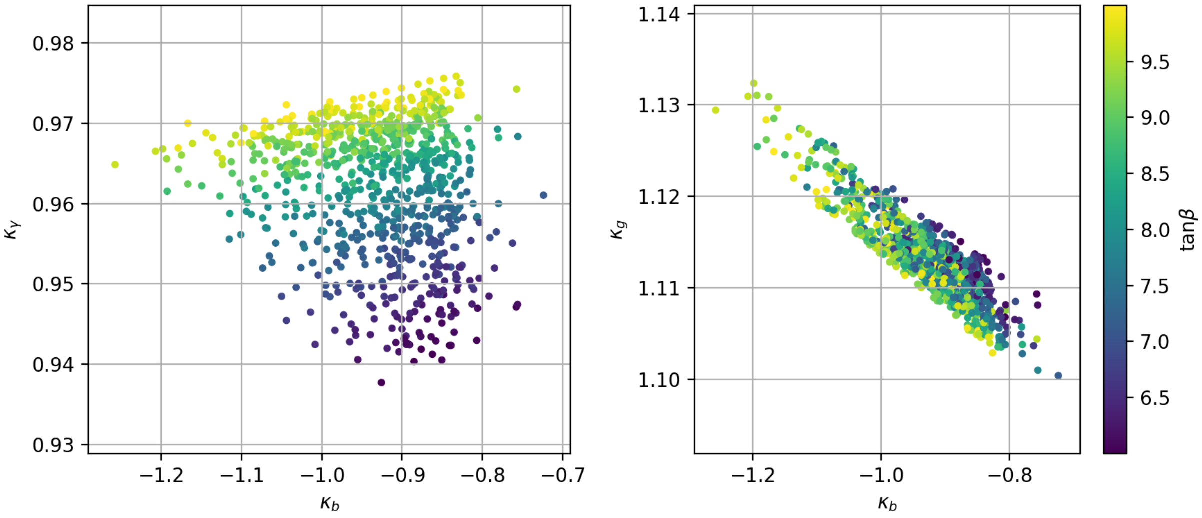

Figure 5.5: Scatter plots of the couplings for the SM-like Higgs to γ (left) and gluons (right) against κ_b. The color bar indicates the value of t_β. We find that κ_γ is reduced by 3-6% and displays a linear dependence on t_β, while κ_g is enhanced by approximately 10-13%.

fusion production cross section. Ref. [142] provides expected error estimates for κ_g of 6-8% for an integrated luminosity of 300 fb^{-1} and 3-5% for an integrated luminosity of 3000 fb^{-1}. It is clear from these numbers that hints may become observable by the end of Run 2 and the effects should be clearly resolvable by the end of Run 3.

The value of κ_γ within our set of points ranges from approximately 0.94 to 0.98. Estimates for LHC uncertainties in the measurement of κ_γ are given as 5-7% for 300 fb^{-1} integrated luminosity and 2-5% for 3000 fb^{-1} integrated luminosity [142]. The measurement of κ_γ may therefore allow an examination of the viability of the wrong-sign bottom Yukawa within the NMSSM by the end of LHC Run 3.

Let us stress again that the above estimates of the modification of the Higgs couplings to gluons and photons have been performed under the assumption of heavy supersymmetric particles. If, eventually, charged and/or colored supersymmetric particles are detected at the LHC, their effects would have to be taken into account (see, for instance, Refs. [143],[144],[145],[146]) in order to determine the possible effects of the inversion of the bottom coupling.

The modification of the SM-like Higgs coupling to top-quarks and weak gauge bosons tend to be small in the explored region of parameters. Indeed, ignoring for simplicity the Δ_b corrections,

$$\begin{aligned} \kappa_W &= s_{\beta-\alpha} \simeq 1 - \frac{2}{t_\beta^2} \\ \kappa_t &= s_{\beta-\alpha} + \frac{c_{\beta-\alpha}}{t_\beta} \simeq 1, \end{aligned} \tag{5.41}$$

where we have used the fact that $c_{\beta-\alpha} \simeq 2/t_\beta$.

In Fig. 5.6 we show the correlation between the Higgs-induced weak diboson production cross section and the coupling of the SM-like Higgs decay into bottom quarks, normalized to the values obtained for a Higgs of the same mass in the SM. The strong correlation may be explained by the fact that the $BR(h \to WW, ZZ)$ is mostly determined by the variation of the total width induced by the modification of the bottom-quark coupling to the Higgs and by the values of $\kappa_g^2 \simeq 1.25$ (see Fig. 5.5). The outlier points which do not follow this linear relationship are associated with small values of κ, for which the SM-like Higgs boson can decay into the lightest neutralino and have therefore a non-vanishing branching ratio of decays into invisible particles.

Radiative Higgs Decay to Quarkonia

Another particular Higgs process affected by the bottom Yukawa coupling is the radiative decay of the Higgs to Quarkonium, in particular to the Υ meson, which is composed of $b\bar{b}$. This process has also been examined within a general 2HDM in the wrong-sign regime by [147]. Within the Standard Model, the direct and indirect Feynman diagrams have an approximate accidental cancelation, which effectively excludes this decay process at all but

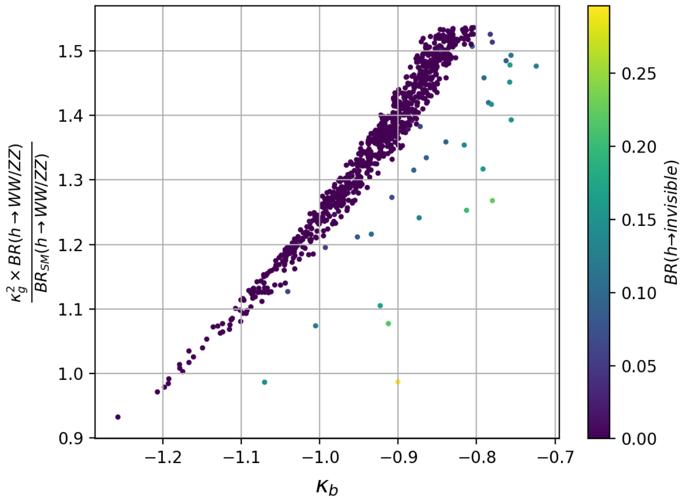

Figure 5.6: Plot showing the product of κ_g^2 and the branching ratio of h to WW or ZZ against κ_b. The $h \to WW/ZZ$ rates are normalized to the SM rate for the particular SM-like Higgs mass. The colorbar shows the branching ratio of the SM Higgs to neutralinos; we see that the points which do not follow the linear trend have a larger branching ratio to invisible particles.

very high luminosities. The decay widths of $H \to \Upsilon(nS) + \gamma$ in terms of κ_b are given by [78]

$$\begin{aligned}
\Gamma[H \to \Upsilon(1S) + \gamma] &= |(3.33 \pm 0.03) - (3.49 \pm 0.15)\kappa_b|^2 \times 10^{-10} \text{ GeV} \\
\Gamma[H \to \Upsilon(2S) + \gamma] &= |(2.18 \pm 0.03) - (2.48 \pm 0.11)\kappa_b|^2 \times 10^{-10} \text{ GeV} \qquad (5.42) \\
\Gamma[H \to \Upsilon(3S) + \gamma] &= |(1.83 \pm 0.02) - (2.15 \pm 0.10)\kappa_b|^2 \times 10^{-10} \text{ GeV}
\end{aligned}$$

where the first term derives from the indirect diagram and the second term, which is modified by κ_b, derives from the direct diagram. Note that the change in sign from $\kappa_b = 1$ to $\kappa_b = -1$ gives a factor increase of between 10^2 and 10^4 in the decay widths. Using $\Gamma(H) = 4.195^{+0.164}_{-0.159} \times 10^{-3}$ GeV, the Higgs branching ratio to $\Upsilon(1S, 2S, 3S) + \gamma$ final states for the SM are (0.610, 2.15, 2.44)$\times 10^{-9}$. For $\kappa_b = -1$, the branching ratios are (1.11, 0.518, 0.378)$\times 10^{-6}$, which are still small but significantly larger than the SM values.

The predicted number of $H \to \Upsilon(nS) + \gamma$ events at the LHC is calculated as

$$N = \frac{\Gamma(H \to \Upsilon(nS) + \gamma)}{\Gamma(H)} \times \sigma(p + p \to H) \times \mathcal{L}_{int}. \tag{5.43}$$

We calculate the expected number of $H \to \Upsilon(nS) + \gamma$ events for both $\kappa_b = 1$ and $\kappa_b = -1$. The Higgs total cross section is taken to be $\sigma(p + p \to H) = 5.57 \times 10^4$ fb. We examine the number of expected events by the end of LHC Run 3, for which the approximate target integrated luminosity is 300 fb^{-1}. The predicted number of events are less than 1 for $\kappa_b = 1$ and $N(\Upsilon(1S), \Upsilon(2S), \Upsilon(3S)) = (18.5 \pm 0.7, 8.65 \pm 0.36, 6.31 \pm 0.26)$ for $\kappa_b = -1$. The number of events at the 3 ab^{-1} high-luminosity LHC is simply an order of magnitude larger than the one predicted at the end of Run 3, namely a few hundred events.

Searches for $h \to \Upsilon(nS) + \gamma$ have been performed previously for the 8 TeV runs with approximately 20.3 fb^{-1} of luminosity [148]. The current upper limits on the branching ratios at 95% CL are given for $\Upsilon(1S, 2S, 3S) + \gamma$ final states as (1.3, 1.9, 1.3)$\times 10^{-3}$ ([149], [148]). An increase in sensitivity for these decays on the order of 10^3 with respect to the one at Run 1 is therefore required in order to probe the effects of a wrong-sign bottom Yukawa. Therefore, despite the significant enhancement of the number of events with respect to the SM, this process is not currently an effective method of searching for a wrong-sign bottom Yukawa, and its detection will demand a significant improvement of the current analysis.

Decay channels of the heavy neutral Higgs

A particular characteristic of those surviving points in Table 5.1 is that they all have low charged Higgs mass. The mass difference between H, A_1, and $H^{\pm}$ allows the $H \to H^{\pm} W^{\mp}$ channel to open up and become the dominant decay mode of the heavier neutral Higgs H, as well as of the lighter CP-odd Higgs A_1. This observation has many phenomenological consequences. On one hand, the branching ratio of $H \to \tau^+\tau^-$ is suppressed even when t_β is large, so that one may push t_β higher than the current bounds on this channel [118, 119]. These arguments are confirmed by Fig. 5.7, in which we see that all $BR(H \to \tau\tau)$ values

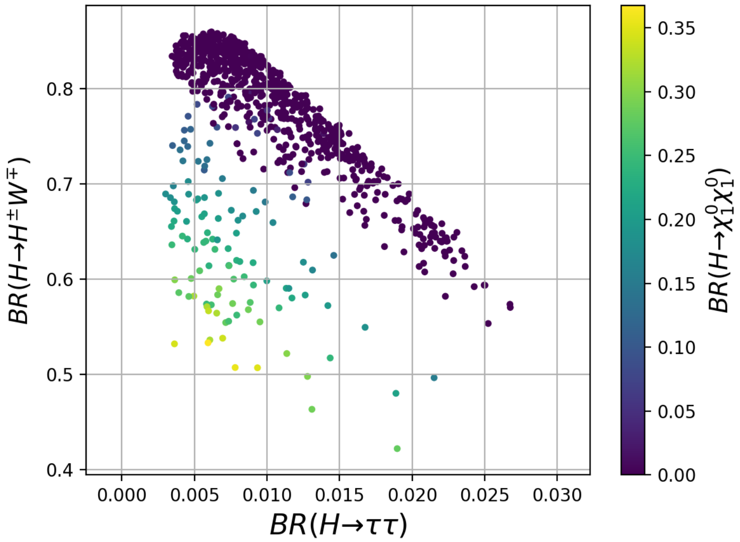

Figure 5.7: Branching ratios for the decay of the heavier neutral Higgs H to $H^{\pm}W^{\mp}$ and $\tau\tau$, with the branching ratio of $H \to \chi_1^0\chi_1^0$ as the colorbar.

are lower than 3%. For low values of κ, the singlino may become light and, as shown in Fig. 5.7, the invisible decay branching ratio of the heavy Higgs bosons may become relevant, and imply a further decrease of the decay into τ-leptons. On the other hand, this large $BR(H \to H^{\pm}W^{\mp})$ also means that this exotic decay channel provides a possibly interesting search channel at the LHC. Within these models, $BR(H \to H^{\pm}W^{\mp})$ is greater than 0.4 for all models and reaches values up to 0.8. Fig. 5.8 shows the predicted rate of H decaying to $H^{\pm}W^{\mp}$ through gluon fusion production in pb; we find a rate on the order of a few tenths of pb.

Flavor Constraints

As discussed in the previous section, the presence of a light charged Higgs opens new channels for the neutral Higgs decays that can be searched at the LHC. A light charged Higgs, however, can also induce large corrections to flavor observables, in particular to the radiative decay of B mesons into strange ones. In type II 2HDM's, the $b \to s\gamma$ rate is indeed highly

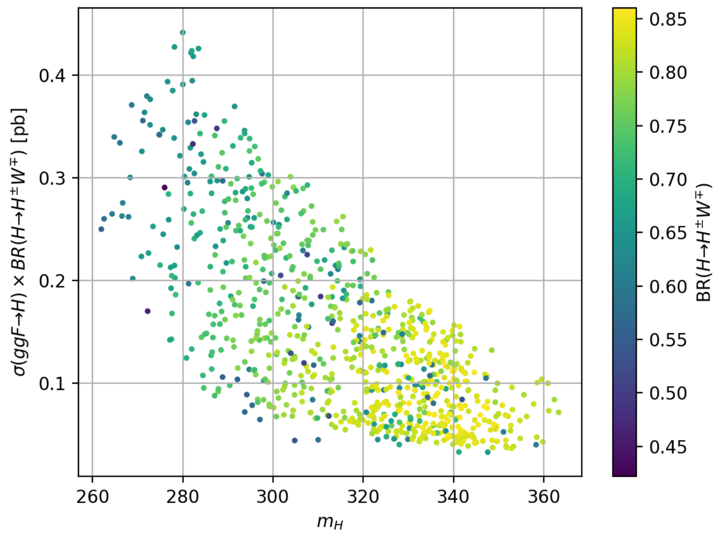

Figure 5.8: Predicted rate in pb of ggF-produced H decaying into $H^{\pm}W^{\mp}$

enhanced in the presence of a charged Higgs [150],[151]. In supersymmetric theories, however, this rate depends strongly on other contributions coming from supersymmetric particles, and therefore a light charged Higgs cannot be ruled out by these considerations. On one hand, there are the contributions coming from the charginos and stops. It is indeed known that in the supersymmetric limit these cancel exactly the SM contributions to the dipole operators contributing to the $b \to s\gamma$ transition [152]. On the other hand, there are flavor violating contributions of the neutral Higgs bosons, as well as modifications of the charged Higgs couplings, coming from similar radiative corrections to the ones that contribute to Δ_b, discussed in section 5.1.3 [153–156]. All these corrections are included in the NMSSMTools code we use [139]. Finally, there are contributions that are more difficult to evaluate and come from possible flavor violation in the scalar fermion sector. Those corrections are induced whenever there is a misalignment of the basis in which the quark and squark mass matrix are diagonalized, and lead to large corrections induced by gluino-squark loops [157]. These corrections are induced at the loop level even if they are not present at tree-level at the supersymmetry breaking scale [158].

In view of the above, we have not considered the flavor constraints in this work. We have checked, however, that for the solutions we are presenting the flavor bounds coded in NMSSMTools have a strong dependence on the gluino mass and that small changes to μ on the order of 10 GeV along with changes of a few hundred GeV of the gluino mass, from the 2 TeV value we are considering, move models from being excluded to being in good agreement with flavor constraints. These adjustments leave the behaviors of interest in the Higgs sector unchanged. In addition, as discussed above, the low values of the charged Higgs mass depend strongly on the assumption of having just a potential tadpole for the singlet. One may push upward the value of the charged Higgs mass with the inclusion of ξ_F in the superpotential, which decreases the mass splitting between the charged and CP-odd Higgs. In this case, the dependence on the gluino mass remains and flavor constraints can be satisfied with few hundred GeV adjustments of M_3.

5.1.6 Heavy charged Higgs

Additional decay channels : $A_1 \to hZ$

As shown above, models of wrong sign Yukawa couplings have interesting phenomenological properties that go beyond the SM-like Higgs properties, and include novel decays of the heavy CP-even and CP-odd Higgs bosons that may be tested in the near future. ATLAS has recently published results which show an excess of events consistent with the production of a pseudoscalar resonance of mass about 400 GeV, produced alongside $b\bar{b}$ and decaying into hZ [159]; the CMS analysis of this channel is still ongoing and has yet to be released. Although one may model this signal with a light singlet [160],[161], producing such a pseudoscalar at a high enough rate through $pp \to b\bar{b}A$ production within an effective two Higgs doublet model requires large values of $c_{\beta-\alpha}$ and sizable values of the bottom-Yukawa coupling, which are consistent with the properties of the wrong-sign bottom Yukawa coupling models under study, and is therefore of interest here [100]. However, one cannot gain an $A_1 \to hZ$

branching ratio of the necessary magnitude using the minimal models examined above due to the enhanced $A_1 \to H^\pm W^\mp$ decay.

In order to model the hZ decay within these models, we include a non-zero value of the superpotential tadpole term ξ_F. Because ξ_F is a dimension 2 parameter, it is therefore naturally of the order of -10^5 GeV^2 to -10^7 GeV^2. As noted previously from Eqs. (5.38) and (5.40), the inclusion of this term reduces the mass difference between the neutral and charged Higgs bosons and therefore suppresses the decay of the CP-odd Higgs boson into the charged Higgs, increasing the possible decays into h and Z.

Introducing a non-zero ξ_F also allows for larger values of m_H and lower values of λ while still satisfying $\kappa_b \approx -1$. As we showed explicitly in Eq. (5.39), the additional term arising from $\delta\lambda_7$ provides a positive contribution to the value of $t_\beta c_{\beta-\alpha}$.

This analysis relies on our approximations of corrections to the $\lambda_{4,5,7}$ couplings; the expressions for $\delta\lambda_4$ and $\delta\lambda_5$ are verified against the mass splitting $m_{H^\pm}^2 - m_A^2$ computed by NMSSMTools for large ξ_F in Fig. 5.9. We find very good agreement between the actual splitting from our data and the values calculated using the approximations given in Eq. (5.37).

No.	t_β	μ	λ	κ	ξ_S	A_λ	ξ_F	κ_b	m_h	m_H	$m_{H^\pm}$	m_S	m_{A_1}	Rate
1	9.6	-587	1.39	0.326	3.0×10^9	-2779	-1.2×10^6	-1.11	124.6	359	384	2670	396	0.19
2	9.2	-579	1.33	0.500	2.6×10^9	-3157	-1.5×10^6	-1.22	125.1	334	411	2470	414	0.19
3	10.5	-576	1.54	0.328	2.9×10^9	-2140	-0.8×10^6	-1.15	123.0	398	378	2747	421	0.18
4	8.0	-784	1.45	0.405	5.9×10^9	-3321	-1.9×10^6	-1.18	123.3	351	372	3325	397	0.21
5	10.8	-586	1.28	0.464	3.0×10^9	-3345	-1.6×10^6	-1.21	122.3	355	426	2583	424	0.18

Table 5.2: Benchmark scenarios for $b\bar{b}$-associated production of A_1 decaying into hZ. The column "Rate" represents the quantity $\sigma(pp \to b\bar{b}A_1 \to hZ) \times BR(h \to b\bar{b})$. All masses are given in GeV.

We calculate the $\sigma(pp \to b\bar{b}A_1)$ production cross section by scaling the SM cross section by the square of the scaling of the A_1 and b coupling relative to the SM value, which is

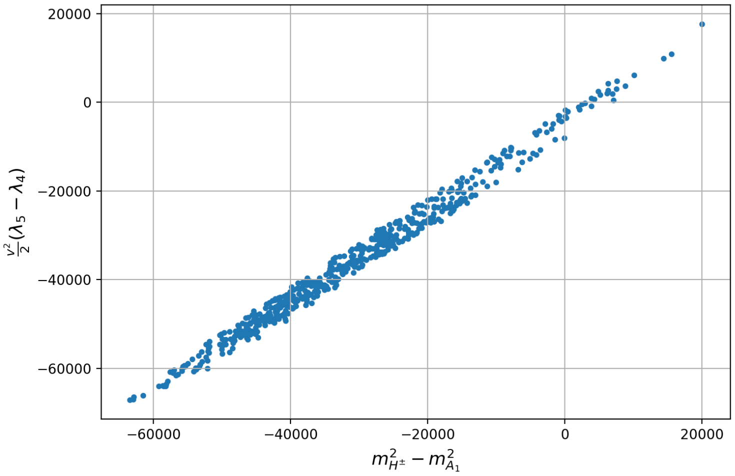

Figure 5.9: Plot showing the $H^{\pm}$ and A_1 mass split calculated using our derived expression for $\frac{v^2}{2}(\lambda_5 - \lambda_4)$ against the actual mass split for models with sizeable ξ_F. There is good agreement between the two values.

provided by NMSSMTools. The SM cross section scales downward with the Higgs mass, and we fit this dependence by using the SM values provided by the Higgs working group [61]. The calculated value for $\sigma(pp \to b\bar{b}A_1)$ ranges from 300 to 1600 fb for our particular models, with most falling within the range of 400-800 fb. With these cross section values, we find $\sigma(pp \to b\bar{b}A_1) \times BR(A_1 \to hZ) \times BR(h \to b\bar{b})$ between 0.05 pb and 0.30 pb. A plot of the predicted rate against the mass of the pseudoscalar is shown in Fig. 5.10. We find that these models can approximately produce the observed excess at around 400 GeV, which is currently measured as $\sigma(pp \to b\bar{b}A) \times BR(A \to hZ) \times BR(h \to b\bar{b}) \approx 0.2$ pb [159]. Relevant parameter values which have been changed from the models discussed in the previous section are given by $A_\lambda \in [-3500, -2000]$ GeV, $\xi_S \in [2.5 \times 10^9, 1.6 \times 10^{10}]$ GeV^3, $\mu \in [-900, -500]$ GeV, $t_\beta \in [8, 11]$, $\lambda \in [1.0, 1.6]$, $\kappa \in [0.2, 1.0]$, and $M_A \in [400, 410]$ GeV. Table 5.2 shows typical parameter values which give a rate for the pseudoscalar production near 0.2 with m_{A_1} near 400 GeV.

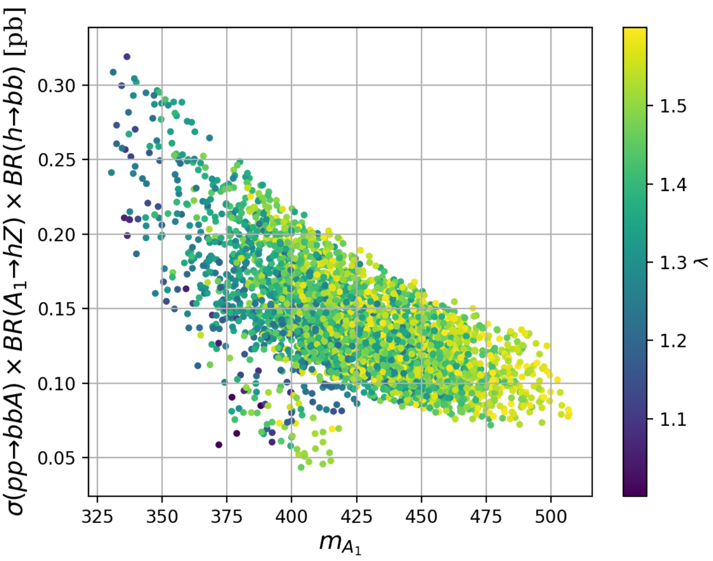

Figure 5.10: Predicted value of $\sigma(pp \to b\bar{b}A_1 \to hZ) \times BR(h \to b\bar{b})$ plotted against the mass of the pseudoscalar. The value of lambda for each model is given by the colorbar. We note that one may have a production rate near 0.2 pb for $m_{A_1} \approx 400$ GeV.

With an enhanced $A_1 \to hZ$ decay, one also expects a corresponding enhancement to the related decay $H \to hh$. CMS has updated limits on the production of a spin-0 particle produced via gluon fusion and subsequently decaying into $hh \to bb\bar{b}\bar{b}$ [162], and one should check that this enhanced $H \to hh$ process does not exceed these limits. Indeed, the branching ratio $BR(H \to hh)$ ranges mainly between about 0.5 to 0.8 in these models. However, the production rate of H via gluon fusion is suppressed due to relative signs of the H coupling with the top quark and the bottom quark. Within our models, $s_\alpha \simeq c_\beta$ and $c_\alpha \simeq s_\beta \simeq 1$, which differs from the case with $c_{\beta-\alpha} = 0$, where instead $s_\alpha \simeq -c_\beta$. In our case, then, the coupling of the heavy Higgs to the top-quark relative to the SM value is given by $\frac{s_\alpha}{s_\beta} = \frac{1}{t_\beta}$ as opposed to $\frac{-1}{t_\beta}$ in the alignment limit. Because the gluon fusion production cross section depends on top and bottom loop contributions, such a change of sign impacts the production rate of H through gluon fusion. In our models, the calculated production rate $\sigma(pp \to H \to hh \to bb\bar{b}\bar{b})$ falls below the limits given by CMS. Fig. 5.11 shows the production rate for this process against m_H for each model. Similar conclusions apply to the $H \to ZZ$ channel.

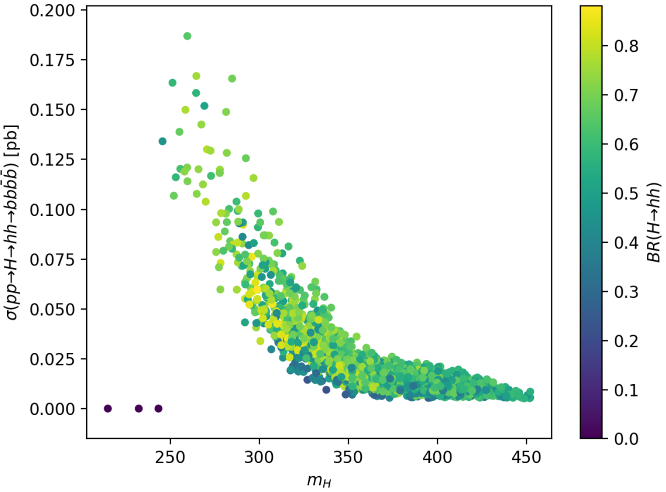

Figure 5.11: Predicted rate of H production through gluon fusion, decaying into hh and subsequently into $bb\bar{b}\bar{b}$, against the mass of the heavy CP-even Higgs. The colorbar shows the branching ratio of $H \to hh$, which is enhanced in these models. The production rates fall below the current experimental upper limits from CMS.

Precision electroweak measurements

In the regime of large $c_{\beta-\alpha}$, precision electroweak measurements become a relevant constraint on the parameter space. We therefore calculate the values of the parameters T and S within our models to compare with experimental bounds. Since the singlets are heavy, we can compute the precision measurement observables within the low energy 2HDM effective theory. The expression for ΔT is given by [163–165]

$$\begin{aligned}\Delta T =& \frac{1}{16\pi s_W^2 m_W^2}\Big(c_{\beta-\alpha}^2[f(m_A, m_{H^\pm}) + f(m_{H^\pm}, m_h) - f(m_A, m_h)] \\ &+ s_{\beta-\alpha}^2[f(m_A, m_{H^\pm}) + f(m_{H^\pm}, m_H) - f(m_A, m_H)]\Big) \\ &+ c_{\beta-\alpha}^2 \Delta T_{SM}(m_H) + s_{\beta-\alpha}^2 \Delta T_{SM}(m_h) - \Delta T_{SM}(m_h)\end{aligned} \tag{5.44}$$

where $s_W = \sin(\theta_W)$ and

$$f(x,y) = \frac{x^2+y^2}{2} - \frac{x^2y^2}{x^2-y^2}\log\frac{x^2}{y^2} \tag{5.45}$$

$$\Delta T_{SM}(m) = \frac{3}{16\pi s_W^2 m_W^2}[f(m,m_Z) - f(m,m_W)] - \frac{1}{8\pi c_W^2} \tag{5.46}$$

while ΔS is given by [163–165]

$$\begin{aligned}\Delta S =& \frac{1}{12\pi}\Big(c_{\beta-\alpha}^2\Big[\log\frac{m_H^2}{m_{H^{SM}}^2} + \log\frac{m_h m_A}{m_{H^\pm}^2} + 2\frac{m_h^2 m_A^2}{(m_h^2-m_A^2)^2} \\ &+ \frac{(m_h^2+m_A^2)(m_h^4+m_A^4-4m_h^2m_A^2)}{(m_h^2-m_A^2)^3}\log\frac{m_h}{m_A}\Big] \\ &+ s_{\beta-\alpha}^2[(m_h \leftrightarrow m_H)] - \frac{5}{6}\Big)\end{aligned} \tag{5.47}$$

Note that due to the custodial symmetry properties, for low splitting between m_A and $m_{H^\pm}$, the terms $f(m_{H^\pm}, m_{h,H})$ and $f(m_A, m_{h,H})$ in ΔT will approximately cancel; for larger splitting between the masses, i.e. lower $m_{H^\pm}$, these terms have a larger contribution. The effects of these variations can be seen in Fig. 5.12. On the left-hand side is a plot of ΔT versus ΔS for $\xi_F = 0$; on the right-hand side is the same plot for models with $\xi_F \neq 0$. In the $\xi_F \neq 0$ case, the splitting between $m_{H^\pm}$ and m_A is reduced, as discussed in Section 5.1.3. In this case, we see low values of ΔT. The left-hand plot also shows the dependence of ΔT on m_H in the $\xi_F = 0$ case, with larger values of m_H leading to increased values of ΔT.

In both cases, the value of ΔS is within the experimental limits. However, for the models presented in Section 5.1.4, the value of ΔT exceeds the experimental limits for a number of points. In particular, for the range of $\Delta S \approx 0.035$, the upper limit on ΔT at 99% CL is approximately 0.3 [166]. For $\xi_F = 0$, one may avoid these constraints by constraining the parameter space to lower m_H, i.e. $m_H \lesssim 320$ GeV; an examination of Fig. 5.4 shows that this corresponds to $\lambda \lesssim 1.5$. One may also clearly satisfy these constraints by including a

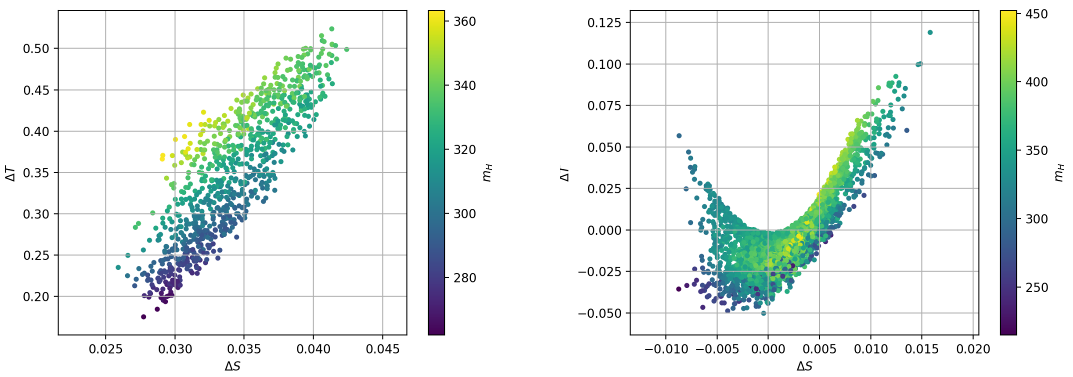

Figure 5.12: Plots of the precision electroweak parameters ΔT and ΔS for the models discussed in Section 5.1.4 (left), with $\xi_F = 0$, and models with $\xi_F \neq 0$ (right). One sees much smaller magnitudes of ΔT for models with non-zero ξ_F. For large negative values of ξ_F, as in the models displayed on the right, the value of ΔT is well within experimental limits.

non-zero value of ξ_F. In light of these results, we conclude that while precision electroweak measurements do provide relevant constraints on the allowed parameter space for the models in Section 5.1.4, there are a number of existing points which agree with these constraints, and there is additionally a larger class of models which are in good agreement with measurements.

5.1.7 Dark Matter Density and Direct Interaction Cross Section

The question of Dark Matter in the NMSSM has been investigated by several authors [167–173]. In our analysis we have kept the gaugino masses and the Higgsino mass parameter μ at the TeV scale, implying that, provided $|\kappa| < \lambda/2$, the lightest neutralino is mostly a singlino with mass

$$m_{\tilde{S}} \simeq 2\left|\frac{\kappa\mu}{\lambda}\right|. \tag{5.48}$$

As seen in Fig. 5.3, this condition is fulfilled in most of the parameter space we explored in this article. Such a singlino tends to mix with the Higgsino in a relevant way and, due to the large size of the couplngs λ and κ governing its interactions with the Higgs sector, the relic density tend to be too small to be consistent with the experimentally observed one.

Since the relic density could have a different origin from the one associated with the lightest neutralino, a small neutralino component does not lead to any phenomenological problem. However, it is easy to obtain the observed relic density by modifying the mass parameters and without affecting the Higgs phenomenology. This may be achieved, for instance, by lowering the value of the hypercharge gaugino mass M_1. For low enough values of M_1 the lightest neutralino would be Bino-like and the observed relic density could be reproduced under two circumstances

- Values of M_1 close to a half of the lightest non-standard Higgs masses, $m_H/2$ or $m_{A_1}/2$ [174],[175], for which resonant annihilation could take place,
- Values of M_1 close to but lower than $m_{\tilde{S}}$, the so-called well-tempered singlino-bino region [176].

If either of those conditions were fulfilled, not only could the relic density be brought to agreement with the experimentally observed value, but also the spin-independent and spin-dependent interaction cross section with nuclei will be small enough to be in agreement with the current experimental constraints. In our scans, we have modified the values of M_1 and verified that this is indeed the case. In particular, for the values of the parameters present in the benchmark model 4 in Table 5.1, Fig. 5.13 shows the value of Ωh^2 for these two regions of M_1. For this point, the singlino mass is approximately 600 GeV, while the mass of the heavy CP-even Higgs is about 280 GeV. The widening of the shape of the plots is due to scanning μ within a range of 10 GeV, which alters the value of m_H by a few GeV. It is clear that as the value of M_1 falls below $m_{\tilde{S}}$ and therefore the lightest neutralino becomes primarily bino-like, the relic density increases. On the other hand, for M_1 near $m_H/2$, we see the two regions with $\Omega h^2 \approx 0.1$ on either side of $m_H/2 \simeq 140$ GeV, where the relic density is suppressed by the resonant annihilation.

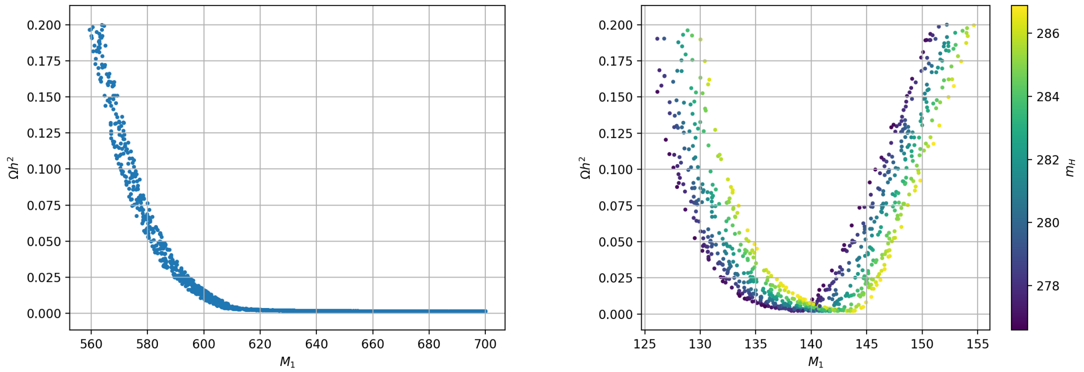

Figure 5.13: Plots showing the dependence of Ωh^2 on the value of M_1 for a single model which gives $\kappa_b = -1$. The left-hand plot shows the region where $M_1 \approx m_{\tilde{S}}$, which for this model is about 600 GeV; we see the expected increase in Ωh^2 when $M_1 \lesssim m_{\tilde{S}}$ due to the lightest neutralino becoming primarily bino-like. The right-hand plot shows the region for which $M_1 \approx m_H/2$, where we see the expected two solutions and strong suppression when M_1 is about 140 GeV. The widening of the shape of the plots is due to scanning μ within a range of 10 GeV, which alters the value of m_H by a few GeV.

5.1.8 Discussion

The current uncertainties in the determination of the Higgs coupling to bottom quarks leave room for a change of magnitude and sign of this coupling. In this article we have studied the possible implementation of this idea within the MSSM and the NMSSM. We have shown that in the MSSM this could only be achieved for values of m_A and t_β that are ruled out by current searches for heavy Higgs bosons decaying into tau pairs. On the other hand, in the NMSSM, consistent solutions that avoid current experimental limits may be found, but for values of the couplings λ and κ that lead to a Landau pole at scales below the Planck scale. This perturbativity problem may be solved by either assuming a composite Higgs model or by the introduction of an extended gauge sector that slows down the evolution of λ at high energies.

The change of sign of the bottom coupling leads to a modification of the loop-induced couplings of the SM-like Higgs to photons and gluons that may be tested at higher luminosities at the LHC. In particular, it leads to an enhancement of the order of 20 to 25 percent of the Higgs production in the gluon fusion mode and a reduction of order of 5 to 10 percent of the width of the decay of Higgs into two photons. The modification of the gluon fusion production cross section leads already to an enhancement of the Higgs-induced diboson production cross section, which will allow one to put constraints on the allowed parameter space of the theory.

The modification of the sign of the bottom coupling also leads to a large enhancement of the radiative decay of the SM-Higgs into photons and the Υ meson. While such an enhancement leads to a sizable number of radiative decay events at the high luminosity LHC, the efficiency of the current searches has to be improved in order to lead to an observable signal.

In this work, we have added tadpole terms to the singlet fields that allow us to raise the value of the scalar singlets and obtain a realistic scalar spectrum. When only a tadpole for the scalar term is included, the required low values of m_A and large values of λ tend to lead to a charged Higgs boson mass that is lower than the top quark mass, and hence such models are strongly constrained by searches for charged Higgs bosons proceeding from the decay of top quarks. Models that avoid these constraints have masses of the charged Higgs within 10 to 15 GeV of the top quark mass. In these models the second lightest CP-even and the lightest CP-odd scalars, which have mainly doublet components, tend to decay strongly into $H^{\pm}W^{\mp}$, which provides an interesting search channel.

On the other hand, when a tadpole term is also included in the superpotential, the splitting between the CP-odd and the charged Higgs boson masses may be reduced, suppressing the decay rate of the neutral scalars into charged boson states. In this case, the decay modes $A_1 \to hZ$ and $H \to hh$ are strongly enhanced. In particular, for values of m_{A_1} of order of 400 GeV, which are naturally obtained within these models, the production mode $pp \to b\bar{b}A_1 \to b\bar{b}hZ$ may be sizable and can lead to an explanation of an apparent excess of hZ events at the ATLAS experiment without being in conflict with the current bounds on

$H \to hh$ production.

Models with light charged Higgs masses are constrained by flavor and precision measurement constraints. While the flavor constraints may be avoided by suitable supersymmetric contributions, the precision measurement constraints set a limit on the possible splittings of the charged and neutral Higgs bosons. Finally, the observed Dark Matter relic density may be obtained by suitable choice of the gaugino mass parameter M_1, without affecting the Higgs phenomenology.

5.2 Dynamically obtaining the alignment limit

Now we move to an examination of the alignment limit in the NMSSM. Because the observed 125 GeV Higgs is so far SM-like to about 10% precision, any BSM theory involving an extended Higgs sector must include an SM-like Higgs in its phenomenology. Supersymmetric theories such as the NMSSM include a Type II 2HDM in the Higgs sector, and can obtain an SM-like Higgs within the so-called alignment limit, in which the lighter CP-even mass eigenstate is aligned with the SM-like Higgs basis state. This alignment limit corresponds to a specific parameter range, and it is reasonable to ask why the relevant parameters might fall within this particular region. In this work, we examine how one may dynamically obtain the alignment limit in the NMSSM with a fat Higgs theory at the GUT scale, which runs down to the alignment limit. This work was performed in collaboration with Carlos Wagner.

5.2.1 The alignment limit of the NMSSM

Within the NMSSM Higgs sector, which contains two doublets and a singlet, there are two methods through which one may obtain a SM-like Higgs of 125 GeV: decoupling and alignment. In the decoupling case, the heavier non-standard Higgs bosons are pushed to high masses, such that the mixing with the SM-like Higgs boson is suppressed. In the case of alignment, the parameters of the Higgs sector are such that the mixing terms of the squared-mass matrix between the SM-like Higgs boson and the neutral, non-SM-like one and singlet are small. More specifically, if we work in the Higgs basis [102–107] with the SM-like Higgs doublet denoted by the subscript 1, the symmetric CP-even Higgs mass-squared matrix is given generally by

$$\mathcal{M}^2 = \begin{pmatrix} \mathcal{M}^2_{11} & \mathcal{M}^2_{12} & \mathcal{M}^2_{13} \\ & \mathcal{M}^2_{22} & \mathcal{M}^2_{23} \\ & & \mathcal{M}^2_{33} \end{pmatrix} \tag{5.49}$$

and the alignment condition is

$$\mathcal{M}^2_{12}, \mathcal{M}^2_{13} \ll \mathcal{O}(v^2). \tag{5.50}$$

With minimal mixing, we also therefore have that

$$m_h^2 \approx \mathcal{M}^2_{11} = (125 \text{ GeV})^2. \tag{5.51}$$

The alignment limit of the NMSSM and its phenomenological properties have previously been thoroughly investigated in Ref. [135]. Here we give a brief review of the relevant properties.

We define the relevant couplings defining the interaction of the Higgs fields through the superpotential

$$W = \lambda S H_u H_d + \frac{\kappa}{3} S^3 + h_u Q H_u U_R^c + h_d H_d Q D_R^c, \tag{5.52}$$

where the Higgsino mass parameter is proportional to the vacuum expectation value of the singlet field $\mu = \lambda v_s$. We shall follow the conventions of Refs. [135],[40].

In the Higgs basis $\{H_{SM}, H_{NSM}, H_S\}$, where H^{SM} denotes the SM-like Higgs, H^{NSM} the non-standard Higgs doublet contribution and H^S the singlet contribution, the CP-even

Higgs tree-level squared-mass matrix can be explicitly written as

$$\begin{pmatrix} \bar{M}_Z^2 c_{2\beta}^2 + \frac{1}{2}\lambda^2 v^2 & -\bar{M}_Z^2 s_{2\beta} c_{2\beta} & \sqrt{2}\lambda v\mu(1 - \frac{M_A^2}{4\mu^2} s_{2\beta}^2 - \frac{\kappa}{2\lambda} s_{2\beta}) \\ & M_A^2 + \bar{M}_Z^2 s_{2\beta}^2 & -\frac{1}{\sqrt{2}}\lambda v\mu c_{2\beta}(\frac{M_A^2}{2\mu^2} s_{2\beta} + \frac{\kappa}{\lambda}) \\ & & \frac{1}{4}\lambda^2 v^2 s_{2\beta}(\frac{M_A^2}{2\mu^2} s_{2\beta} - \frac{\kappa}{\lambda}) + \frac{\kappa\mu}{\lambda}(A_\kappa + \frac{4\kappa\mu}{\lambda}) \end{pmatrix} \tag{5.53}$$

where $s_{2\beta} = \sin 2\beta$, etc. and we have defined

$$\bar{M}_Z^2 \equiv m_Z^2 - \frac{1}{2}\lambda^2 v^2. \tag{5.54}$$

Including up to the first order stop loop corrections [117, 126, 128, 129], the entries involving the doublets are given by

$$\mathcal{M}_{11}^2 = \bar{M}_Z^2 c_{2\beta}^2 + \frac{1}{2}\lambda^2 v^2 + \frac{3v^2 s_\beta^4 h_t^4}{8\pi^2}\left[\ln\left(\frac{M_S^2}{m_t^2}\right) + \frac{X_t}{M_S^2}\left(1 - \frac{X_t^2}{12M_S^2}\right)\right] \tag{5.55}$$

$$\mathcal{M}_{22}^2 = M_A^2 + s_{2\beta}^2\left(\bar{M}_Z^2 + \frac{3v^2 h_t^4}{32\pi^2}\left[\ln\left(\frac{M_S^2}{m_t^2}\right) + \frac{X_t Y_t}{M_S^2}\left(1 - \frac{X_t Y_t}{12M_S^2}\right)\right]\right) \tag{5.56}$$

$$\mathcal{M}_{12}^2 = -s_{2\beta}\left(\bar{M}_Z^2 c_{2\beta} - \frac{3v^2 s_\beta^2 h_t^2}{16\pi^2}\left[\ln\left(\frac{M_S^2}{m_t^2}\right) + \frac{X_t(X_t + Y_t)}{2M_S^2} - \frac{X_t^3 Y_t}{12M_S^4}\right]\right) \tag{5.57}$$

where $X_t = A_t - \mu\cot\beta$, $Y_t = A_t + \mu\tan\beta$, A_t is the stop mixing mass parameter and M_S is the geometric mean of the two stop mass eigenstates.

One may rewrite the expression for $\mathcal{M}_{12}^2$ in terms of $\mathcal{M}_{11}^2$ by relating the first-order stop loop correction terms, in which case the conditions for exact alignment up to first-order stop loop corrections become

$$\mathcal{M}_{12}^2 = \frac{1}{\tan\beta}\left[\mathcal{M}_{11}^2 - c_{2\beta} m_Z^2 - \lambda^2 v^2 s_\beta^2\right] + \frac{3v^2 s_\beta^2 h_t^4 \mu X_t}{16\pi^2 M_S^2}\left(1 - \frac{X_t^2}{6M_S^2}\right) = 0, \tag{5.58}$$

$$\mathcal{M}_{13}^2 = \sqrt{2}\lambda v\mu\left(1 - \frac{M_A^2 s_{2\beta}^2}{4\mu^2} - \frac{\kappa s_{2\beta}}{2\lambda}\right) = 0 \tag{5.59}$$

Values of the μ parameter close to the weak scale and therefore much lower than the stop masses are preferred in order to obtain a mostly Bino or singlino Dark Matter (DM) candidate and to reduce the fine tuning associated with electroweak symmetry breaking [176, 177]. As shown in Eq. (5.58), the stop loop corrections to $\mathcal{M}_{12}^2$ not included in $\mathcal{M}_{11}^2$ are suppressed by $\mu/M_S \ll 1$, and one may therefore neglect the stop corrections to find an approximate relation between the values of λ and $\tan\beta$ which satisfy exact alignment. Taking $\mathcal{M}_{11}^2 = m_h^2$, Eq. (5.58) gives [135]

$$(\lambda^A)^2 = \frac{m_h^2 - m_Z^2 c_{2\beta}}{v^2 s_\beta^2}. \tag{5.60}$$

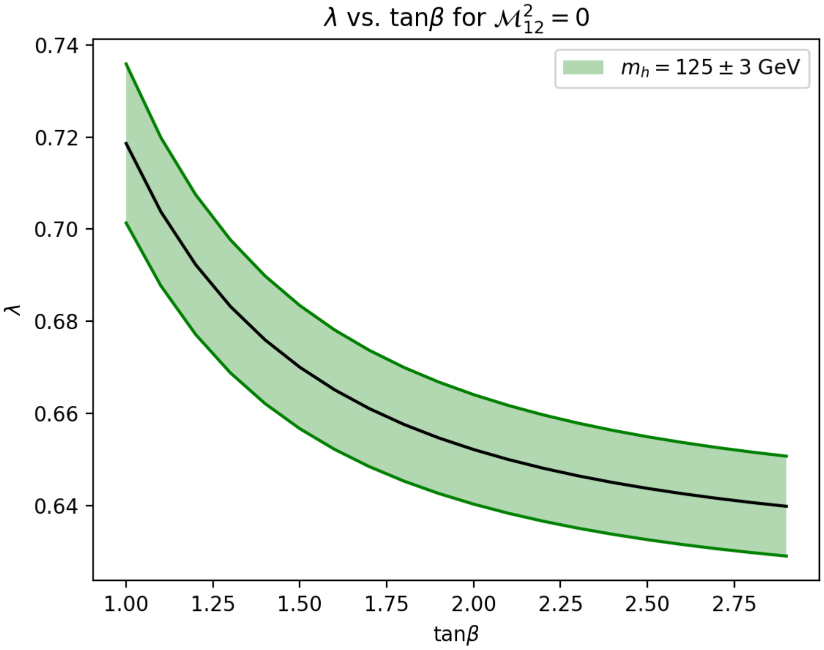

Figure 5.14: λ vs. $\tan\beta$ curves which gives $\mathcal{M}_{12}^2 = 0$. The solid black line shows exact alignment for $m_h = 125$ GeV. The shaded region covers $m_h = 125 \pm 3$ GeV, with the upper edge corresponding to $m_h = 128$ GeV and the lower edge to $m_h = 122$ GeV.

Fig. 5.14 shows the λ vs. $\tan\beta$ curves given by Eq. (5.60) for $m_h = (125 \pm 3)$ GeV, where we have included an uncertainty of 3 GeV characterizing the theoretical uncertainties in the determination of the Higgs mass. Points within this region will be close to fulfilling exact alignment, while points close to this region should have small mixing between the two doublets. We will better define “small" mixing quantitatively in our later analyses. In order to analyze a possible dynamical origin of these parameters, we are interested in identifying the high energy-scale values of NMSSM parameters which naturally run down to this alignment limit at low energies.

Although the above conditions of alignment have been derived by performing an analysis by including only one loop corrections, models that lead to an appropriate phenomenology at low energies tend to be consistent with those conditions, as shown by the similarity of the phenomenological properties of the benchmark scenarios derived in Ref. [135] compared with more complete numerical analysis as those performed in Refs. [178]–[179].

5.2.2 Running of NMSSM couplings to alignment

Results of running GUT-scale parameters to weak scale

As is well known, in minimal low energy supersymmetric models the values of the gauge couplings tend to evolve at a common value at a large energy scale denoted as the Grand Unification scale, M_{GUT}, of about 2×10^{16} GeV [180–182]. The values of λ and $\tan\beta$ shown in the previous section naturally lead to large values of $\lambda(M_{GUT})$ and $h_t(M_{GUT})$ under the NMSSM Renormalization Group equations (RGE) [40]. This running seems to suggest a composite nature for the Higgs bosons, for which the relevant couplings, in this case λ and h_t, become large near the compositeness scale. In particular, if the compositeness scale is of the order of M_{GUT}, it appears that one naturally obtains the NMSSM alignment condition $\mathcal{M}_{12}^2 = 0$ at the weak scale. Fig. 5.15 shows the general behavior of the running of λ and h_t up to the GUT scale. In this plot, we have chosen three different points within the exact alignment region, with a low value of the non-standard Higgs bosons masses, $M_A = 300$ GeV and a characteristic stop mass scale $M_{SUSY} = 1$ TeV. Since ignoring decoupling effects $h_t(m_t) \sim m_t(m_t)/(v s_\beta)$, where m_t is the running top quark mass, the value of h_t becomes weaker at larger values of $\tan\beta$. On the other hand, taking into account decoupling effects, increases in the heavy Higgs boson scale tend to lead to somewhat lower values of h_t at the GUT-scale.

In order to thoroughly examine the range of GUT-scale parameter values for which one obtains Higgs alignment, and to identify the stability of this running to the alignment limit, we begin with a range of values for $\lambda(M_{GUT})$ and $h_t(M_{GUT})$ and run each pair downward in energy. There are three primary regions between M_Z and M_{GUT}: the low-energy effective SM theory below M_A, the 2HDM region between approximately M_A and M_{SUSY}, and the NMSSM region above M_{SUSY}. We employ the relevant RGE equations within each region; the equations for each region are listed in Sections 3.1.5 and 3.2.2. At the boundary between the SM and 2HDM running at M_A, we relate the single effective Higgs field in the SM to the two Higgs doublets by $\phi = H_d \cos\beta + i\tau H_u^* \sin\beta$. This relation gives $h_t^{\rm eff} = h_t \sin\beta$. We approximately identify the scale of the singlet with M_{SUSY}, and therefore run the parameter λ between M_{GUT} and M_{SUSY}, stopping its running below this scale. The value of $\tan\beta$ is determined by requiring that the running top mass is equal to approximately $m_t(M_t) \simeq 163$ GeV, leading to a pole top quark mass of approximately the observed value, $M_t \simeq 173$ GeV.

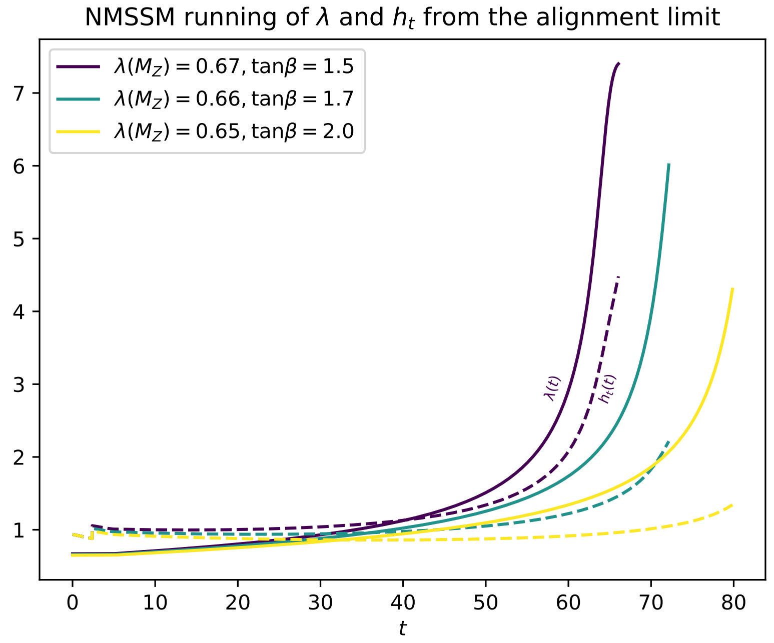

Figure 5.15: Running of λ (solid lines) and h_t (dashed lines) from the weak scale to higher energies, with $t = \ln\left(\frac{Q^2}{M_Z^2}\right)$. We display the running for initial values of $(\lambda(M_Z), \tan\beta) = (0.67, 1.5), (0.66, 1.7)$, and $(0.65, 2.0)$, which lie within the alignment region shown in the previous section.

Fig. 5.16 shows the results of running down from M_{GUT} to M_Z, with initial values of λ between 1 and 5 and values of h_t between 0.75 and 3.0 at the GUT scale. The value of κ is set to 0. We find that the results are stable under TeV-scale variations in the value of the running boundary M_{SUSY}, and thus ignore the small thresholds arising from the decoupling of the supersymmetric particles. We display the results for $M_{SUSY} = 1$ TeV. The value of M_A is chosen to be 300 GeV. Significantly larger values of M_A, on the order of M_{SUSY}, push the $h_t(M_{GUT}) \leq 1$ curves toward large values of $\tan\beta$. For values of $M_A \lesssim 500$ GeV, the results have little variation.

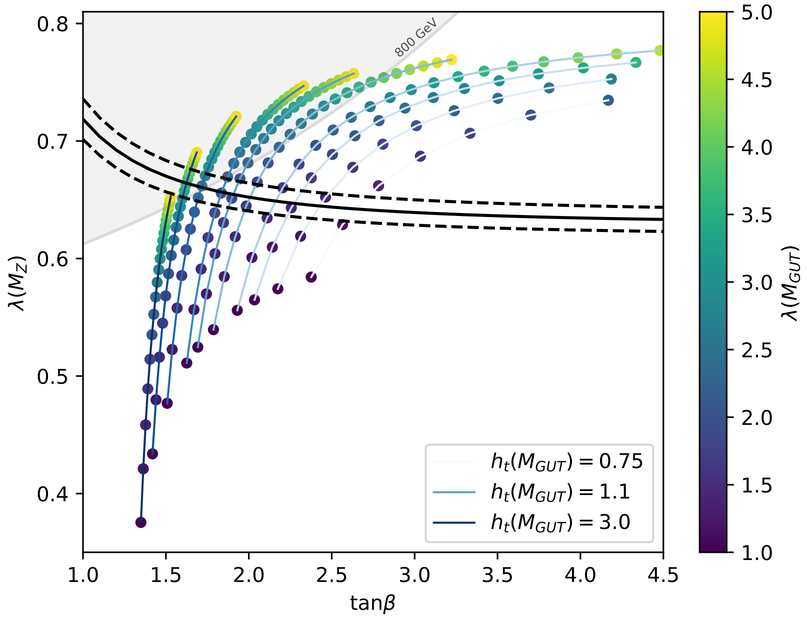

Figure 5.16: Plot showing the $(\tan\beta,\, \lambda(M_Z))$ points obtained by running down from M_{GUT} with large $\lambda(M_{GUT})$ and moderate $h_t(M_{GUT})$. The different contours arise from varying $h_t(M_{GUT})$, while the colorbar indicates the value of $\lambda(M_{GUT})$. Results are displayed for $M_{SUSY} = 1$ TeV. The solid and dashed black lines indicate the region of exact alignment for $m_h = 125 \pm 3$ GeV. The shaded grey region indicates the region in which it is difficult to obtain a lighter Higgs mass of 125 GeV without tension with existing stop mass limits.

The obtention of $m_h = 125$ GeV comes into tension with existing stop mass constraints for small values of $\tan\beta$ and large values of $\lambda(M_Z)$, for which the tree level contribution to m_h becomes large. Tree-level contributions close to the observed Higgs mass result in the need for small stop loop corrections and hence small values of the stop masses (see Eq. 5.57). Based on recent results from stop searches [183–186], we use a stop mass bound of $M_S > 800$ GeV. We employ a lower bound than some of the quoted values after noting that the bounds may be relaxed depending on the specific stop decay paths and neutralino and chargino masses within the model. The scenario presented in Fig. 12 of Ref. [183] most closely aligns with the neutralino/chargino spectrum we obtain in scenarios with a realistic Dark Matter candidate, which are further discussed in Section 5.2.3. Splittings between the right- and left-handed stops, multiple decay modes mediated by neutralinos and charginos, and decays through heavier Higgsinos may further relax the 800 GeV bound. In particular, we note that for lightest neutralino masses of order $m_{\tilde{\chi}_1^0} \gtrsim 200$ GeV the bounds may be relaxed significantly, and in fact no meaningful bounds are placed for $m_{\tilde{\chi}_1^0} \gtrsim 300$ GeV in that particular analysis.

Moreover, for small stop mixing, a bound on M_S is approximately equivalent from the point of view of the radiative corrections to the Higgs mass to a bound on the geometric average of the two stop masses. Hence, when comparing with experimental results one should recall that a bound $M_S > 800$ GeV is approximately equivalent to a bound on the right handed stop mass $m_{\tilde{t}_R} > 600$ GeV and on the left handed stop mass (which is close in mass to the left handed sbottom) $m_{\tilde{t}_L} > 1.1$ TeV.

From the results in Fig. 5.16, we see that lower values of h_t at the GUT scale tend to push $\tan\beta$ and $\lambda(M_Z)$ to larger values, while lower values of $\lambda(M_{GUT})$ lead to lower values of $\lambda(M_Z)$, as might be expected. Our points fall mostly within a range of $\lambda(M_Z) \in (0.5, 0.8)$ with moderate $\tan\beta$.

Alignment in the doublet sector

The points obtained from running down from large values of $\lambda(M_{GUT})$, as required for a composite Higgs theory with a compositeness scale close to $M_{\rm GUT}$, fall close to the region required for exact alignment. To start with, we reduce the problem to an effective two Higgs doublet model by assuming heavy singlets and examine the mixing in the doublet sector; the suppression of the singlet mixing will be examined in the next section. To quantify how well the points fall within the alignment limit, we vary along M_S and X_t curves to examine the quantity

$$\cos(\beta - \alpha) = \frac{-\mathcal{M}_{12}^2}{\sqrt{(m_H^2 - m_h^2)(m_H^2 - \mathcal{M}_{11}^2)}} \tag{5.61}$$

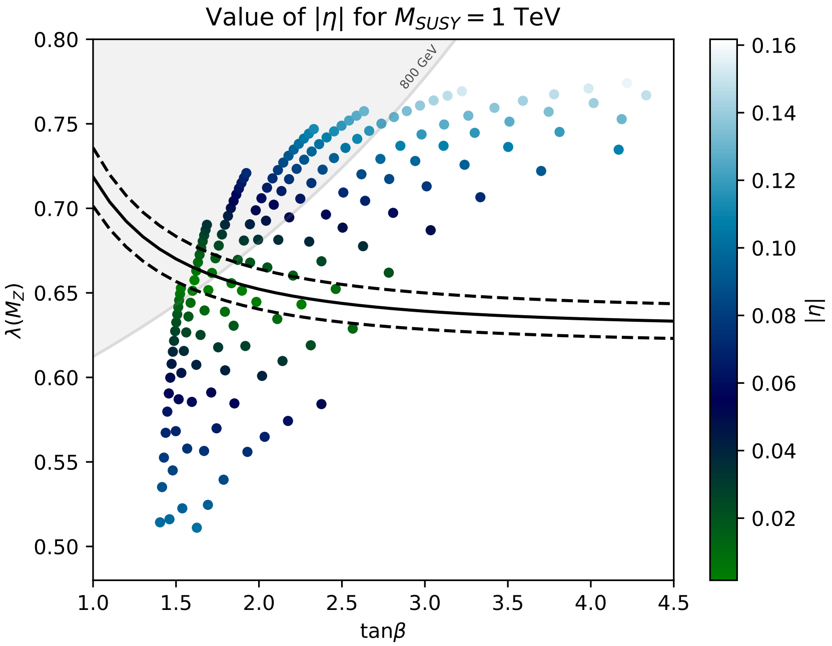

Figure 5.17: Values of the quantity $|\eta|$ for the points obtained from running down from M_{GUT}. We plot only the points which can obtain the correct Higgs mass at the 2-loop level. Points in the larger $\tan\beta$ region tend to have lower values of $\mathcal{M}^2_{12}/(\mathcal{M}^2_{22} - \mathcal{M}^2_{11})$, but due to the larger values of $\tan\beta$ they obtain larger values of $|\eta|$ than those points at low $\tan\beta$ and λ. The shaded grey region indicates the region in which it is difficult to obtain a lighter Higgs mass of 125 GeV without tension with existing stop mass limits.

which reflects the mixing between the two doublets and reduces to $-\mathcal{M}^2_{12}/(\mathcal{M}^2_{22} - \mathcal{M}^2_{11})$ with $m^2_H \approx \mathcal{M}^2_{22}$ and $m^2_h \approx \mathcal{M}^2_{11}$. The M_S vs. X_t curve for each $(\tan\beta, \lambda(M_Z))$ point is determined by requiring that $\mathcal{M}^2_{11} = (125 \text{ GeV})^2$ up to the dominant two-loop terms. For low values of $\tan\beta$, the stop loop corrections tend to be smaller than the tree level values, and there is therefore little variation about the average value along each curve. As required from the choices made in the running, we use $M_A = 300$ GeV in the calculation of M^2_{22}. Larger values of M_A increase $\mathcal{M}^2_{22}$ and therefore decrease the mixing.

In the effective 2HDM, the deviations of the SM-like coupling may be parametrized by [110, 187]

$$
\begin{aligned}
g_{hb\bar{b}} &= g^{\rm SM}_{hb\bar{b}}\,(1-\eta) && (5.62)\\
g_{ht\bar{t}} &= g^{\rm SM}_{ht\bar{t}}\left(1+\frac{\eta}{\tan^2\beta}\right) && (5.63)\\
g_{hVV} &= g^{\rm SM}_{hVV}\left(1-\frac{\eta^2}{2\tan^2\beta}\right) && (5.64)
\end{aligned}
$$

where

$$\eta \simeq -\tan\beta\,\frac{\mathcal{M}^2_{12}}{\mathcal{M}^2_{22}-\mathcal{M}^2_{11}}. \qquad (5.65)$$

From Eqs. (5.62)-(5.64) we see that for $\tan\beta > 1$, the tree-level bottom coupling is the one mostly affected by mixing with the non-standard states and, due to the relevant decay branching ratio of the SM-like Higgs to bottom quarks, it has a relevant effect on all Higgs branching ratios. We plot the quantity $|\eta|$, which parametrizes the variation of the bottom coupling, for our weak-scale points in Fig. 5.17.

Inspection of Fig. 5.17 shows that the deviation of the parameter $|\eta|$ is below 0.1 for the majority of points, restricting the deviations of all couplings to values below ten percent, in agreement with current experimental observations [53, 55] (in this work, we shall not consider the region in which the bottom Yukawa coupling acquires a wrong sign, $\eta \simeq 2$, which can also be achieved within the NMSSM for heavy singlets [188]). The points on the extreme ends of the $\tan\beta$ region reach larger values of $|\eta|$, but do not exceed a deviation of 0.16. Following the same analysis with a value of $M_A = 400$ GeV, we find a maximum value of $|\eta| = 0.08$, which follows the expected scaling of approximately $1/M_A^2$. We therefore find that a composite Higgs model with a compositeness scale near the GUT scale may naturally lead to the alignment limit for the doublet sector at low energies. In Section 5.2.3, we will describe a general implementation of an NMSSM Fat Higgs model with a scale Λ of the order of $M_{\rm GUT}$.

Alignment Condition

As discussed above, the alignment condition in the NMSSM does not arise from a symmetry condition. To further investigate the origin of the alignment in the doublet sector, one can write the effective two Higgs doublet potential

$$\begin{aligned} V = \quad & m_{11}^2\Phi_1^\dagger\Phi_1 + m_{22}^2\Phi_2^\dagger\Phi_2 - m_{12}^2(\Phi_1^\dagger\Phi_2 + \text{h.c.}) + \frac{1}{2}\lambda_1(\Phi_1^\dagger\Phi_1)^2 + \frac{1}{2}\lambda_2(\Phi_2^\dagger\Phi_2)^2 \\ & +\lambda_3(\Phi_1^\dagger\Phi_1)(\Phi_2^\dagger\Phi_2) + \lambda_4(\Phi_1^\dagger\Phi_2)(\Phi_2^\dagger\Phi_1) \\ & + \left\{\frac{1}{2}\lambda_5(\Phi_1^\dagger\Phi_2)^2 + [\lambda_6(\Phi_1^\dagger\Phi_1) + \lambda_7(\Phi_2^\dagger\Phi_2)]\Phi_1^\dagger\Phi_2 + \text{h.c.}\right\} \ . \end{aligned} \tag{5.66}$$

For small values of the Higgsino mass parameter compared to the stop mass scale $\mu/M_S \ll 1$—the dependence of the quartic couplings on the stop mass parameters is given, for instance, in Refs. [115, 116]—one may take $\lambda_6 \simeq \lambda_7 \sim 0$ as a good approximation. The condition of alignment can then be rewritten as [187]

$$\begin{aligned} m_h^2 &= \left(\lambda_1 \cos^4\beta + 2\tilde{\lambda}_3 \sin^2\beta\cos^2\beta + \lambda_2 \sin^4\beta\right) \\ m_h^2 &= \left(\lambda_1 \cos^2\beta + \tilde{\lambda}_3 \sin^2\beta\right) v^2, \end{aligned} \tag{5.67}$$

where $\tilde{\lambda}_3 = \lambda_3 + \lambda_4 + \lambda_5$.

In the literature, symmetry considerations have been invoked to relate the quartic couplings [189–193]. In particular, the condition $\lambda_1 = \lambda_2 = \tilde{\lambda}_3$ ensures alignment whenever $m_h^2 = \lambda_2 v^2$. In the NMSSM, however, the couplings λ_1 and λ_2 differ by the sizable stop loop corrections and these conditions cannot be fulfilled. For moderate or large values of $\tan\beta \gtrsim 2.5$, however, the alignment conditions reduce approximately to $\lambda_2 \simeq \tilde{\lambda}_3$, with $m_h^2 = \lambda_2 v^2$. Taking into account that

$$\tilde{\lambda}_3 \simeq -\frac{g_1^2 + g_2^2}{4} + \lambda^2, \tag{5.68}$$

one recovers the previously-obtained relation, Eq. (5.60), which in this regime of $\tan\beta$ reads

$$\lambda^2 \simeq \frac{M_Z^2 + m_h^2}{v^2}. \tag{5.69}$$

Moreover, as said above, $\lambda_2 v^2$ differs from its tree-level value $M_Z^2 \simeq \lambda_1 v^2$ due to the sizable stop radiative corrections.

The relation $\lambda_2 \simeq \tilde{\lambda}_3 \simeq m_h^2/v^2$ is therefore an emergent condition arising dynamically in the infrared limit, and it is not coming from any fundamental symmetry. Alignment for smaller values of $\tan\beta$ emerges in a similar way in the infrared limit.

Alignment in the singlet sector

We must additionally examine how the mixing with the singlet Higgs might be naturally limited or suppressed due to the high-energy behavior of the theory. A similar analysis to the one performed for the doublet sector gives the exact alignment condition involving M_{13}^2 as

$$\frac{M_A^2 s_{2\beta}^2}{4\mu^2} - \frac{\kappa s_{2\beta}}{2\lambda} = 1. \tag{5.70}$$

For the region of λ and $\tan\beta$ obtained by running down from the GUT scale, the value of $\sin(2\beta)$ is approximately 1. We may thusly reduce the singlet-sector alignment condition to the approximate relation

$$\frac{M_A^2}{4\mu^2} \approx 1, \tag{5.71}$$

where we have assumed that $\kappa/2\lambda$ is significantly lower than one, as necessary to obtain a singlino state lighter than the Higgsino one, $2\kappa/\lambda < 1$, for which a natural Dark Matter candidate may be obtained [176]. Alignment for the singlet therefore additionally depends on the relationship between the parameters M_A and μ, which is not determined by the running down from M_{GUT} performed above. We therefore conclude that this alignment condition cannot obviously be imposed through choices in the high-energy theory.

We thusly examine whether one may effectively decouple the singlet due to aspects of the high-energy theory. We note that the addition of a tadpole term can effectively decouple the singlet from the doublet sector by increasing the singlet mass. In particular, the general form for $\mathcal{M}_{33}^2$ is given by [40]

$$\mathcal{M}_{33}^2 = \frac{1}{4}\lambda^2 v^2 s_{2\beta}\left(\frac{M_A^2}{2\mu^2} - \frac{\kappa}{\lambda}\right) + \frac{\kappa\mu}{\lambda}\left(A_\kappa + \frac{4\kappa\mu}{\lambda}\right) - \frac{\lambda}{\mu}\xi_S \tag{5.72}$$

where ξ_S is the constant in a tadpole term in the Higgs potential of the form $\xi_S S \subset V_H$. A large value of ξ_S can lead to large $\mathcal{M}_{33}^2$, thereby decoupling the singlet and limiting the mixing with the doublet sector. If the high-energy theory produces a singlet tadpole term in the Higgs potential, as we will examine in the next section, then the singlet mixing may be efficiently suppressed.

5.2.3 Fat Higgs models

Here we focus on the possible composite nature of the Higgs, and present an example of an NMSSM Fat Higgs model [194–196] which may run down to alignment at the weak scale as examined in the previous section. The primary traits we require are large values of λ at the GUT scale and a singlet tadpole term which may decouple the singlet from mixing with the doublet sector. We therefore choose a compositeness scale of $\Lambda_H \approx M_{GUT} \approx 10^{16}$ GeV, and include a supersymmetric mass term for the two new superfields which form the singlet at low energies, thereby generating a tadpole term for S.

We specifically follow the construction set forth by Harnik et al. in Ref. [194], which presents an NMSSM Fat Higgs model. A new gauge symmetry $SU(2)_H$ is introduced, which becomes strong at a scale Λ_H, and six new superfields $T^{1,\dots 6}$ are introduced which are doublets under $SU(2)_H$. (T_1, T_2) also transform as a doublet under $SU(2)_L$, while (T_3, T_4) and (T_5, T_6) transform as singlets under $SU(2)_L$. The tree-level superpotential is given by

$$W = \ yS'T^1T^2 + yS''T^3T^4 - mT^5T^6 + ... \tag{5.73}$$

where S' and S'' are new singlet superfields included to ensure dynamic electroweak symmetry breaking. Making the identifications

$$S \propto T^5T^6, \qquad \begin{pmatrix} H_u^+ \\ H_u^0 \end{pmatrix} \propto \begin{pmatrix} T^1T^3 \\ T^2T^3 \end{pmatrix}, \qquad \begin{pmatrix} H_d^0 \\ H_d^- \end{pmatrix} \propto \begin{pmatrix} T^1T^4 \\ T^2T^4 \end{pmatrix} \tag{5.74}$$

one obtains a dynamically-generated superpotential of

$$W = \lambda S(H_uH_d - v_0^2). \tag{5.75}$$

Using Naive Dimensional Analysis [197–200], one expects that

$$v_0^2 \sim \frac{m\Lambda_H}{(4\pi)^2} \tag{5.76}$$

$$\lambda(\Lambda_H) \sim 4\pi. \tag{5.77}$$

Of particular interest in our case is the very small value of m required to obtain $v_0 \approx \mathcal{O}(100)$ GeV for a compositeness scale of $\Lambda_H \approx 10^{16}$ GeV; in particular, m must be on the order of 10^{-1} eV.

We note that a term of the form mT^5T^6 may arise from the vev of a scalar superfield, in which case one would have a term of the form $g\Phi T^5T^6$, where g is a dimensionless coupling. As a scalar superfield, Φ may have the form $\Phi = \varphi + \theta\theta F$, where φ and F have some vacuum expectation values. When integrating to obtain the potential, one therefore finds an additional term linear in the Higgs singlet S arising from the $F-$term. Thus, the presence of a tadpole term of the form $\xi_F \hat{S}$ in the superpotential may naturally give rise to a tadpole term in the potential of the form $\xi_S S$.

The necessary scales can be estimated based on the values of m we require due to the compositeness scale, as well as the scale of ξ_S required to decouple the singlet from the doublet sector. We write the Higgs singlet terms with the vev of $\langle \Phi \rangle = \langle \varphi \rangle + \theta\theta \langle F_\phi \rangle$ by

$$g\left(\langle \varphi \rangle + \theta\theta \langle F_\varphi \rangle\right) T^5 T^6 \tag{5.78}$$

where the first term generates the supersymmetric mass term mT^5T^6 while the second term generates the tadpole term in the potential. We estimate that $\langle \varphi \rangle$ and $\sqrt{|\langle F \rangle|}$ should both be on the order of a TeV. In order to obtain $m \sim \mathcal{O}(10^{-1})$ eV, we therefore require $g \sim \mathcal{O}(10^{-13})$. The scalar part of $\hat{S}$ then acquires a tadpole term in the potential with $\xi_S = \frac{\Lambda_H g \langle F \rangle}{4\pi}$; we require ξ_S on the order of 10^9 GeV^3 for decoupling, which indicates that Λ_H is around 10^{15} GeV. We thus obtain a similar compositeness scale to the one that matches the NMSSM running, as described in Section 5.2.2.

The problem now reduces to the generation of the small coupling g. Such a small coupling may be explained by using a seesaw mechanism, similar to the one associated with the Majorana neutrino mass models. In order to propose such a model, let's follow Ref. [194] and introduce two additional $SU(2)_H$ doublets T^7 and T^8. We shall assume the presence of certain flavor symmetries which forbid an explicit T^5T^6 mass term, but allow mixing between these states and the T^7 and T^8 term via the analogue of a Giudice Masiero mechanism [201] and a T^7T^8 mass term via the interaction with an additional superfield, Ψ. Under these assumptions, the superpotential reads

$$W = \Psi T^7 T^8 + m_{\text{SUSY}} T^5 T^8 + m_{\text{SUSY}} T^6 T^7 \tag{5.79}$$

where the m_{SUSY} term comes from the Giudice Masiero relation between the effective bilinear superfield term and the supersymmetry breaking scale. We shall assume that

$$\langle\Psi\rangle \simeq M + F\theta^2 \tag{5.80}$$

where F is proportional to the square of the supersymmetry breaking scale, such that the superpartner masses $m_{\mathrm{SUSY}} \simeq F/M_{\mathrm{GUT}}$, and M is of the order of the GUT scale. Integrating out the heavy superfields T^7 and T^8, one can identify the supersymmetry conserving and breaking terms that appear at low energies. This can be done diagrammatically. For instance, the supersymmetry breaking tadpole term may be obtained by considering the presence of the scalar mixing terms in the scalar potential,

$$V \simeq M^2(T_7T_7^* + T_8T_8^*) + m_{\mathrm{SUSY}}M(T_5T_7^* + T_6T_8^*) + FT_7T_8 + h.c., \tag{5.81}$$

where the first four terms arise from F terms in the superpotential, of the form $|\partial W/\partial T_7|^2$ and $|\partial W/\partial T_8|^2$, and we replace Ψ by its vacuum expectation value. After integrating out the heavy fields, the above terms lead to a supersymmetry breaking term

$$V \simeq m_{\mathrm{SUSY}}^2\frac{F}{M^2}T_5T_6 + h.c.. \tag{5.82}$$

This induces a tadpole of the right size for the scalar component of S.

Alternatively, one can also obtain the same result by doing a simple expansion considering the supersymmetry breaking terms like a perturbation of the values obtained in the supersymmetric limit. Let's start with the supersymmetric case, with superpotential

$$W = MT^7T^8 + m_{\mathrm{SUSY}}T^5T^8 + m_{\mathrm{SUSY}}T^6T^7. \tag{5.83}$$

Integrating out the heavy superfields, we get the effective superpotential

$$W = -\frac{m_{\rm SUSY}^2}{M} T_5 T_6. \tag{5.84}$$

This term, together with the supersymmetry breaking term, Eq.(5.82), leads to the supersymmetric and non-supersymmetric tadpole contributions of the singlet S. We can then formally identify the spectator field Φ introduced in Eq. (5.78) with

$$g \langle \Phi \rangle \simeq -\frac{m_{\rm SUSY}^2}{\langle \Psi \rangle}, \tag{5.85}$$

where the above expression acquires meaning after decoupling the heavy superfields T^7, T^8 and performing the above mentioned expansion [202], from which we obtain

$$\begin{aligned} g &\simeq -\frac{m_{\rm SUSY}}{M}, \\ \langle \Phi \rangle &= m_{\rm SUSY} - \frac{m_{\rm SUSY} F}{M} \theta^2 \sim m_{\rm SUSY} - m_{\rm SUSY}^2 \theta^2. \end{aligned} \tag{5.86}$$

Hence, we reproduce the diagrammatic result for the supersymmetry breaking tadpole and obtain the required values of the coupling and the effective superfield Φ vacuum expectation values in a natural way.

While the interactions of the singlet field S with the Higgs field have the required structure to obtain alignment, the self interactions of S are not determined in a clear way from our discussion above. We shall assume that the flavor symmetries forbid a superpotential mass term for S but allow the presence of a cubic term in S, induced by strong interactions at the scale M and characterized by the usual κ term at low energies.

Phenomenological Properties

The low energy limit of the model presented above is equivalent to the $\mathbb{Z}_3$ invariant NMSSM, with the addition of tadpole terms that lift the scalar components of the singlet fields to values larger than the weak scale, implying the suppression of the mixing of the singlet with the SM Higgs bosons. Moreover, the values of λ ensure approximate alignment in the doublet Higgs sector. The combination of alignment in the doublet Higgs sector with the decoupling of the singlet scalar fields imply that the observed Higgs boson has approximate Standard Model-like properties, in agreement with experiments.

This model does not predict the exact value of the non-standard Higgs boson masses, but the moderate values of $\tan\beta$ imply that the production cross section is governed by top-Yukawa induced processes. Due to the alignment condition, which suppresses the decay into pairs of weak gauge bosons or SM-like Higgs bosons [135], and the absence of light singlets, the non-standard Higgs bosons decay mostly into fermion states. Therefore, the decay branching ratio depends on whether the decay into pairs of top-quarks and electroweakinos is allowed. If top-quark decay is dominant, searches for the heavy Higgs doublets become difficult due to interference effects with the large top-quark production background [203]–[204]. Therefore, the only region that is currently constrained is for low values of $\tan\beta < 2$ and values of the heavy Higgs mass below about 350 GeV, where the top-quark decay process is absent. The main constraint comes from the decay of the heavy Higgs bosons into τ pairs [118, 119] which, however, can be efficiently suppressed if the electroweakinos are light [205].

Regarding the chargino and neutralino sectors, the model provides an acceptable Dark Matter candidate in terms of the lightest neutralino [40]. Assuming this particle to be either predominantly Bino or singlino, spin independent direct detection bounds may be efficiently suppressed provided [176]

$$m_\chi \sim \pm\mu \sin 2\beta, \tag{5.87}$$

where the plus sign corresponds to the singlino case, while the minus sign corresponds to the Bino case. However, the suppression of the direct detection cross section in the singlino case relies on the interference between the SM-like and singlet scalar Higgs contributions, which requires a light scalar singlet. In the case of singlet decoupling, it is difficult to obtain a small direct detection cross section. However, the Bino case remains viable under direct detection limits. Moreover, values of the singlino mass close to the Bino mass and somewhat lower than the Higgsino mass μ ensure the obtention of the proper relic density via co-annihilation of the Bino with the singlino. An acceptable relic density may therefore be obtained consistently with the condition of avoiding the direct detection bounds in this model. Using NMSSMTools [139] we have verified that one may indeed obtain approximate alignment with an acceptable Dark Matter candidate, for instance for $\tan\beta \simeq 2.5$ and $\lambda(M_Z) \simeq 0.69$ with values of $M_1 = 240$ GeV, $M_A \simeq 400$ GeV and $\mu = -300$ GeV, $\kappa \simeq 0.33$ and $M_S \simeq 800$ GeV (or equivalently $m_{\tilde{t}_R} \simeq 600$ GeV and $m_{\tilde{t}_L} \simeq 1.1$ TeV).

A further phenomenological consideration is the charged Higgs contribution to the $b \to s\gamma$ rate. Within a basic Type II 2HDM model, a light charged Higgs on the order of a few hundred GeV enhances $b \to s\gamma$ rates and therefore becomes constrained by experimental measurements [150, 151, 206, 207]. However, within supersymmetric theories these flavor rates also depend strongly on the contributions from other supersymmetric particles; these include charginos and stops, which can exactly cancel the SM contributions to the $b \to s\gamma$ transition in the limit of exact supersymmetry [152, 154–156]. Furthermore, there are contributions arising from possible flavor violation in the scalar fermion sector; these can be large corrections arising from gluino-squark loops. This can occur when there is a misalignment between the bases in which the quark and squark mass matrices are diagonalized [157]. In light of this, we do not further consider flavor constraints; however, we have confirmed using NMSSMTools that the models described above can be in agreement with flavor constraints up to the SUSY contributions included in NMSSMTools.

5.2.4 Unification of h_b and h_τ

Although it is not directly related to the alignment in the Higgs sector, another intriguing aspect of the running of the RG evolution from the alignment limit is the unification of h_b and h_τ at the GUT scale. Fig. 5.18 shows the values of $h_b(M_{GUT})$ and $h_\tau(M_{GUT})$ obtained by running the weak-scale points in Fig. 5.16 upward to the GUT scale. As expected from previous work [208]–[209], for such large values of $h_t(M_{GUT})$ the values approach the $h_b(M_{GUT}) = h_\tau(M_{GUT})$ line as h_t increases. The values of h_t approach an infrared fixed point [210], which is also a feature of top condensate models [211–213], which is a different realization of compositeness in the Higgs doublet sector.

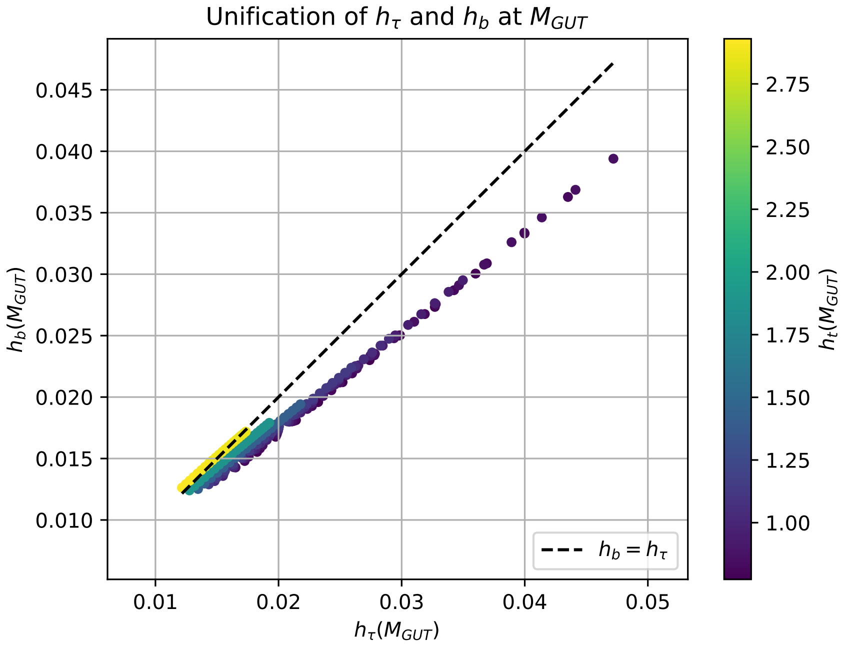

Figure 5.18: Plot of the values of $h_\tau(M_{GUT})$ and $h_b(M_{GUT})$ obtained from running the weak-scale points shown in Fig. 5.16 up to the GUT scale. The color bar indicates the value of $h_t(M_{GUT})$, for which larger values push the values of h_τ and h_b closer to unification at the GUT scale.

The unification of the bottom and tau Yukawa couplings suggests that the bottom-quark and τ-lepton share the same representations of the high-energy theory, as would happen in an effective $SU(5)$ theory at the GUT scale. However, GUT scenarios tend to encounter a number of phenomenological issues (see, for example, Refs. [214]–[215]), and an examination of how one may build a successful grand unification theory with the NMSSM as the low-energy theory, along with composite Higgs bosons, is beyond the scope of this paper.

5.2.5 Discussion

The condition of alignment in the Higgs sector allows for the possibility of obtaining a relatively light Higgs spectrum without being in conflict with the LHC Higgs precision measurements. Quite generally, alignment is not dictated by any symmetry consideration and, barring the possibility of being an accidental condition, requires a dynamical explanation. In this article we concentrated on the NMSSM, in which the alignment condition is associated with a narrow range of values of the superpotential coupling λ, which governs the interactions of the singlet to doublet Higgs states. For low values of $\tan\beta \lesssim 3$, this range of values of λ leads to the observed value of the Higgs mass without requiring a very large stop spectrum. Moreover, as shown in this article, the renormalization group evolution of the coupling λ shows that for low energy values which lead to alignment in the Higgs sector, λ tends to become strong at scales of the order of the GUT scale. Furthermore, the top Yukawa coupling also tends to large values at similar large energy scales.

In this work we interpreted the large values of λ at the GUT scale as a signal of compositeness of the Higgs states. Following this idea, we constructed a Fat Higgs Model with a compositeness scale that is close to the GUT scale, which leads to the desired Higgs spectrum and allows for the presence of a tadpole contribution that leads to the natural decoupling of the singlet scalar states in the low energy theory. This implies that the alignment in the doublet sector, governed by λ, ensures the SM-like properties of the lightest Higgs, as required by the LHC precision measurements.

In addition to obtaining a Higgs sector which is consistent with current experimental constraints, the model also includes a Dark Matter candidate, which is mostly Bino-like and obtains the correct relic density through coannihilation with light singlinos. Moreover, for values of the Dark Matter mass close to $-\mu \sin 2\beta$, direct detection constraints can be avoided in the Bino case. All these conditions may be simultaneously satisfied within these models.

Finally, we stress that the relatively strong values of the top Yukawa coupling lead to the unification of the bottom and tau Yukawa couplings at the GUT scale. This suggests the possible embedding of this theory within a GUT scenario, like $SU(5)$, in which the bottom-quark and tau-lepton share the same multiplets. However, an investigation of such a theory is reserved for future analyses.

CHAPTER 6

NEW PHYSICS IN NEUTRINO ACCELERATOR EXPERIMENTS

Now we turn to the subject of new physics searches within neutrino accelerator experiments. These experiments detect neutrino interactions with target nuclei, with the neutrino energies in the few hundred MeV to few GeV range. Within this regime, the kinematics span both perturbative and non-perturbative regimes, with regions of overlap between different interaction processes providing a particular modeling challenge. As such, these experiments must deal with the systematic uncertainties introduced through cross section modeling. In this chapter, we examine the impact that such cross section uncertainties have on near detector new physics searches. This work was performed in collaboration with Shirley Li and Pedro Machado.

6.1 Background

Near detectors in long-baseline neutrino oscillation experiment are designed to mitigate the uncertainties from both the neutrino beams and neutrino-nucleus cross sections. Conceptually, this procedure may seem straightforward:

$$P(\nu_\alpha \to \nu_\beta; E_\nu) = C \frac{\dfrac{dN_\beta^{\mathrm{FD}}}{dE_\nu} \Big/ \sigma_\beta(E_\nu)}{\dfrac{dN_\alpha^{\mathrm{ND}}}{dE_\nu} \Big/ \sigma_\alpha(E_\nu)}, \tag{6.1}$$

where $P(\nu_\alpha \to \nu_\beta; E_\nu)$ is the oscillation probability the experiment is trying to measure, C is a constant accounting for detector sizes and distances to the source, the superscripts ND and FD denote near and far detectors, and $dN_{\alpha,\beta}/dE_\nu$ are the event rates of $\nu_{\alpha,\beta}$ in terms of true neutrino energy. The differences between σ_α and σ_β, if $\alpha \neq \beta$, could in principle be computed theoretically [216]. The oscillation probability can be directly derived from the unoscillated event rate dN_α/dE_ν measured at the ND and the oscillated event rate dN_β/dE_ν measured at the FD.

In reality, this "logical division" is not practical because one cannot directly measure neutrino energy, the near and far detectors have different systematics, and even the unoscillated neutrino fluxes are different at the near and far detectors solely due to the different solid angles. We can appreciate this more concretely by studying the following equation,

$$\frac{N_{\rm FD}}{N_{\rm ND}}(E_{\rm reco}) = C\frac{\displaystyle\int dE_\nu \frac{d\phi_\alpha^{\rm FD}}{dE_\nu} P(\nu_\alpha \to \nu_\beta; E_\nu)\sigma_\beta(E_\nu)\mathcal{M}_\beta^{\rm FD}(E_\nu, E_{\rm reco})}{\displaystyle\int dE_\nu \frac{d\phi_\alpha^{\rm ND}}{dE_\nu}\sigma_\alpha(E_\nu)\mathcal{M}_\alpha^{\rm ND}(E_\nu, E_{\rm reco})}, \tag{6.2}$$

where $N_{\rm FD/ND}$ encode the reconstructed neutrino event spectra, $d\phi_\alpha^{\rm FD/ND}/dE_\nu$ are the fluxes at the far and near detectors without oscillation, $\sigma_{\alpha,\beta}(E_\nu)$ are the total cross sections, and $\mathcal{M}_\alpha^{\rm FD/ND}$ are the migration matrices. The challenge here is that experiments measure the left-hand side of Eq. (6.2) and they need to infer the oscillation probability P on the right-hand side. The main difficulty is encoded in the term $\sigma_\alpha(E_\nu)\mathcal{M}_\alpha(E_\nu, E_{\rm reco})$, where the reconstruction of the true neutrino energy depends on the details of neutrino-nucleus interaction, as well as detector responses to different final-state particles. An obvious example is neutrons, for which both the modeling of neutrons produced by neutrino interactions and the corresponding detector responses are relevant. Currently, predictions on the number of outgoing nucleons in a neutrino-nucleus scattering event, as well as their energy and isospin, differ drastically among generators [217, 218]. In addition, neutron detector responses suffer from significant uncertainties due to neutron propagation and event reconstruction [219–221].

Because of these complications, oscillation experiments adopt a near-detector tuning procedure. Assuming SM physics, one can predict the measured neutrino energy spectrum in the ND with an accelerator neutrino beam simulation, an event generator such as `GENIE` [222], `NuWro` [223], `GiBUU` [224], or `ACHILLES` [225] that simulates neutrino-nucleus interaction cross sections and final states, and a detector simulation predicting the migration matrix. When the predicted and measured neutrino spectra disagree, one can modify the cross section simulations until they match. Because of the nature of such calculations and the complexities of these simulation packages, there is no unique, agreed-upon way to tune the models. One can vary the model parameters, adopt alternative models, or take a model-agnostic approach and add more degrees of freedom.

In addition, it is well appreciated that neutrino beams have sizable uncertainties and they interfere with cross section uncertainties. Different experiments also treat the flux tuning and the cross section tuning differently. NOvA, for instance, only uses hadronic production data, in-situ measurements of horn position and current, beam parameters, etc., and MINERvA neutrino-electron scattering data to tune their flux prediction [226]. T2K, on the other hand, uses ND neutrino-nucleus scattering data in addition to auxiliary data to tune their flux and cross section models at the same time [227].

In this work, we follow the tuning procedure outlined by NOvA [228]. The NOvA experiment is a long-baseline experiment comprised of two scintillator detectors (CH_2) placed along a $\nu_\mu/\bar{\nu}_\mu$ beamline produced by the NuMI facility at Fermilab: a near and a far detector placed 1 km and 810 km from the beam source, respectively. The 14 kton FD observes the muon neutrino beam after long-baseline oscillations, intended to measure oscillation parameters including Δm^2_{32} and θ_{23}. The smaller 0.3 kton ND is nearly identical to the FD to minimize systematic uncertainties.

The ND tune procedure is detailed in Ref. [229]. Neutrino interactions with the material in the ND are first generated using `GENIE` v2.12.2 with the default models and parameters. Then, the following changes are applied to the `GENIE` simulation based on auxiliary theoretical and experimental studies, i.e., *NOvA ND data is not used for this step*:

- adjusting the value of axial mass, m_A, from 0.99 to 1.04 GeV, based on recent re-analysis [230] of neutrino-deuterium scattering data;
- modifying the momentum distributions of the initial nucleons for quasi-elastic scattering, based on a MINERvA study [231];
- lowering the magnitude of neutrino-scattering in non-resonance pion production regime by 57%, motivated by re-analysis of old bubble chamber data [232];
- suppressing delta resonance production in low-Q^2 region, motivated by measurements by MiniBooNE [233], MINOS [234], MINERvA [235, 236], and T2K [237].

All these changes are to improve the baseline model in `GENIE`.

After these changes are applied to `GENIE`, there are still large discrepancies between the measured neutrino spectrum in NOvA ND and the simulated spectrum. The last step of NOvA's ND tune is the crucial step of which we are studying the effect. To understand how it works, let us first define the kinematics of neutrino interactions, then explain how kinematic variables are measured in NOvA. Theoretically, an incoming neutrino with energy E_ν produces an outgoing lepton with energy E_l and a hadronic system. The four-momentum transfer is $(q_0, \vec{q})$ with $q_0 = E_\nu - E_l$. In NOvA, as in any experiment, the neutrino energy is not directly observable and is instead measured through $E_\nu^{\text{reco}} \equiv E_l^{\text{reco}} + q_0^{\text{reco}}$. For charged-current interactions, which are the signal channels for oscillation analyses, E_l can be measured relatively well either from the total scintillation light associated with the electron or muon or from the muon range, i.e., $E_l^{\text{reco}} \simeq E_l$. The transferred energy, q_0, gets distributed between kinetic energy for knocked out nucleons, total energy for mesons, and binding energy of the initial nucleus. The sum of nucleon kinetic energy, T, and meson total energy E, roughly proportional to the amount of scintillation light detected, is called the hadronic energy, E_{had}, i.e.,

$$q_0^{\text{reco}} \simeq E_{\text{had}} = \sum_i^{\text{nucleons}} T_i + \sum_j^{\text{mesons}} E_j. \tag{6.3}$$

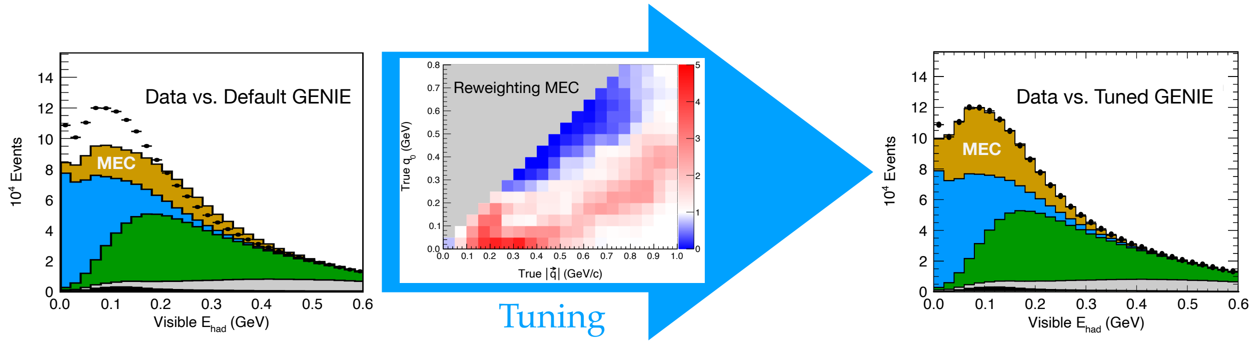

Figure 6.1: Schematic illustration of NOvA's tuning. On the left, we show the NOvA data versus the output of default `GENIE` 2.12.2 (colored histograms). The tuning happens in two steps, first, a few adjustments to `GENIE` are made, such as redefining m_A, and then the meson-exchange current (MEC) component of the cross section is reweighted to data (see text for details). The result is the plot on the right, where the output of tuned `GENIE` matches the data well. Details have been omitted for clarity. Source: Ref. [229].

We include a 30% smearing on $E_{\rm had}$, which roughly accounts for NOvA's detector response. Lastly, NOvA tune uses the reconstructed three-momentum transfer, $|\vec{q}^{\rm \,reco}|^2 = 2(E_{\rm had} + E_\mu)(E_\mu + p_\mu \cos\theta_\mu) - m_\mu^2 + E_{\rm had}^2$, where E_μ, p_μ, θ_μ are the energy, momentum, and the angle with respect to the beam of the muon, for ν_μ charged-current events. After all the modifications to `GENIE` described above, in the NOvA ND tune, one then compares the simulated event distribution to the measured one in the 2D plane of reconstructed variables $(|\vec{q}^{\rm \,reco}|, q_0^{\rm reco})$ with 20 bins in $|\vec{q}^{\rm \,reco}|$ and 16 bins in $q_0^{\rm reco}$. With the assumption that all the discrepancies between the simulated and measured distributions are due to mis-modeling of the meson-exchange current (MEC), one multiplies the MEC event rate predicted by `GENIE` in every bin by a weight, i.e., "tune," such that the tuned prediction matches the measurement. The total number of free parameters in this tuning is 200. See Fig. 6.1 for a schematic illustration.

6.2 Sterile neutrinos

To estimate the impact of the tuning procedure on BSM searches, we choose to study two illustrative models: eV-scale sterile neutrinos [238] and light neutrinophilic scalars [239].

The reason for choosing these two models is their different experimental signatures. In this section, we start with sterile neutrinos with masses around the eV scale, for which oscillations of active neutrinos to sterile neutrinos will look like wiggles in the ND neutrino energy spectrum.

6.2.1 Model description

As discussed in Section 3.3, short baseline oscillations may be approximated by

$$P(\nu_\alpha \to \nu_\beta) \simeq \delta_{\alpha\beta} - 4|U_{\alpha 4}|^2(\delta_{\alpha\beta} - |U_{\beta 4}|^2)\sin^2\left(\frac{\Delta m^2_{41} L}{4E_\nu}\right), \tag{6.4}$$

where $U_{\alpha i}$ denotes the extended $4{\times}4$ PMNS matrix, $\Delta m^2_{41} \equiv m_4^2 - m_1^2$, and E_ν is the neutrino energy. Explaining the LSND and MiniBooNE anomalies requires $\nu_\mu \to \nu_e$ transitions, and thus a nonzero U_{e4} and $U_{\mu 4}$. This, in turn, implies short baseline ν_μ and ν_e disappearance.

Here, we are interested in the ν_μ disappearance channel at NOvA ND for which

$$P(\nu_\mu \to \nu_\mu) \simeq 1 - \sin^2 2\theta_{\mu\mu} \sin^2\left(\frac{\Delta m^2_{41} L}{4E_\nu}\right), \tag{6.5}$$

where we have defined the effective ν_μ disappearance angle $\sin^2 2\theta_{\mu\mu} \equiv 4|U_{\mu 4}|^2(1 - |U_{\mu 4}|^2)$. Oscillations in NOvA ND, located about 1 km from the beam target, are depicted for illustrative oscillation parameters in Fig. 6.2. Clearly, a sterile neutrino could induce an oscillatory pattern in NOvA's neutrino spectrum at the ND. The question we want to ask is how much of this oscillatory pattern will be affected by NOvA's tuning procedure, and what the corresponding impact is on NOvA's sensitivity to sterile neutrinos.

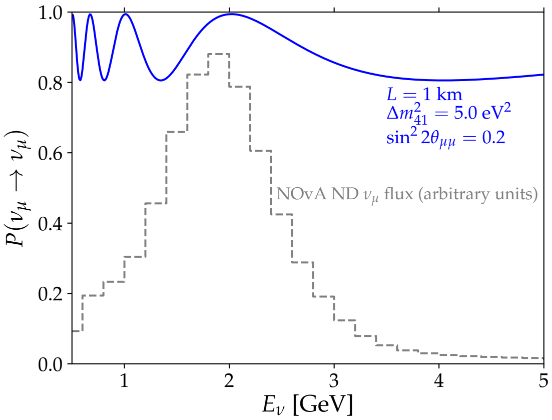

Figure 6.2: Oscillation probability in the ν_μ disappearance channel for illustrative sterile neutrino oscillation parameters as a function of the true neutrino energy E_ν (blue line). We also show the shape of the NOvA ν_μ flux in neutrino mode for reference (gray histogram) [240].

6.2.2 Analysis

Let us start with the general approach used to perform analyses in this work. To mimic a sterile neutrino search in NOvA, we first use an event generator $\mathcal{G}$ to generate mock data for both ND and FD that contain a sterile neutrino signal. We then use either the same or a different event generator $\mathcal{G}'$ to tune a SM event set to the mock data in the ND. The idea behind using a different generator to fit the mock data is to account for possible mismodeling of neutrino-nucleus scattering. Lastly, we do a chi-square analysis using the mock data and the tuned generator $\mathcal{G}'$ to see if we can recover the sterile signals and to examine how the sensitivity changes because of the tuning.

More concretely, we use the `GENIE` v2.12.2 event generator to produce mock data. We produce a set of ν_μ-carbon charged current events and reweight them according to the NOvA flux and the oscillation probability $P(\nu_\mu \to \nu_\mu)$ at the ND. We account for the varying decay lengths of the pions in the decay pipe. Following Ref. [241], we take a random oscillation length L from an exponential distribution that has a maximum at $L = 1$ km and extends to $L = 0.3$ km. The reconstructed neutrino energy is obtained following the procedure discussed in Sec. 6.1: $E_\nu^{\text{reco}} = E_\mu + q_0^{\text{reco}}$, where q_0^{reco} is the hadronic energy E_{had} smeared by 30%.

To fit the data, we study several cases. We use either `GENIE` v2.12.2 or `NuWro` v19.02.2 [1] to generate the SM spectra, reweighting the events as above. We fit mock data both with and without performing the tuning procedure to understand the extent of the impact of the tuning, especially its interplay with cross section mis-modeling, on the experimental sensitivity.

For the tuning, we follow NOvA's procedure as discussed in Sec. 6.1; however, because we are working with two sets of simulated events, we perform the tune entirely in the true $(|\vec{q}|, q_0)$ plane. When considering sterile neutrinos in the fit generator $\mathcal{G}'$, one could either first reweight according to the oscillation probability and then tune, or the other way around. Performing the analysis by first reweighting ensures us that when we use the same generator for both mock data and fit model, and we compare the same parameters for sterile neutrinos, the tuning does not make any changes to the generated events because, by design, the mock data and the fit generator predict the same ND spectra.

To appreciate the impact of the tuning, we present Fig. 6.3. In the left panel, we compare the mock data (black points) against the fit spectra using `GENIE` without (blue) and with (red) tuning. Mock data was generated with a sterile neutrino signal, assuming $\Delta m^2_{41} = 5$ eV^2 and $\sin^2 2\theta_{\mu\mu} = 0.2$, while the fit spectra have no sterile signal. The top panel shows the spectra and the bottom panel shows the ratios of the data to fit spectra. The blue lines reflect the situation that one would intuitively expect in a sterile neutrino analysis. In the top panel, we see that the data rate is lower than the SM rate because of the existence of a sterile neutrino; in the bottom panel, the blue line shows the characteristic oscillatory feature of a sterile neutrino signal. The wiggles look slightly different from Fig. 6.2 due to energy and baseline smearing. The red lines, meanwhile, illustrate the effect of tuning. The top panel shows that the tuning does not "fix" all the discrepancies between the fit generator prediction and the data. This might be surprising because the tuning has many degrees of

---

[1] For the MEC component, `GENIE` adopts the so-called "Empirical MEC" or "Dytman" model [242], while `NuWro` uses the "Nieves" model [243].

freedom; however, the tuning is performed in the $(\vec{q}, q_0)$ plane, and these observables do not correlate with E_ν in a straightforward way. In fact, the red line in the bottom panel shows that if our modeling of the SM neutrino-carbon interactions is perfect (when we use `GENIE` to model both the data and the fit spectra), the tuning almost perfectly preserves the sterile neutrino feature.

The right panel of Fig. 6.3 shows the same mock data but with the fit generator being `NuWro`. This is a more realistic situation, where our modeling of neutrino-carbon interactions, i.e., by the fit generator `NuWro`, is different from the true interactions, i.e., by the mock data generator `GENIE`. To mimic the situation in NOvA ND, in which the pre-tune model (`NuWro`) predicts fewer overall events than the data (`GENIE`), we rescale the model weights relative to the data by an overall factor of 0.9. For reference, we plot in the bottom panel the ratio between SM `GENIE` and SM `NuWro` spectra (grey dashed line). We can see from the red and blue lines in the bottom panel that some oscillatory features are still present in the ratio between mock data and fits, but less prominent than in the left panel. This can be partially attributed to the intrinsic differences between baseline generators, without the presence of any new physics, which can be seen in the grey dashed line. We can already see that this may cause a bias in the experimental sensitivity to sterile neutrinos.

To estimate NOvA's sensitivity, we build a covariance matrix, accounting for the following systematics: 20% overall normalization, 4% normalization of ND relative to FD, 2% correlated near-to-far spectral uncertainty (bin-by-bin), and fully uncorrelated 2% bin-to-bin uncertainty on both near and far detectors. Our covariance matrix is meant to capture the general features of NOvA's sensitivity, and not to reproduce precisely the experimental results. The sensitivity is estimated by a chi-square function $\chi^2 = (D-F)\cdot C^{-1}\cdot(D-F)$, where D and F are the data and fit spectra, and C is the covariance matrix including statistical uncertainties.

We perform a sensitivity analysis for the tuned and untuned case after adding a sterile

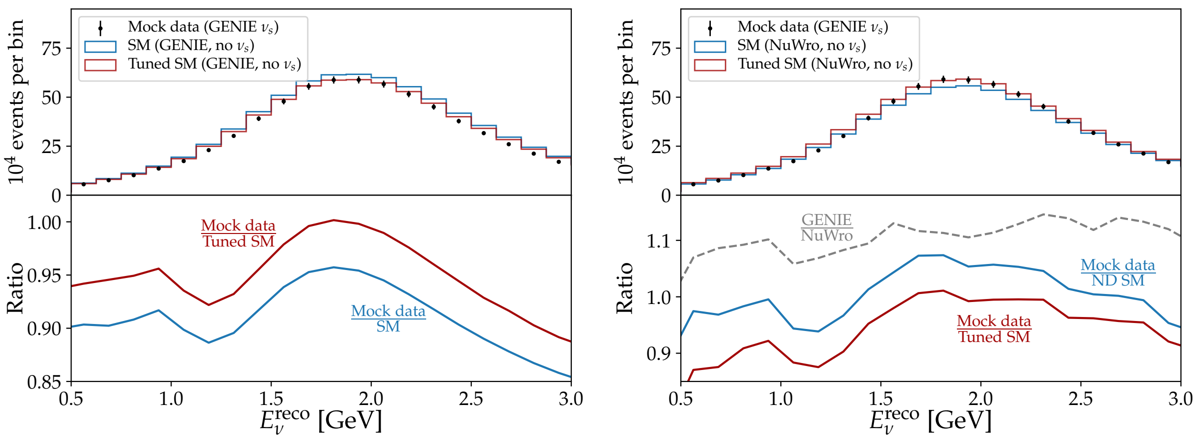

Figure 6.3: ND distributions of E_ν^{reco} for sterile data and SM expectation for $\Delta m_{41}^2 = 5$ eV^2 and $\sin^2(2\theta_{\mu\mu}) = 0.2$. In the left panel, the data and model are both generated using `GENIE`; in the right panel, the model is generated using `NuWro`. The top panel shows a histogram of events for the SM (blue), mock data (black points), and tuned SM (red) at the ND, while the lower panel shows the ratio ND data / ND SM for both the tuned (red) and untuned (blue) SM expectation.

neutrino signal with $\sin^2 2\theta_{\mu\mu} = 0.1$ and two choices of mass splittings, $\Delta m_{41}^2 = 5.0$ eV^2 and 2.0 eV^2, as shown in the left and right panels of Fig. 6.4. Again, we generate the mock data with `GENIE` and estimate the sensitivities for four cases: `GENIE` without tuning (shaded region), `GENIE` with tuning (thin line), `NuWro` without tuning (blue), and `NuWro` with tuning (red). Let us start with the left panel. The grey shaded region indicates an ideal analysis, where our fit generator and the data generator are the same, and there is no tuning. In this case, we recover the true input parameter, and the systematic uncertainties determine the region size. Note that because the FD has very few events, it contributes very little to the χ^2, and the grey region would look almost the same if we did a ND-only analysis. We also show the impact of the tuning procedure if one had the correct model of neutrino-carbon interaction (thin line). We can see that tuning indeed enlarges the region slightly, but the changes are small. The blue region shows that when we mis-model neutrino-carbon interaction and we do not tune our generator, we would still identify a sterile neutrino signal, but the fit parameters would be biased by more than 2σ. Lastly, the red region shows that if

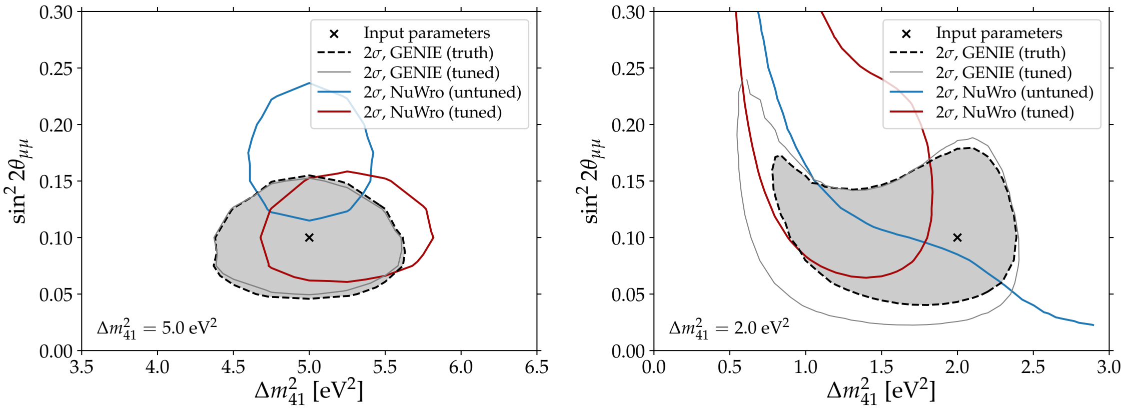

Figure 6.4: Sensitivities to sterile neutrinos for different choices of event generators and tuning, assuming sterile neutrino parameters $\sin^2 2\theta_{\mu\mu} = 0.1$ and $\Delta m^2_{41} = 5$ eV^2 (left panel) and $\Delta m^2_{41} = 2$ eV^2 (right panel).

we adopt the ND tuning, we improve the accuracy of the fitted parameters. This could seem to indicate that the tuning procedure makes the sensitivity more robust to mis-modeling.

The right panel of Fig. 6.4 tells a different story. With just a different Δm^2_{41}, we see that neither the untuned nor the tuned regions include the real input values at 2σ. The untuned region is consistent with no sterile neutrinos, and the tuned region prefers large mixing angles. This illustrates that cross section mis-modeling can significantly bias the experimental sensitivities and that the tuning procedure does not fix this issue.

6.3 Light neutrinophilic scalars

The second scenario we analyze is the light neutrinophilic scalar model proposed in Refs. [239, 244]. Its experimental signature consists of an excess of missing transverse momentum. This is a good example of a class of models in which the experimental signature depends on certain aspects of the interaction kinematics on an event-by-event basis. The correlations between these kinematic variables and the tuning variables q_0 and $|\vec{q}|$ can be nontrivial. By studying a representative signature, we hope to uncover common lessons for these kinematic searches.

6.3.1 Model description

Light neutrinophilic scalars could mediate interactions between neutrinos and dark matter candidates. These scalars would couple to neutrinos via the effective operator,

$$\mathcal{O} = \frac{(L_\alpha H)(L_\beta H)}{\Lambda^2_{\alpha\beta}}\phi + \text{h.c.} \to \frac{1}{2}\lambda_{\alpha\beta}\nu_\alpha\nu_\beta\phi + \text{h.c.}, \tag{6.6}$$

where ϕ is the neutrinophilic scalar itself; H and L_α are the Higgs and lepton doublets; $\alpha, \beta = e, \mu, \tau$; $\Lambda_{\alpha\beta}$ is the scale of the dimension-6 operator; $\lambda_{\alpha\beta} = v^2/\Lambda^2_{\alpha\beta}$ is an effective coupling between the ϕ and neutrinos after electroweak symmetry breaking; and lastly, $v = 246$ GeV is the Higgs vacuum expectation value. A sum over flavor indices is implicit. In addition to this neutrino interaction term, ϕ could also couple to dark matter, so it serves as a portal between neutrinos and the dark sector.

In this scenario, when a neutrino scatters via charged current interactions, it may radiate a ϕ, which would either leave the detector or decay invisibly to neutrinos or dark matter, thus constituting missing momentum. From Eq. (6.6), we note that ϕ carries lepton number; thus, when emitted, ϕ changes a neutrino to an antineutrino and vice versa. We depict the Feynman diagram inducing this transition in Fig. 6.5. Note that we have not been very explicit on the hadronic current, as the neutrino may scatter on nucleons, quarks, and even two-body currents. This signature has been named the mono-neutrino signal, in tandem with collider mono-X searches [245].

The typical experimental signature of this scenario will be an excess of missing transverse momentum, $\not{p}_T$, compared to usual neutrino scattering events. The missing transverse momentum is defined as the magnitude of the sum of the transverse momenta of the visible particles,

$$\not{p}_T = \left| \sum_{\text{i,vis}} (\vec{p}_T)_i \right| . \tag{6.7}$$

While the ϕ emission will necessarily lead to a missing momentum, standard neutrino-nucleus

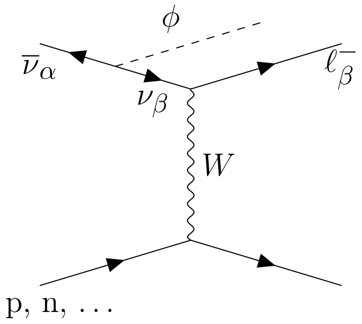

Figure 6.5: Feynman diagram relevant to the mono-neutrino signal. Note that the hadronic current can go beyond nucleon level (e.g. two-body currents, deep inelastic scattering), so we leave it general.

interactions could also display relatively large missing transverse momenta. There are three main reasons for that. If a neutrino interacts with a nucleon inside a nucleus, the struck nucleon is not at rest due to Fermi motion. The Fermi momentum is typically of the order of 250 MeV or so, leading to an unavoidable spectrum of $\not{p}_T$. Moreover, neutrinos scatter with particles inside a dense nuclear medium. As particles propagate throughout the nucleus, secondary scatterings may occur, referred to as final state interactions. This effect is fairly common and may lead to large $\not{p}_T$. Lastly, outgoing hadrons, particularly neutrons, could escape detection and thus lead to $\not{p}_T$.

6.3.2 Analysis

To simulate a set of mono-neutrino events, we use MadGraph5 [246] to generate $\overline{\nu}_\mu + n \to \mu^- + \phi + p$ events, treating the proton and neutron as elementary particles. Although this neglects Fermi motion and final state interactions, the emission of a ϕ dominates the missing transverse momentum distribution. We choose to work with an antineutrino beam because the final-state protons are visible and can be used to reduce SM backgrounds, as we will discuss later. We generate events at fixed neutrino energies, then weight the events by the convolution of the mono-neutrino cross section and the NOvA antineutrino flux at the given energy for each event. In this analysis, we use `NuWro` to simulate SM interactions, which accounts for Fermi motion and final state interactions. Here we treat neutrons as missing energy and include a 30% smearing on hadronic momenta. Mock data is obtained by combining the signal and background events, producing a simulated expected missing momentum spectrum at the ND for this model. To account for mis-modeling of neutrino-nucleus interactions, we use `GENIE` to simulate our SM fit background.

In the left panel of Fig. 6.6, we show the missing momentum spectra for the mock data background (black points), the fit model (blue), and the mono-neutrino signal (red) for coupling $\lambda_{\mu\mu} = 0.5$ and scalar mass $m_\phi = 0.5$ GeV. As we can see, the mono-neutrino signal is more than two orders of magnitude below the background. This is partially due to the multiplicity of the final states of the signal. The extra phase space factor of three- compared to two-body final states leads to a suppression of about two orders of magnitude on the cross section. This low signal rate forces us to impose experimental cuts to improve the signal-to-background ratio.

In antineutrino mode, the signal events are given by $\overline{\nu}_\mu + n \to \mu^- + \phi + p$. The visible final states in the detector are the muon and the proton. In contrast, we can think of the background events naively as given by $\overline{\nu}_\mu + p \to \mu^+ + n$. The presence of a neutron could lead to large $\not{p}_T$, which would mimic the signal. While neutrons are hard to reconstruct, those above 100 MeV are likely to have hard interactions with nuclear matter, leading to hadronic activity that allows us to identify its presence. Given this, we cut events with neutrons above 100 MeV. [2] Moreover, we only select events with exactly one visible proton, that is, protons with kinetic energy above 100 MeV, and no pions at all. We include a 30% smearing on hadronic momenta.

The result of these cuts can be seen in the right panel of Fig. 6.6. While the signal-to-background ratio has improved considerably, a new issue arises: the background-only mock

---

[2] This is consistent with setting all the neutron energy as missing energy. We assume that, even though NOvA can identify the presence of a neutron above 100 MeV, they cannot reconstruct its energy, and therefore its energy still goes to missing energy.

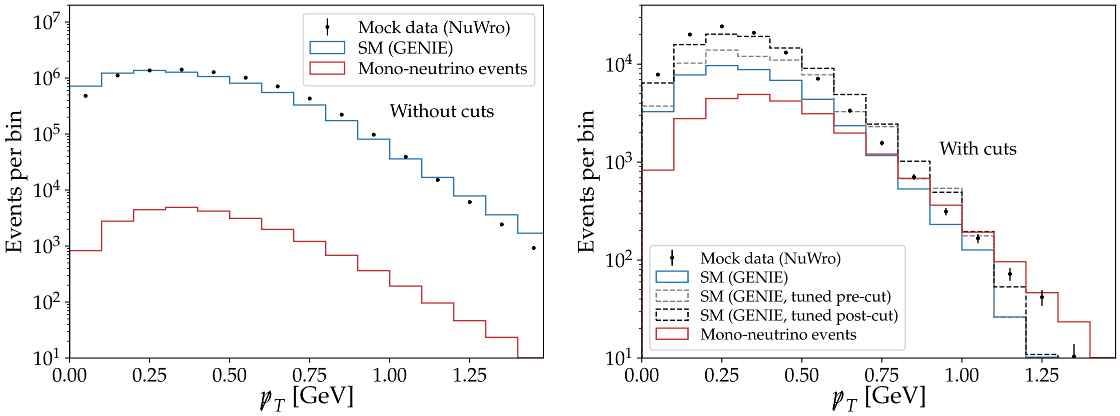

Figure 6.6: Missing p_T distributions before (left) and after (right) cuts. Mock SM data (black points) was generated with `NuWro`, while `GENIE` was used as fit model (blue). The mono-neutrino signal is given in red. In the right panel we also show the predicted $\not{p}_T$ spectra for tuned fit model when the tuning is performed before cuts (gray) or after cuts (black).

data is significantly different from the fit model (blue). Under further consideration, this should not be surprising because the more exclusive we look at cross section predictions, the larger the expected theoretical uncertainties and discrepancies. To understand the extent to which this large discrepancy could be addressed by ND tuning, we perform the tuning before (gray) and after (black) experimental cuts. We can clearly see that neither options can reproduce the mock data spectrum. But, more importantly, the tuned spectra depend strongly on the cuts used, so even if a tune is performed with one event sample and measured with another, this dependence may introduce biases in the experimental analyses. On top of that, the differences between tuned model and data are larger than the signal rate itself.

This large discrepancy between mock data and tuned fit model already shows us that the mis-modeling of neutrino-nucleus interactions may render an experiment completely unable to probe certain BSM physics scenarios. Regardless, we can perform a statistical analysis of the experimental sensitivity to appreciate quantitatively how relevant cross section modeling is to this BSM search. We perform the analysis by employing a similar covariance matrix to that built in the previous section, but excluding the FD data, and with the uncertainties now applicable to bins of $\not{p}_T$. For systematics we take an overall normalization uncertainty of 20%

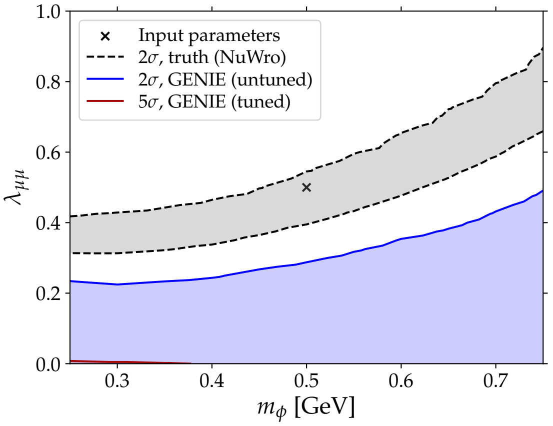

Figure 6.7: Sensitivity for a mono-neutrino signal with $\lambda_{\mu\mu} = 0.5$ and $m_\phi = 0.5$ GeV for different choices of event generators and tuning. Because the 2σ tuned region is not visible on the figure, we show the 5σ region (in the lower left corner).

and a bin-to-bin uncorrelated uncertainty of 5%; our chi-square is $\chi^2 = (D-F) \cdot C^{-1} \cdot (D-F)$, where D and F are the data and fit model binned in $\not{p}_T$. While this is not a realistic treatment of experimental sensitivity to missing momentum signals, it suffices for our purposes.

Figure 6.7 shows our results, assuming the presence of a mono-neutrino signal with coupling $\lambda_{\mu\mu} = 0.5$ and $m_\phi = 0.5$ GeV. In grey, we present the allowed region when using the same generator for the signal and the fit model, which would correspond to the case of perfect modeling of neutrino-nucleus interactions. We also show the allowed region for data and fit model using different generators, which would correspond to cross section mis-modeling. We see that without tuning (blue), the fit prefers no new physics, as the allowed region includes $\lambda_{\mu\mu} = 0$. In fact, the fit excludes the true parameter point at more than 5σ. With tuning (red), the results actually get worse, as the fit strongly prefers no new physics. We can conclude that the discrepancy between mock data and the tuned fit model dominates the experimental sensitivity.

This shows that while near detectors have the potential to probe new physics, without proper modeling of neutrino-nucleus interactions, we may lose this potential. Tuning is not the solution.

6.4 Discussion

In this work, we have estimated the impact of the ND neutrino-nucleus cross section tuning procedure on BSM signatures at neutrino experiments. To perform a realistic study, we follow very closely the NOvA collaboration tuning procedure, and we simulate neutrino scattering events with state-of-the-art event generators `GENIE` and `NuWro`. We study two illustrative BSM scenarios: eV-scale sterile neutrinos, which would manifest via wiggles in the ν_μ survival oscillation probability; and neutrinophilic scalars, which could be emitted by neutrinos in charged current interactions leading to large amounts of missing transverse momentum.

Our results show that the interplay between cross section mis-modeling, ND tuning, and sensitivity to new physics is far from trivial. Concretely, the wiggles in the ND neutrino energy spectrum induced by eV-scale sterile neutrino oscillations largely remain after tuning. That is, the tuning of the neutrino-nucleus cross section cannot mimic sterile neutrino signatures. Nevertheless, mis-modeling neutrino-nucleus interactions can lead to discrepancies between theory and data that may introduce a bias on the experimental sensitivity.

The situation for neutrinophilic scalars is quite different. First, the beyond standard model signature is significantly lower than the standard model background. This forces us to impose experimental cuts to improve the signal-to-background ratio. In doing so, we go to regions of parameter space in which the background is suppressed but most of the signal remains; however, in these regions the tuning of the fit model is inefficient at reproducing the data, leading to large discrepancies between data and theory. We have seen that for the case of neutrinophilic scalars, this discrepancy dominates the experimental sensitivity, rendering it unrealistic.

In both BSM scenarios studied here, the mis-modeling of neutrino-nucleus interactions can lead to significant biases on the experimental sensitivity, regardless of the tuning procedure. One may wonder if this is a widespread issue in BSM searches at neutrino experiments, such as T2K, HK, and DUNE. It is reasonable to presume that a tuning based on the correct physics would be able to resolve mis-modeling; however, ad hoc tunings will most likely fail to capture the correct physics of neutrino-nucleus interactions, e.g. by lacking important correlations or by being arbitrarily limited to specific processes. Without the correct physics, a tuning will only be able to reproduce experimental data by chance. Agreement between an ad hoc tuning and data in one observable does not necessarily imply that any other observable will be well described by the tuning, as can be seen for instance in recent MINERvA analyses [247]. It should therefore not come as a surprise that a tuning that is not correlated with a BSM signature and thus does not wash it out is also not capable of addressing mis-modeling.

One may think that practically, a conservative approach would be to assign a large systematic error that includes the possibility that there is indeed gross mis-modeling of the cross sections. However, this does not change the fact that significant cross section mis-modeling and therefore large systematic errors would render the ND blind to new physics. Our findings reveal the importance of properly accounting for the tuning procedure, as well as properly estimating cross section uncertainties for BSM searches. This will be even more relevant for the future experiments HK and DUNE due to their high statistics.

CHAPTER 7

THEORETICAL BOUNDS ON THE GENERAL 2HDM

We now move to an examination of theoretical bounds on general 2HDMs. As we have seen previously, two Higgs doublet models may differ in the mechanism of generation of fermion masses. If both Higgs doublets couple to fermions of a given charge, their couplings will be associated to two different, complex sets of Yukawa couplings, which would form two different matrices in flavor space. The fermion mass matrices would be the sum of these, each multiplied by the corresponding Higgs vacuum expectation value. So diagonalization of the fermion mass matrices does not lead to the diagonalization of the fermion Yukawa matrices. Such theories are then associated with large flavor violating couplings of the Higgs bosons at low energies—a situation which is experimentally strongly disfavored. Hence, it is usually assumed that each charged fermion species couples only to one of the two Higgs doublets. In most works related to 2HDM, this is accomplished by implementing a suitable $\mathbb{Z}_2$ symmetry. The different possible charge assignments for this $\mathbb{Z}_2$ symmetry then fix the Higgs–fermion coupling choices and define different types of 2HDMs.

This $\mathbb{Z}_2$ symmetry not only fixes the Higgs–fermion couplings but also forbids certain terms in the Higgs potential that are far less problematic with respect to flavor violation. As a starting point for an investigation of the phenomenological implications of these terms, we will in this work discuss the theoretical bounds on the boson sector of the theory (without any need to specify the nature of the Higgs-fermion couplings). We will concentrate on the constraints that come from the perturbative unitarity of the theory, the stability of the physical vacuum, and the requirement that the effective potential is bounded from below. Existing works [37, 248–260] focus either on the $\mathbb{Z}_2$-symmetric case or only provide a numerical procedure to test these constraints in the general 2HDM (see Ref. [261] for a recent work on analytic conditions for boundedness-from-below). We will go beyond current studies by deriving analytic bounds that apply to the most general, renormalizable realization of

2HDMs. Our conditions will be given in terms of the mass parameters and dimensionless couplings of the 2HDM tree-level potential. At the quantum level, however, these parameters are scale dependent; although we will refrain from doing so here, one can apply these conditions at arbitrarily high energy scales by using the renormalization group evolution of these parameters.

The following chapter is organized as follows. Section 7.1 reviews three theorems from linear algebra which will allow us to derive analytic bounds in the coming sections. In Section 7.2, we concentrate on the requirement of perturbative unitarity. Section 7.3 presents the bounds coming from the requirement that the tree-level potential be bounded from below. In Section 7.4, we discuss the vacuum stability. Finally, we reserve Section 7.5 for a brief analysis of the phenomenological implications, focusing on $\mathcal{CP}$ violation. This work was performed in collaboration with Henning Bahl, Marcela Carena, Aurora Ireland, and Carlos Wagner.

7.1 Methods for bounding matrix eigenvalues

In this work, much of the analysis of perturbative unitarity and vacuum stability involves placing bounds on matrix eigenvalues. In the most general 2HDM, analytic expressions for these constraints are either very complicated or simply cannot be formulated. To obtain some analytic insight, we derive conditions which are either necessary or sufficient. Their derivation is based on three linear algebra theorems which we briefly review here.

7.1.1 Frobenius norm

One may derive a bound on the magnitude of the eigenvalues of a matrix using the matrix norm. The following definition and theorem are needed:

Theorem: *The magnitude of the eigenvalues e_i of a square matrix A are bounded from above by the matrix norm: $|e_i| \leq ||A||$.*

where a matrix norm is defined as:

Definition: *Given two $m \times n$ matrices A and B, the matrix norm $||A||$ satisfies the following properties:*

- $||A|| \geq 0$,
- $||A|| = 0 \Leftrightarrow A = 0_{m,n}$,
- $||\alpha A|| = |\alpha| ||A||$,
- $||A + B|| \leq ||A|| + ||B||$.

The above theorem holds for any choice of matrix norm, and thus one may employ the Frobenius norm [262], $||A|| = \sqrt{\mathrm{Tr}(A^\dagger A)}$, to find the following result:

$$|e_i| \leq \sqrt{\mathrm{Tr}(A^\dagger A)} \tag{7.1}$$

This bound on the eigenvalues will be used to derive sufficient bounds in the following sections.

7.1.2 Gershgorin disk theorem

We will use the Gershgorin disk theorem [263] in upcoming sections to derive sufficient conditions for perturbative unitarity and vacuum stability of the 2HDM potential. The theorem is typically used to constrain the spectra of complex square matrices. The basic idea is that one identifies each of the diagonal elements with a point in the complex plane and then constructs a disk around this central point, with the radius given by the sum of the magnitudes of the other $n-1$ entries of the corresponding row.[1] The theorem says that all eigenvalues must lie within the union of these disks. Formally, we have the following definition and theorem:

Definition: *Let A be a complex $n \times n$ matrix with entries a_{ij}, and let R_i be the sum of the magnitudes of the non-diagonal entries of the i^{th} row, $R_i = \sum_{j \neq i} |a_{ij}|$. Then the Gershgorin disk $D(a_{ii}, R_i)$ is defined as the closed disk in the complex plane centered on a_{ii} with radius R_i.*

Theorem: *Every eigenvalue of A lies within at least one such Gershgorin disk $D(a_{ii}, R_i)$.*
This theorem can be used to derive an upper bound on the magnitude of the eigenvalues of a matrix. We will use this technique below when discussing perturbative unitarity and vacuum stability. Since all the matrices we will consider in the subsequent sections on perturbative unitarity and boundedness from below are Hermitian matrices, each eigenvalue will lie within the intervals formed by the intersection of the Gershgorin disks with the real axis.

We shall proceed in the following manner: We will first construct the intervals containing the eigenvalues of each matrix A. For each interval, the rightmost and leftmost endpoints $x_i^{\pm}$ will be given by the sum and difference, respectively, of the center and the radius,

$$x_i^{\pm} \equiv a_{ii} \pm R_i \,, \quad \text{with} \quad R_i = \sum_{j \neq i} |a_{ij}| \,. \tag{7.2}$$

We then identify which $x_i^{\pm}$ extends furthest in the positive or negative direction. We know that every eigenvalue e_k must lie within the endpoints of the largest possible total interval,

$$\min(x_i^-) \leq e_k \leq \max(x_i^+) \,. \tag{7.3}$$

---

[1] One can also construct the radius by summing the magnitudes of the $n-1$ column entries.

This may be rephrased into an upper bound on $|e_k|$ as:

$$|e_k| \leq \max_i \left(\sum_j |a_{ij}| \right) , \tag{7.4}$$

where the left-hand side of Eq. 7.4 represents the absolute value of any given eigenvalue e_k and the right-hand side represents the maximum value of $\sum_j |a_{ij}|$ over all rows i of the matrix A. In fact, this condensed statement of Gershgorin circle theorem is an application of the matrix norm theorem, employing the norm $||A|| = \max_i(\sum_j |a_{ij}|)$.

7.1.3 Principal minors

In order to derive necessary conditions, one may employ Sylvester's criterion in a clever way, as proposed in Ref. [264]. Sylvester's criterion involves the principal minors D_k of a matrix, where D_k is the determinant of the upper-left $k \times k$ sub-matrix. The statement of Sylvester's criterion is the following:

Theorem: *Let M be a Hermitian $n \times n$ matrix. M is positive definite if and only if all of the principal minors $D_k(M)$ are positive.*

We further need the following result about Hermitian matrices:

Theorem: *Let M be a Hermitian matrix. Then M is positive definite if and only if all of its eigenvalues are positive.*

One can apply this to derive an upper bound on the eigenvalues of a diagonalizable matrix in the following way:

Theorem: *Let M be an $n \times n$ diagonalizable, Hermitian (symmetric) matrix and let c be a positive real number. The eigenvalues e_i of M are bounded as $|e_i| < c$ if and only if all principal minors $D_k(c\mathbb{1} - M)$ and $D_k(c\mathbb{1} + M)$ are positive for all $k = 1...n$.*

To see this, consider applying a unitary transformation which diagonalizes M to the matrix $c\mathbb{1} \pm \text{diag}(M)$. Then for symmetric or Hermitian matrices, the statement that $c\mathbb{1} \pm M$ is positive definite becomes a statement on the relative values of e_i and c. In this manner, the application of Sylvester's criterion to these specific matrices allows one to put an upper bound on the magnitude of the eigenvalues without diagonalizing the matrix M. Note that for the absolute value $|e_i|$ to be bounded by c, we require the use of both $c\mathbb{1} \pm M$ matrices. On the other hand, if one has only an upper bound on e_i, i.e. $e_i < c$, as we will have in the case of vacuum stability, then one only requires the principal minors of the matrix $c\mathbb{1} - M$ to be positive.

We note that the use specifically of the upper-left sub-matrices in Sylvester's criterion is an arbitrary choice, and basis-dependent. One could instead consider the lower-right sub-matrices, or any matrices along the diagonal. As such, it is possible to derive further conditions using this criteria by further considering, for example, the upper-left, lower-right, and central 2×2 sub-matrices of a 4×4 matrix. We will do so in later analyses to strengthen the lower-k bounds.

This use of sub-determinants has been proposed in Ref. [264] as a method to increase the efficiency of parameter scans in models with large scattering matrices. For such theories (e.g. the model with N Higgs doublets, NHDM, considered in Ref. [264] for higher N), the numerical calculation of the scattering matrix eigenvalues is computationally expensive. We note that the use of the Gershgorin disk theorem proposed in Section 7.1.2 provides an additional complementary method to speed-up parameter scans.

7.2 Perturbative Unitarity

Tree-level constraints for perturbative unitarity in the most general 2HDM have already been investigated in the literature [252, 257, 265]. However, for a non-zero λ_6 and λ_7, no exact analytic conditions have been obtained yet. Here, we will first review the existing literature and then derive analytic expressions for the case of non-vanishing λ_6 and λ_7.

7.2.1 Numerical bound

Perturbative unitarity is usually imposed by demanding that the eigenvalues e_i of the scalar scattering matrix at high energy be less than the unitarity limit, $|e_i| < 8\pi$. Thus to derive the constraints on the quartic couplings, one must construct the scattering matrix for all physical scalar states.

We are interested in all processes $AB \to CD$, where the fields $A...D$ represent any combination of the physical scalars $(H_1, H_2, H_3, H^\pm, W_L^\pm, Z_L)$. The interactions and hence S-matrix take a complicated form in terms of the physical states. However since we are only interested in the eigenvalues of the S-matrix, we may choose any basis related to the physical basis by a unitary transformation. The derivation is simplest in the basis of the original Higgs fields $(w_i^\pm, h_i, z_i)$, appearing as

$$\Phi_i = \begin{pmatrix} w_i^+ \\ \frac{1}{\sqrt{2}}(v_i + h_i + iz_i) \end{pmatrix} , \tag{7.5}$$

with $v = \sqrt{\sum_i v_i^2} = 246$ GeV.

Out of these fields, we can construct 14 neutral two-body states: $|w_i^+ w_i^-\rangle$, $\frac{1}{\sqrt{2}}|z_i z_i\rangle$, $\frac{1}{\sqrt{2}}|h_i h_i\rangle$, $|h_i z_i\rangle$, $|w_1^+ w_2^-\rangle$, $|w_2^+ w_1^-\rangle$, $|z_1 z_2\rangle$, $|h_1 h_2\rangle$, $|z_1 h_2\rangle$, and $|h_1 z_2\rangle$. By constructing states which are linear combinations with definite hypercharge and total weak isospin, denoted by (Y, I), and grouping the ones with the same set of quantum numbers, the matrix of S-wave amplitudes a_0 takes a block diagonal form (for more details see Refs. [252, 257, 265]). For the neutral scattering channels, this is:

$$a_0^{(0)} = \frac{1}{16\pi} \begin{pmatrix} X_{(0,0)} & & & \\ & X_{(0,1)} & & \\ & & X_{(1,1)} & \\ & & & X_{(1,1)} \end{pmatrix}, \tag{7.6}$$

where the subscript of each submatrix denotes the quantum numbers (Y, I) of the corresponding states. The entries are:

$$X_{(0,0)} = \begin{pmatrix} 3\lambda_1 & 2\lambda_3 + \lambda_4 & 3\lambda_6 & 3\lambda_6^* \\ 2\lambda_3 + \lambda_4 & 3\lambda_2 & 3\lambda_7 & 3\lambda_7^* \\ 3\lambda_6^* & 3\lambda_7^* & \lambda_3 + 2\lambda_4 & 3\lambda_5^* \\ 3\lambda_6 & 3\lambda_7 & 3\lambda_5 & \lambda_3 + 2\lambda_4 \end{pmatrix}, \tag{7.7a}$$

$$X_{(0,1)} = \begin{pmatrix} \lambda_1 & \lambda_4 & \lambda_6 & \lambda_6^* \\ \lambda_4 & \lambda_2 & \lambda_7 & \lambda_7^* \\ \lambda_6^* & \lambda_7^* & \lambda_3 & \lambda_5^* \\ \lambda_6 & \lambda_7 & \lambda_5 & \lambda_3 \end{pmatrix}, \tag{7.7b}$$

$$X_{(1,1)} = \begin{pmatrix} \lambda_1 & \lambda_5 & \sqrt{2}\lambda_6 \\ \lambda_5^* & \lambda_2 & \sqrt{2}\lambda_7^* \\ \sqrt{2}\lambda_6^* & \sqrt{2}\lambda_7 & \lambda_3 + \lambda_4 \end{pmatrix}. \tag{7.7c}$$

For the 8 singly-charged two-body states $|w_i^+ z_i\rangle$, $|w_i^+ h_i\rangle$, $|w_1^+ z_2\rangle$, $|w_1^+ h_2\rangle$, $|w_2^+ z_1\rangle$, $|w_2^+ h_1\rangle$, the block diagonal 8×8 singly-charged S-matrix is given by:

$$a_0^{(+)} = \frac{1}{16\pi} \begin{pmatrix} X_{(0,1)} & & \\ & X_{(1,0)} & \\ & & X_{(1,1)} \end{pmatrix} , \tag{7.8}$$

where the new entry $X_{(1,0)}$ is just the one-dimensional eigenvalue:

$$X_{(1,0)} = \lambda_3 - \lambda_4 \,. \tag{7.9}$$

Finally, the 3×3 S-matrix for the three doubly-charged 2-body states $|w_i^+ w_i^+\rangle$, $|w_1^+ w_2^+\rangle$ is given by:

$$a_0^{(++)} = \frac{1}{16\pi} X_{(1,1)} \,. \tag{7.10}$$

We impose perturbative unitarity by demanding that the eigenvalues of the scattering matrix are smaller than 8π implying that $|a_0| < \frac{1}{2}$. Indeed, the eigenvalues of the submatrices $X_{(0,0)}$, $X_{(0,1)}$, $X_{(1,0)}$, and $X_{(1,1)}$, which we denote as e_i, must all satisfy

$$|e_i| < 8\pi \,. \tag{7.11}$$

Obtaining analytic expressions for the eigenvalues requires solving cubic and quartic equations, and the result is complicated and not very useful. Given a choice of input parameters, however, it is easy to check this condition numerically.

Assuming all $\lambda_{1\ldots 7}$ to be equal, the strongest constraint arises from the 4×4 matrix X_{00}. If we set all $\lambda_i \equiv \lambda$ and solve for the eigenvalues, we find the bound:

$$\lambda < \frac{2\pi}{3} \,. \tag{7.12}$$

This value is an order of magnitude smaller than 8π, implying that if all quartic couplings are

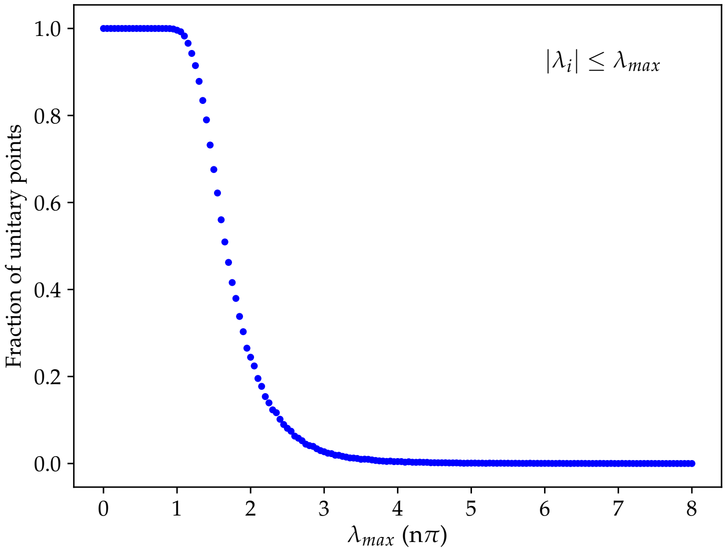

Figure 7.1: Plot showing the fraction of points that pass the unitarity bound $|e_i| < 8\pi$ for different choices of λ_{max}, in units of multiples of π. The values of the λ_i are each chosen randomly such that $|\lambda_i| < \lambda_{max}$. We test 20,000 random sets of λ_i for each λ_{max}.

sizable (i.e. of $\mathcal{O}(1)$), perturbative unitarity may be lost even at values of the couplings much smaller than 4π, which is a bound often encountered in the literature to ensure perturbativity.

We investigate the validity of such an upper bound further in Fig. 7.1. For this figure, we randomly choose each λ_i within the range $|\lambda_i| < \lambda_{\text{max}}$ and then show the fraction of test points which pass the numerical unitarity constraint, as a function of λ_{max}. For $\lambda_{\text{max}} \lesssim \pi$ almost all points survive the perturbative unitarity constraint. For larger λ_{max} values the survival rate quickly drops to almost zero for $\lambda_{\text{max}} \gtrsim 4\pi$. This highlights again that the simplified perturbativity bound of $|\lambda_i| < 4\pi$, which is often encountered in the literature, is too loose. Based on the results in Fig. 7.1, a better choice of bound might be $|\lambda_i| \lesssim \pi$ or $|\lambda_i| \lesssim 3\pi/2$.

7.2.2 A necessary condition for perturbative unitarity

To gain some intuition for the perturbative unitarity constraint, we now turn to derive some simplified analytic conditions which are either necessary or sufficient, though not both.

In this section we will focus on the former, which can be used to quickly rule out invalid parameter sets which violate perturbative unitarity. One can derive necessary conditions by invoking the method of principal minors, which is reviewed in Section 7.1.3 and can be used to give an upper bound on the maximal value of the eigenvalues of a Hermitian matrix. Since the scattering matrices are Hermitian, demanding the eigenvalues to be bounded as $|e_i| < 8\pi$, as required by perturbative unitarity, amounts to requiring:

$$D_k(8\pi\mathbb{1} + X) > 0 \text{ and } D_k(8\pi\mathbb{1} - X) > 0\,, \tag{7.13}$$

for $k = 1, 2, 3, 4$. Since satisfying both criteria for all $k = 1, 2, 3, 4$ is a necessary and sufficient condition, any single k condition provides a necessary condition.

Since the eigenvalues of $X_{(0,0)}$ are generically the largest and therefore the most constraining, we will focus on bounds coming from this matrix. We begin with the upper left 2×2 submatrices. Taking the determinant, we have:

$$D_2^L(8\pi\mathbb{1} + X_{(0,0)}) > 0 \;\;\Rightarrow\;\; 64\pi^2 + 24\pi(\lambda_1 + \lambda_2) + 9\lambda_1\lambda_2 - (2\lambda_3 + \lambda_4)^2 > 0\,, \tag{7.14a}$$

$$D_2^L(8\pi\mathbb{1} - X_{(0,0)}) > 0 \;\;\Rightarrow\;\; 64\pi^2 - 24\pi(\lambda_1 + \lambda_2) + 9\lambda_1\lambda_2 - (2\lambda_3 + \lambda_4)^2 > 0\,. \tag{7.14b}$$

Clearly the latter constraint coming from $D_2^L(8\pi\mathbb{1} - X)$ will be the stronger of the two, since $\lambda_1, \lambda_2 > 0$ if boundedness from below is imposed. Thus the necessary $k = 2$ condition reduces to Eq. (7.14b). We also examine the constraints that arise from using the lower-right and center 2×2 sub-matrices, as proposed in Section 7.1.3. The analytic conditions from the lower-right D^R and center D^C sub-matrices are, respectively,

$$D_2^R(8\pi\mathbb{1} - X_{(0,0)}) = 64\pi^2 + (\lambda_3 - 16\pi)\lambda_3 + (4(\lambda_3 + \lambda_4) - 32\pi)\lambda_4 - 9|\lambda_5|^2 \;\; > 0\,, \tag{7.15a}$$

$$D_2^C(8\pi\mathbb{1} - X_{(0,0)}) = 64\pi^2 - 8\pi(\lambda_3 + 3\lambda_2 + 2\lambda_4) + 3\lambda_3\lambda_2 + 6\lambda_2\lambda_4 - 9|\lambda_7|^2 \;\; > 0\,. \tag{7.15b}$$

The combination of these three expressions provides a stronger constraint than just the upper-left minor constraint alone.

While it is immediately clear that $D_2^L(8\pi\mathbb{1} - X)$ is stronger than the addition-based bound for the upper-left matrix, it is not clear for the center and lower-right matrices; in fact, including these bounds provides a slightly more constraining result. We thus employ the $D_2^{C,R}(8\pi\mathbb{1} + X)$ constraints in our analysis of the $k = 2$ bound as well:

$$D_2^R(8\pi\mathbb{1} + X_{(0,0)}) = 64\pi^2 + (\lambda_3 + 16\pi)\lambda_3 + (4(\lambda_3 + \lambda_4) + 32\pi)\lambda_4 - 9|\lambda_5|^2 \quad > 0\,, \tag{7.16a}$$

$$D_2^C(8\pi\mathbb{1} + X_{(0,0)}) = 64\pi^2 + 8\pi(\lambda_3 + 3\lambda_2 + 2\lambda_4) + 3\lambda_3\lambda_2 + 6\lambda_2\lambda_4 - 9|\lambda_7|^2 \quad > 0\,. \tag{7.16b}$$

Next, we look at the upper left 3×3 submatrices. Unlike the $k = 2$ case, it is not clear that one of these is generically more constraining than the other. To be consistent with the $k = 2$ case, we will examine the $8\pi\mathbb{1} - X_{(0,0)}$ matrix. We additionally consider the lower-right 3×3 sub-matrix. These give the following bounds:

$$\begin{aligned} D_3^L(8\pi\mathbb{1} - X_{(0,0)}) =& (8\pi - \lambda_3 - 2\lambda_4)((8\pi - 3\lambda_1)(8\pi - 3\lambda_2) - (2\lambda_3 + \lambda_4)^2) \\ & - 9(8\pi - 3\lambda_2)|\lambda_6|^2 - 9(8\pi - 3\lambda_1)|\lambda_7|^2 \\ & - 9(2\lambda_3 + \lambda_4)(\lambda_6\lambda_7^* + \lambda_6^*\lambda_7) > 0\,, \end{aligned} \tag{7.17a}$$

$$\begin{aligned} D_3^R(8\pi\mathbb{1} - X_{(0,0)}) =& (8\pi - \lambda_3 - 2\lambda_4)^2(8\pi - 3\lambda_2) - 9|\lambda_5|^2(8\pi - 3\lambda_2) \\ & - 27(\lambda_5^*\lambda_7^2 + \lambda_5(\lambda_7^*)^2) - 18(8\pi - \lambda_3 - 2\lambda_4)|\lambda_7|^2 > 0\,. \end{aligned} \tag{7.17b}$$

Meanwhile, considering $8\pi\mathbb{1} + X_{(0,0)}$ gives

$$\begin{aligned} D_3^L(8\pi\mathbb{1} + X_{(0,0)}) =& (8\pi + \lambda_3 + 2\lambda_4)((8\pi + 3\lambda_1)(8\pi + 3\lambda_2) - (2\lambda_3 + \lambda_4)^2) \\ & - 9(8\pi + 3\lambda_2)|\lambda_6|^2 - 9(8\pi + 3\lambda_1)|\lambda_7|^2 \\ & + 9(2\lambda_3 + \lambda_4)(\lambda_6\lambda_7^* + \lambda_6^*\lambda_7) > 0\,, \end{aligned} \tag{7.18a}$$

$$\begin{aligned} D_3^R(8\pi\mathbb{1} + X_{(0,0)}) =&(8\pi + \lambda_3 + 2\lambda_4)^2(8\pi + 3\lambda_2) - 9|\lambda_5|^2(8\pi + 3\lambda_2) \\ &+ 27(\lambda_5^*\lambda_7^2 + \lambda_5(\lambda_7^*)^2) - 18(8\pi + \lambda_3 + 2\lambda_4)|\lambda_7|^2 > 0\,. \end{aligned} \tag{7.18b}$$

While the $D_3(8\pi\mathbb{1} - X_{(0,0)})$ provide the strongest constraints for values of $|\lambda_i| \lesssim 4\pi$, the inclusion of the $D_3(8\pi\mathbb{1} + X_{(0,0)})$ and D_2 bounds improves the performance of the $k = 3$ bounds at higher $|\lambda_i|$. We omit analytic expressions for the $k = 4$ case, since they cannot be simplified to a useful form. Moreover, the $k = 3$ expressions already provide constraints very close to the full numerical bound (see Fig. 7.2).

7.2.3 Sufficient conditions for perturbative unitarity

Next, we turn to derive sufficient conditions for perturbative unitarity by applying the Gershgorin disk theorem, which is reviewed in Section 7.1.2 and gives an upper bound on the maximal value of the eigenvalues. By demanding that this upper bound is less than 8π, we obtain a sufficient condition for perturbative unitarity.

We first construct the intervals $x_i^{(Y,I)}$ containing the eigenvalues of each of the scattering matrices, $X_{(0,0)}$, $X_{(0,1)}$, $X_{(1,0)}$, and $X_{(1,1)}$. We know that in order to uphold perturbative unitarity, we must have $|e_i| < 8\pi$. Thus we arrive at the sufficient condition:

$$\max(x_i^{(Y,I)}) < 8\pi\,. \tag{7.19}$$

For each of the X matrices, we can work out the $x_i^{(Y,I)}$ explicitly. For $X_{(0,0)}$, we obtain:

$$x_1^{(0,0)} = 3|\lambda_1| + (|2\lambda_3 + \lambda_4| + 6|\lambda_6|)\,, \tag{7.20a}$$

$$x_2^{(0,0)} = 3|\lambda_2| + (|2\lambda_3 + \lambda_4| + 6|\lambda_7|)\,, \tag{7.20b}$$

$$x_3^{(0,0)} = x_4^{(0,0)} = |\lambda_3 + 2\lambda_4| + 3(|\lambda_5| + |\lambda_6| + |\lambda_7|)\,. \tag{7.20c}$$

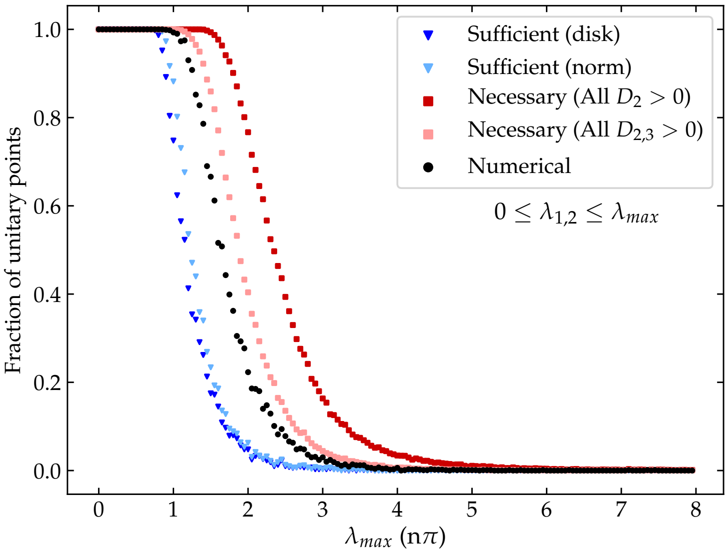

Figure 7.2: Plot comparing the number of points that pass the exact numerical bound $|e_i| < 8\pi$ (black), the sufficient bound from the Gershgorin disk theorem Eq. (7.24) (dark blue), the sufficient bound from the Frobenius norm Eq. (7.25) (light blue), the necessary condition $D_2(8\pi\mathbb{1} \pm X_{(0,0)}) > 0$ (dark red), and the necessary condition $D_{2,3}(8\pi\mathbb{1} \pm X_{(0,0)}) > 0$ (light red). The λ_i values are randomly chosen from the range of values satisfying $|\lambda_i| < \lambda_{max}$, where λ_{max} is given by the x-axis in units of multiples of π. The minimal bounded from below condition $\lambda_{1,2} \geq 0$ is enforced. The $\lambda_{5,6,7}$ values are allowed to be complex. The total number of points checked for each λ_{max} is 10,000.

For $X_{(0,1)}$, they are:

$$x_1^{(0,1)} = |\lambda_1| + (|\lambda_4| + 2|\lambda_6|)\,, \tag{7.21a}$$

$$x_2^{(0,1)} = |\lambda_2| + (|\lambda_4| + 2|\lambda_7|)\,, \tag{7.21b}$$

$$x_3^{(0,1)} = x_4^{(0,1)} = |\lambda_3| + (|\lambda_5| + |\lambda_6| + |\lambda_7|)\,. \tag{7.21c}$$

For $X_{(1,1)}$, we have:

$$x_1^{(1,1)} = |\lambda_1| + (|\lambda_5| + \sqrt{2}|\lambda_6|)\,, \tag{7.22a}$$

$$x_2^{(1,1)} = |\lambda_2| + (|\lambda_5| + \sqrt{2}|\lambda_7|)\,, \tag{7.22b}$$

$$x_3^{(1,1)} = |\lambda_3 + \lambda_4| + \sqrt{2}(|\lambda_6| + |\lambda_7|)\,. \tag{7.22c}$$

Finally, $X_{(1,0)}$, we have:

$$x_1^{(1,0)} = |\lambda_3 - \lambda_4|\,. \tag{7.23}$$

In examining these conditions, the leading coefficient of 3 in the first set suggests that the $x_i^{(0,0)}$ corresponding to $X_{(0,0)}$ will generically be larger than those corresponding to $X_{(0,1)}$, $X_{(1,0)}$, and $X_{(1,1)}$; a numerical check confirms this intuition. Thus the sufficient condition for perturbative unitarity simplifies slightly to

$$\max\big(x_i^{(0,0)}\big) < 8\pi\,. \tag{7.24}$$

One may alternatively employ the bound arising from the Frobenius norm, as discussed in Section 7.1.1. Taking the dominant $X_{(0,0)}$ matrix, one finds the condition:

$$\sqrt{9(\lambda_1^2 + \lambda_2^2) + 10(\lambda_3^2 + \lambda_4^2) + 16\lambda_3\lambda_4 + 18(|\lambda_5|^2 + 2|\lambda_6|^2 + 2|\lambda_7|^2)} \leq 8\pi \tag{7.25}$$

The dependence here on the signs of the λ_i is similar to the dependence seen in the Gershgorin disk conditions: the bound is not sensitive to the signs of any λ_i except for the relative sign between λ_3 and λ_4.

7.2.4 Numerical comparison

In order to compare the various bounds derived in this section, in Fig. 7.2 we plot the number of points which pass the exact, sufficient, and necessary conditions for different values of λ_{max}. For each λ_{max}, we consider 10,000 randomly-drawn values for the λ_i within the range $|\lambda_i| < \lambda_{max}$. For the necessary conditions, the results are derived from the combination of all possible 2×2 (3×3) sub-matrices along the diagonal for the $D_{2(3)}$ bound. We enforce the minimal bounded from below condition $\lambda_{1,2} > 0$, which has been derived e.g. in Ref. [37]. We find that the necessary $D_3(8\pi\mathbb{1} - X_{(0,0)})$ condition lies very close to the exact condition and is effective at ruling out parameter sets which fail perturbative unitarity, while for $\lambda_{max} \lesssim \pi$ all tested points satisfy perturbative unitarity.

7.3 Boundedness from below

Next, we seek to determine the conditions on the parameters such that the potential of the general 2HDM is bounded from below (BFB). For this, it is necessary to ensure that the quartic part of the potential does not acquire negative values. If negative values were present, one could easily find indefinite negative values of the potential by rescaling all fields to infinity in the same direction as the one in which the negative value was found. We remark that analytic expressions have been formulated previously in Ref. [261], though for the case of explicit $\mathcal{CP}$ conservation. We will make no such assumption. There are also previous analyses of the BFB condition using the eigenvalues of a 4×4 matrix [259]; however, these analyses do not lead to analytical expressions, and we will follow an alternative approach.

We begin by reparameterizing the potential via $\Phi_1^\dagger\Phi_1 = \frac{1}{2}h_1^2$, $\Phi_2^\dagger\Phi_2 = \frac{1}{2}h_2^2$, $\Phi_1^\dagger\Phi_2 =$

$\frac{1}{2}h_1 h_2 \rho e^{i\eta}$, with $\rho \in [0,1]$. Moreover, we decompose the complex couplings λ_5, λ_6, λ_7 into real and imaginary parts as: $\lambda_i e^{i\eta} + \lambda_i^* e^{-i\eta} = 2\mathrm{Re}[\lambda_i]\cos\eta - 2\mathrm{Im}[\lambda_i]\sin\eta$. The quartic part of the potential then becomes:

$$\begin{aligned} V_{\text{quartic}} = \frac{1}{4}\bigg\{ & \frac{\lambda_1}{2}h_1^4 + \frac{\lambda_2}{2}h_2^4 + \big[\lambda_3 + \big(\lambda_4 + \mathrm{Re}[\lambda_5]\cos 2\eta - \mathrm{Im}[\lambda_5]\sin 2\eta\big)\rho^2\big] h_1^2 h_2^2 \\ & + 2\big(\mathrm{Re}[\lambda_6]\cos\eta - \mathrm{Im}[\lambda_6]\sin\eta\big)\rho\, h_1^3 h_2 \\ & + 2\big(\mathrm{Re}[\lambda_7]\cos\eta - \mathrm{Im}[\lambda_7]\sin\eta\big)\rho\, h_1 h_2^3 \bigg\}. \end{aligned} \tag{7.26}$$

We can then cast V_{quartic} into the form

$$V_{\text{quartic}} = \frac{1}{4}h_2^4 \left[a\left(\frac{h_1}{h_2}\right)^4 + b\left(\frac{h_1}{h_2}\right)^3 + c\left(\frac{h_1}{h_2}\right)^2 + d\left(\frac{h_1}{h_2}\right) + e \right], \tag{7.27}$$

with

$$a = \frac{\lambda_1}{2}, \quad e = \frac{\lambda_2}{2}, \tag{7.28a}$$

$$b = 2\big(\mathrm{Re}[\lambda_6]\cos\eta - \mathrm{Im}[\lambda_6]\sin\eta\big)\rho, \tag{7.28b}$$

$$c = \Big[\lambda_3 + \big(\lambda_4 + \mathrm{Re}[\lambda_5]\cos 2\eta - \mathrm{Im}[\lambda_5]\sin 2\eta\big)\rho^2\Big], \tag{7.28c}$$

$$d = 2\big(\mathrm{Re}[\lambda_7]\cos\eta - \mathrm{Im}[\lambda_7]\sin\eta\big)\rho. \tag{7.28d}$$

Clearly $a > 0$ and $e > 0$ has to be fulfilled as a minimum condition for BFB. We can then divide out by $e\, h_2^4$ and define the simplified polynomial:

$$f(x) = x^4 + \alpha x^3 + \beta x^2 + \gamma x + 1, \tag{7.29}$$

with $x = \frac{a^{1/4}}{e^{1/4}}\frac{h_1}{h_2}$ and:

$$\alpha = b a^{-3/4} e^{-1/4}, \quad \beta = c a^{-1/2} e^{-1/2}, \quad \gamma = d a^{-1/4} e^{-3/4}. \tag{7.30}$$

We then define the following quantities:

$$\Delta = 4[\beta^2 - 3\alpha\gamma + 12]^3 - [72\beta + 9\alpha\beta\gamma - 2\beta^3 - 27\alpha^2 - 27\gamma^2]^2\,, \tag{7.31a}$$

$$\chi_1 = (\alpha-\gamma)^2 - 16(\alpha+\beta+\gamma+2)\,, \tag{7.31b}$$

$$\chi_2 = (\alpha-\gamma)^2 - \frac{4(\beta+2)}{\sqrt{\beta-2}}\left(\alpha+\gamma+4\sqrt{\beta-2}\right)\,. \tag{7.31c}$$

The positivity of V_{quartic} is ensured if and only if one of the following conditions holds [266]:

$$\begin{aligned}
&(1)\ \ \beta < -2 \text{ and } \Delta \leq 0 \text{ and } \alpha+\gamma > 0\,,\\
&(2)\ \ -2 \leq \beta \leq 6 \text{ and } \Delta \leq 0 \text{ and } \alpha+\gamma > 0\,,\\
&(3)\ \ -2 \leq \beta \leq 6 \text{ and } \Delta \geq 0 \text{ and } \chi_1 \leq 0\,,\\
&(4)\ \ \beta > 6 \text{ and } \Delta \leq 0 \text{ and } \alpha+\gamma > 0\,,\\
&(5)\ \ \beta > 6 \text{ and } \alpha > 0 \text{ and } \gamma > 0\,,\\
&(6)\ \ \beta > 6 \text{ and } \Delta \geq 0 \text{ and } \chi_2 \leq 0\,.
\end{aligned} \tag{7.32}$$

If any of these conditions is true for a given set of input parameters $\lambda_{1\ldots7}$ and for all possible values of $\rho \in [0,1]$, $\eta \in [0,2\pi)$, then the potential is BFB.

Note that under the transformation $\eta \to \eta + \pi$, both α and γ are anti-symmetric ($\alpha \to -\alpha$ and $\gamma \to -\gamma$). This in turn implies that conditions (1), (2), (4), and (5) are always violated for some value of η, and therefore can never guarantee the positivity of V_{quartic}. Consequently, we are left with only two conditions under which the potential is BFB:

$$\text{The potential is BFB if and only if: } \Delta \geq 0 \text{ and } \begin{cases} -2 \leq \beta \leq 6 \text{ and } \chi_1 \leq 0\,,\text{or} \\ \beta > 6 \text{ and } \chi_2 \leq 0\,. \end{cases} \tag{7.33}$$

Note that upon setting $\lambda_6 = \lambda_7 = 0$, and after extremizing with respect to η, Eq. (7.33) becomes

$$\beta + 2 \geq 0 \;\Rightarrow\; \lambda_3 + \rho^2(\lambda_4 - |\lambda_5|) \geq -\sqrt{\lambda_1\lambda_2}\,. \tag{7.34}$$

This is a monotonic function of ρ, and hence the strongest constraints are derived for either $\rho = 1$ or $\rho = 0$, namely

$$\lambda_3 + \lambda_4 - |\lambda_5| \geq -\sqrt{\lambda_1\lambda_2}\,, \quad \text{and} \tag{7.35}$$

$$\lambda_3 \geq -\sqrt{\lambda_1\lambda_2}\,, \tag{7.36}$$

These conditions reproduce the well-known conditions for BFB in the $\mathbb{Z}_2$-symmetric 2HDM [37]. Let us also stress that, for $\rho = 0$, Eq. (7.33) leads to Eq. (7.36) independently of the value of the other quartic couplings and hence this equation is a necessary condition for the potential stability even in the generic 2HDM case.

7.3.1 Necessary conditions for boundedness from below

The two options of Eq. (7.33) present a necessary and sufficient condition for BFB. In order to implement this bound, one should scan over all possible values of ρ and η, which can be computationally expensive for large parameter spaces. Thus we present here two simplified necessary (though not sufficient) conditions which can be used to quickly rule out invalid parameter sets and speed up scans.

We can first derive generalized versions of the existing literature bounds [37] by setting $x = 1$ and taking $\rho = 1$ and $\eta = \frac{n\pi}{4}$, with $n = \{0, ..., 7\}$, in Eqs. (7.26) and (7.29). Applying this procedure to Eq. (7.26) leads to the following conditions:

$$\frac{\lambda_1+\lambda_2}{2}+\lambda_3+\lambda_4+\lambda_5^R-2|\lambda_6^R+\lambda_7^R|>0\,, \tag{7.37a}$$

$$\frac{\lambda_1+\lambda_2}{2}+\lambda_3+\lambda_4-\lambda_5^R-2|\lambda_6^I+\lambda_7^I|>0\,, \tag{7.37b}$$

$$\frac{\lambda_1+\lambda_2}{2}+\lambda_3+\lambda_4+\lambda_5^I-\sqrt{2}\left|(\lambda_6^R+\lambda_7^R)+(\lambda_6^I+\lambda_7^I)\right|>0\,, \tag{7.37c}$$

$$\frac{\lambda_1+\lambda_2}{2}+\lambda_3+\lambda_4-\lambda_5^I-\sqrt{2}\left|(\lambda_6^R+\lambda_7^R)-(\lambda_6^I+\lambda_7^I)\right|>0\,, \tag{7.37d}$$

while applying the same procedure to Eq. (7.29) leads to the conditions:

$$\sqrt{\lambda_1\lambda_2}+\lambda_3+\lambda_4+\lambda_5^R-2\left|\tilde\lambda_6^R+\tilde\lambda_7^R\right|>0\,, \tag{7.38a}$$

$$\sqrt{\lambda_1\lambda_2}+\lambda_3+\lambda_4-\lambda_5^R-2\left|\tilde\lambda_6^I+\tilde\lambda_7^I\right|>0\,, \tag{7.38b}$$

$$\sqrt{\lambda_1\lambda_2}+\lambda_3+\lambda_4+\lambda_5^I-\sqrt{2}\left|(\tilde\lambda_6^R+\tilde\lambda_7^R)+(\tilde\lambda_6^I+\tilde\lambda_7^I)\right|>0\,, \tag{7.38c}$$

$$\sqrt{\lambda_1\lambda_2}+\lambda_3+\lambda_4-\lambda_5^I-\sqrt{2}\left|(\tilde\lambda_6^R+\tilde\lambda_7^R)-(\tilde\lambda_6^I+\tilde\lambda_7^I)\right|>0\,. \tag{7.38d}$$

Note that we have combined the $\eta, \eta+\pi$ conditions in each set to obtain four conditions instead of eight.

Alternatively, we can collapse the two conditions of Eq. (7.33) into a single necessary condition as follows. Consider the two different branches with $\chi_{1,2}<0$. Under the transformation $\eta \to \eta+\pi$, $\chi_1 \leq 0$ produces two conditions that must be satisfied simultaneously: $(\alpha-\gamma)^2-16(\alpha+\beta+\gamma+2)\leq 0$ and $(\alpha-\gamma)^2-16(-\alpha+\beta-\gamma+2)\leq 0$. We can add these together to obtain the simplified condition: $(\alpha-\gamma)^2\leq 16(\beta+2)$. Similarly, demanding that $\chi_2\leq 0$ for both η and $\eta+\pi$ gives us the simplified condition $(\alpha-\gamma)^2\leq 16(\beta+2)$. So, we see that demanding $\chi_1\leq 0$ and $\chi_2\leq 0$ are equivalent, and both translate to the constraint:

$$\chi_1\leq 0\,,\chi_2\leq 0 \;\Rightarrow\; (\alpha-\gamma)^2\leq 16(\beta+2)\,. \tag{7.39}$$

In this way, the condition for the potential to be BFB can be reduced to the form:

$$\Delta \geq 0 \text{ and } \beta \geq -2 \text{ and } (\alpha-\gamma)^2 \leq 16(\beta+2)\,. \tag{7.40}$$

Note that both $\beta \geq -2$ and $(\alpha-\gamma)^2 \leq 16(\beta+2)$ restrict β, but that the latter will always be a stronger condition since $(\alpha-\gamma)^2 \geq 0$. Then this necessary but not sufficient BFB condition simplifies further to

$$\Delta \geq 0 \text{ and } \beta \geq \frac{1}{16}(\alpha-\gamma)^2 - 2\,. \tag{7.41}$$

This condition still depends on ρ and η. Without loss of generality, we set[2] $\rho = 1$. As for η, we need to find the value which extremizes the expression for each condition. Take for instance the latter condition of Eq. (7.41) and define

$$f(\eta) \equiv \beta - \frac{1}{16}(\alpha-\gamma)^2 + 2 \geq 0\,. \tag{7.42}$$

Using the definitions of Eqs. (7.28) and (7.31), we can recast everything in terms of $\cos 2\eta$ and $\sin 2\eta$ such that $f(\eta)$ only depends on these quantities. We can then easily determine the extremal value of η_{min} which gives the minimal f_{min}. After some algebra, the positivity condition $f_{\text{min}} \geq 0$ reads:

$$2(\lambda_1\lambda_2 + \sqrt{\lambda_1\lambda_2}(\lambda_3+\lambda_4)) - \frac{1}{2}\left|\tilde{\lambda}_6 - \tilde{\lambda}_7\right|^2 - \left|2\sqrt{\lambda_1\lambda_2}\,\lambda_5 - \frac{1}{2}(\tilde{\lambda}_6 - \tilde{\lambda}_7)^2\right| \geq 0\,, \tag{7.43}$$

where we have defined the rescaled couplings:

$$\tilde{\lambda}_6 \equiv \left(\frac{\lambda_2}{\lambda_1}\right)^{1/4}\lambda_6\,,\;\; \tilde{\lambda}_7 \equiv \left(\frac{\lambda_1}{\lambda_2}\right)^{1/4}\lambda_7\,. \tag{7.44}$$

---

[2] This gives us one necessary condition. We could obtain others by choosing $\rho < 1$, but these tend to be less constraining in most cases.

Eqs. (7.37), (7.38), and (7.43) present simplified necessary conditions for BFB and are the main result of this section.

7.3.2 Sufficient conditions for boundedness from below

It is also useful to have simplified sufficient conditions which allow one to quickly determine if the potential is BFB for a given parameter set. Consider the top branch of Eq. (7.33)—i.e. $\Delta \geq 0$ and $-2 \leq \beta \leq 6$ and $\chi_1 \leq 0$. One can show that a stronger condition (which will lead to a sufficient condition) is $\beta \leq 6$ *and* $\alpha + \frac{1}{2}(\beta+2) > 0$ and $\gamma + \frac{1}{2}(\beta+2) > 0$. To see this, note that $\alpha = -\frac{1}{2}(\beta+2)$ and $\gamma = -\frac{1}{2}(\beta+2)$ are the directions along which $\Delta = 0$. In order to satisfy the $\chi_1 \leq 0$ condition, relevant for $\beta \leq 6$, we must have $\alpha + \frac{1}{2}(\beta+2) \geq 0$ and $\gamma + \frac{1}{2}(\beta+2) \geq 0$. So long as $\beta \geq -2$, these conditions combined will always yield positive Δ. Then Eq. (7.45) is a sufficient condition that follows from the top branch of Eq. (7.33).

In terms of the λ's, this translates to the sufficient condition:

$$\begin{aligned}
&3\sqrt{\lambda_1\lambda_2} - (\lambda_3 + |\lambda_4| + |\lambda_5|) \geq 0\,, \\
&\text{and } \sqrt{\lambda_1\lambda_2} + \lambda_3 - (|\lambda_4| + |\lambda_5| + 4|\tilde{\lambda}_6|) > 0\,, \\
&\text{and } \sqrt{\lambda_1\lambda_2} + \lambda_3 - (|\lambda_4| + |\lambda_5| + 4|\tilde{\lambda}_7|) > 0\,.
\end{aligned} \tag{7.45}$$

Now consider the bottom branch of Eq. (7.33)—i.e. $\Delta \geq 0$ *and* $\beta > 6$ *and* $\chi_2 \leq 0$. To arrive at an analytic sufficient condition, consider the stronger bound $\beta > 6$ *and* $\alpha + 2\sqrt{\beta - 2} > 0$ *and* $\gamma + 2\sqrt{\beta-2} > 0$. In terms of the potential parameters, this condition reads:

$$\begin{aligned}
&\lambda_3 - (3\sqrt{\lambda_1\lambda_2} + |\lambda_4| + |\lambda_5|) \geq 0\,, \\
&\text{and } \sqrt{\lambda_3 - (\sqrt{\lambda_1\lambda_2} + |\lambda_4| + |\lambda_5|)} - \frac{\sqrt{2}}{(\lambda_1\lambda_2)^{1/4}}|\tilde{\lambda}_6| > 0\,, \\
&\text{and } \sqrt{\lambda_3 - (\sqrt{\lambda_1\lambda_2} + |\lambda_4| + |\lambda_5|)} - \frac{\sqrt{2}}{(\lambda_1\lambda_2)^{1/4}}|\tilde{\lambda}_7| > 0\,.
\end{aligned} \tag{7.46}$$

Eqs. (7.45) and (7.46) are the main result of this section.

7.3.3 Numerical analysis

To compare the performance of our analytic conditions with the numerical BFB condition, we perform a scan over 10,000 randomly chosen points in the 7-dimensional parameter space of $\{\lambda_1, ...\lambda_7\}$. We take as allowed ranges $\lambda_{1,2} \in [0, 2\pi]$ and $|\lambda_{3,4,5,6,7}| \leq \frac{\pi}{2}$, with $\lambda_{5,6,7}$ complex, as this choice yields about half of the points BFB. Fig. 7.3 shows the number of points which pass the numerical condition Eq. (7.33) as well as the number which pass the combination of our necessary conditions Eqs. (7.37), (7.38), and (7.43) and the number which pass the combination of our sufficient conditions Eqs. (7.45) and (7.46). While we display in the figure the result of combining all necessary conditions derived in Section 7.3.1, we note that Eq. (7.38) provides the strongest necessary condition, with the combination of all conditions improving the results by a few percent.

We see that our necessary conditions are very effective at eliminating points which are not BFB, with only approximately 51% of points passing this condition, as compared with the 45% of points which actually satisfy BFB. Meanwhile, our analytic sufficient conditions guarantee approximately 11% of points are BFB. Of these points, essentially all are obtained from Eq. (7.45), which was derived from the upper branch of Eq. (7.33). The second condition Eq. (7.46), derived from the lower branch, is too strong and admits almost no points, which also reflects the fact that most of the points sampled fall within the regime of the first branch.

An examination of the analytical expressions indicates that the quantity $\sqrt{\lambda_1 \lambda_2}$ may play an important role in the determination of BFB. To examine whether the analytical form of our bounds indeed captures the primary underlying behavior of BFB with respect to the λ_i, we plot a histogram in $\sqrt{\lambda_1 \lambda_2}$ of the fraction of tested points which pass the numerical, necessary, and sufficient bounds of Eqs. (7.33), (7.37), (7.38), (7.43) and (7.45), respectively. As in Fig. 7.3, we choose parameters in the range $\lambda_{1,2} \in [0, 2\pi]$ and $|\lambda_{3,4,5,6,7}| \leq \pi/2$ with

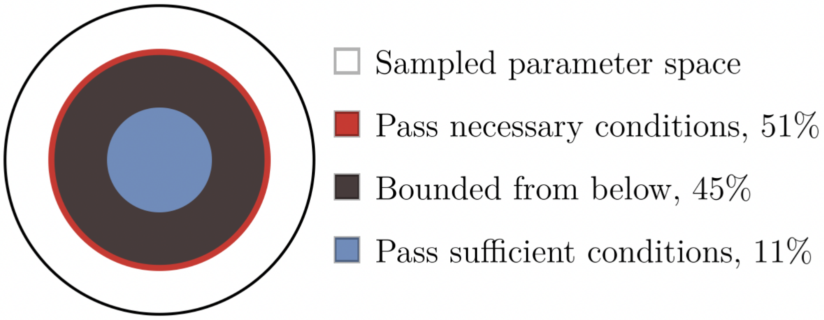

Figure 7.3: The white circle represents 10,000 randomly chosen points in the 7-dimensional parameter space of couplings $\{\lambda_1, ...\lambda_7\}$. We take as priors $\lambda_{1,2} \in [0, 2\pi]$ and $|\lambda_{3,4,5,6,7}| \leq \frac{\pi}{2}$, with $\lambda_{5,6,7}$ allowed to be complex. The red circle encompasses the points which pass our analytic necessary conditions of Eqs. (7.37), (7.38), and (7.43); the black circle contains the points which pass the necessary and sufficient BFB condition of Eq. 7.33; and the innermost blue circle contains the points which pass our sufficient condition of Eq. 7.45.

$\lambda_{5,6,7}$ allowed to be complex. The resulting figure is shown in Fig. 7.4. As can be seen from the figure, more points pass the BFB condition for higher $\sqrt{\lambda_1\lambda_2}$, as indicated by the forms of the necessary and sufficient conditions. We find that both the necessary and sufficient bounds follow the same behavior as the exact numerical results, indicating that the analytic bounds do indeed capture the relevant behavior in $\sqrt{\lambda_1\lambda_2}$.

Finally, we note that within the existing literature, some simplified analytic BFB constraints for the most general 2HDM (i.e. involving $\lambda_{6,7} \neq 0$) do exist. For example, the authors of Ref. [37] find as a necessary condition:

$$\frac{1}{2}(\lambda_1 + \lambda_2) + \lambda_3 + \lambda_4 + \lambda_5 - 2|\lambda_6 + \lambda_7| > 0\,. \tag{7.47}$$

This expression, that agrees with Eq. (7.37) in the appropriate limit, is derived by assuming that the Higgs doublets are aligned in field space, and is limited to the case that all λ_i are taken to be real. Restricting ourselves to this regime, we find that the literature expression excludes approximately 17% of points while ours excludes approximately 49%, making our condition the stronger of the two by a large margin.

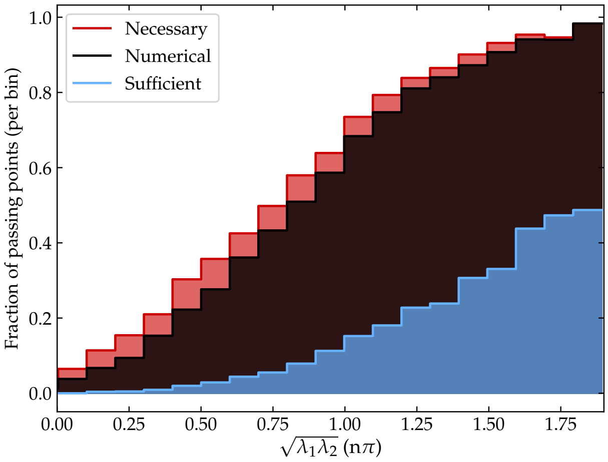

Figure 7.4: Histogram of $\sqrt{\lambda_1\lambda_2}$ displaying the fraction of tested points per bin which pass the necessary conditions Eqs. (7.43, 7.37, 7.38) (red), numerical test Eq. (7.33) (black), and sufficient condition Eq. (7.45) (blue). As in Fig. 7.3, we take as priors $\lambda_{1,2} \in [0, 2\pi]$ and $|\lambda_{3,4,5,6,7}| \in [0, \frac{\pi}{2}]$, with $\lambda_{5,6,7}$ allowed to be complex.

7.4 Vacuum stability

We can also place constraints on the allowed 2HDM potential parameters by demanding the existence of a stable neutral vacuum. Strictly speaking, this not a necessary requirement: it is only necessary that the vacuum is meta-stable, with a lifetime longer than the age of the Universe. Here, we just derive the conditions for absolute stability, more precisely the absence of deeper minima at scales of the order of the TeV scale.

The discriminant D introduced in Ref. [267, 268] offers a prescription for distinguishing the nature of a solution obtained by extremizing the potential. We summarize the method here, beginning by writing the potential as:

$$V = -M_\mu \mathsf{r}^\mu + \frac{1}{2}\Lambda_{\mu\nu}\mathsf{r}^\mu \mathsf{r}^\nu - \frac{1}{2}\zeta \mathsf{r}^\mu \mathsf{r}_\mu \,, \tag{7.48}$$

where M_μ encodes the mass terms:

$$M_\mu = \left(-\tfrac{1}{2}(m_{11}^2 + m_{22}^2), \quad (m_{12}^2)^R, \quad -(m_{12}^2)^I, \quad -\tfrac{1}{2}(m_{11}^2 - m_{22}^2)\right)\,, \tag{7.49}$$

r^μ is a vector of field bilinears:

$$\mathsf{r}^\mu = \left(|\Phi_1|^2 + |\Phi_2|^2, \ \ 2\mathrm{Re}[\Phi_1^\dagger \Phi_2], \ \ 2\mathrm{Im}[\Phi_1^\dagger \Phi_2], \ \ |\Phi_1|^2 - |\Phi_2|^2 \right) , \tag{7.50}$$

and $\Lambda_{\mu\nu}$ encodes the quartic terms:

$$\Lambda_{\mu\nu} = \frac{1}{2} \begin{pmatrix} \frac{1}{2}(\lambda_1 + \lambda_2) + \lambda_3 & \lambda_6^R + \lambda_7^R & -(\lambda_6^I + \lambda_7^I) & \frac{1}{2}(\lambda_1 - \lambda_2) \\ (\lambda_6^R + \lambda_7^R) & (\lambda_4 + \lambda_5^R) & -\lambda_5^I & \lambda_6^R - \lambda_7^R \\ -(\lambda_6^I + \lambda_7^I) & -\lambda_5^I & \lambda_4 - \lambda_5^R & -(\lambda_6^I - \lambda_7^I) \\ \frac{1}{2}(\lambda_1 - \lambda_2) & \lambda_6^R - \lambda_7^R & -(\lambda_6^I - \lambda_7^I) & \frac{1}{2}(\lambda_1 + \lambda_2) - \lambda_3 \end{pmatrix} . \tag{7.51}$$

The last term in Eq. (7.48) is a Lagrange multiplier we have introduced to enforce the condition $\mathsf{r}^\mu \mathsf{r}_\mu = 0$, which ensures we are in a charge-neutral minimum; we enforce this condition since charge-breaking and normal minima cannot coexist in the 2HDM (see [255, 267] for more details). In the above equations, indices are raised and lowered using a Minkowski metric.

Provided the matrix $\Lambda_{\mu\nu}$, which contains the coefficients of the quartic terms in the potential, is positive definite, corresponding to a potential which is BFB, it can be brought into a diagonal form by an $SO(1,3)$ transformation:

$$\Lambda_{\mu\nu}^{\mathrm{diag}} = \begin{pmatrix} \Lambda_0 & 0 & 0 & 0 \\ 0 & -\Lambda_1 & 0 & 0 \\ 0 & 0 & -\Lambda_2 & 0 \\ 0 & 0 & 0 & -\Lambda_3 \end{pmatrix} , \tag{7.52}$$

with Λ_0 the "timelike" eigenvalue and Λ_i "spacelike". Let us define the "signature matrix" S

as $S \equiv \Lambda_{\mu\nu} - \zeta g_{\mu\nu}$. In diagonal form, it looks like:

$$S = \begin{pmatrix} \Lambda_0 - \zeta & 0 & 0 & 0 \\ 0 & \zeta - \Lambda_1 & 0 & 0 \\ 0 & 0 & \zeta - \Lambda_2 & 0 \\ 0 & 0 & 0 & \zeta - \Lambda_3 \end{pmatrix} . \tag{7.53}$$

The discriminant is generically given by the determinant of the signature matrix:

$$D = \det S \, . \tag{7.54}$$

By using the diagonal form above, we can write this as:

$$D = (\Lambda_0 - \zeta)(\zeta - \Lambda_1)(\zeta - \Lambda_2)(\zeta - \Lambda_3) \, . \tag{7.55}$$

We finally come to the vacuum stability condition. Suppose we have already verified that our potential is BFB and calculated the discriminant, time-like eigenvalue Λ_0, and Lagrange multiplier ζ.

$$\text{We are in a global minimum if and only if : } \begin{cases} D > 0 \, , \text{ or} \\ D < 0 \ \text{ and } \ \zeta > \Lambda_0 \, . \end{cases} \tag{7.56}$$

For our purposes, it is more useful to work with the “Euclideanized" version of $\Lambda_{\mu\nu}$

obtained by lowering one of the indices with the Minkowski metric, $\Lambda_E \equiv \Lambda^\mu_\nu$. Explicitly:

$$\Lambda_E = \frac{1}{2}\begin{pmatrix} \frac{1}{2}(\lambda_1+\lambda_2)+\lambda_3 & \lambda_6^R+\lambda_7^R & -(\lambda_6^I+\lambda_7^I) & \frac{1}{2}(\lambda_1-\lambda_2) \\ -(\lambda_6^R+\lambda_7^R) & -(\lambda_4+\lambda_5^R) & \lambda_5^I & -(\lambda_6^R-\lambda_7^R) \\ \lambda_6^I+\lambda_7^I & \lambda_5^I & -(\lambda_4-\lambda_5^R) & \lambda_6^I-\lambda_7^I \\ -\frac{1}{2}(\lambda_1-\lambda_2) & -(\lambda_6^R-\lambda_7^R) & \lambda_6^I-\lambda_7^I & -\frac{1}{2}(\lambda_1+\lambda_2)+\lambda_3 \end{pmatrix} . \qquad (7.57)$$

In terms of Λ_E, the discriminant is:

$$D = -\det[\Lambda_E - \mathbb{1}\zeta] . \qquad (7.58)$$

The other quantity necessary for formulating the discriminant is the Lagrange multiplier ζ. This may be obtained by looking at any component of the minimization condition:

$$\Lambda^\mu_\nu r^\nu - M^\mu = \zeta r^\mu . \qquad (7.59)$$

We parameterize the vacuum expectation values (vevs) of the doublets as:

$$\langle\Phi_1\rangle = \frac{1}{\sqrt{2}}\begin{pmatrix} 0 \\ v_1 \end{pmatrix} , \ \langle\Phi_2\rangle = \frac{1}{\sqrt{2}}\begin{pmatrix} 0 \\ v_2 e^{i\eta} \end{pmatrix} . \qquad (7.60)$$

Then the expectation value of field bilinears $r^\mu \equiv \langle \mathsf{r}^\mu \rangle$ is:

$$r^\mu = \left(\tfrac{1}{2}(v_1^2+v_2^2), \quad v_1 v_2 \cos\eta, \quad v_1 v_2 \sin\eta, \quad \tfrac{1}{2}(v_1^2-v_2^2) \right) . \qquad (7.61)$$

The expression for ζ is particularly simple if we choose the “1” component. In particular if we take $\eta = 0$, then:

$$\zeta = \frac{(m_{12}^2)^R}{v_1 v_2} - \frac{1}{2}\left(\frac{v_1}{v_2}\lambda_6^R + \frac{v_2}{v_1}\lambda_7^R + (\lambda_4+\lambda_5^R) \right) . \qquad (7.62)$$

Note that this has the interpretation of the charged Higgs mass over the vev v squared,

$$\zeta = \frac{M_{H^\pm}^2}{v^2}\,, \tag{7.63}$$

as first demonstrated in Refs. [259, 260].

If $D > 0$, then the physical minimum is the global one, implying absolute stability. If, instead, $D < 0$, we need to compare the timelike eigenvalue Λ_0 with ζ: we are in a global minimum if $\zeta > \Lambda_0$; otherwise, the minimum is metastable. Provided we have already verified that the potential is BFB, however, there is an even simpler way to assess the nature of the extremum.

As an aside, working at the level of eigenvalues the two options of Eq. (7.56) for an extremum to be the global minimum can actually be collapsed into one. Recall that when the potential is BFB, $\Lambda^{\mu\nu}$ is positive definite and $\Lambda_0 > \Lambda_{1,2,3}$. Then from Eq. (7.55), $D > 0$ necessarily implies that we have the ordering $\Lambda_0 > \zeta > \Lambda_{1,2,3}$. Similarly $D < 0$ and $\zeta > \Lambda_0$ necessarily implies the ordering $\zeta > \Lambda_0 > \Lambda_{1,2,3}$. So we see that the relative ordering of Λ_0 and ζ does not actually matter—all that matters for a potential which has been verified to be BFB is that ζ be larger than the spatial eigenvalues, $\zeta > \Lambda_{1,2,3}$.

7.4.1 Sufficient conditions for stability

Gershgorin bounds

As in Section 7.2.3, we can bound the eigenvalues of Λ_E using the Gershgorin disk theorem in order to derive a sufficient condition for a given vacuum solution to be stable. We first construct the intervals containing the eigenvalues of Λ_E and define the endpoint of each interval as $\Gamma_i \equiv a_{ii} + R_i$, with $R_i = \sum_{j\neq i} |a_{ij}|$:

$$\Gamma_1 = \frac{1}{4}(\lambda_1+\lambda_2) + \frac{\lambda_3}{2} + \frac{1}{2}\left(|\lambda_6^R+\lambda_7^R| + |\lambda_6^I+\lambda_7^I| + \frac{1}{2}|\lambda_1-\lambda_2|\right)\,, \tag{7.64a}$$

$$\Gamma_2 = -\frac{1}{4}(\lambda_1+\lambda_2) + \frac{\lambda_3}{2} + \frac{1}{2}\left(|\lambda_6^R-\lambda_7^R| + |\lambda_6^I-\lambda_7^I| + \frac{1}{2}|\lambda_1-\lambda_2|\right)\,, \tag{7.64b}$$

$$\Gamma_3 = -\frac{1}{2}(\lambda_4+\lambda_5^R) + \frac{1}{2}\Big(|\lambda_5^I| + |\lambda_6^R+\lambda_7^R| + |\lambda_6^R-\lambda_7^R|\Big)\,, \tag{7.64c}$$

$$\Gamma_4 = -\frac{1}{2}(\lambda_4-\lambda_5^R) + \frac{1}{2}\Big(|\lambda_5^I| + |\lambda_6^I+\lambda_7^I| + |\lambda_6^I-\lambda_7^I|\Big)\,. \tag{7.64d}$$

We know that all eigenvalues must be less than the endpoint of the interval extending the furthest in the $+\hat{x}$ direction,

$$\max[\Gamma_i] \geq \Lambda_{0,1,2,3}\,. \tag{7.65}$$

Meanwhile, an extremum will be the global minimum if $\zeta > \Lambda_{1,2,3}$. Thus, it is sufficient to demand:

$$\zeta > \max[\Gamma_i]\,. \tag{7.66}$$

Frobenius bounds

One may also bound the eigenvalues using the Frobenius norm to obtain a single-equation condition. We require the maximum eigenvalue be less than ζ, which gives the constraint:

$$\zeta > \frac{1}{2}\sqrt{\lambda_1^2+\lambda_2^2+2(\lambda_3^2+\lambda_4^2+|\lambda_5|^2)+4(|\lambda_6|^2+|\lambda_7|^2)} \tag{7.67}$$

Note that in this case, the Frobenius bound is insensitive to the signs of the λ_i, while the Gershgorin condition is sensitive to the signs of λ_3, λ_4, and λ_5^R. We thus expect the Gershgorin bound to be the stronger of the two.

Principal minors

In the case of a non-symmetric matrix such as Λ_E, Sylvester's criterion no longer holds and so cannot be applied in a straightforward manner. However, the following statement does hold: if the symmetric part of a matrix M is positive-definite, then the real parts of the eigenvalues of M are positive. This statement does not hold in the other direction, and therefore cannot be used to derive necessary conditions. However, we can apply Sylvester's criterion to the symmetric part of Λ_E to obtain a sufficient condition.

The symmetric part of Λ_E is given by

$$\begin{aligned}\Lambda_E^S &= \frac{1}{2}(\Lambda_E^T + \Lambda_E) \\ &= \frac{1}{2}\begin{pmatrix} \frac{1}{2}(\lambda_1+\lambda_2)+\lambda_3 & 0 & 0 & 0 \\ 0 & -(\lambda_4+\lambda_5^R) & \lambda_5^I & -(\lambda_6^R-\lambda_7^R) \\ 0 & \lambda_5^I & -(\lambda_4-\lambda_5^R) & \lambda_6^I-\lambda_7^I \\ 0 & -(\lambda_6^R-\lambda_7^R) & \lambda_6^I-\lambda_7^I & -\frac{1}{2}(\lambda_1+\lambda_2)+\lambda_3 \end{pmatrix}\end{aligned} \tag{7.68}$$

We require the matrix $\zeta\mathbb{1} - \Lambda_E^S$ to be positive-definite. Since the lower-right 3×3 matrix decouples from the "11" element, we can analyze them separately when considering positive-definiteness. We require the "11" element to be positive, and apply Sylvester's criterion to the lower-right 3×3 submatrix. This gives the following set of conditions:

$$\zeta - \frac{1}{4}(\lambda_1+\lambda_2) - \frac{1}{2}\lambda_3 > 0\,, \tag{7.69a}$$

$$\zeta + \frac{1}{2}\lambda_4 + \frac{1}{2}\lambda_5^R > 0\,, \tag{7.69b}$$

$$\big(\zeta + \frac{1}{2}\lambda_4\big)^2 - \frac{1}{4}|\lambda_5|^2 > 0\,, \tag{7.69c}$$

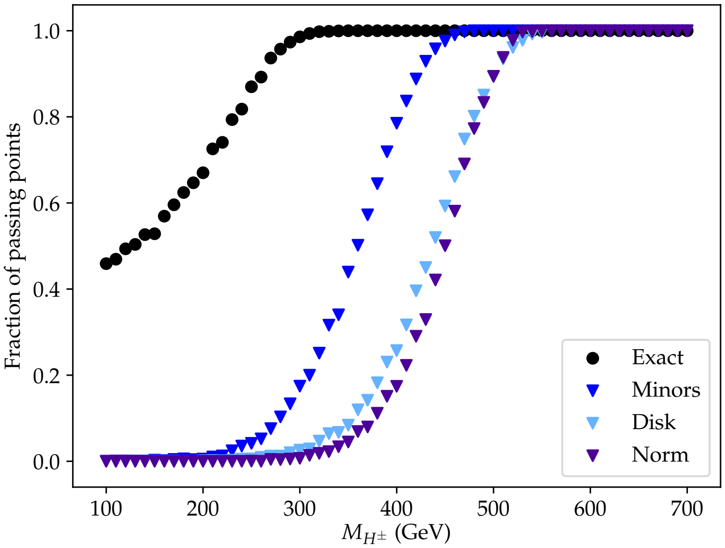

Figure 7.5: Comparison of the fraction of points that pass the exact stability conditions, Eq. (7.56) (black dots), with respect to the fraction passing the three sufficient conditions for vacuum stability: principal minors Eq. (7.69) (blue), Gershgorin disk theorem Eq. (7.66) (light blue), and Frobenius norm Eq. (7.67) (purple). We plot the fraction of points that pass each condition as a function of $M_{H^\pm}$. We take $\lambda_{1,2} \in [0, 2\pi]$ and $|\lambda_{3,4,5,6,7}| \leq \frac{\pi}{2}$, with $\lambda_{5,6,7}$ allowed to be complex, and restrict to examining points which are BFB.

$$\begin{aligned}(4\zeta + \lambda_1 + \lambda_2 - 2\lambda_3)((2\zeta + \lambda_4)^2 - |\lambda_5|^2)\\ + \lambda_5(\lambda_6^* - \lambda_7^*)^2 + \lambda_5^*(\lambda_6 - \lambda_7)^2 - 2(2\zeta + \lambda_4)|\lambda_6 - \lambda_7|^2 > 0\,.\end{aligned} \tag{7.69d}$$

Taken together, the Eqs. (7.69) provide a sufficient condition for vacuum stability.

7.4.2 Numerical comparison

In Fig. 7.5 we plot the performance of the three sufficient conditions for vacuum stability, Eqs. (7.66), (7.67), (7.69), as a function of the charged Higgs mass $M_{H^\pm}$. We compare these results with the fraction that pass the exact stability condition, Eq. (7.56). As in previous sections, we choose the λ_i randomly with $\lambda_{1,2} \in [0, 2\pi]$ and $|\lambda_{3,4,5,6,7}| \leq \frac{\pi}{2}$, with $\lambda_{5,6,7}$ allowed to be complex. The y-axis shows the fraction of tested points which pass the respective stability condition; we restrict to testing points which are BFB, to ensure the validity of the stability conditions implemented in Fig. 7.5. We find that the set of conditions arising from the application of Sylvester's criterion capture the most stable points, while all three bounds capture more stable points when the λ_i are small compared to the ratio $M_{H^\pm}^2/v^2$.

7.4.3 Vacuum stability in the Higgs basis

It is particularly interesting to study vacuum stability in the Higgs basis, in which only one of the doublets possesses a vev (see 3.1.4 for a review of the conversion to the Higgs basis as well as our conventions). One advantage of this basis is that the potential parameters are closely related to physical observables: for example, Z_1 controls the trilinear coupling of three SM-like Higgs bosons hhh, Z_6 controls the trilinear coupling of two SM-like and one non-SM-like $\mathcal{CP}$-even Higgs bosons hhH, etc. (see e.g. [135] for an exhaustive list of couplings). Since none of the bounds obtained in this article have relied on the choice of basis, they can equally well be applied to Higgs basis parameters. Using the close relationship between the Higgs basis parameters and physical quantities, we here aim at obtaining approximate bounds on the physical observables of the model.

In our notation (choosing $\eta = 0$), the scalar which obtains a vev is denoted by ϕ_1^0. The mass matrix for the neutral scalars $\vec{\phi} = (\phi_1^0, \phi_2^0, a_0)^{\mathrm{T}}$ reads:

$$\mathcal{M}^2 = v^2 \begin{pmatrix} Z_1 & Z_6^R & -Z_6^I \\ Z_6^R & \frac{M_{H^\pm}^2}{v^2} + \frac{1}{2}(Z_4 + Z_5^R) & -\frac{1}{2}Z_5^I \\ -Z_6^I & -\frac{1}{2}Z_5^I & \frac{M_{H^\pm}^2}{v^2} + \frac{1}{2}(Z_4 - Z_5^R) \end{pmatrix}, \tag{7.70}$$

where $M_{H^\pm}^2$ is the charged Higgs mass:

$$M_{H^\pm}^2 = M_{22}^2 + \frac{1}{2}Z_3 v^2 \,. \tag{7.71}$$

We will restrict ourselves to the alignment limit, which is the limit in which ϕ_1^0 is aligned with the 125 GeV mass eigenstate. In this case, the 125 GeV Higgs couples to the electroweak gauge bosons and all fermions with SM strength, and the alignment limit is therefore phenomenologically well-motivated by precision Higgs results from the LHC [53, 55].

Examining the above matrix, it appears that there are two ways in which one may obtain alignment. The first option, known as the decoupling limit, corresponds to taking $M_{H^\pm}^2 + \frac{1}{2}(Z_4 \pm Z_5^R)v^2 \gg Z_1 v^2$. Under this limit, the heavy mass eigenstates h_2 and h_3 and the heavy charged Higgs $H^\pm$ decouple from the light mass eigenstate, leaving h_1 aligned with ϕ_1^0. More interesting from a phenomenological standpoint is the approximate *alignment without decoupling* limit, as it leaves the non-standard Higgs states potentially within collider reach. This corresponds to taking $|Z_6| \ll 1$, for which the mixing between ϕ_1^0 and the other neutral scalars vanishes, leading to the identification of ϕ_1^0 with the mass eigenstate h_1. For the following discussion we will take $|Z_6| \ll 1$ and work in the alignment without decoupling limit.

We define $h_1 \equiv h$ to be the SM-like Higgs boson, which has a mass given by

$$M_h^2 = Z_1 v^2 \,. \tag{7.72}$$

To obtain a physical Higgs mass close to the experimental value of 125 GeV, it is required that we fix $Z_1 \approx 0.25$. The remaining 2×2 mass matrix can be diagonalized to obtain the masses of the remaining scalars h_2 and h_3:

$$M_{h_3,h_2}^2 = M_{H^\pm}^2 + \frac{1}{2}(Z_4 \pm |Z_5|)v^2 \,. \tag{7.73}$$

There are two possibilities for the $\mathcal{CP}$ properties of these states. So long as $Z_5^I \neq 0$, h_2 and h_3 have mixed $\mathcal{CP}$ properties. In the limit of $Z_5^I = 0$, meanwhile, the non-standard Higgs mass matrix becomes diagonal, and we obtain mass eigenstates H and A with definite

$\mathcal{CP}$ character,

$$M^2_{H,A} = M^2_{H^\pm} + \frac{1}{2}(Z_4 \pm Z_5^R)v^2\,. \tag{7.74}$$

The masses of the general mass eigenstates and the states of definite $\mathcal{CP}$ character can be related by

$$\begin{aligned} M_H^2 &= M^2_{h_3,h_2} + \frac{1}{2}(Z_5^R \mp |Z_5|)v^2 \\ M_A^2 &= M^2_{h_3,h_2} - \frac{1}{2}(Z_5^R \pm |Z_5|)v^2. \end{aligned} \tag{7.75}$$

In the following analysis we will make no assumptions about the $\mathcal{CP}$ character of the mass eigenstates, and will work with the generic physical masses M_{h_3,h_2}.

With the above definitions, we can rephrase our sufficient vacuum stability conditions into constraints on physical quantities. We start with the Gershgorin condition of Eq. (7.66). Expressing the Γ's in terms of physical masses, a sufficient condition for vacuum stability becomes:

$$\begin{aligned} &M^2_{h_2} > \frac{1}{2}(|Z_5^I| - Z_5^R - |Z_5|)v^2 + \frac{1}{2}|Z_7^R|v^2 \ \text{ and} \\ &M^2_{h_3} > \frac{1}{2}(|Z_5^I| + Z_5^R + |Z_5|)v^2 + \frac{1}{2}|Z_7^I|v^2 \ \text{ and} \\ &M^2_{H^\pm} > \frac{1}{2}\max[M_h^2,\, Z_2v^2] + \frac{1}{2}(Z_3 + |Z_7^R| + |Z_7^I|)v^2\,. \end{aligned} \tag{7.76}$$

Next, we can recast the Frobenius sufficient condition, Eq. (7.67), in terms of the physical masses; doing so results in the following condition:

$$2M^2_{H^\pm}\big(M^2_{h_2} + M^2_{h_3}\big) - \big(M^4_{H^\pm} + M^4_{h_2} + M^4_{h_3} + \frac{1}{4}M_h^4\big) > \frac{1}{4}(Z_2^2 + 2Z_3^2 + 4|Z_7|^2)v^4\,. \tag{7.77}$$

Finally, Sylvester's criterion provides an additional set of sufficient conditions. A sample set of sufficient conditions for vacuum stability in the alignment limit based on Eq. (7.69) is:

$$\begin{aligned}
&4M_{H^\pm}^2 - M_h^2 > (Z_2 + 2Z_3)v^2, \\
&M_{h_3}^2 > \frac{1}{2}(|Z_5| - Z_5^R), \\
&M_{h_2}^2 M_{h_3}^2 > 0, \\
4M_{h_2}^2 M_{h_3}^2 (4M_{H^\pm}^2 + M_h^2 + Z_2v^2 - 2Z_3v^2) - 2(M_{h_2}^2 + M_{h_3}^2)|Z_7|^2 &+ Z_5 Z_7^{*2} + Z_5^* Z_7^2 > 0\,.
\end{aligned} \tag{7.78}$$

7.5 $\mathcal{CP}$ Violation in the general 2HDM

The bounds we have derived in this work have implications for the allowed values of physical parameters in a given 2HDM. This can be seen in a straightforward way in the previous section, where the conditions for vacuum stability were recast into expressions that restrict the physical masses of the bosonic sector. One particularly interesting question to which our bounds can be applied is that of the amount of $\mathcal{CP}$ violation permitted in the alignment limit. This possibility has largely been neglected in the many previous studies which restrict themselves to the $\mathbb{Z}_2$-symmetric 2HDM. This is understandable since exact alignment implies $\mathcal{CP}$ conservation in the $\mathbb{Z}_2$-symmetric case. When working in the fully general 2HDM, however, it is possible to have $\mathcal{CP}$ violation whilst still keeping the SM-like Higgs boson fully aligned.

To justify this claim, recall that there are four complex parameters in the 2HDM: $\{M_{12}^2, Z_5, Z_6, Z_7\}$. One of these is fixed by the minimization condition $M_{12}^2 = -\frac{1}{2}Z_6 v^2$, leaving just three independent parameters, which we take to be the couplings $\{Z_5, Z_6, Z_7\}$. These complex parameters enter into the three basic $\mathcal{CP}$ violating invariants of the 2HDM scalar sector J_1, J_2, and J_3, which can be thought of as analogous to the Jarlskog invariant J of the SM quark sector. They are worked out explicitly in [36, 104]; the important fact is that they scale as $J_1 \sim \mathrm{Im}[Z_5^* Z_6^2]$, $J_2 \sim \mathrm{Im}[Z_5^* Z_7^2]$, $J_3 \sim \mathrm{Im}[Z_6^* Z_7]$. It is then clear that the condition for the Higgs sector to be $\mathcal{CP}$ invariant is:

$$\mathrm{Im}[Z_5^* Z_6^2] = \mathrm{Im}[Z_5^* Z_7^2] = \mathrm{Im}[Z_6^* Z_7] = 0\,. \tag{7.79}$$

There are two ways in which this can be satisfied [269]: either $Z_5^I = Z_6^R = Z_7^R = 0$ or $Z_5^I = Z_6^I = Z_7^I = 0$. Note that in the limit of exact alignment we have $Z_6 = 0$, so this reduces to demanding either $Z_5^I = Z_7^R = 0$ or $Z_5^I = Z_7^I = 0$.

Meanwhile in the 2HDM with a (softly broken) $\mathbb{Z}_2$ symmetry, the fact that $\lambda_6 = \lambda_7 = 0$ implies the following two relations between the parameters in the Higgs basis (see Eq. (3.24) in the review of 2HDMs) [270, 271]

$$Z_6 + Z_7 = \frac{1}{2}\tan 2\beta (Z_2 - Z_1), \tag{7.80}$$

$$Z_6 - Z_7^* = \frac{1}{\tan 2\beta}(Z_1 + 2Z_6 \cot 2\beta - Z_3 - Z_4 - Z_5). \tag{7.81}$$

It immediately follows that:

$$Z_7^I = -Z_6^I, \tag{7.82}$$

$$Z_5^I = 2\,\frac{1-\tan^2 2\beta}{\tan 2\beta} Z_6^I. \tag{7.83}$$

These conditions imply that in the exact alignment limit (i.e. $Z_6 = 0$), it will necessarily be the case that $Z_5^I = Z_7^I = 0$. Thus, exact alignment directly leads to $\mathcal{CP}$ conservation in the $\mathbb{Z}_2$-symmetric or softly broken $\mathbb{Z}_2$-symmetric 2HDM. This need not be the case in the fully general 2HDM, where the above relations no longer hold. If we allow for a small misalignment (i.e. $|Z_6| \gtrsim 0$), $|Z_5^I|$, which controls the mixing between the H and A bosons (see Eq. (7.70)), can still be large for large $\tan\beta$.

The physical consequences of the difference in the $\mathcal{CP}$ properties in the alignment limit between the (softly broken) $\mathbb{Z}_2$-symmetric and the general 2HDMs are illustrated in Fig. 7.6,

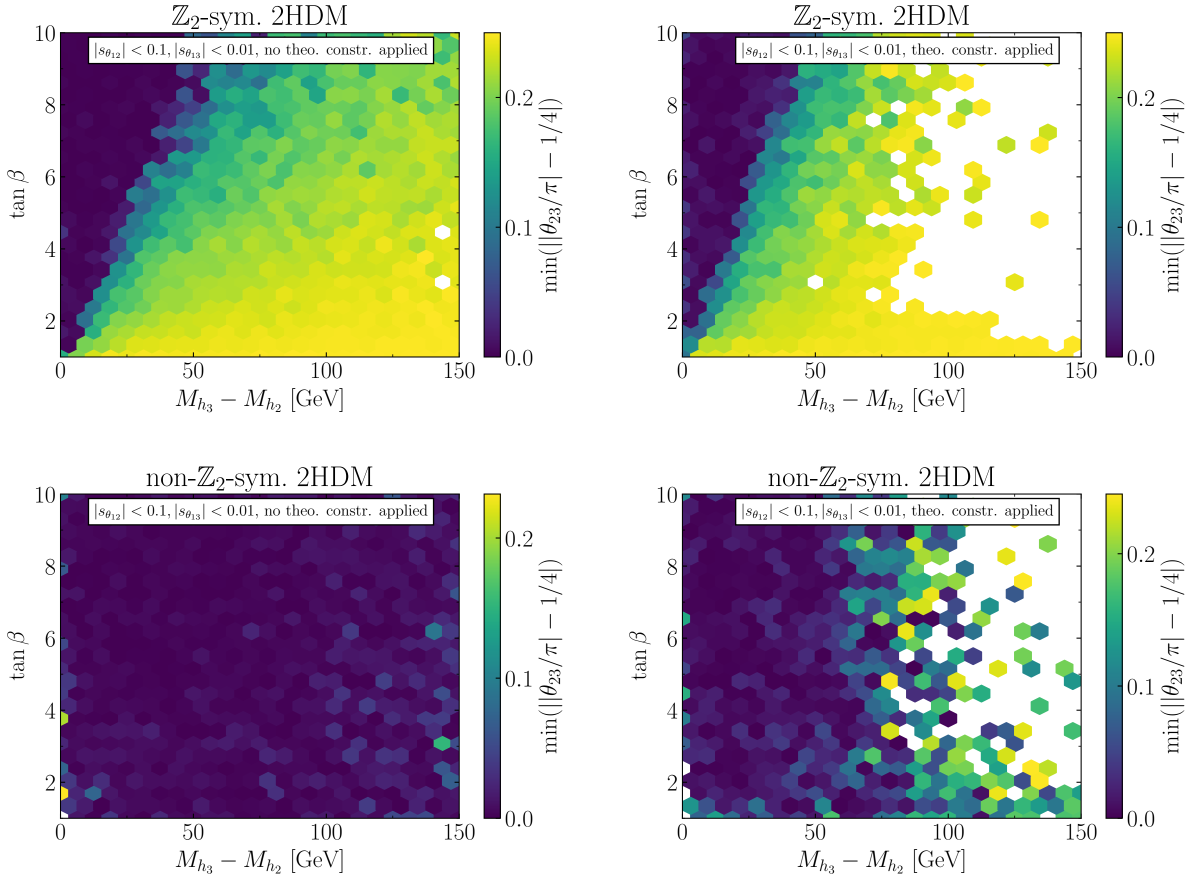

Figure 7.6: *Upper left:* Parameter scan of the 2HDM with a softly broken $\mathbb{Z}_2$ symmetry in the $(M_{h_3} - M_{h_2}, \tan\beta)$ parameter plane with parameter range $\lambda_{1,2} \in [0, 2\pi]$ and $|\lambda_{3,4,5}| \in [0, \pi]$. The conditions $|\sin\theta_{12}| < 0.1$ and $|\sin\theta_{13}| < 0.01$ are imposed. The colour indicates the minimal value of $|\theta_{23}/\pi - 1/4|$ in each hexagonal patch. *Upper right:* Same as upper left, but constraints from perturbative unitary, BFB, and vacuum stability are applied in addition. *Lower left:* Same as upper left, but the scan is performed in the general 2HDM without a (softly broken) $\mathbb{Z}_2$ symmetry ($|\lambda_{6,7}| \in [0, \pi]$). *Lower right:* Same as lower left, but constraints from perturbative unitary, BFB, and vacuum stability are applied in addition.

in which we show the results of several parameter scans. Motivated by Higgs precision [53, 55] and electric dipole moment bounds (see e.g. [272, 273]), we demand a small mixing of the h and the H states and an even smaller mixing of the h and the A states; we impose these constraints on the mixing in an approximate manner by demanding $|\sin\theta_{12}| < 0.1$ and $|\sin\theta_{13}| < 0.01$, where θ_{12} and θ_{13} are the respective mixing angles. The colour code in the figure indicates the minimum value of $|\theta_{23}/\pi - 1/4|$ in each hexagonal patch, where θ_{23} is the mixing angle between the H and A states. This variable is chosen such that the maximal mixing case corresponds to a value of zero. Correspondingly, a dark blue color indicates that a large $\mathcal{CP}$-violating mixing between the H and A states can be realized; a bright yellow color instead signals that no large mixing can be realized.

In the upper left panel of Fig. 7.6 we present a parameter scan of the 2HDM with a softly broken $\mathbb{Z}_2$ symmetry in the $(M_{h_3} - M_{h_2}, \tan\beta)$ parameter plane. We observe that for large $\tan\beta$, a large mixing between the neutral BSM Higgs bosons can be realized if their mass difference is below ~ 70 GeV. Larger mass differences originate from differences between the diagonal terms of the Higgs mass matrix (see Eq. (7.70)), suppressing possible mixing effects induced by the off-diagonal $\frac{1}{2}Z_5^I v^2$ term. For lower $\tan\beta$, the condition $|\sin\theta_{13}| < 0.01$ directly implies that Z_5^I is small (see Eq. (7.83)), resulting in substantial mixing only when the mass difference is close to zero.

In the upper right panel of Fig. 7.6, we again consider a softy broken $\mathbb{Z}_2$ symmetry but additionally impose perturbative unitarity, boundedness-from-below, and vacuum stability constraints following the discussions in the previous Sections. Aside from lowering the maximal possible mass difference between h_3 and h_2, the region in which large mixing between the BSM Higgs bosons can be realized is also reduced.

If we instead investigate the general 2HDM without a (softly broken) $\mathbb{Z}_2$ symmetry (see lower panels of Fig. 7.6), large mixing between the H and A states can be realized throughout the shown parameter plane. Applying the bounds derived in the previous sections only

Conditions	Perturbative unitarity	Bounded from below	Vacuum stability
Exact	Eq. (7.11)	Eq. (7.33)	Eq. (7.56)
Necessary	Eqs. (7.14),(7.17)	Eq. (7.38)	—
Sufficient	Eq. (7.25)	Eq. (7.45)	Eq. (7.69)

Table 7.1: Overview of the primary results of this paper; further constraints and their analysis may be found in the main text.

excludes the region with $M_{h_3} - M_{h_2} \gtrsim 100$ GeV.

Finally, we want to remark that $\mathcal{CP}$ violation can become manifest not only in the neutral mass matrix but also in the bosonic couplings. This occurs if either $\tilde{Z}_7^R \neq 0$ or $\tilde{Z}_7^I \neq 0$, since these couplings enter into couplings like $g_{h_1h_2h_3}$ [269]. Exotic decays like $h_3 \to h_1h_2 \to 3h_1$ would then be indicative of $\mathcal{CP}$ violation in the bosonic sector (see e.g. [274]).

7.6 Discussion

Two Higgs doublet models present a natural extension of the Standard Model description. In spite of the simplicity of this SM extension, many new parameters appear in this theory, and it is very important to understand the constraints on these parameters which will impact in a relevant way the 2HDM phenomenology. Most existing studies concentrate on the case in which a $\mathbb{Z}_2$ symmetry is imposed on the 2HDM potential and Yukawa sector. While this symmetry is an easy way to avoid flavor-changing neutral currents, it also forbids certain terms in the Higgs potential which do not induce flavor-changing neutral currents at tree level. In fact, in many scenarios in which the 2HDM is the low-energy effective field theory of a more complete high-scale model, these couplings are predicted to be non-zero.

Based on this motivation, in this work we present a step towards a systematic exploration of the non-$\mathbb{Z}_2$-symmetric 2HDM. We studied three of the most important theoretical constraints on the scalar potential parameters: perturbative unitarity, boundedness from below, and vacuum stability. In all three cases, we concentrated on the most general renormalizable potential (not restricted by any discrete symmetry) extending previous works by deriving analytic necessary and sufficient conditions for these constraints. For convenience, our main results (i.e., those conditions which approximate the exact conditions the best) are summarized in Table 7.1.

The derivation of our constraints makes use of several relevant mathematical properties, of which many have not been exploited in the literature before. These properties are not only applicable to the 2HDM but are also useful for the exploration of other models with extended Higgs sectors.

As a first phenomenological application of our bounds, we studied how much $\mathcal{CP}$-violating mixing between the BSM Higgs bosons can be realized in the general 2HDM in comparison to a 2HDM with a (softly broken) $\mathbb{Z}_2$ symmetry. While we found that large $\mathcal{CP}$-violating mixing can only be realized for large $\tan\beta$ in the 2HDM with a softly broken $\mathbb{Z}_2$ symmetry, no such theoretical constraints exist for the general 2HDM.

CHAPTER 8

CONCLUSION

In this thesis, we have examined just a few of the ways in which we can use experimental data to constrain new physics models, search for signals of new physics, and motivate new approaches to model building. We have looked at interpreting the LHC Higgs results in a variety of ways: first by employing existing data to derive indirect bounds on Higgs properties, then by examining the types of supersymmetric models that can be consistent with LHC observations while departing from the Standard Model, and finally by employing these results as motivation for an analysis of a high-energy theory. We then carefully examined the feasibility of searching for new physics in neutrino accelerator experiments, concluding that specialized experimental approaches and improved theory predictions are needed to help unlock the full potential of these experiments. Finally, we moved to a more theoretically-motivated examination of two Higgs doublet models, with an application of theoretical bounds to the phenomenology of these models.

Of course, there is a huge range of models, signals, and experiments beyond what has been presented here; a lifetime of work could not hope to cover them all, and the combined efforts of many physicists will ultimately be what unlocks new discoveries. The future of particle physics is exciting because it is uncertain—we know there must be something new out there to find, but as of yet, we have only hints of what it might be. As the most popular solutions to these questions are confronted by a lack of experimental evidence, we find ourselves challenged to re-evaluate the ways in which these models might manifest in nature and to identify novel new physics that can explain the biggest mysteries. Whether we finally confirm concrete hints of new physics or continue to observe a mysterious lack of evidence, the result has exciting consequences. We will have to see what comes next!

BIBLIOGRAPHY

[1] Abdelhak Djouadi. "The Anatomy of electro-weak symmetry breaking. I: The Higgs boson in the standard model". In: Phys. Rept. 457 (2008), pp. 1–216. DOI: 10.1016/j.physrep.2007.10.004. arXiv: hep-ph/0503172.

[2] Eite Tiesinga et al. "CODATA recommended values of the fundamental physical constants: 2018". In: Rev. Mod. Phys. 93 (2 June 2021), p. 025010. DOI: 10.1103/RevModPhys.93.025010. URL: https://link.aps.org/doi/10.1103/RevModPhys.93.025010.

[3] Ziro Maki, Masami Nakagawa, and Shoichi Sakata. "Remarks on the unified model of elementary particles". In: Prog. Theor. Phys. 28 (1962), pp. 870–880. DOI: 10.1143/PTP.28.870.

[4] B. Pontecorvo. "Inverse beta processes and nonconservation of lepton charge". In: Zh. Eksp. Teor. Fiz. 34 (1957), p. 247.

[5] Ivan Esteban et al. "Global analysis of three-flavour neutrino oscillations: synergies and tensions in the determination of θ_{23}, δ_{CP}, and the mass ordering". In: JHEP 01 (2019), p. 106. DOI: 10.1007/JHEP01(2019)106. arXiv: 1811.05487 [hep-ph].

[6] L. Wolfenstein. "Neutrino Oscillations in Matter". In: Phys. Rev. D 17 (1978), pp. 2369–2374. DOI: 10.1103/PhysRevD.17.2369.

[7] V. C. Rubin, N. Thonnard, and W. K. Ford Jr. "Rotational properties of 21 SC galaxies with a large range of luminosities and radii, from NGC 4605 /R = 4kpc/ to UGC 2885 /R = 122 kpc/". In: Astrophys. J. 238 (1980), p. 471. DOI: 10.1086/158003.

[8] Paolo Salucci. "The distribution of dark matter in galaxies". In: Astron. Astrophys. Rev. 27.1 (2019), p. 2. DOI: 10.1007/s00159-018-0113-1. arXiv: 1811.08843 [astro-ph.GA].

[9] Steven W. Allen, August E. Evrard, and Adam B. Mantz. "Cosmological Parameters from Observations of Galaxy Clusters". In: 49.1 (Sept. 2011), pp. 409–470. DOI: 10.1146/annurev-astro-081710-102514. arXiv: 1103.4829 [astro-ph.CO].

[10] Andrew J. S. Hamilton and Max Tegmark. "The Real space power spectrum of the PSCz survey from 0.01 to 300 h Mpc**-1". In: Mon. Not. Roy. Astron. Soc. 330 (2002), p. 506. DOI: 10.1046/j.1365-8711.2002.05033.x. arXiv: astro-ph/0008392.

[11] Benjamin Audren et al. "Strongest model-independent bound on the lifetime of Dark Matter". In: JCAP 12 (2014), p. 028. DOI: 10.1088/1475-7516/2014/12/028. arXiv: 1407.2418 [astro-ph.CO].

[12] M. Aker et al. "Direct neutrino-mass measurement with sub-electronvolt sensitivity". In: Nature Phys. 18.2 (2022), pp. 160–166. DOI: 10.1038/s41567-021-01463-1. arXiv: 2105.08533 [hep-ex].

[13] Vedran Brdar et al. "Type-I Seesaw as the Common Origin of Neutrino Mass, Baryon Asymmetry, and the Electroweak Scale". In: Phys. Rev. D 100 (2019), p. 075029. DOI: 10.1103/PhysRevD.100.075029. arXiv: 1905.12634 [hep-ph].

[14] A. D. Sakharov. "Violation of CP Invariance, C asymmetry, and baryon asymmetry of the universe". In: Pisma Zh. Eksp. Teor. Fiz. 5 (1967), pp. 32–35. DOI: 10.1070/PU1991v034n05ABEH002497.

[15] David E. Morrissey and Michael J. Ramsey-Musolf. "Electroweak baryogenesis". In: New J. Phys. 14 (2012), p. 125003. DOI: 10.1088/1367-2630/14/12/125003. arXiv: 1206.2942 [hep-ph].

[16] Sacha Davidson, Enrico Nardi, and Yosef Nir. "Leptogenesis". In: Phys. Rept. 466 (2008), pp. 105–177. DOI: `10.1016/j.physrep.2008.06.002`. arXiv: `0802.2962 [hep-ph]`.

[17] Raymond T. Co and Keisuke Harigaya. "Axiogenesis". In: Phys. Rev. Lett. 124.11 (2020), p. 111602. DOI: `10.1103/PhysRevLett.124.111602`. arXiv: `1910.02080 [hep-ph]`.

[18] A. Aguilar-Arevalo et al. "Evidence for neutrino oscillations from the observation of $\bar{\nu}_e$ appearance in a $\bar{\nu}_\mu$ beam". In: Phys. Rev. D 64 (2001), p. 112007. DOI: `10.1103/PhysRevD.64.112007`. arXiv: `hep-ex/0104049`.

[19] A. A. Aguilar-Arevalo et al. "Updated MiniBooNE neutrino oscillation results with increased data and new background studies". In: Phys. Rev. D 103.5 (2021), p. 052002. DOI: `10.1103/PhysRevD.103.052002`. arXiv: `2006.16883 [hep-ex]`.

[20] Th. A. Mueller et al. "Improved Predictions of Reactor Antineutrino Spectra". In: Phys. Rev. C 83 (2011), p. 054615. DOI: `10.1103/PhysRevC.83.054615`. arXiv: `1101.2663 [hep-ex]`.

[21] G. Mention et al. "The Reactor Antineutrino Anomaly". In: Phys. Rev. D 83 (2011), p. 073006. DOI: `10.1103/PhysRevD.83.073006`. arXiv: `1101.2755 [hep-ex]`.

[22] Patrick Huber. "On the determination of anti-neutrino spectra from nuclear reactors". In: Phys. Rev. C 84 (2011). [Erratum: Phys.Rev.C 85, 029901 (2012)], p. 024617. DOI: `10.1103/PhysRevC.85.029901`. arXiv: `1106.0687 [hep-ph]`.

[23] W. Hampel et al. "Final results of the Cr-51 neutrino source experiments in GALLEX". In: Phys. Lett. B 420 (1998), pp. 114–126. DOI: `10.1016/S0370-2693(97)01562-1`.

[24] J. N. Abdurashitov et al. "Measurement of the response of the Russian-American gallium experiment to neutrinos from a Cr-51 source". In: Phys. Rev. C 59 (1999), pp. 2246–2263. DOI: `10.1103/PhysRevC.59.2246`. arXiv: `hep-ph/9803418`.

[25] J. N. Abdurashitov et al. "Measurement of the response of a Ga solar neutrino experiment to neutrinos from an Ar-37 source". In: Phys. Rev. C 73 (2006), p. 045805. DOI: `10.1103/PhysRevC.73.045805`. arXiv: `nucl-ex/0512041`.

[26] F. Kaether et al. "Reanalysis of the GALLEX solar neutrino flux and source experiments". In: Phys. Lett. B 685 (2010), pp. 47–54. DOI: `10.1016/j.physletb.2010.01.030`. arXiv: `1001.2731 [hep-ex]`.

[27] Carlo Giunti and Marco Laveder. "Statistical Significance of the Gallium Anomaly". In: Phys. Rev. C 83 (2011), p. 065504. DOI: `10.1103/PhysRevC.83.065504`. arXiv: `1006.3244 [hep-ph]`.

[28] V. V. Barinov et al. "Results from the Baksan Experiment on Sterile Transitions (BEST)". In: Phys. Rev. Lett. 128.23 (2022), p. 232501. DOI: `10.1103/PhysRevLett.128.232501`. arXiv: `2109.11482 [nucl-ex]`.

[29] D. Buskulic et al. "A Direct measurement of the invisible width of the Z from single photon counting". In: Phys. Lett. B 313 (1993), pp. 520–534. DOI: `10.1016/0370-2693(93)90027-F`.

[30] R. Akers et al. "Measurement of single photon production in e+ e- collisions near the Z0 resonance". In: Z. Phys. C 65 (1995), pp. 47–66. DOI: `10.1007/BF01571303`.

[31] M. Acciarri et al. "Determination of the number of light neutrino species from single photon production at LEP". In: Phys. Lett. B 431 (1998), pp. 199–208. DOI: `10.1016/S0370-2693(98)00519-X`.

[32] P. Abreu et al. "Cross-sections and leptonic forward backward asymmetries from the Z0 running of LEP". In: Eur. Phys. J. C 16 (2000), pp. 371–405. DOI: `10.1007/s100520000392`.

[33] Lars Fromme, Stephan J. Huber, and Michael Seniuch. "Baryogenesis in the two-Higgs doublet model". In: JHEP 11 (2006), p. 038. DOI: `10.1088/1126-6708/2006/11/038`. arXiv: `hep-ph/0605242`.

[34] "A detailed map of Higgs boson interactions by the ATLAS experiment ten years after the discovery". In: Nature 607.7917 (2022). [Erratum: Nature 612, E24 (2022)], pp. 52–59. DOI: `10.1038/s41586-022-04893-w`. arXiv: `2207.00092 [hep-ex]`.

[35] Armen Tumasyan et al. "A portrait of the Higgs boson by the CMS experiment ten years after the discovery". In: Nature 607.7917 (2022), pp. 60–68. DOI: `10.1038/s41586-022-04892-x`. arXiv: `2207.00043 [hep-ex]`.

[36] Sacha Davidson and Howard E. Haber. "Basis-independent methods for the two-Higgs-doublet model". In: Phys. Rev. D 72 (2005). [Erratum: Phys.Rev.D 72, 099902 (2005)], p. 035004. DOI: `10.1103/PhysRevD.72.099902`. arXiv: `hep-ph/0504050`.

[37] G. C. Branco et al. "Theory and phenomenology of two-Higgs-doublet models". In: Phys. Rept. 516 (2012), pp. 1–102. DOI: `10.1016/j.physrep.2012.02.002`. arXiv: `1106.0034 [hep-ph]`.

[38] Stephen P. Martin. "A Supersymmetry primer". In: Adv. Ser. Direct. High Energy Phys. 18 (1998). Ed. by Gordon L. Kane, pp. 1–98. DOI: `10.1142/9789812839657_0001`. arXiv: `hep-ph/9709356`.

[39] Fernando Quevedo, Sven Krippendorf, and Oliver Schlotterer. "Cambridge Lectures on Supersymmetry and Extra Dimensions". In: (Nov. 2010). arXiv: `1011.1491 [hep-th]`.

[40] Ulrich Ellwanger, Cyril Hugonie, and Ana M. Teixeira. "The Next-to-Minimal Supersymmetric Standard Model". In: Phys. Rept. 496 (2010), pp. 1–77. DOI: `10.1016/j.physrep.2010.07.001`. arXiv: `0910.1785 [hep-ph]`.

[41] A. Djouadi, U. Ellwanger, and A. M. Teixeira. "Phenomenology of the constrained NMSSM". In: JHEP 04 (2009), p. 031. DOI: `10.1088/1126-6708/2009/04/031`. arXiv: `0811.2699 [hep-ph]`.

[42] Mona Dentler et al. "Updated Global Analysis of Neutrino Oscillations in the Presence of eV-Scale Sterile Neutrinos". In: JHEP 08 (2018), p. 010. DOI: `10.1007/JHEP08(2018)010`. arXiv: `1803.10661 [hep-ph]`.

[43] M. H. Moulai et al. "Combining Sterile Neutrino Fits to Short Baseline Data with IceCube Data". In: Phys. Rev. D 101.5 (2020), p. 055020. DOI: `10.1103/PhysRevD.101.055020`. arXiv: `1910.13456 [hep-ph]`.

[44] Carlo Giunti and T. Lasserre. "eV-scale Sterile Neutrinos". In: Ann. Rev. Nucl. Part. Sci. 69 (2019), pp. 163–190. DOI: `10.1146/annurev-nucl-101918-023755`. arXiv: `1901.08330 [hep-ph]`.

[45] P. Adamson et al. "Improved Constraints on Sterile Neutrino Mixing from Disappearance Searches in the MINOS, MINOS+, Daya Bay, and Bugey-3 Experiments". In: Phys. Rev. Lett. 125.7 (2020), p. 071801. DOI: `10.1103/PhysRevLett.125.071801`. arXiv: `2002.00301 [hep-ex]`.

[46] M. G. Aartsen et al. "Searches for Sterile Neutrinos with the IceCube Detector". In: Phys. Rev. Lett. 117.7 (2016), p. 071801. DOI: `10.1103/PhysRevLett.117.071801`. arXiv: `1605.01990 [hep-ex]`.

[47] M. G. Aartsen et al. “Searching for eV-scale sterile neutrinos with eight years of atmospheric neutrinos at the IceCube Neutrino Telescope”. In: Phys. Rev. D 102.5 (2020), p. 052009. DOI: `10.1103/PhysRevD.102.052009`. arXiv: `2005.12943 [hep-ex]`.

[48] B. Aharmim et al. “An Independent Measurement of the Total Active B-8 Solar Neutrino Flux Using an Array of He-3 Proportional Counters at the Sudbury Neutrino Observatory”. In: Phys. Rev. Lett. 101 (2008), p. 111301. DOI: `10.1103/PhysRevLett.101.111301`. arXiv: `0806.0989 [nucl-ex]`.

[49] K. Abe et al. “Solar Neutrino Measurements in Super-Kamiokande-IV”. In: Phys. Rev. D 94.5 (2016), p. 052010. DOI: `10.1103/PhysRevD.94.052010`. arXiv: `1606.07538 [hep-ex]`.

[50] M. Agostini et al. “Comprehensive measurement of *pp*-chain solar neutrinos”. In: Nature 562.7728 (2018), pp. 505–510. DOI: `10.1038/s41586-018-0624-y`.

[51] Z. Atif et al. “Search for sterile neutrino oscillations using RENO and NEOS data”. In: Phys. Rev. D 105.11 (2022), p. L111101. DOI: `10.1103/PhysRevD.105.L111101`. arXiv: `2011.00896 [hep-ex]`.

[52] I Alekseev et al. “Search for sterile neutrinos at the DANSS experiment”. In: Phys. Lett. B 787 (2018), pp. 56–63. DOI: `10.1016/j.physletb.2018.10.038`. arXiv: `1804.04046 [hep-ex]`.

[53] Georges Aad et al. “Combined measurements of Higgs boson production and decay using up to 80 fb^{-1} of proton-proton collision data at $\sqrt{s} = 13$ TeV collected with the ATLAS experiment”. In: Phys. Rev. D 101.1 (2020), p. 012002. DOI: `10.1103/PhysRevD.101.012002`. arXiv: `1909.02845 [hep-ex]`.

[54] Morad Aaboud et al. “Observation of $H \to b\bar{b}$ decays and VH production with the ATLAS detector”. In: Phys. Lett. B 786 (2018), pp. 59–86. DOI: `10.1016/j.physletb.2018.09.013`. arXiv: `1808.08238 [hep-ex]`.

[55] Albert M Sirunyan et al. “Combined measurements of Higgs boson couplings in proton–proton collisions at $\sqrt{s} = 13\,\text{TeV}$”. In: Eur. Phys. J. C 79.5 (2019), p. 421. DOI: `10.1140/epjc/s10052-019-6909-y`. arXiv: `1809.10733 [hep-ex]`.

[56] A. David et al. “LHC HXSWG interim recommendations to explore the coupling structure of a Higgs-like particle”. In: (Sept. 2012). arXiv: `1209.0040 [hep-ph]`.

[57] J R Andersen et al. “Handbook of LHC Higgs Cross Sections: 3. Higgs Properties”. In: (July 2013). Ed. by S Heinemeyer et al. DOI: `10.5170/CERN-2013-004`. arXiv: `1307.1347 [hep-ph]`.

[58] Rick S. Gupta, Alex Pomarol, and Francesco Riva. “BSM Primary Effects”. In: Phys. Rev. D 91.3 (2015), p. 035001. DOI: `10.1103/PhysRevD.91.035001`. arXiv: `1405.0181 [hep-ph]`.

[59] Roberto Contino et al. “Effective Lagrangian for a light Higgs-like scalar”. In: JHEP 07 (2013), p. 035. DOI: `10.1007/JHEP07(2013)035`. arXiv: `1303.3876 [hep-ph]`.

[60] Adam Falkowski. “Effective field theory approach to LHC Higgs data”. In: Pramana 87.3 (2016), p. 39. DOI: `10.1007/s12043-016-1251-5`. arXiv: `1505.00046 [hep-ph]`.

[61] D. de Florian et al. “Handbook of LHC Higgs Cross Sections: 4. Deciphering the Nature of the Higgs Sector”. In: 2/2017 (Oct. 2016). DOI: `10.23731/CYRM-2017-002`. arXiv: `1610.07922 [hep-ph]`.

[62] D. Zeppenfeld et al. “Measuring Higgs boson couplings at the CERN LHC”. In: Phys. Rev. D 62 (2000), p. 013009. DOI: `10.1103/PhysRevD.62.013009`. arXiv: `hep-ph/0002036`.

[63] A. Djouadi et al. "The Higgs working group: Summary report". In: 1st Les Houches Workshop on Physics at TeV Colliders. Feb. 2000. arXiv: `hep-ph/0002258`.

[64] M. Duhrssen et al. "Extracting Higgs boson couplings from CERN LHC data". In: Phys. Rev. D 70 (2004), p. 113009. DOI: `10.1103/PhysRevD.70.113009`. arXiv: `hep-ph/0406323`.

[65] G. Belanger et al. "Global fit to Higgs signal strengths and couplings and implications for extended Higgs sectors". In: Phys. Rev. D 88 (2013), p. 075008. DOI: `10.1103/PhysRevD.88.075008`. arXiv: `1306.2941 [hep-ph]`.

[66] Karl Pearson F.R.S. (1901) LIII. "On lines and planes of closest fit to systems of points in space". In: The London, Edinburgh, and Dublin Philosophical Magazine and Journal of Science 2:11 (), pp. 559–572. DOI: `10.1080/14786440109462720`.

[67] H. Hotelling. "Analysis of a complex of statistical variables into principal components". In: Journal of Educational Psychology 24(6) (1933), pp. 417–441. DOI: `10.1037/h0071325`.

[68] Morad Aaboud et al. "Constraints on off-shell Higgs boson production and the Higgs boson total width in $ZZ \to 4\ell$ and $ZZ \to 2\ell 2\nu$ final states with the ATLAS detector". In: Phys. Lett. B 786 (2018), pp. 223–244. DOI: `10.1016/j.physletb.2018.09.048`. arXiv: `1808.01191 [hep-ex]`.

[69] Albert M Sirunyan et al. "Measurements of the Higgs boson width and anomalous HVV couplings from on-shell and off-shell production in the four-lepton final state". In: Phys. Rev. D 99.11 (2019), p. 112003. DOI: `10.1103/PhysRevD.99.112003`. arXiv: `1901.00174 [hep-ex]`.

[70] Adam Falkowski, Francesco Riva, and Alfredo Urbano. "Higgs at last". In: JHEP 11 (2013), p. 111. DOI: `10.1007/JHEP11(2013)111`. arXiv: `1303.1812 [hep-ph]`.

[71] "Projections for measurements of Higgs boson cross sections, branching ratios, coupling parameters and mass with the ATLAS detector at the HL-LHC". In: (2018).

[72] "Sensitivity projections for Higgs boson properties measurements at the HL-LHC". In: (2018).

[73] "Off-shell Higgs boson couplings measurement using $H \to ZZ \to 4l$ events at High Luminosity LHC". In: (2015).

[74] Gilad Perez et al. "Constraining the charm Yukawa and Higgs-quark coupling universality". In: Phys. Rev. D 92.3 (2015), p. 033016. DOI: `10.1103/PhysRevD.92.033016`. arXiv: `1503.00290 [hep-ph]`.

[75] Gilad Perez et al. "Prospects for measuring the Higgs boson coupling to light quarks". In: Phys. Rev. D 93.1 (2016), p. 013001. DOI: `10.1103/PhysRevD.93.013001`. arXiv: `1505.06689 [hep-ph]`.

[76] Matthias König and Matthias Neubert. "Exclusive Radiative Higgs Decays as Probes of Light-Quark Yukawa Couplings". In: JHEP 08 (2015), p. 012. DOI: `10.1007/JHEP08(2015)012`. arXiv: `1505.03870 [hep-ph]`.

[77] Geoffrey T. Bodwin et al. "Higgs boson decays to quarkonia and the $H\bar{c}c$ coupling". In: Phys. Rev. D 88.5 (2013), p. 053003. DOI: `10.1103/PhysRevD.88.053003`. arXiv: `1306.5770 [hep-ph]`.

[78] Geoffrey T. Bodwin et al. "Relativistic corrections to Higgs boson decays to quarkonia". In: Phys. Rev. D 90.11 (2014), p. 113010. DOI: `10.1103/PhysRevD.90.113010`. arXiv: `1407.6695 [hep-ph]`.

[79] Morad Aaboud et al. "Searches for exclusive Higgs and Z boson decays into $J/\psi\gamma$, $\psi(2S)\gamma$, and $\Upsilon(nS)\gamma$ at $\sqrt{s} = 13$ TeV with the ATLAS detector". In: Phys. Lett. B 786 (2018), pp. 134–155. DOI: `10.1016/j.physletb.2018.09.024`. arXiv: `1807.00802 [hep-ex]`.

[80] J. Alwall et al. "The automated computation of tree-level and next-to-leading order differential cross sections, and their matching to parton shower simulations". In: JHEP 07 (2014), p. 079. DOI: `10.1007/JHEP07(2014)079`. arXiv: `1405.0301 [hep-ph]`.

[81] "Search for the Standard Model Higgs and Z Boson decays to $J/\psi\,\gamma$: HL-LHC projections". In: (Sept. 2015).

[82] Geoffrey T. Bodwin et al. "New approach to the resummation of logarithms in Higgs-boson decays to a vector quarkonium plus a photon". In: Phys. Rev. D 95.5 (2017), p. 054018. DOI: `10.1103/PhysRevD.95.054018`. arXiv: `1603.06793 [hep-ph]`.

[83] Ilaria Brivio, Florian Goertz, and Gino Isidori. "Probing the Charm Quark Yukawa Coupling in Higgs+Charm Production". In: Phys. Rev. Lett. 115.21 (2015), p. 211801. DOI: `10.1103/PhysRevLett.115.211801`. arXiv: `1507.02916 [hep-ph]`.

[84] M. Aaboud et al. "Search for the Decay of the Higgs Boson to Charm Quarks with the ATLAS Experiment". In: Phys. Rev. Lett. 120.21 (2018), p. 211802. DOI: `10.1103/PhysRevLett.120.211802`. arXiv: `1802.04329 [hep-ex]`.

[85] "Prospects for $H \to c\bar{c}$ using Charm Tagging with the ATLAS Experiment at the HL-LHC". In: (2018).

[86] "Performance of Deep Tagging Algorithms for Boosted Double Quark Jet Topology in Proton-Proton Collisions at 13 TeV with the Phase-0 CMS Detector". In: (2018).

[87] Felix Yu. "Phenomenology of Enhanced Light Quark Yukawa Couplings and the $W^{\pm}h$ Charge Asymmetry". In: JHEP 02 (2017), p. 083. DOI: `10.1007/JHEP02(2017)083`. arXiv: `1609.06592 [hep-ph]`.

[88] Fady Bishara et al. "Constraining Light-Quark Yukawa Couplings from Higgs Distributions". In: Phys. Rev. Lett. 118.12 (2017), p. 121801. DOI: `10.1103/PhysRevLett.118.121801`. arXiv: `1606.09253 [hep-ph]`.

[89] Yotam Soreq, Hua Xing Zhu, and Jure Zupan. "Light quark Yukawa couplings from Higgs kinematics". In: JHEP 12 (2016), p. 045. DOI: `10.1007/JHEP12(2016)045`. arXiv: `1606.09621 [hep-ph]`.

[90] Gage Bonner and Heather E. Logan. "Constraining the Higgs couplings to up and down quarks using production kinematics at the CERN Large Hadron Collider". In: (Aug. 2016). arXiv: `1608.04376 [hep-ph]`.

[91] Albert M Sirunyan et al. "Measurement and interpretation of differential cross sections for Higgs boson production at $\sqrt{s} = 13$ TeV". In: Phys. Lett. B 792 (2019), pp. 369–396. DOI: `10.1016/j.physletb.2019.03.059`. arXiv: `1812.06504 [hep-ex]`.

[92] P. M. Ferreira et al. "Probing wrong-sign Yukawa couplings at the LHC and a future linear collider". In: Phys. Rev. D 89.11 (2014), p. 115003. DOI: `10.1103/PhysRevD.89.115003`. arXiv: `1403.4736 [hep-ph]`.

[93] Daniel Aloni, Yosef Nir, and Emmanuel Stamou. "Large BR($h \to \tau\mu$) in the MSSM?" In: JHEP 04 (2016), p. 162. DOI: `10.1007/JHEP04(2016)162`. arXiv: `1511.00979 [hep-ph]`.

[94] Martin Bauer, Marcela Carena, and Katrin Gemmler. "Flavor from the Electroweak Scale". In: JHEP 11 (2015), p. 016. DOI: `10.1007/JHEP11(2015)016`. arXiv: `1506.01719 [hep-ph]`.

[95] Kenzo Inoue et al. "Low-Energy Parameters and Particle Masses in a Supersymmetric Grand Unified Model". In: Prog. Theor. Phys. 67 (1982), p. 1889. DOI: `10.1143/PTP.67.1889`.

[96] Ricardo A. Flores and Marc Sher. "Higgs Masses in the Standard, Multi-Higgs and Supersymmetric Models". In: Annals Phys. 148 (1983), p. 95. DOI: `10.1016/0003-4916(83)90331-7`.

[97] J. F. Gunion and Howard E. Haber. "Higgs Bosons in Supersymmetric Models. 1." In: Nucl. Phys. B 272 (1986). [Erratum: Nucl.Phys.B 402, 567–569 (1993)], p. 1. DOI: `10.1016/0550-3213(86)90340-8`.

[98] Marcela Carena and Howard E. Haber. "Higgs Boson Theory and Phenomenology". In: Prog. Part. Nucl. Phys. 50 (2003), pp. 63–152. DOI: `10.1016/S0146-6410(02)00177-1`. arXiv: `hep-ph/0208209`.

[99] Abdelhak Djouadi. "The Anatomy of electro-weak symmetry breaking. II. The Higgs bosons in the minimal supersymmetric model". In: Phys. Rept. 459 (2008), pp. 1–241. DOI: `10.1016/j.physrep.2007.10.005`. arXiv: `hep-ph/0503173`.

[100] Pedro M. Ferreira, Stefan Liebler, and Jonas Wittbrodt. "$pp \to A \to Zh$ and the wrong-sign limit of the two-Higgs-doublet model". In: Phys. Rev. D 97.5 (2018), p. 055008. DOI: `10.1103/PhysRevD.97.055008`. arXiv: `1711.00024 [hep-ph]`.

[101] Dipankar Das, Anirban Kundu, and Ipsita Saha. "Higgs data does not rule out a sequential fourth generation with an extended scalar sector". In: Phys. Rev. D 97.1 (2018), p. 011701. DOI: `10.1103/PhysRevD.97.011701`. arXiv: `1707.03000 [hep-ph]`.

[102] Howard Georgi and Dimitri V. Nanopoulos. "Suppression of Flavor Changing Effects From Neutral Spinless Meson Exchange in Gauge Theories". In: Phys. Lett. B 82 (1979), pp. 95–96. DOI: `10.1016/0370-2693(79)90433-7`.

[103] John F. Donoghue and Ling Fong Li. "Properties of Charged Higgs Bosons". In: Phys. Rev. D 19 (1979), p. 945. DOI: `10.1103/PhysRevD.19.945`.

[104] L. Lavoura and Joao P. Silva. "Fundamental CP violating quantities in a SU(2) x U(1) model with many Higgs doublets". In: Phys. Rev. D 50 (1994), pp. 4619–4624. DOI: `10.1103/PhysRevD.50.4619`. arXiv: `hep-ph/9404276`.

[105] L. Lavoura. "Signatures of discrete symmetries in the scalar sector". In: Phys. Rev. D 50 (1994), pp. 7089–7092. DOI: `10.1103/PhysRevD.50.7089`. arXiv: `hep-ph/9405307`.

[106] F. J. Botella and Joao P. Silva. "Jarlskog - like invariants for theories with scalars and fermions". In: Phys. Rev. D 51 (1995), pp. 3870–3875. DOI: `10.1103/PhysRevD.51.3870`. arXiv: `hep-ph/9411288`.

[107] Gustavo C. Branco, Luis Lavoura, and Joao P. Silva. CP Violation. Vol. 103. 1999.

[108] John F. Gunion and Howard E. Haber. "The CP conserving two Higgs doublet model: The Approach to the decoupling limit". In: Phys. Rev. D 67 (2003), p. 075019. DOI: `10.1103/PhysRevD.67.075019`. arXiv: `hep-ph/0207010`.

[109] Nathaniel Craig, Jamison Galloway, and Scott Thomas. "Searching for Signs of the Second Higgs Doublet". In: (May 2013). arXiv: `1305.2424 [hep-ph]`.

[110] Marcela Carena et al. "Complementarity between Nonstandard Higgs Boson Searches and Precision Higgs Boson Measurements in the MSSM". In: Phys. Rev. D 91.3 (2015), p. 035003. DOI: `10.1103/PhysRevD.91.035003`. arXiv: `1410.4969 [hep-ph]`.

[111] Jérémy Bernon et al. "Scrutinizing the alignment limit in two-Higgs-doublet models: m_h=125 GeV". In: Phys. Rev. D 92.7 (2015), p. 075004. DOI: `10.1103/PhysRevD.92.075004`. arXiv: `1507.00933 [hep-ph]`.

[112] Jérémy Bernon et al. "Scrutinizing the alignment limit in two-Higgs-doublet models. II. m_H=125 GeV". In: Phys. Rev. D 93.3 (2016), p. 035027. DOI: `10.1103/PhysRevD.93.035027`. arXiv: `1511.03682 [hep-ph]`.

[113] Howard E. Haber. "The Higgs data and the Decoupling Limit". In: 1st Toyama International Workshop on Higgs as a Probe of New Physics 2013. Dec. 2013. arXiv: `1401.0152 [hep-ph]`.

[114] Marcela Carena et al. "Distinguishing a MSSM Higgs boson from the SM Higgs boson at a linear collider". In: Phys. Rev. D 65 (2002). [Erratum: Phys.Rev.D 65, 099902 (2002)], p. 055005. DOI: `10.1103/PhysRevD.65.055005`. arXiv: `hep-ph/0106116`.

[115] Howard E. Haber and Ralf Hempfling. "The Renormalization group improved Higgs sector of the minimal supersymmetric model". In: Phys. Rev. D 48 (1993), pp. 4280–4309. DOI: `10.1103/PhysRevD.48.4280`. arXiv: `hep-ph/9307201`.

[116] Marcela Carena et al. "Analytical expressions for radiatively corrected Higgs masses and couplings in the MSSM". In: Phys. Lett. B 355 (1995), pp. 209–221. DOI: `10.1016/0370-2693(95)00694-G`. arXiv: `hep-ph/9504316`.

[117] Gabriel Lee and Carlos E. M. Wagner. "Higgs bosons in heavy supersymmetry with an intermediate m_A". In: Phys. Rev. D 92.7 (2015), p. 075032. DOI: `10.1103/PhysRevD.92.075032`. arXiv: `1508.00576 [hep-ph]`.

[118] Morad Aaboud et al. "Search for additional heavy neutral Higgs and gauge bosons in the ditau final state produced in 36 fb^1 of pp collisions at $\sqrt{s} = 13$ TeV with the ATLAS detector". In: JHEP 01 (2018), p. 055. DOI: `10.1007/JHEP01(2018)055`. arXiv: `1709.07242 [hep-ex]`.

[119] Albert M Sirunyan et al. "Search for additional neutral MSSM Higgs bosons in the $\tau\tau$ final state in proton-proton collisions at $\sqrt{s} = 13$ TeV". In: JHEP 09 (2018), p. 007. DOI: `10.1007/JHEP09(2018)007`. arXiv: `1803.06553 [hep-ex]`.

[120] Nikita Blinov and David E. Morrissey. "Vacuum Stability and the MSSM Higgs Mass". In: JHEP 03 (2014), p. 106. DOI: `10.1007/JHEP03(2014)106`. arXiv: `1310.4174 [hep-ph]`.

[121] Marcela Carena, S. Mrenna, and C. E. M. Wagner. "MSSM Higgs boson phenomenology at the Tevatron collider". In: Phys. Rev. D 60 (1999), p. 075010. DOI: `10.1103/PhysRevD.60.075010`. arXiv: `hep-ph/9808312`.

[122] R. Hempfling. "Yukawa coupling unification with supersymmetric threshold corrections". In: Phys. Rev. D 49 (11 June 1994), pp. 6168–6172. DOI: `10.1103/PhysRevD.49.6168`. URL: `https://link.aps.org/doi/10.1103/PhysRevD.49.6168`.

[123] Lawrence J. Hall, Riccardo Rattazzi, and Uri Sarid. "The Top quark mass in supersymmetric SO(10) unification". In: Phys. Rev. D 50 (1994), pp. 7048–7065. DOI: `10.1103/PhysRevD.50.7048`. arXiv: `hep-ph/9306309`.

[124] Marcela Carena et al. "Electroweak symmetry breaking and bottom - top Yukawa unification". In: Nucl. Phys. B 426 (1994), pp. 269–300. DOI: `10.1016/0550-3213(94)90313-1`. arXiv: `hep-ph/9402253`.

[125] J. R. Espinosa and M. Quiros. "On Higgs boson masses in nonminimal supersymmetric standard models". In: Phys. Lett. B 279 (1992), pp. 92–97. DOI: `10.1016/0370-2693(92)91846-2`.

[126] Howard E. Haber and Ralf Hempfling. "Can the mass of the lightest Higgs boson of the minimal supersymmetric model be larger than m(Z)?" In: Phys. Rev. Lett. 66 (1991), pp. 1815–1818. DOI: `10.1103/PhysRevLett.66.1815`.

[127] Henning Bahl and Wolfgang Hollik. "Precise prediction for the light MSSM Higgs boson mass combining effective field theory and fixed-order calculations". In:

Eur. Phys. J. C 76.9 (2016), p. 499. DOI: 10.1140/epjc/s10052-016-4354-8. arXiv: 1608.01880 [hep-ph].

[128] Yasuhiro Okada, Masahiro Yamaguchi, and Tsutomu Yanagida. "Upper bound of the lightest Higgs boson mass in the minimal supersymmetric standard model". In: Prog. Theor. Phys. 85 (1991), pp. 1–6. DOI: 10.1143/ptp/85.1.1.

[129] John R. Ellis, Giovanni Ridolfi, and Fabio Zwirner. "Radiative corrections to the masses of supersymmetric Higgs bosons". In: Phys. Lett. B 257 (1991), pp. 83–91. DOI: 10.1016/0370-2693(91)90863-L.

[130] Marcela Carena et al. "Reconciling the two loop diagrammatic and effective field theory computations of the mass of the lightest CP - even Higgs boson in the MSSM". In: Nucl. Phys. B 580 (2000), pp. 29–57. DOI: 10.1016/S0550-3213(00)00212-1. arXiv: hep-ph/0001002.

[131] Emanuele Bagnaschi et al. "Higgs Mass and Unnatural Supersymmetry". In: JHEP 09 (2014), p. 092. DOI: 10.1007/JHEP09(2014)092. arXiv: 1407.4081 [hep-ph].

[132] T. Hahn et al. "High-Precision Predictions for the Light CP -Even Higgs Boson Mass of the Minimal Supersymmetric Standard Model". In: Phys. Rev. Lett. 112.14 (2014), p. 141801. DOI: 10.1103/PhysRevLett.112.141801. arXiv: 1312.4937 [hep-ph].

[133] Javier Pardo Vega and Giovanni Villadoro. "SusyHD: Higgs mass Determination in Supersymmetry". In: JHEP 07 (2015), p. 159. DOI: 10.1007/JHEP07(2015)159. arXiv: 1504.05200 [hep-ph].

[134] Patrick Draper, Gabriel Lee, and Carlos E. M. Wagner. "Precise estimates of the Higgs mass in heavy supersymmetry". In: Phys. Rev. D 89.5 (2014), p. 055023. DOI: 10.1103/PhysRevD.89.055023. arXiv: 1312.5743 [hep-ph].

[135] Marcela Carena et al. "Alignment limit of the NMSSM Higgs sector". In: Phys. Rev. D 93.3 (2016), p. 035013. DOI: 10.1103/PhysRevD.93.035013. arXiv: 1510.09137 [hep-ph].

[136] C. Panagiotakopoulos and K. Tamvakis. "Stabilized NMSSM without domain walls". In: Phys. Lett. B 446 (1999), pp. 224–227. DOI: 10.1016/S0370-2693(98)01493-2. arXiv: hep-ph/9809475.

[137] C. Panagiotakopoulos and K. Tamvakis. "New minimal extension of MSSM". In: Phys. Lett. B 469 (1999), pp. 145–148. DOI: 10.1016/S0370-2693(99)01247-2. arXiv: hep-ph/9908351.

[138] C. Panagiotakopoulos and A. Pilaftsis. "Higgs scalars in the minimal nonminimal supersymmetric standard model". In: Phys. Rev. D 63 (2001), p. 055003. DOI: 10.1103/PhysRevD.63.055003. arXiv: hep-ph/0008268.

[139] Ulrich Ellwanger, John F. Gunion, and Cyril Hugonie. "NMHDECAY: A Fortran code for the Higgs masses, couplings and decay widths in the NMSSM". In: JHEP 02 (2005), p. 066. DOI: 10.1088/1126-6708/2005/02/066. arXiv: hep-ph/0406215.

[140] "Search for charged Higgs bosons with the H+ to tau nu decay channel in the fully hadronic final state at sqrt s = 8 TeV". In: (2014).

[141] "Combined measurements of Higgs boson production and decay in the $H \to ZZ^{\to 4\ell}$ and $H \to \gamma\gamma$ channels using $\sqrt{s} = 13$ TeV pp collision data collected with the ATLAS experiment". In: (July 2017).

[142] Sally Dawson et al. "Working Group Report: Higgs Boson". In: Community Summer Study 2013: Snowmass on the Mississippi. Oct. 2013. arXiv: 1310.8361 [hep-ex].

[143] Abdelhak Djouadi. “Squark effects on Higgs boson production and decay at the LHC”. In: Phys. Lett. B 435 (1998), pp. 101–108. DOI: `10.1016/S0370-2693(98)00784-9`. arXiv: `hep-ph/9806315`.

[144] Radovan Dermisek and Ian Low. “Probing the Stop Sector and the Sanity of the MSSM with the Higgs Boson at the LHC”. In: Phys. Rev. D 77 (2008), p. 035012. DOI: `10.1103/PhysRevD.77.035012`. arXiv: `hep-ph/0701235`.

[145] Marcela Carena et al. “A 125 GeV SM-like Higgs in the MSSM and the $\gamma\gamma$ rate”. In: JHEP 03 (2012), p. 014. DOI: `10.1007/JHEP03(2012)014`. arXiv: `1112.3336 [hep-ph]`.

[146] Marcela Carena et al. “Light Stops, Light Staus and the 125 GeV Higgs”. In: JHEP 08 (2013), p. 087. DOI: `10.1007/JHEP08(2013)087`. arXiv: `1303.4414 [hep-ph]`.

[147] Tanmoy Modak et al. “Constraining wrong-sign hbb couplings with $h \to \Upsilon\gamma$”. In: Phys. Rev. D 94.7 (2016), p. 075017. DOI: `10.1103/PhysRevD.94.075017`. arXiv: `1607.07876 [hep-ph]`.

[148] Georges Aad et al. “Search for Higgs and Z Boson Decays to J/$\psi\gamma$ and $\Upsilon(nS)\gamma withtheATLASDetector$”. In: Phys. Rev. Lett. 114.12 (2015), p. 121801. DOI: `10.1103/PhysRevLett.114.121801`. arXiv: `1501.03276 [hep-ex]`.

[149] R. Contino et al. “Physics at a 100 TeV pp collider: Higgs and EW symmetry breaking studies”. In: (June 2016). DOI: `10.23731/CYRM-2017-003.255`. arXiv: `1606.09408 [hep-ph]`.

[150] Joanne L. Hewett. “Can b —> s gamma close the supersymmetric Higgs production window?” In: Phys. Rev. Lett. 70 (1993), pp. 1045–1048. DOI: `10.1103/PhysRevLett.70.1045`. arXiv: `hep-ph/9211256`.

[151] Mikolaj Misiak and Matthias Steinhauser. “Weak radiative decays of the B meson and bounds on $M_{H^\pm}$ in the Two-Higgs-Doublet Model”. In: Eur. Phys. J. C 77.3 (2017), p. 201. DOI: `10.1140/epjc/s10052-017-4776-y`. arXiv: `1702.04571 [hep-ph]`.

[152] Riccardo Barbieri and G. F. Giudice. “b —> s gamma decay and supersymmetry”. In: Phys. Lett. B 309 (1993), pp. 86–90. DOI: `10.1016/0370-2693(93)91508-K`. arXiv: `hep-ph/9303270`.

[153] Marco Ciuchini et al. “Next-to-leading QCD corrections to $B \to X_s\gamma$: Standard model and two Higgs doublet model”. In: Nucl. Phys. B 527 (1998), pp. 21–43. DOI: `10.1016/S0550-3213(98)00244-2`. arXiv: `hep-ph/9710335`.

[154] G. Degrassi, P. Gambino, and G. F. Giudice. “B —> X(s gamma) in supersymmetry: Large contributions beyond the leading order”. In: JHEP 12 (2000), p. 009. DOI: `10.1088/1126-6708/2000/12/009`. arXiv: `hep-ph/0009337`.

[155] Marcela Carena et al. “$b \to s\gamma$ and supersymmetry with large $\tan\beta$”. In: Phys. Lett. B 499 (2001), pp. 141–146. DOI: `10.1016/S0370-2693(01)00009-0`. arXiv: `hep-ph/0010003`.

[156] Andrzej J. Buras et al. “$\Delta M_{d,s}, B^0 d, s \to \mu^+\mu^-$ and $B \to X_s\gamma$ in supersymmetry at large $\tan\beta$”. In: Nucl. Phys. B 659 (2003), p. 3. DOI: `10.1016/S0550-3213(03)00190-1`. arXiv: `hep-ph/0210145`.

[157] F. Gabbiani et al. “A Complete analysis of FCNC and CP constraints in general SUSY extensions of the standard model”. In: Nucl. Phys. B 477 (1996), pp. 321–352. DOI: `10.1016/0550-3213(96)00390-2`. arXiv: `hep-ph/9604387`.

[158] M. Carena, A. Menon, and C. E. M. Wagner. “Minimal Flavor Violation and the Scale of Supersymmetry Breaking”. In: Phys. Rev. D 79 (2009), p. 075025. DOI: `10.1103/PhysRevD.79.075025`. arXiv: `0812.3594 [hep-ph]`.

[159] "Search for heavy resonances decaying to a W or Z boson and a Higgs boson in final states with leptons and b-jets in 36.1~fb^{-1} of pp collision data at $\sqrt{s} = 13$~TeV with the ATLAS detector". In: (July 2017). Ed. by Paolo Checchia et al.

[160] Stefan von Buddenbrock et al. "Multi-lepton signatures of additional scalar bosons beyond the Standard Model at the LHC". In: J. Phys. G 45.11 (2018), p. 115003. DOI: 10.1088/1361-6471/aae3d6. arXiv: 1711.07874 [hep-ph].

[161] Stefan von Buddenbrock et al. "Phenomenological signatures of additional scalar bosons at the LHC". In: Eur. Phys. J. C 76.10 (2016), p. 580. DOI: 10.1140/epjc/s10052-016-4435-8. arXiv: 1606.01674 [hep-ph].

[162] Albert M. Sirunyan et al. "Search for resonant pair production of Higgs bosons decaying to bottom quark-antiquark pairs in proton-proton collisions at 13 TeV". In: JHEP 08 (2018), p. 152. DOI: 10.1007/JHEP08(2018)152. arXiv: 1806.03548 [hep-ex].

[163] T. Inami, C. S. Lim, and A. Yamada. "Radiative correction parameter S in beyond the standard models". In: Mod. Phys. Lett. A 7 (1992), pp. 2789–2798. DOI: 10.1142/S021773239200416X.

[164] Piotr H. Chankowski et al. "Do precision electroweak constraints guarantee e+ e- collider discovery of at least one Higgs boson of a two Higgs doublet model?" In: Phys. Lett. B 496 (2000). Ed. by Ties Behnke et al., pp. 195–205. DOI: 10.1016/S0370-2693(00)01293-4. arXiv: hep-ph/0009271.

[165] Debajyoti Choudhury, Timothy M. P. Tait, and C. E. M. Wagner. "Probing heavy Higgs boson models with a TeV linear collider". In: Phys. Rev. D 65 (2002), p. 115007. DOI: 10.1103/PhysRevD.65.115007. arXiv: hep-ph/0202162.

[166] C. Patrignani et al. "Review of Particle Physics". In: Chin. Phys. C 40.10 (2016), p. 100001. DOI: 10.1088/1674-1137/40/10/100001.

[167] D. G. Cerdeno et al. "Theoretical predictions for the direct detection of neutralino dark matter in the NMSSM". In: JHEP 12 (2004), p. 048. DOI: 10.1088/1126-6708/2004/12/048. arXiv: hep-ph/0408102.

[168] G. Belanger et al. "Relic density of dark matter in the NMSSM". In: JCAP 09 (2005), p. 001. DOI: 10.1088/1475-7516/2005/09/001. arXiv: hep-ph/0505142.

[169] John F. Gunion, Dan Hooper, and Bob McElrath. "Light neutralino dark matter in the NMSSM". In: Phys. Rev. D 73 (2006), p. 015011. DOI: 10.1103/PhysRevD.73.015011. arXiv: hep-ph/0509024.

[170] D. G. Cerdeno et al. "Phenomenological viability of neutralino dark matter in the NMSSM". In: JCAP 06 (2007), p. 008. DOI: 10.1088/1475-7516/2007/06/008. arXiv: hep-ph/0701271.

[171] Jun-Jie Cao et al. "Light dark matter in NMSSM and implication on Higgs phenomenology". In: Phys. Lett. B 703 (2011), pp. 292–297. DOI: 10.1016/j.physletb.2011.07.086. arXiv: 1104.1754 [hep-ph].

[172] Jonathan Kozaczuk and Stefano Profumo. "Light NMSSM neutralino dark matter in the wake of CDMS II and a 126 GeV Higgs boson". In: Phys. Rev. D 89.9 (2014), p. 095012. DOI: 10.1103/PhysRevD.89.095012. arXiv: 1308.5705 [hep-ph].

[173] Lei Wang, Rongle Shi, and Xiao-Fang Han. "Wrong sign Yukawa coupling of the 2HDM with a singlet scalar as dark matter confronted with dark matter and Higgs data". In: Phys. Rev. D 96.11 (2017), p. 115025. DOI: 10.1103/PhysRevD.96.115025. arXiv: 1708.06882 [hep-ph].

[174] Kim Griest and David Seckel. "Three exceptions in the calculation of relic abundances". In: Phys. Rev. D 43 (1991), pp. 3191–3203. DOI: 10.1103/PhysRevD.43.3191.

[175] Manuel Drees and Mihoko M. Nojiri. “The Neutralino relic density in minimal $N = 1$ supergravity”. In: Phys. Rev. D 47 (1993), pp. 376–408. DOI: `10.1103/PhysRevD.47.376`. arXiv: `hep-ph/9207234`.

[176] Sebastian Baum et al. “Higgs portals for thermal Dark Matter. EFT perspectives and the NMSSM”. In: JHEP 04 (2018), p. 069. DOI: `10.1007/JHEP04(2018)069`. arXiv: `1712.09873 [hep-ph]`.

[177] Christopher Brust et al. “SUSY, the Third Generation and the LHC”. In: JHEP 03 (2012), p. 103. DOI: `10.1007/JHEP03(2012)103`. arXiv: `1110.6670 [hep-ph]`.

[178] Ulrich Ellwanger. “A Higgs boson near 125 GeV with enhanced di-photon signal in the NMSSM”. In: JHEP 03 (2012), p. 044. DOI: `10.1007/JHEP03(2012)044`. arXiv: `1112.3548 [hep-ph]`.

[179] S. F. King et al. “Discovery Prospects for NMSSM Higgs Bosons at the High-Energy Large Hadron Collider”. In: Phys. Rev. D 90.9 (2014), p. 095014. DOI: `10.1103/PhysRevD.90.095014`. arXiv: `1408.1120 [hep-ph]`.

[180] John R. Ellis, S. Kelley, and Dimitri V. Nanopoulos. “Probing the desert using gauge coupling unification”. In: Phys. Lett. B 260 (1991), pp. 131–137. DOI: `10.1016/0370-2693(91)90980-5`.

[181] Paul Langacker and Ming-xing Luo. “Implications of precision electroweak experiments for M_t, ρ_0, $\sin^2 \theta_W$ and grand unification”. In: Phys. Rev. D 44 (1991), pp. 817–822. DOI: `10.1103/PhysRevD.44.817`.

[182] Ugo Amaldi, Wim de Boer, and Hermann Furstenau. “Comparison of grand unified theories with electroweak and strong coupling constants measured at LEP”. In: Phys. Lett. B 260 (1991), pp. 447–455. DOI: `10.1016/0370-2693(91)91641-8`.

[183] Morad Aaboud et al. “Search for a scalar partner of the top quark in the jets plus missing transverse momentum final state at $\sqrt{s}$=13 TeV with the ATLAS detector”. In: JHEP 12 (2017), p. 085. DOI: `10.1007/JHEP12(2017)085`. arXiv: `1709.04183 [hep-ex]`.

[184] Morad Aaboud et al. “Search for top-squark pair production in final states with one lepton, jets, and missing transverse momentum using 36 fb^1 of $\sqrt{s} = 13$ TeV pp collision data with the ATLAS detector”. In: JHEP 06 (2018), p. 108. DOI: `10.1007/JHEP06(2018)108`. arXiv: `1711.11520 [hep-ex]`.

[185] Albert M Sirunyan et al. “Search for direct top squark pair production in events with one lepton, jets, and missing transverse momentum at 13 TeV with the CMS experiment”. In: JHEP 05 (2020), p. 032. DOI: `10.1007/JHEP05(2020)032`. arXiv: `1912.08887 [hep-ex]`.

[186] “Search for direct top squark pair production in the 3-body decay mode with a final state containing one lepton, jets, and missing transverse momentum in $\sqrt{s} = 13$TeV pp collision data with the ATLAS detector”. In: (May 2019).

[187] Marcela Carena et al. “Impersonating the Standard Model Higgs Boson: Alignment without Decoupling”. In: JHEP 04 (2014), p. 015. DOI: `10.1007/JHEP04(2014)015`. arXiv: `1310.2248 [hep-ph]`.

[188] Nina M. Coyle, Bing Li, and Carlos E. M. Wagner. “Wrong sign bottom Yukawa coupling in low energy supersymmetry”. In: Phys. Rev. D 97.11 (2018), p. 115028. DOI: `10.1103/PhysRevD.97.115028`. arXiv: `1802.09122 [hep-ph]`.

[189] P. S. Bhupal Dev and Apostolos Pilaftsis. “Maximally Symmetric Two Higgs Doublet Model with Natural Standard Model Alignment”. In: JHEP 12 (2014). [Erratum: JHEP 11, 147 (2015)], p. 024. DOI: `10.1007/JHEP12(2014)024`. arXiv: `1408.3405 [hep-ph]`.

[190] P. S. Bhupal Dev and Apostolos Pilaftsis. “Natural Alignment in the Two Higgs Doublet Model”. In: J. Phys. Conf. Ser. 873.1 (2017). Ed. by Bohdan Grzadkowski, Jan Kalinowski, and Maria Krawczyk, p. 012008. DOI: `10.1088/1742-6596/873/1/012008`. arXiv: `1703.05730 [hep-ph]`.

[191] Karim Benakli, Mark D. Goodsell, and Sophie L. Williamson. “Higgs alignment from extended supersymmetry”. In: Eur. Phys. J. C 78.8 (2018), p. 658. DOI: `10.1140/epjc/s10052-018-6125-1`. arXiv: `1801.08849 [hep-ph]`.

[192] Karim Benakli, Yifan Chen, and Gaëtan Lafforgue-Marmet. “R-symmetry for Higgs alignment without decoupling”. In: Eur. Phys. J. C 79.2 (2019), p. 172. DOI: `10.1140/epjc/s10052-019-6676-9`. arXiv: `1811.08435 [hep-ph]`.

[193] Neda Darvishi and Apostolos Pilaftsis. “Quartic Coupling Unification in the Maximally Symmetric 2HDM”. In: Phys. Rev. D 99.11 (2019), p. 115014. DOI: `10.1103/PhysRevD.99.115014`. arXiv: `1904.06723 [hep-ph]`.

[194] Roni Harnik et al. “The Minimal supersymmetric fat Higgs model”. In: Phys. Rev. D 70 (2004), p. 015002. DOI: `10.1103/PhysRevD.70.015002`. arXiv: `hep-ph/0311349`.

[195] Spencer Chang, Can Kilic, and Rakhi Mahbubani. “The New fat Higgs: Slimmer and more attractive”. In: Phys. Rev. D 71 (2005), p. 015003. DOI: `10.1103/PhysRevD.71.015003`. arXiv: `hep-ph/0405267`.

[196] Antonio Delgado and Timothy M. P. Tait. “A Fat Higgs with a Fat top”. In: JHEP 07 (2005), p. 023. DOI: `10.1088/1126-6708/2005/07/023`. arXiv: `hep-ph/0504224`.

[197] Howard Georgi, Aneesh Manohar, and Gregory W. Moore. “Constraints on a Two Higgs Interpretation of the Zeta (8.3)”. In: Phys. Lett. B 149 (1984), pp. 234–238. DOI: `10.1016/0370-2693(84)91591-0`.

[198] Howard Georgi and Lisa Randall. “Flavor Conserving CP Violation in Invisible Axion Models”. In: Nucl. Phys. B 276 (1986), pp. 241–252. DOI: `10.1016/0550-3213(86)90022-2`.

[199] Markus A. Luty. “Naive dimensional analysis and supersymmetry”. In: Phys. Rev. D 57 (1998), pp. 1531–1538. DOI: `10.1103/PhysRevD.57.1531`. arXiv: `hep-ph/9706235`.

[200] Andrew G. Cohen, David B. Kaplan, and Ann E. Nelson. “Counting 4 pis in strongly coupled supersymmetry”. In: Phys. Lett. B 412 (1997), pp. 301–308. DOI: `10.1016/S0370-2693(97)00995-7`. arXiv: `hep-ph/9706275`.

[201] G. F. Giudice and A. Masiero. “A Natural Solution to the mu Problem in Supergravity Theories”. In: Phys. Lett. B 206 (1988), pp. 480–484. DOI: `10.1016/0370-2693(88)91613-9`.

[202] G. F. Giudice and R. Rattazzi. “Extracting supersymmetry breaking effects from wave function renormalization”. In: Nucl. Phys. B 511 (1998), pp. 25–44. DOI: `10.1016/S0550-3213(97)00647-0`. arXiv: `hep-ph/9706540`.

[203] D. Dicus, A. Stange, and S. Willenbrock. “Higgs decay to top quarks at hadron colliders”. In: Phys. Lett. B 333 (1994), pp. 126–131. DOI: `10.1016/0370-2693(94)91017-0`. arXiv: `hep-ph/9404359`.

[204] Marcela Carena and Zhen Liu. “Challenges and opportunities for heavy scalar searches in the $t\bar{t}$ channel at the LHC”. In: JHEP 11 (2016), p. 159. DOI: `10.1007/JHEP11(2016)159`. arXiv: `1608.07282 [hep-ph]`.

[205] Emanuele Bagnaschi et al. “MSSM Higgs Boson Searches at the LHC: Benchmark Scenarios for Run 2 and Beyond”. In: Eur. Phys. J. C 79.7 (2019), p. 617. DOI: `10.1140/epjc/s10052-019-7114-8`. arXiv: `1808.07542 [hep-ph]`.

[206] M. Misiak et al. "Updated NNLO QCD predictions for the weak radiative B-meson decays". In: Phys. Rev. Lett. 114.22 (2015), p. 221801. DOI: 10.1103/PhysRevLett.114.221801. arXiv: 1503.01789 [hep-ph].

[207] Mikolaj Misiak. "Bounds on $M_{H^\pm}$ from $\bar{B} \to X_{s,d}\gamma$ Decays". In: Acta Phys. Polon. B 48 (2017), p. 2173. DOI: 10.5506/APhysPolB.48.2173.

[208] Haukur Arason et al. "Top quark and Higgs mass bounds from a numerical study of superGUTs". In: Phys. Rev. Lett. 67 (1991), p. 2933. DOI: 10.1103/PhysRevLett.67.2933.

[209] Christopher F. Kolda et al. "Predictions for constrained minimal supersymmetry with bottom tau mass unification". In: Phys. Rev. D 50 (1994), pp. 3498–3507. DOI: 10.1103/PhysRevD.50.3498. arXiv: hep-ph/9404253.

[210] William A. Bardeen et al. "Infrared Fixed Point Solution for the Top Quark Mass and Unification of Couplings in the MSSM". In: Phys. Lett. B 320 (1994), pp. 110–116. DOI: 10.1016/0370-2693(94)90832-X. arXiv: hep-ph/9309293.

[211] William A. Bardeen, Christopher T. Hill, and Manfred Lindner. "Minimal Dynamical Symmetry Breaking of the Standard Model". In: Phys. Rev. D 41 (1990), p. 1647. DOI: 10.1103/PhysRevD.41.1647.

[212] T. E. Clark, S. T. Love, and William A. Bardeen. "The Top Quark Mass in a Supersymmetric Standard Model with Dynamical Symmetry Breaking". In: Phys. Lett. B 237 (1990), pp. 235–241. DOI: 10.1016/0370-2693(90)91435-E.

[213] Marcela S. Carena et al. "Dynamical symmetry breaking and the top quark mass in the minimal supersymmetric standard model". In: Nuclear Physics. B 369.1-2 (1992). ISSN: 0550-3213. DOI: 10.1016/0550-3213(92)90377-N. URL: https://www.osti.gov/biblio/1155534.

[214] Shinji Komine and Masahiro Yamaguchi. "Bottom tau unification in SUSY SU(5) GUT and constraints from b —> s gamma and muon g-2". In: Phys. Rev. D 65 (2002), p. 075013. DOI: 10.1103/PhysRevD.65.075013. arXiv: hep-ph/0110032.

[215] Howard Baer et al. "Sparticle mass spectra from SU(5) SUSY GUT models with $b-\tau$ Yukawa coupling unification". In: JHEP 03 (2012), p. 047. DOI: 10.1007/JHEP03(2012)047. arXiv: 1201.4412 [hep-ph].

[216] Oleksandr Tomalak et al. "QED radiative corrections to neutrino-nucleon elastic scattering". In: (May 2021). arXiv: 2105.07939 [hep-ph].

[217] Artur M. Ankowski et al. "Lepton-Nucleus Cross Section Measurements for DUNE with the LDMX Detector". In: Phys. Rev. D 101.5 (2020), p. 053004. DOI: 10.1103/PhysRevD.101.053004. arXiv: 1912.06140 [hep-ph].

[218] M. Khachatryan et al. "Electron-beam energy reconstruction for neutrino oscillation measurements". In: Nature 599.7886 (2021), pp. 565–570. DOI: 10.1038/s41586-021-04046-5.

[219] Alexander Friedland and Shirley Weishi Li. "Understanding the energy resolution of liquid argon neutrino detectors". In: Phys. Rev. D 99.3 (2019), p. 036009. DOI: 10.1103/PhysRevD.99.036009. arXiv: 1811.06159 [hep-ph].

[220] B. Bhandari et al. "First Measurement of the Total Neutron Cross Section on Argon Between 100 and 800 MeV". In: Phys. Rev. Lett. 123.4 (2019), p. 042502. DOI: 10.1103/PhysRevLett.123.042502. arXiv: 1903.05276 [hep-ex].

[221] Alexander Friedland and Shirley Weishi Li. "Simulating hadron test beams in liquid argon". In: Phys. Rev. D 102.9 (2020), p. 096005. DOI: 10.1103/PhysRevD.102.096005. arXiv: 2007.13336 [hep-ph].

[222] C. Andreopoulos et al. "The GENIE Neutrino Monte Carlo Generator". In: Nucl. Instrum. Meth. A 614 (2010), pp. 87–104. DOI: `10.1016/j.nima.2009.12.009`. arXiv: `0905.2517 [hep-ph]`.

[223] T. Golan, J. T. Sobczyk, and J. Zmuda. "NuWro: the Wroclaw Monte Carlo Generator of Neutrino Interactions". In: Nucl. Phys. B Proc. Suppl. 229-232 (2012). Ed. by George S. Tzanakos, pp. 499–499. DOI: `10.1016/j.nuclphysbps.2012.09.136`.

[224] O. Buss et al. "Transport-theoretical Description of Nuclear Reactions". In: Phys. Rept. 512 (2012), pp. 1–124. DOI: `10.1016/j.physrep.2011.12.001`. arXiv: `1106.1344 [hep-ph]`.

[225] Joshua Isaacson et al. "ACHILLES: A novel event generator for electron- and neutrino-nucleus scattering". In: (May 2022). arXiv: `2205.06378 [hep-ph]`.

[226] M. A. Acero et al. "Improved measurement of neutrino oscillation parameters by the NOvA experiment". In: Phys. Rev. D 106.3 (2022), p. 032004. DOI: `10.1103/PhysRevD.106.032004`. arXiv: `2108.08219 [hep-ex]`.

[227] K. Abe et al. "Improved constraints on neutrino mixing from the T2K experiment with $\mathbf{3.13 \times 10^{21}}$ protons on target". In: Phys. Rev. D 103.11 (2021), p. 112008. DOI: `10.1103/PhysRevD.103.112008`. arXiv: `2101.03779 [hep-ex]`.

[228] M. A. Acero et al. "New constraints on oscillation parameters from ν_e appearance and ν_μ disappearance in the NOvA experiment". In: Phys. Rev. D 98 (2018), p. 032012. DOI: `10.1103/PhysRevD.98.032012`. arXiv: `1806.00096 [hep-ex]`.

[229] M. A. Acero et al. "Adjusting neutrino interaction models and evaluating uncertainties using NOvA near detector data". In: Eur. Phys. J. C 80.12 (2020), p. 1119. DOI: `10.1140/epjc/s10052-020-08577-5`. arXiv: `2006.08727 [hep-ex]`.

[230] Aaron S. Meyer et al. "Deuterium target data for precision neutrino-nucleus cross sections". In: Phys. Rev. D 93.11 (2016), p. 113015. DOI: `10.1103/PhysRevD.93.113015`. arXiv: `1603.03048 [hep-ph]`.

[231] Richard Gran. "Model Uncertainties for Valencia RPA Effect for MINERvA". In: (May 2017). arXiv: `1705.02932 [hep-ex]`.

[232] Philip Rodrigues, Callum Wilkinson, and Kevin McFarland. "Constraining the GENIE model of neutrino-induced single pion production using reanalyzed bubble chamber data". In: Eur. Phys. J. C 76.8 (2016), p. 474. DOI: `10.1140/epjc/s10052-016-4314-3`. arXiv: `1601.01888 [hep-ex]`.

[233] A. A. Aguilar-Arevalo et al. "Measurement of Neutrino-Induced Charged-Current Charged Pion Production Cross Sections on Mineral Oil at $E_\nu \sim 1$ GeV". In: Phys. Rev. D 83 (2011), p. 052007. DOI: `10.1103/PhysRevD.83.052007`. arXiv: `1011.3572 [hep-ex]`.

[234] P. Adamson et al. "Study of quasielastic scattering using charged-current $\nu\mu$ -iron interactions in the MINOS near detector". In: Phys. Rev. D 91.1 (2015), p. 012005. DOI: `10.1103/PhysRevD.91.012005`. arXiv: `1410.8613 [hep-ex]`.

[235] C. L. McGivern et al. "Cross sections for ν_μ and $\bar{\nu}_\mu$ induced pion production on hydrocarbon in the few-GeV region using MINERvA". In: Phys. Rev. D 94.5 (2016), p. 052005. DOI: `10.1103/PhysRevD.94.052005`. arXiv: `1606.07127 [hep-ex]`.

[236] O. Altinok et al. "Measurement of ν_μ charged-current single π^0 production on hydrocarbon in the few-GeV region using MINERvA". In: Phys. Rev. D 96.7 (2017), p. 072003. DOI: `10.1103/PhysRevD.96.072003`. arXiv: `1708.03723 [hep-ex]`.

[237] K. Abe et al. "Measurement of the muon neutrino charged-current single π^+ production on hydrocarbon using the T2K off-axis near detector ND280". In: Phys. Rev. D

101.1 (2020), p. 012007. DOI: `10.1103/PhysRevD.101.012007`. arXiv: `1909.03936 [hep-ex]`.

[238] K. Kainulainen, J. Maalampi, and J. T. Peltoniemi. "Inert neutrinos in supernovae". In: Nucl. Phys. B 358 (1991), pp. 435–446. DOI: `10.1016/0550-3213(91)90354-Z`.

[239] Kevin J. Kelly and Yue Zhang. "Mononeutrino at DUNE: New Signals from Neutrinophilic Thermal Dark Matter". In: Phys. Rev. D 99.5 (2019), p. 055034. DOI: `10.1103/PhysRevD.99.055034`. arXiv: `1901.01259 [hep-ph]`.

[240] NOvA Collaboration. Flux Histograms for 2017 Analysis. `http://publicdocs.fnal.gov/cgi-bin/ShowDocument?docid=8`.

[241] Keloth, Rijeesh. NOvA Short-Baseline Tau-Neutrino Appearance Search. `https://absuploads.aps.org/presentation.cfm?pid=12831`.

[242] Teppei Katori. "Meson Exchange Current (MEC) Models in Neutrino Interaction Generators". In: AIP Conf. Proc. 1663.1 (2015). Ed. by H. Da Motta, Jorge G. Morfin, and M. Sakuda, p. 030001. DOI: `10.1063/1.4919465`. arXiv: `1304.6014 [nucl-th]`.

[243] J. Nieves, I. Ruiz Simo, and M. J. Vicente Vacas. "Inclusive Charged–Current Neutrino–Nucleus Reactions". In: Phys. Rev. C 83 (2011), p. 045501. DOI: `10.1103/PhysRevC.83.045501`. arXiv: `1102.2777 [hep-ph]`.

[244] Jeffrey M. Berryman et al. "Lepton-Number-Charged Scalars and Neutrino Beamstrahlung". In: Phys. Rev. D 97.7 (2018), p. 075030. DOI: `10.1103/PhysRevD.97.075030`. arXiv: `1802.00009 [hep-ph]`.

[245] Daniel Abercrombie et al. "Dark Matter benchmark models for early LHC Run-2 Searches: Report of the ATLAS/CMS Dark Matter Forum". In: Phys. Dark Univ. 27 (2020). Ed. by Antonio Boveia et al., p. 100371. DOI: `10.1016/j.dark.2019.100371`. arXiv: `1507.00966 [hep-ex]`.

[246] Johan Alwall et al. "MadGraph 5 : Going Beyond". In: JHEP 06 (2011), p. 128. DOI: `10.1007/JHEP06(2011)128`. arXiv: `1106.0522 [hep-ph]`.

[247] A. Filkins et al. "Double-differential inclusive charged-current ν_μ cross sections on hydrocarbon in MINERvA at $<E_\nu> \sim 3.5$ GeV". In: Phys. Rev. D 101.11 (2020), p. 112007. DOI: `10.1103/PhysRevD.101.112007`. arXiv: `2002.12496 [hep-ex]`.

[248] K. G. Klimenko. "On Necessary and Sufficient Conditions for Some Higgs Potentials to Be Bounded From Below". In: Theor. Math. Phys. 62 (1985), pp. 58–65. DOI: `10.1007/BF01034825`.

[249] A. Barroso, P. M. Ferreira, and R. Santos. "Neutral minima in two-Higgs doublet models". In: Phys. Lett. B 652 (2007), pp. 181–193. DOI: `10.1016/j.physletb.2007.07.010`. arXiv: `hep-ph/0702098`.

[250] Igor P. Ivanov. "Minkowski space structure of the Higgs potential in 2HDM. II. Minima, symmetries, and topology". In: Phys. Rev. D 77 (2008), p. 015017. DOI: `10.1103/PhysRevD.77.015017`. arXiv: `0710.3490 [hep-ph]`.

[251] P. M. Ferreira and D. R. T. Jones. "Bounds on scalar masses in two Higgs doublet models". In: JHEP 08 (2009), p. 069. DOI: `10.1088/1126-6708/2009/08/069`. arXiv: `0903.2856 [hep-ph]`.

[252] D. Jurvciukonis and L. Lavoura. "The three- and four-Higgs couplings in the general two-Higgs-doublet model". In: JHEP 12 (2018), p. 004. DOI: `10.1007/JHEP12(2018)004`. arXiv: `1807.04244 [hep-ph]`.

[253] Shinya Kanemura, Takahiro Kubota, and Eiichi Takasugi. "Lee-Quigg-Thacker bounds for Higgs boson masses in a two doublet model". In: Phys. Lett. B 313 (1993), pp. 155–160. DOI: `10.1016/0370-2693(93)91205-2`. arXiv: `hep-ph/9303263`.

[254] Andrew G. Akeroyd, Abdesslam Arhrib, and El-Mokhtar Naimi. "Note on tree level unitarity in the general two Higgs doublet model". In: Phys. Lett. B 490 (2000), pp. 119–124. DOI: `10.1016/S0370-2693(00)00962-X`. arXiv: `hep-ph/0006035`.

[255] P. M. Ferreira, R. Santos, and A. Barroso. "Stability of the tree-level vacuum in two Higgs doublet models against charge or CP spontaneous violation". In: Phys. Lett. B 603 (2004). [Erratum: Phys.Lett.B 629, 114–114 (2005)], pp. 219–229. DOI: `10.1016/j.physletb.2004.10.022`. arXiv: `hep-ph/0406231`.

[256] J. Horejsi and M. Kladiva. "Tree-unitarity bounds for THDM Higgs masses revisited". In: Eur. Phys. J. C 46 (2006), pp. 81–91. DOI: `10.1140/epjc/s2006-02472-3`. arXiv: `hep-ph/0510154`.

[257] I. F. Ginzburg and I. P. Ivanov. "Tree-level unitarity constraints in the most general 2HDM". In: Phys. Rev. D 72 (2005), p. 115010. DOI: `10.1103/PhysRevD.72.115010`. arXiv: `hep-ph/0508020`.

[258] A. Barroso, P. M. Ferreira, and R. Santos. "Charge and CP symmetry breaking in two Higgs doublet models". In: Phys. Lett. B 632 (2006), pp. 684–687. DOI: `10.1016/j.physletb.2005.11.031`. arXiv: `hep-ph/0507224`.

[259] I. P. Ivanov. "Minkowski space structure of the Higgs potential in 2HDM". In: Phys. Rev. D 75 (2007). [Erratum: Phys.Rev.D 76, 039902 (2007)], p. 035001. DOI: `10.1103/PhysRevD.75.035001`. arXiv: `hep-ph/0609018`.

[260] M. Maniatis et al. "Stability and symmetry breaking in the general two-Higgs-doublet model". In: Eur. Phys. J. C 48 (2006), pp. 805–823. DOI: `10.1140/epjc/s10052-006-0016-6`. arXiv: `hep-ph/0605184`.

[261] Yisheng Song. "Co-positivity of tensors and Stability conditions of two Higgs potentials". In: (Mar. 2022). arXiv: `2203.11462 [hep-ph]`.

[262] Kenneth Ross Garren. "Bounds for the Eigenvalues of a Matrix". PhD thesis. William and Mary, 1965. DOI: `10.21220/s2-p2tn-7046`.

[263] S. Gershgorin. "Über die Abgrenzung der Eigenwerte einer Matrix". In: Bulletin de l'Academie des Sciences de l'URSS 6.3 (1931), pp. 749–754.

[264] Miguel P. Bento, Jorge C. Romão, and João P. Silva. "Unitarity bounds for all symmetry-constrained 3HDMs". In: (Apr. 2022). arXiv: `2204.13130 [hep-ph]`.

[265] Shinya Kanemura and Kei Yagyu. "Unitarity bound in the most general two Higgs doublet model". In: Phys. Lett. B 751 (2015), pp. 289–296. DOI: `10.1016/j.physletb.2015.10.047`. arXiv: `1509.06060 [hep-ph]`.

[266] Gary Ulrich and Layne T. Watson. "Positivity Conditions for Quartic Polynomials". In: SIAM Journal on Scientific Computing 15.3 (1994), pp. 528–544. DOI: `10.1137/0915035`. eprint: `https://doi.org/10.1137/0915035`. URL: `https://doi.org/10.1137/0915035`.

[267] A. Barroso et al. "Metastability bounds on the two Higgs doublet model". In: JHEP 06 (2013), p. 045. DOI: `10.1007/JHEP06(2013)045`. arXiv: `1303.5098 [hep-ph]`.

[268] I. P. Ivanov and Joao P. Silva. "Tree-level metastability bounds for the most general two Higgs doublet model". In: Phys. Rev. D 92.5 (2015), p. 055017. DOI: `10.1103/PhysRevD.92.055017`. arXiv: `1507.05100 [hep-ph]`.

[269] Ian Low, Nausheen R. Shah, and Xiao-Ping Wang. "Higgs alignment and novel CP-violating observables in two-Higgs-doublet models". In: Phys. Rev. D 105.3 (2022), p. 035009. DOI: `10.1103/PhysRevD.105.035009`. arXiv: `2012.00773 [hep-ph]`.

[270] Howard E. Haber and Oscar Stål. "New LHC benchmarks for the $\mathcal{CP}$ -conserving two-Higgs-doublet model". In: Eur. Phys. J. C 75.10 (2015). [Erratum: Eur.Phys.J.C

76, 312 (2016)], p. 491. DOI: `10.1140/epjc/s10052-015-3697-x`. arXiv: `1507.04281 [hep-ph]`.

[271] Rafael Boto et al. "Basis-independent treatment of the complex 2HDM". In: Phys. Rev. D 101.5 (2020), p. 055023. DOI: `10.1103/PhysRevD.101.055023`. arXiv: `2001.01430 [hep-ph]`.

[272] V. Andreev et al. "Improved limit on the electric dipole moment of the electron". In: Nature 562.7727 (2018), pp. 355–360. DOI: `10.1038/s41586-018-0599-8`.

[273] Wolfgang Altmannshofer et al. "Electron EDM in the complex two-Higgs doublet model". In: Phys. Rev. D 102.11 (2020), p. 115042. DOI: `10.1103/PhysRevD.102.115042`. arXiv: `2009.01258 [hep-ph]`.

[274] Howard E. Haber, Venus Keus, and Rui Santos. "P-even, CP-violating Signals in Scalar-Mediated Processes". In: (June 2022). arXiv: `2206.09643 [hep-ph]`.

[275] M. Tanabashi et al. "Review of Particle Physics". In: Phys. Rev. D 98.3 (2018), p. 030001. DOI: `10.1103/PhysRevD.98.030001`.

[276] Tevatron Electroweak Working Group. "2012 Update of the Combination of CDF and D0 Results for the Mass of the W Boson". In: (Apr. 2012). arXiv: `1204.0042 [hep-ex]`.

[277] S. Schael et al. "Precision electroweak measurements on the Z resonance". In: Phys. Rept. 427 (2006), pp. 257–454. DOI: `10.1016/j.physrep.2005.12.006`. arXiv: `hep-ex/0509008`.

[278] the SLD Electroweak. "A Combination of preliminary electroweak measurements and constraints on the standard model". In: (Dec. 2003). arXiv: `hep-ex/0312023`.

[279] S. Schael et al. "Electroweak Measurements in Electron-Positron Collisions at W-Boson-Pair Energies at LEP". In: Phys. Rept. 532 (2013), pp. 119–244. DOI: `10.1016/j.physrep.2013.07.004`. arXiv: `1302.3415 [hep-ex]`.

[280] Georges Aad et al. "Observation of a new particle in the search for the Standard Model Higgs boson with the ATLAS detector at the LHC". In: Phys. Lett. B 716 (2012), pp. 1–29. DOI: `10.1016/j.physletb.2012.08.020`. arXiv: `1207.7214 [hep-ex]`.

[281] Serguei Chatrchyan et al. "Observation of a New Boson at a Mass of 125 GeV with the CMS Experiment at the LHC". In: Phys. Lett. B 716 (2012), pp. 30–61. DOI: `10.1016/j.physletb.2012.08.021`. arXiv: `1207.7235 [hep-ex]`.

[282] Georges Aad et al. "Combined Measurement of the Higgs Boson Mass in pp Collisions at $\sqrt{s} = 7$ and 8 TeV with the ATLAS and CMS Experiments". In: Phys. Rev. Lett. 114 (2015), p. 191803. DOI: `10.1103/PhysRevLett.114.191803`. arXiv: `1503.07589 [hep-ex]`.

[283] Antonio Delgado, Germano Nardini, and Mariano Quiros. "A Light Supersymmetric Higgs Sector Hidden by a Standard Model-like Higgs". In: JHEP 07 (2013), p. 054. DOI: `10.1007/JHEP07(2013)054`. arXiv: `1303.0800 [hep-ph]`.

[284] Howard E. Haber, Sven Heinemeyer, and Tim Stefaniak. "The Impact of Two-Loop Effects on the Scenario of MSSM Higgs Alignment without Decoupling". In: Eur. Phys. J. C 77.11 (2017), p. 742. DOI: `10.1140/epjc/s10052-017-5243-5`. arXiv: `1708.04416 [hep-ph]`.

[285] G. Degrassi et al. "Towards high precision predictions for the MSSM Higgs sector". In: Eur. Phys. J. C 28 (2003), pp. 133–143. DOI: `10.1140/epjc/s2003-01152-2`. arXiv: `hep-ph/0212020`.

[286] Gian F. Giudice and Alessandro Strumia. "Probing High-Scale and Split Supersymmetry with Higgs Mass Measurements". In: Nucl. Phys. B 858 (2012), pp. 63–83. DOI: `10.1016/j.nuclphysb.2012.01.001`. arXiv: `1108.6077 [hep-ph]`.

[287] John F. Gunion, Yun Jiang, and Sabine Kraml. "The Constrained NMSSM and Higgs near 125 GeV". In: Phys. Lett. B 710 (2012), pp. 454–459. DOI: `10.1016/j.physletb.2012.03.027`. arXiv: `1201.0982 [hep-ph]`.

[288] S. F. King, M. Muhlleitner, and R. Nevzorov. "NMSSM Higgs Benchmarks Near 125 GeV". In: Nucl. Phys. B 860 (2012), pp. 207–244. DOI: `10.1016/j.nuclphysb.2012.02.010`. arXiv: `1201.2671 [hep-ph]`.

[289] Jun-Jie Cao et al. "A SM-like Higgs near 125 GeV in low energy SUSY: a comparative study for MSSM and NMSSM". In: JHEP 03 (2012), p. 086. DOI: `10.1007/JHEP03(2012)086`. arXiv: `1202.5821 [hep-ph]`.

[290] Daniel Albornoz Vasquez et al. "The 125 GeV Higgs in the NMSSM in light of LHC results and astrophysics constraints". In: Phys. Rev. D 86 (2012), p. 035023. DOI: `10.1103/PhysRevD.86.035023`. arXiv: `1203.3446 [hep-ph]`.

[291] Ulrich Ellwanger and Cyril Hugonie. "Higgs bosons near 125 GeV in the NMSSM with constraints at the GUT scale". In: Adv. High Energy Phys. 2012 (2012), p. 625389. DOI: `10.1155/2012/625389`. arXiv: `1203.5048 [hep-ph]`.

[292] Kaustubh Agashe, Yanou Cui, and Roberto Franceschini. "Natural Islands for a 125 GeV Higgs in the scale-invariant NMSSM". In: JHEP 02 (2013), p. 031. DOI: `10.1007/JHEP02(2013)031`. arXiv: `1209.2115 [hep-ph]`.

[293] Kamila Kowalska et al. "Constrained next-to-minimal supersymmetric standard model with a 126 GeV Higgs boson: A global analysis". In: Phys. Rev. D 87 (2013), p. 115010. DOI: `10.1103/PhysRevD.87.115010`. arXiv: `1211.1693 [hep-ph]`.

[294] S. F. King et al. "Natural NMSSM Higgs Bosons". In: Nucl. Phys. B 870 (2013), pp. 323–352. DOI: `10.1016/j.nuclphysb.2013.01.020`. arXiv: `1211.5074 [hep-ph]`.

[295] Tony Gherghetta et al. "The Scale-Invariant NMSSM and the 126 GeV Higgs Boson". In: JHEP 02 (2013), p. 032. DOI: `10.1007/JHEP02(2013)032`. arXiv: `1212.5243 [hep-ph]`.

[296] Riccardo Barbieri et al. "Exploring the Higgs sector of a most natural NMSSM". In: Phys. Rev. D 87.11 (2013), p. 115018. DOI: `10.1103/PhysRevD.87.115018`. arXiv: `1304.3670 [hep-ph]`.

[297] Marcin Badziak, Marek Olechowski, and Stefan Pokorski. "New Regions in the NMSSM with a 125 GeV Higgs". In: JHEP 06 (2013), p. 043. DOI: `10.1007/JHEP06(2013)043`. arXiv: `1304.5437 [hep-ph]`.

[298] Ulrich Ellwanger. "Higgs pair production in the NMSSM at the LHC". In: JHEP 08 (2013), p. 077. DOI: `10.1007/JHEP08(2013)077`. arXiv: `1306.5541 [hep-ph]`.

[299] Florian Domingo and Georg Weiglein. "NMSSM interpretations of the observed Higgs signal". In: JHEP 04 (2016), p. 095. DOI: `10.1007/JHEP04(2016)095`. arXiv: `1509.07283 [hep-ph]`.

[300] Nathaniel Craig et al. "The Hunt for the Rest of the Higgs Bosons". In: JHEP 06 (2015), p. 137. DOI: `10.1007/JHEP06(2015)137`. arXiv: `1504.04630 [hep-ph]`.

[301] Sunghoon Jung, Jeonghyeon Song, and Yeo Woong Yoon. "Dip or nothingness of a Higgs resonance from the interference with a complex phase". In: Phys. Rev. D 92.5 (2015), p. 055009. DOI: `10.1103/PhysRevD.92.055009`. arXiv: `1505.00291 [hep-ph]`.

[302] Stefania Gori et al. “Closing the Wedge: Search Strategies for Extended Higgs Sectors with Heavy Flavor Final States”. In: Phys. Rev. D 93.7 (2016), p. 075038. DOI: `10.1103/PhysRevD.93.075038`. arXiv: `1602.02782 [hep-ph]`.

[303] B. C. Allanach and S. F. King. “Bottom - tau Yukawa unification in the next-to-minimal supersymmetric Standard Model”. In: Phys. Lett. B 328 (1994), pp. 360–368. DOI: `10.1016/0370-2693(94)91491-5`. arXiv: `hep-ph/9403212`.

[304] Marcela Carena, S. Pokorski, and C. E. M. Wagner. “On the unification of couplings in the minimal supersymmetric Standard Model”. In: Nucl. Phys. B 406 (1993), pp. 59–89. DOI: `10.1016/0550-3213(93)90161-H`. arXiv: `hep-ph/9303202`.

[305] Paul Langacker and Nir Polonsky. “The Bottom mass prediction in supersymmetric grand unification: Uncertainties and constraints”. In: Phys. Rev. D 49 (1994), pp. 1454–1467. DOI: `10.1103/PhysRevD.49.1454`. arXiv: `hep-ph/9306205`.

[306] Paul Langacker and Nir Polonsky. “Implications of Yukawa unification for the Higgs sector in supersymmetric grand unified models”. In: Phys. Rev. D 50 (1994), pp. 2199–2217. DOI: `10.1103/PhysRevD.50.2199`. arXiv: `hep-ph/9403306`.

[307] Barbara Schrempp. “Infrared fixed points and fixed lines in the top bottom τ sector in supersymmetric grand unification”. In: Phys. Lett. B 344 (1995), pp. 193–200. DOI: `10.1016/0370-2693(94)01559-U`. arXiv: `hep-ph/9411241`.

[308] J. Sato, K. Tobe, and T. Yanagida. “A Constraint on Yukawa coupling unification from lepton flavor violating processes”. In: Phys. Lett. B 498 (2001), pp. 189–194. DOI: `10.1016/S0370-2693(00)01395-2`. arXiv: `hep-ph/0010348`.

[309] Csaba Balazs and Radovan Dermisek. “Yukawa coupling unification and nonuniversal gaugino mediation of supersymmetry breaking”. In: JHEP 06 (2003), p. 024. DOI: `10.1088/1126-6708/2003/06/024`. arXiv: `hep-ph/0303161`.

[310] Daniel Auto et al. “Yukawa coupling unification in supersymmetric models”. In: JHEP 06 (2003), p. 023. DOI: `10.1088/1126-6708/2003/06/023`. arXiv: `hep-ph/0302155`.

[311] DUNE Collaboration. “`http://home.fnal.gov/~ljf26/DUNEFluxes/`”. In: ().

[312] Jeffrey M. Berryman et al. “Sterile neutrino at the Deep Underground Neutrino Experiment”. In: Phys. Rev. D 92.7 (2015), p. 073012. DOI: `10.1103/PhysRevD.92.073012`. arXiv: `1507.03986 [hep-ph]`.

[313] Murray Gell-Mann, Pierre Ramond, and Richard Slansky. “Complex Spinors and Unified Theories”. In: Conf. Proc. C 790927 (1979), pp. 315–321. arXiv: `1306.4669 [hep-th]`.

[314] Tsutomu Yanagida. “Horizontal gauge symmetry and masses of neutrinos”. In: Conf. Proc. C 7902131 (1979). Ed. by Osamu Sawada and Akio Sugamoto, pp. 95–99.

[315] Rabindra N. Mohapatra and Goran Senjanovic. “Neutrino Mass and Spontaneous Parity Nonconservation”. In: Phys. Rev. Lett. 44 (1980), p. 912. DOI: `10.1103/PhysRevLett.44.912`.

[316] J. Schechter and J. W. F. Valle. “Neutrino Masses in SU(2) x U(1) Theories”. In: Phys. Rev. D 22 (1980), p. 2227. DOI: `10.1103/PhysRevD.22.2227`.

[317] M. Magg and C. Wetterich. “Neutrino Mass Problem and Gauge Hierarchy”. In: Phys. Lett. B 94 (1980), pp. 61–64. DOI: `10.1016/0370-2693(80)90825-4`.

[318] Rabindra N. Mohapatra and Goran Senjanovic. “Neutrino Masses and Mixings in Gauge Models with Spontaneous Parity Violation”. In: Phys. Rev. D 23 (1981), p. 165. DOI: `10.1103/PhysRevD.23.165`.

[319] George Lazarides, Q. Shafi, and C. Wetterich. “Proton Lifetime and Fermion Masses in an SO(10) Model”. In: Nucl. Phys. B 181 (1981), pp. 287–300. DOI: `10.1016/0550-3213(81)90354-0`.

[320] Ernest Ma and Utpal Sarkar. "Neutrino masses and leptogenesis with heavy Higgs triplets". In: Phys. Rev. Lett. 80 (1998), pp. 5716–5719. DOI: `10.1103/PhysRevLett.80.5716`. arXiv: `hep-ph/9802445`.

[321] Robert Foot et al. "Seesaw Neutrino Masses Induced by a Triplet of Leptons". In: Z. Phys. C 44 (1989), p. 441. DOI: `10.1007/BF01415558`.

[322] Ernest Ma. "Pathways to naturally small neutrino masses". In: Phys. Rev. Lett. 81 (1998), pp. 1171–1174. DOI: `10.1103/PhysRevLett.81.1171`. arXiv: `hep-ph/9805219`.

[323] R. N. Mohapatra and J. W. F. Valle. "Neutrino Mass and Baryon Number Nonconservation in Superstring Models". In: Phys. Rev. D 34 (1986), p. 1642. DOI: `10.1103/PhysRevD.34.1642`.

[324] Teppei Katori and Marco Martini. "Neutrino–nucleus cross sections for oscillation experiments". In: J. Phys. G 45.1 (2018), p. 013001. DOI: `10.1088/1361-6471/aa8bf7`. arXiv: `1611.07770 [hep-ph]`.

[325] Brian Batell, Maxim Pospelov, and Adam Ritz. "Exploring Portals to a Hidden Sector Through Fixed Targets". In: Phys. Rev. D 80 (2009), p. 095024. DOI: `10.1103/PhysRevD.80.095024`. arXiv: `0906.5614 [hep-ph]`.

[326] Patrick deNiverville, Maxim Pospelov, and Adam Ritz. "Observing a light dark matter beam with neutrino experiments". In: Phys. Rev. D 84 (2011), p. 075020. DOI: `10.1103/PhysRevD.84.075020`. arXiv: `1107.4580 [hep-ph]`.

[327] Patrick deNiverville, David McKeen, and Adam Ritz. "Signatures of sub-GeV dark matter beams at neutrino experiments". In: Phys. Rev. D 86 (2012), p. 035022. DOI: `10.1103/PhysRevD.86.035022`. arXiv: `1205.3499 [hep-ph]`.

[328] R. Dharmapalan et al. "Low Mass WIMP Searches with a Neutrino Experiment: A Proposal for Further MiniBooNE Running". In: (Nov. 2012). arXiv: `1211.2258 [hep-ex]`.

[329] Eder Izaguirre et al. "New Electron Beam-Dump Experiments to Search for MeV to few-GeV Dark Matter". In: Phys. Rev. D 88 (2013), p. 114015. DOI: `10.1103/PhysRevD.88.114015`. arXiv: `1307.6554 [hep-ph]`.

[330] Brian Batell et al. "Leptophobic Dark Matter at Neutrino Factories". In: Phys. Rev. D 90.11 (2014), p. 115014. DOI: `10.1103/PhysRevD.90.115014`. arXiv: `1405.7049 [hep-ph]`.

[331] Bogdan A. Dobrescu and Claudia Frugiuele. "GeV-Scale Dark Matter: Production at the Main Injector". In: JHEP 02 (2015), p. 019. DOI: `10.1007/JHEP02(2015)019`. arXiv: `1410.1566 [hep-ph]`.

[332] Pilar Coloma et al. "Dark matter beams at LBNF". In: JHEP 04 (2016), p. 047. DOI: `10.1007/JHEP04(2016)047`. arXiv: `1512.03852 [hep-ph]`.

[333] Patrick deNiverville et al. "Light dark matter in neutrino beams: production modelling and scattering signatures at MiniBooNE, T2K and SHiP". In: Phys. Rev. D 95.3 (2017), p. 035006. DOI: `10.1103/PhysRevD.95.035006`. arXiv: `1609.01770 [hep-ph]`.

[334] Gabriel Magill and Ryan Plestid. "Neutrino Trident Production at the Intensity Frontier". In: Phys. Rev. D 95.7 (2017), p. 073004. DOI: `10.1103/PhysRevD.95.073004`. arXiv: `1612.05642 [hep-ph]`.

[335] P. Adamson et al. "Search for sterile neutrinos in MINOS and MINOS+ using a two-detector fit". In: Phys. Rev. Lett. 122.9 (2019), p. 091803. DOI: `10.1103/PhysRevLett.122.091803`. arXiv: `1710.06488 [hep-ex]`.

[336] Enrico Bertuzzo et al. "Dark Neutrino Portal to Explain MiniBooNE excess". In: Phys. Rev. Lett. 121.24 (2018), p. 241801. DOI: `10.1103/PhysRevLett.121.241801`. arXiv: `1807.09877 [hep-ph]`.

[337] Adam Falkowski, Giovanni Grilli di Cortona, and Zahra Tabrizi. "Future DUNE constraints on EFT". In: JHEP 04 (2018), p. 101. DOI: `10.1007/JHEP04(2018)101`. arXiv: `1802.08296 [hep-ph]`.

[338] Gabriel Magill et al. "Millicharged particles in neutrino experiments". In: Phys. Rev. Lett. 122.7 (2019), p. 071801. DOI: `10.1103/PhysRevLett.122.071801`. arXiv: `1806.03310 [hep-ph]`.

[339] Peter Ballett, Silvia Pascoli, and Mark Ross-Lonergan. "U(1)' mediated decays of heavy sterile neutrinos in MiniBooNE". In: Phys. Rev. D 99 (2019), p. 071701. DOI: `10.1103/PhysRevD.99.071701`. arXiv: `1808.02915 [hep-ph]`.

[340] André de Gouvêa et al. "Dark Tridents at Off-Axis Liquid Argon Neutrino Detectors". In: JHEP 01 (2019), p. 001. DOI: `10.1007/JHEP01(2019)001`. arXiv: `1809.06388 [hep-ph]`.

[341] Peter Ballett et al. "Neutrino Trident Scattering at Near Detectors". In: JHEP 01 (2019), p. 119. DOI: `10.1007/JHEP01(2019)119`. arXiv: `1807.10973 [hep-ph]`.

[342] Patrick deNiverville and Claudia Frugiuele. "Hunting sub-GeV dark matter with the NOνA near detector". In: Phys. Rev. D 99.5 (2019), p. 051701. DOI: `10.1103/PhysRevD.99.051701`. arXiv: `1807.06501 [hep-ph]`.

[343] Johnathon R. Jordan et al. "Signatures of Pseudo-Dirac Dark Matter at High-Intensity Neutrino Experiments". In: Phys. Rev. D 98.7 (2018), p. 075020. DOI: `10.1103/PhysRevD.98.075020`. arXiv: `1806.05185 [hep-ph]`.

[344] Johnathon R. Jordan et al. "Severe Constraints on New Physics Explanations of the MiniBooNE Excess". In: Phys. Rev. Lett. 122.8 (2019), p. 081801. DOI: `10.1103/PhysRevLett.122.081801`. arXiv: `1810.07185 [hep-ph]`.

[345] Peter Ballett et al. "Z's in neutrino scattering at DUNE". In: Phys. Rev. D 100.5 (2019), p. 055012. DOI: `10.1103/PhysRevD.100.055012`. arXiv: `1902.08579 [hep-ph]`.

[346] Roni Harnik, Zhen Liu, and Ornella Palamara. "Millicharged Particles in Liquid Argon Neutrino Experiments". In: JHEP 07 (2019), p. 170. DOI: `10.1007/JHEP07(2019)170`. arXiv: `1902.03246 [hep-ph]`.

[347] R. Acciarri et al. "Improved Limits on Millicharged Particles Using the ArgoNeuT Experiment at Fermilab". In: Phys. Rev. Lett. 124.13 (2020), p. 131801. DOI: `10.1103/PhysRevLett.124.131801`. arXiv: `1911.07996 [hep-ex]`.

[348] Wolfgang Altmannshofer et al. "Neutrino Tridents at DUNE". In: Phys. Rev. D 100.11 (2019), p. 115029. DOI: `10.1103/PhysRevD.100.115029`. arXiv: `1902.06765 [hep-ph]`.

[349] Yu-Dai Tsai, Patrick deNiverville, and Ming Xiong Liu. "Dark Photon and Muon $g-2$ Inspired Inelastic Dark Matter Models at the High-Energy Intensity Frontier". In: Phys. Rev. Lett. 126.18 (2021), p. 181801. DOI: `10.1103/PhysRevLett.126.181801`. arXiv: `1908.07525 [hep-ph]`.

[350] Brian Batell, Joshua Berger, and Ahmed Ismail. "Probing the Higgs Portal at the Fermilab Short-Baseline Neutrino Experiments". In: Phys. Rev. D 100.11 (2019), p. 115039. DOI: `10.1103/PhysRevD.100.115039`. arXiv: `1909.11670 [hep-ph]`.

[351] C. A. Argüelles et al. "New opportunities at the next-generation neutrino experiments I: BSM neutrino physics and dark matter". In: Rept. Prog. Phys. 83.12 (2020), p. 124201. DOI: `10.1088/1361-6633/ab9d12`. arXiv: `1907.08311 [hep-ph]`.

[352] Valentina De Romeri, Kevin J. Kelly, and Pedro A. N. Machado. “DUNE-PRISM Sensitivity to Light Dark Matter”. In: Phys. Rev. D 100.9 (2019), p. 095010. DOI: `10.1103/PhysRevD.100.095010`. arXiv: `1903.10505 [hep-ph]`.

[353] Andre de Gouvea et al. “Measuring the Weak Mixing Angle in the DUNE Near Detector Complex”. In: Phys. Rev. Lett. 125.5 (2020), p. 051803. DOI: `10.1103/PhysRevLett.125.051803`. arXiv: `1912.06658 [hep-ph]`.

[354] Jeffrey M. Berryman et al. “Searches for Decays of New Particles in the DUNE Multi-Purpose Near Detector”. In: JHEP 02 (2020), p. 174. DOI: `10.1007/JHEP02(2020)174`. arXiv: `1912.07622 [hep-ph]`.

[355] B. Abi et al. “Prospects for beyond the Standard Model physics searches at the Deep Underground Neutrino Experiment”. In: Eur. Phys. J. C 81.4 (2021), p. 322. DOI: `10.1140/epjc/s10052-021-09007-w`. arXiv: `2008.12769 [hep-ex]`.

[356] Andreas S. Kronfeld et al. “Lattice QCD and Neutrino-Nucleus Scattering”. In: Eur. Phys. J. A 55.11 (2019), p. 196. DOI: `10.1140/epja/i2019-12916-x`. arXiv: `1904.09931 [hep-lat]`.

[357] Hugo W. Bertini. “Low-Energy Intranuclear Cascade Calculation”. In: Phys. Rev. 131 (1963), pp. 1801–1821. DOI: `10.1103/PhysRev.131.1801`.

[358] J. Cugnon. “Monte Carlo calculation of high-energy heavy-ion interactions”. In: Phys. Rev. C 22 (1980), pp. 1885–1896. DOI: `10.1103/PhysRevC.22.1885`.

[359] G. F. Bertsch, H. Kruse, and S. D. Gupta. “BOLTZMANN EQUATION FOR HEAVY ION COLLISIONS”. In: Phys. Rev. C 29 (1984). [Erratum: Phys.Rev.C 33, 1107–1108 (1986)], pp. 673–675. DOI: `10.1103/PhysRevC.33.1107`.

[360] J. Cugnon, C. Volant, and S. Vuillier. “Improved intranuclear cascade model for nucleon - nucleus interactions”. In: Nucl. Phys. A 620 (1997), pp. 475–509. DOI: `10.1016/S0375-9474(97)00186-3`.

[361] A. Boudard et al. “Intranuclear cascade model for a comprehensive description of spallation reaction data”. In: Phys. Rev. C 66 (2002), p. 044615. DOI: `10.1103/PhysRevC.66.044615`.

[362] Y. Sawada et al. “Intranuclear cascade with emission of light fragment code implemented in the transport code system PHITS”. In: Nucl. Instrum. Meth. B 291 (2012), pp. 38–44. DOI: `10.1016/j.nimb.2012.08.025`.

[363] Yusuke Uozumi et al. “Intranuclear cascade model including collective excitations and trajectory deflections for (p, p-prime x) reactions around 50 MeV”. In: Phys. Rev. C 86 (2012), p. 034610. DOI: `10.1103/PhysRevC.86.034610`.

[364] Tomasz Golan, Cezary Juszczak, and Jan T. Sobczyk. “Final State Interactions Effects in Neutrino-Nucleus Interactions”. In: Phys. Rev. C 86 (2012), p. 015505. DOI: `10.1103/PhysRevC.86.015505`. arXiv: `1202.4197 [nucl-th]`.

[365] Ulrich Mosel. “Neutrino event generators: foundation, status and future”. In: J. Phys. G 46.11 (2019), p. 113001. DOI: `10.1088/1361-6471/ab3830`. arXiv: `1904.11506 [hep-ex]`.

[366] Joshua Isaacson et al. “New approach to intranuclear cascades with quantum Monte Carlo configurations”. In: Phys. Rev. C 103.1 (2021), p. 015502. DOI: `10.1103/PhysRevC.103.015502`. arXiv: `2007.15570 [hep-ph]`.

[367] Steven Dytman et al. “Comparison of validation methods of simulations for final state interactions in hadron production experiments”. In: Phys. Rev. D 104.5 (2021), p. 053006. DOI: `10.1103/PhysRevD.104.053006`. arXiv: `2103.07535 [hep-ph]`.

[368] G. F. Bertsch and S. Das Gupta. "A Guide to microscopic models for intermediate-energy heavy ion collisions". In: Phys. Rept. 160 (1988), pp. 189–233. DOI: 10.1016/0370-1573(88)90170-6.

[369] Kaushik Borah et al. "Parametrization and applications of the low-Q^2 nucleon vector form factors". In: Phys. Rev. D 102.7 (2020), p. 074012. DOI: 10.1103/PhysRevD.102.074012. arXiv: 2003.13640 [hep-ph].

[370] L. Alvarez-Ruso et al. "Snowmass 2021 LoI: Neutrino-induced Shallow- and Deep-Inelastic Scattering". In: 2022 Snowmass Summer Study. Sept. 2020. arXiv: 2009.04285 [hep-ex].

[371] T. Le et al. "Measurement of $\bar{\nu}_\mu$ Charged-Current Single π^- Production on Hydrocarbon in the Few-GeV Region using MINERvA". In: Phys. Rev. D 100.5 (2019), p. 052008. DOI: 10.1103/PhysRevD.100.052008. arXiv: 1906.08300 [hep-ex].

[372] D. Coplowe et al. "Probing nuclear effects with neutrino-induced charged-current neutral pion production". In: Phys. Rev. D 102.7 (2020), p. 072007. DOI: 10.1103/PhysRevD.102.072007. arXiv: 2002.05812 [hep-ex].

[373] D. Ruterbories et al. "Measurement of inclusive charged-current ν_μ cross sections as a function of muon kinematics at $< E_\nu >\sim 6\ GeV$ on hydrocarbon". In: Phys. Rev. D 104.9 (2021), p. 092007. DOI: 10.1103/PhysRevD.104.092007. arXiv: 2106.16210 [hep-ex].

[374] K. Abe et al. "First T2K measurement of transverse kinematic imbalance in the muon-neutrino charged-current single-π^+ production channel containing at least one proton". In: Phys. Rev. D 103.11 (2021), p. 112009. DOI: 10.1103/PhysRevD.103.112009. arXiv: 2102.03346 [hep-ex].

[375] K. Abe et al. "Simultaneous measurement of the muon neutrino charged-current cross section on oxygen and carbon without pions in the final state at T2K". In: Phys. Rev. D 101.11 (2020), p. 112004. DOI: 10.1103/PhysRevD.101.112004. arXiv: 2004.05434 [hep-ex].

[376] M. A. Acero et al. "Measurement of the Double-Differential Muon-neutrino Charged-Current Inclusive Cross Section in the NOvA Near Detector". In: (Sept. 2021). arXiv: 2109.12220 [hep-ex].

[377] Artur M. Ankowski and Alexander Friedland. "Assessing the accuracy of the GENIE event generator with electron-scattering data". In: Phys. Rev. D 102.5 (2020), p. 053001. DOI: 10.1103/PhysRevD.102.053001. arXiv: 2006.11944 [hep-ph].

[378] A. Papadopoulou et al. "Inclusive Electron Scattering And The GENIE Neutrino Event Generator". In: Phys. Rev. D 103 (2021), p. 113003. DOI: 10.1103/PhysRevD.103.113003. arXiv: 2009.07228 [nucl-th].

[379] A. A. Aguilar-Arevalo et al. "The Neutrino Flux prediction at MiniBooNE". In: Phys. Rev. D 79 (2009), p. 072002. DOI: 10.1103/PhysRevD.79.072002. arXiv: 0806.1449 [hep-ex].

[380] K. Abe et al. "Measurements of neutrino oscillation in appearance and disappearance channels by the T2K experiment with 6.6×10^{20} protons on target". In: Phys. Rev. D 91.7 (2015), p. 072010. DOI: 10.1103/PhysRevD.91.072010. arXiv: 1502.01550 [hep-ex].

[381] L. Aliaga et al. "Neutrino Flux Predictions for the NuMI Beam". In: Phys. Rev. D 94.9 (2016). [Addendum: Phys. Rev. D 95, 039903 (2017)], p. 092005. DOI: 10.1103/PhysRevD.94.092005. arXiv: 1607.00704 [hep-ex].

[382] G. Bellini et al. "Neutrinos from the primary proton–proton fusion process in the Sun". In: Nature 512.7515 (2014), pp. 383–386. DOI: 10.1038/nature13702.

[383] Kajetan Niewczas and Jan T. Sobczyk. "Nuclear Transparency in Monte Carlo Neutrino Event Generators". In: Phys. Rev. C 100.1 (2019), p. 015505. DOI: `10.1103/PhysRevC.100.015505`. arXiv: `1902.05618 [hep-ex]`.

[384] Noemi Rocco. "Ab initio Calculations of Lepton-Nucleus Scattering". In: Front. in Phys. 8 (2020), p. 116. DOI: `10.3389/fphy.2020.00116`.

[385] Apostolos Pilaftsis and Carlos E. M. Wagner. "Higgs bosons in the minimal supersymmetric standard model with explicit CP violation". In: Nucl. Phys. B 553 (1999), pp. 3–42. DOI: `10.1016/S0550-3213(99)00261-8`. arXiv: `hep-ph/9902371`.

[386] F. Englert and R. Brout. "Broken Symmetry and the Mass of Gauge Vector Mesons". In: Phys. Rev. Lett. 13 (1964). Ed. by J. C. Taylor, pp. 321–323. DOI: `10.1103/PhysRevLett.13.321`.

[387] Peter W. Higgs. "Broken Symmetries and the Masses of Gauge Bosons". In: Phys. Rev. Lett. 13 (1964). Ed. by J. C. Taylor, pp. 508–509. DOI: `10.1103/PhysRevLett.13.508`.

[388] G. S. Guralnik, C. R. Hagen, and T. W. B. Kibble. "Global Conservation Laws and Massless Particles". In: Phys. Rev. Lett. 13 (1964). Ed. by J. C. Taylor, pp. 585–587. DOI: `10.1103/PhysRevLett.13.585`.

[389] Ian Low, Witold Skiba, and David Tucker-Smith. "Little Higgses from an antisymmetric condensate". In: Phys. Rev. D 66 (2002), p. 072001. DOI: `10.1103/PhysRevD.66.072001`. arXiv: `hep-ph/0207243`.

[390] Henning Bahl and Wolfgang Hollik. "Precise prediction of the MSSM Higgs boson masses for low M_A". In: JHEP 07 (2018), p. 182. DOI: `10.1007/JHEP07(2018)182`. arXiv: `1805.00867 [hep-ph]`.

[391] Henning Bahl, Nick Murphy, and Heidi Rzehak. "Hybrid calculation of the MSSM Higgs boson masses using the complex THDM as EFT". In: Eur. Phys. J. C 81.2 (2021), p. 128. DOI: `10.1140/epjc/s10052-021-08939-7`. arXiv: `2010.04711 [hep-ph]`.

[392] Henning Bahl and Ivan Sobolev. "Two-loop matching of renormalizable operators: general considerations and applications". In: JHEP 03 (2021), p. 286. DOI: `10.1007/JHEP03(2021)286`. arXiv: `2010.01989 [hep-ph]`.

[393] M. Carena et al. "CP Violation in Heavy MSSM Higgs Scenarios". In: JHEP 02 (2016), p. 123. DOI: `10.1007/JHEP02(2016)123`. arXiv: `1512.00437 [hep-ph]`.

[394] Nick Murphy and Heidi Rzehak. "Higgs-Boson Masses and Mixings in the MSSM with CP Violation and Heavy SUSY Particles". In: (Sept. 2019). arXiv: `1909.00726 [hep-ph]`.

[395] Henning Bahl, Stefan Liebler, and Tim Stefaniak. "MSSM Higgs benchmark scenarios for Run 2 and beyond: the low $\tan\beta$ region". In: Eur. Phys. J. C 79.3 (2019), p. 279. DOI: `10.1140/epjc/s10052-019-6770-z`. arXiv: `1901.05933 [hep-ph]`.

[396] T. P. Cheng and Marc Sher. "Mass Matrix Ansatz and Flavor Nonconservation in Models with Multiple Higgs Doublets". In: Phys. Rev. D 35 (1987), p. 3484. DOI: `10.1103/PhysRevD.35.3484`.

[397] Antonio Pich and Paula Tuzon. "Yukawa Alignment in the Two-Higgs-Doublet Model". In: Phys. Rev. D 80 (2009), p. 091702. DOI: `10.1103/PhysRevD.80.091702`. arXiv: `0908.1554 [hep-ph]`.